Systematic study of high-p_T di-jet correlations in nuclear collisions with the PHENIX experiment at RHIC

by

Nathan Conrad Grau

A dissertation submitted to the graduate faculty

in partial fulfillment of the requirements for the degree of

DOCTOR OF PHILOSOPHY

Major: Nuclear Physics

Program of Study Committee:
Craig A. Ogilvie, Major Professor
Steve Kawaler
John G. Lajoie
Gary Tuttle
James Vary

Iowa State University

Ames, Iowa

2005

Graduate College
Iowa State University

This is to certify that the doctoral dissertation of

Nathan Conrad Grau

has met the dissertation requirements of Iowa State University

_____

Major Professor

_____

For the Major Program

DEDICATION

I would like to dedicate this work to my wife Nikki and my son Brandon - the reasons to do anything. Merrily, merrily, merrily ...

TABLE OF CONTENTS

LIST OF TABLES

LIST OF FIGURES

ACKNOWLEDGEMENTS

ABSTRACT

The purpose of the Relativistic Heavy Ion Collider (RHIC) at Brookhaven National Laboratory on Long Island, New York is to study Quantum Chromodynamic (QCD) matter under extreme temperatures and densities. Under these conditions it is expected that normal nuclear matter will not exist but a quark-gluon plasma (QGP) will form where the constituent quarks and gluons within the nucleon will not be bound within the size of the nucleon (~ 1 fm). Such a state of matter is suggested to have been the state of the primordial universe only several μs after the Big Bang.

One of the initial results from collisions of Au+Au ions at nucleon-nucleon center-of-mass energy, $\sqrt{s_{NN}}$, of 130 GeV that indirectly indicated that a quark-gluon plasma was formed was the dramatic suppression of single particle spectra compared to binary-scaled single particle spectra from p+p collisions. This "jet suppression" was predicted and is well reproduced by models where outgoing partons lose energy in the quark-gluon plasma via gluon bremsstrahlung. Further evidence for energy loss comes from two-particle correlations. Two particle correlations, the subject of this thesis, are distributions where low energy jets are studied in a heavy ion collisions where many low energy particle production are present by triggering on a particle with large momentum transverse to the beam direction (p_T) and studying the event shape of other particles in the event relative to the trigger. It is observed that the yield of back-to-back pairs, those offset by π radians, are strongly suppressed indicating that the back-to-back jet loses a significant amount of energy. Further observations from correlations in Au+Au indicate that the the back-to-back pairs are on average not π radians from one another but that a local minimum develops at π radians. In all, there is strong evidence that high-p_T jet properties are modified in the hot, dense medium created in central Au+Au

collisions at RHIC energies.

This thesis represents the first systematic study of jet properties in nuclear collisions. Jet properties using two-particle azimuthal correlations in p+p collisions serve as a necessary baseline for the potential modification of jet properties in nuclear collisions. At RHIC energies d+Au are not predicted to have high enough energy density to produce a quark-gluon plasma. Therefore, any modification of properties in these collisions represent the "cold" nuclear medium effects that will be present in the initial state of A+A collisions at RHIC. Several observables indicate that jet properties in p+p and d+Au collisions are very similar. For example, multiple scattering prior to and after the hard scattering will increase the acoplanarity of di-jets, i.e. how back-to-back are a pair of jets. This has been quantified as $\langle \sin^2 \phi_{jj} \rangle_{d+Au} - \langle \sin^2 \phi_{jj} \rangle$ where ϕ_{jj} is the relative angle between the outgoing jets. The average value from all PHENIX data is 0.004±0.008(stat.)±0.009(sys.). This result is zero within errors meaning there is no measurable difference between the acoplanarity of di-jets in d+Au collisions compared to p+p collisions. This data places a limit on the amount of multiple scattering that the partons undergo in the initial and final state in d+Au collisions at RHIC.

Jet properties from Au+Au collisions greatly extend the p_T reach from the previous jet studies to test whether the modifications observed at lower p_T persist to higher p_T. From energy loss models the back-to-back yield are expected to decrease while the width of the distribution is expected to increase. The data indicate, from direct measurement from the correlations and from a measure of x_E and p_{out} distributions, that the conditional yields are suppressed from peripheral to central collisions while the away-side distribution does not broaden compared to peripheral Au+Au and p+p collisions. These results are inconsistent with a model of energy loss by incoherent scattering. However, such energy loss models are able to reproduce the single particle and pair yield suppression in central Au+Au. It is a challenge now to determine the correct energy loss model that will incorporate the single particle suppression and elliptic flow data at high-p_T with the data from this thesis, i.e. the suppression of the away-side and the lack of away-side broadening.

CHAPTER 1.   Relativistic Heavy Ion Collisions

The purpose of the Relativistic Heavy Ion Collider (RHIC) at Brookhaven National Laboratory on Long Island, New York is to study Quantum Chromodynamic (QCD) matter under extreme temperatures and densities. QCD is the theory of strong interactions which is responsible for binding protons and neutrons in nuclei. Under extreme conditions it is expected that normal nuclear matter will not exist but a quark-gluon plasma (QGP) will form where the constituent quarks and gluons within the nucleon will not be bound within the size of the nucleon (~ 1 fm). Such a state of matter is suggested to have existed in the primordial universe only several μs after the Big Bang. Evidence for the existence of a phase transition is based on lattice calculations. Lattice calculations are numerical solutions of the QCD equations of motion on a four dimensional lattice of space-time points. Fig. 1.1 shows the energy density as a function of temperature where a large increase in the energy density is calculated at the critical temperature. This critical temperature is approximately 170 MeV or, in more familiar units, about 10^{12}K.

1.1   (Strongly-Interacting) Quark Gluon Plasma

In the last year all four RHIC experiments, BRAHMS [Arsene et al., 2005], PHENIX [Adcox et al., 2005], PHOBOS [Back et al., 2005], and STAR [Adams et al., 2005], simultaneously submitted a review of the data from the first three years at RHIC, 2000-2003. During this time p+p, d+Au, and Au+Au collisions at nucleon-nucleon center-of-mass energy $\sqrt{s_{NN}}$ of 200 GeV were run. These reviews resulted in a conclusion that the matter produced at RHIC is unique. That is, the matter acts more like a fluid than a dilute gas of free quarks and gluons. The calculations from the lattice in Fig. 1.1 show that even at 4 times the critical temperature
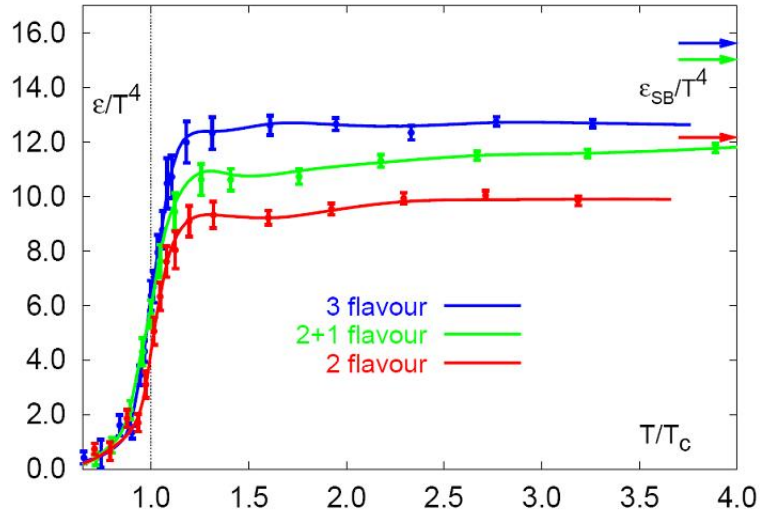
Figure 1.1   QCD energy density as a function of temperature.

the energy density is still below the Stefan-Boltzmann limit. This Stefan-Boltzmann limit describes a dilute gas of non-interacting particles. Since the limit is not reached even at 4 times the critical temperature, the calculations indicate that the matter is strongly interacting. Two key experimental elements of this conclusion that the matter is more fluid-like than a gas are a large energy density at the formation time of the QGP and a strong collective motion of the bulk of the particles, *i.e* those particles produced at low transverse momentum.

The lattice calculations conclude that the energy density required for a phase transition to a QGP is 1 GeV/fm^3 or 10 times the energy density of normal nuclear matter. This energy density can be estimated by experiments using the Bjorken energy density [Bjorken, 1983]. This estimate of the energy density is based on two Lorentz contracted disks that interact and fly apart from one another. The cylindrical region between the disks is the origin of the produced particles.

$$\epsilon_{Bj} = \frac{1}{\pi R^2} \frac{1}{\tau_0} \frac{dE_T}{dy} \tag{1.1}$$

In the above equation R is the nuclear radius, τ_0 is the formation time of the plasma typically taken as 1 fm/c for an order-of-magnitude estimate, and y is the rapidity which is related to the longitudinal velocity of the particle. The energy density is simply the transverse energy

in the cylindrical volume. Using the above formula and data an energy density of at least 15 GeV/fm^3 is estimated in Au+Au collisions at 200 GeV. This is significantly larger than required for the expected phase transition.
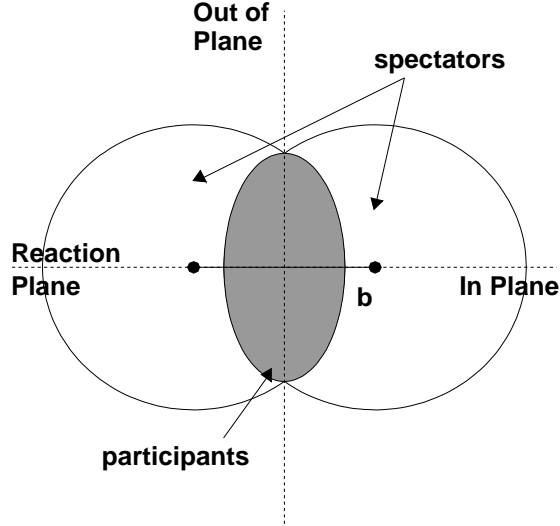
Figure 1.2   Schematic diagram of a peripheral nuclear collision. The over-lap (shaded grey) almond-shaped region is where the nucleons which participate in the interaction are located. The reaction plane is defined as the short length of overlap region.

Evidence for strong collective motion of the bulk of the constituents is observable in elliptic flow. In a non-head-on (peripheral) heavy ion collisions a pressure gradient along the short axis (reaction plane) of the resulting almond-shaped overlap region results (see Fig. 1.2). This pressure gradient correlates particles with the reaction plane. The single particle distribution can be written as a Fourier transform where the 2nd Fourier coefficient is the dominant term.

$$\frac{dN}{d\phi dp_T} = \frac{N}{2\pi} \left(1 + 2v_2\left(p_T\right)\cos\left(2\Delta\phi\right)\right) \tag{1.2}$$

The coefficient v_2 is a measure of the strength of the correlation with the reaction plane and is sensitive to the pressure gradients in the overlap region. Hydrodynamic calculations which assume thermal equilibrium and an input equation of state relating temperature, pressure, and energy density are able, for the first time, to reproduce the measured v_2 at RHIC. This fact

possibly indicates that thermal equilibrium is reached and has only been reached at RHIC.

The hydrodynamic calculations lend support to the idea that the medium produced at RHIC is a thermal system. The v_2 measurements from RHIC (which are sensitive to pressure gradients) are larger than expected, indicating that there exist large pressure gradients and strong collective motion of the elements of the medium. Such collective flow is more indicative of a strongly interacting fluid than that of a weakly interacting gas. Further, hydrodynamic calculations that reproduce the data assuming a zero viscosity. Therefore, it has been argued that the medium produced at RHIC in Au+Au collisions is a perfect fluid. This has also led some to rename the QGP to sQGP for strongly-interacting QGP.

1.2 Effects of the sQGP
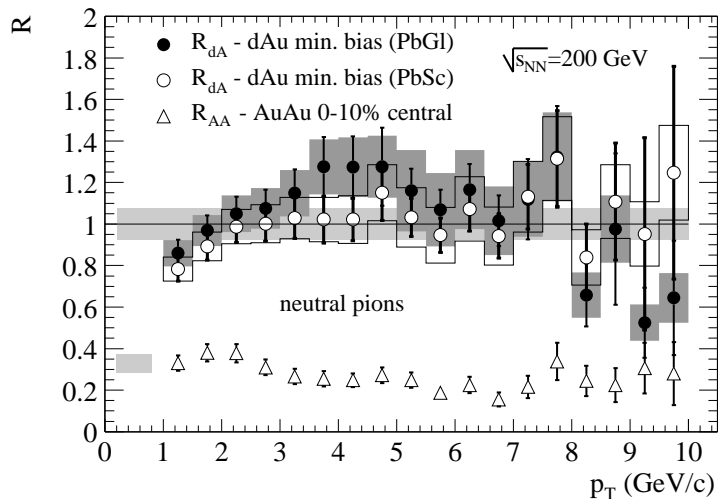
Figure 1.3   Comparison of ratio of single particle spectra in d+Au collisions (open and closed circles) and Au+Au collisions (triangles) compared to binary-scaled p+p collisions.

One of the most exciting results from the first RHIC run of Au+Au at $\sqrt{s_{NN}}$=130 GeV in 2000 was the discovery of high-p_T single particle suppression compared to p+p reactions [Adcox et al., 2002]. This measurement has been extended to higher p_T in a the more recent Au+Au run at $\sqrt{s_{NN}}$ of 200 GeV in 2002-2003, see Fig. 1.3. One can compare inclusive production in

Au+Au collisions with p+p collisions by forming the ratio

$$R_{AA} = \frac{\frac{1}{2\pi p_T N_{evt}} \frac{d^2 N_{Au+Au}}{dp_T dy}}{\langle N_{coll} \rangle \frac{1}{2\pi p_T N_{evt}} \frac{d^2 N_{p+p}}{dp_T dy}} \tag{1.3}$$

where $\langle N_{coll} \rangle$ is the average number of nucleon-nucleon (binary) collisions in the overlap region of the Au+Au collision. The interpretation of R_{AA} is if $R_{AA} = 1$, then the Au+Au production is an incoherent superposition of p+p collisions. If R_{AA} is above 1, then nuclear effects enhance the production compared to p+p collisions. If R_{AA} is less than 1, nuclear effect suppress the production compared to p+p collisions. It is clear from Fig. 1.3 that in central Au+Au collisions there is a factor of ~ 5 suppression compared to binary-scaled p+p collisions. This can be compared to d+Au collision results where no hot, dense nuclear medium is expected to be produced. Instead of a suppression in d+Au collisions a slight enhancement of particle production is observed which is consistent with other p+A measurements at lower energies and is known as the Cronin effect [Cronin et al., 1975]. The typical interpretation of the Cronin effect is the multiple scattering of a parton from projectile nucleus through the target nucleus prior to the hard scattering (initial state), and multiple scattering of the outgoing parton in the cold nuclear medium after the hard scattering (final state). Because the suppression is not present in d+Au collisions the strong suppression in Au+Au is an effect that is unique to the Au+Au collisions.

1.3   Thesis Organization

The content of this thesis is focused on jet shapes and yields from p+p through Au+Au collisions in an attempt to characterize the cold and hot, dense nuclear matter effects on jets. Jets are a correlated spray of hadrons which result from the hadronization of a fast moving parton. Jets are well-known objects and have been studied extensively in $e^+ + e^-$ annihilation, deep-inelastic lepton-hadron scattering, and hadronic collisions over a very large energy range. Before the advent of RHIC, jets in A+A collisions had not been directly studied since the previous A+A collisions at Brookhaven's Alternating Gradient Synchrotron (AGS)

and the CERN's Super Proton Synchrotron (SPS) were performed at $\sqrt{s_{NN}} < 20$ GeV. At these energies high momentum transverse to the beam direction (p_T) processes, i.e. processes producing particles with $p_T > 2$ GeV/c, are extremely rare. At the highest RHIC energy, 200 GeV per nucleon, probing moderate p_T jets has become possible. These jets are an especially useful probe in all nuclear collisions because 1) jets originate from partons which are colored and will interact strongly with any surrounding medium, 2) the effect of these interactions will survive the hadronization process of a QGP, and 3) jet production is a hard process, i.e. a process with large momentum transfer, and is calculable in perturbative QCD (pQCD) so a comparison with theoretical expectations is, in principle, possible.

In order to do a detailed and quantitative study of jet properties and nuclear effects on these properties in heavy ion collisions, it is necessary to measure jet production in p+p collisions as a baseline to define vacuum jet production. Once a p+p baseline has been measured study of p+A collisions measure effects due to initial state interactions that a single nucleon suffers in a heavy ion collision. Finally, by comparing the resulting jet production in heavy ion collisions to p+p and p+A collision, any new final state effects, such as those from due to a QGP, can be measured.

The outline of this thesis is as follows. The second chapter reviews the necessary theoretical and experimental results involving jets, including their discovery in $e^+ + e^-$ annihilation, to the introduction of the parton model and its relevance to deep-inelastic scattering, and jets in $p + p(\bar{p})$ collisions at high energy colliders. A discussion of experimental results from fixed target p+A collisions as well as a theoretical discussion of those results follows. Finally, relevant results from high-p_T and jets in A+A collisions and theoretical work on high-p_T and jets in a QGP are discussed. Chapter 3 introduces the PHENIX detector with a somewhat detailed discussion of the relevant subsystems, as well as a general discussion of the charged particle tracking algorithm, triggering in different species, and centrality determination in different species. Chapter 4 introduces the two-particle correlation method, as well as introducing the jet quantities we will measure and how they are derived from the two-particle correlation function. Chapter 5 details the analysis of data from p+p and d+Au collisions in parallel since

the analysis is very similar. The extracted quantities from the correlation functions are shown. Chapter 6 outlines the analysis of the Au+Au data including all of the correlation functions and the extracted distributions. Finally, Chapter 7 reviews all of the relevant data and relates them to the theoretical discussion from Chapter 2. These results are placed in relationship to similar results to form conclusions about nature of jet modification in p+p, d+Au, and Au+Au collisions at RHIC energies.

CHAPTER 2.   QCD, Hard Scattering, and the Effects of the Nuclear Environment

This chapter reviews the necessary background for understanding jet production in hadronic collisions. First, QCD and the expected phase transition is discussed. Next the history of jet production in $e^+ + e^-$, deep inelastic e^-+p, and p($\bar{p}$)+p collisions is reviewed. The data and interpretation of high-p_T and jet production in p+A collisions are presented. Finally, the data on jet production in A+A collisions is reviewed while introducing energy loss in a QGP.

2.1   Basics of Quantum Chromodynamics

Quantum Chromodynamics (QCD), the strong nuclear force, describes the interactions responsible for the binding of nuclei. QCD is a quantum field theory defined by the free Lagrangian

$$\mathcal{L} = \bar{\psi}_f[i\gamma^\mu\partial_\mu - m_f]\psi_f - \frac{1}{4}\mathbf{F}_A^{\mu\nu}\mathbf{F}_{\mu\nu}^A \tag{2.1}$$

The Lagrangian is written with the Einstein convention of summing over repeated indices. ψ_f is the three-component scaler quark field of flavor f. The three components represent the three color charges red, blue, and green. The flavor f represents the 6 quark flavors up, down, strange, charm, bottom, and top. $\mathbf{A}_\mu$ is one of 8 massless, vector gluon fields. Quarks and gluons are collectively called partons for historical reasons (see below). The field strength tensor, $\mathbf{F}_{\mu\nu}^A$, is defined as

$$\mathbf{F}_{\mu\nu}^A = \partial_\mu\mathbf{A}_\nu^A - \partial_\nu\mathbf{A}_\mu^A - \sqrt{4\pi\alpha_s}f^{ABC}\mathbf{A}_\mu^B\mathbf{A}_\nu^C \tag{2.2}$$

The f^{ABC} are the structure constants of the SU(3) symmetry group, the group which defines the QCD Lagrangian. A,B,C are summed from 1 to 8. α_s is the strong coupling "constant" which defines the strength of the interaction.

From the Lagrangian, the Feynman rules are defined, see Fig. 2.1. The first term in Eqn. 2.2 with Eqn. 2.1 defines the vertex for the interaction of two spin-$\frac{1}{2}$ quarks with a spin-1, massless gluon in analogy with Quantum Electrodynamics (QED). The square of the field strength tensor results in a three and a four gluon vertex. These vertices have no analogy in QED and are responsible for the non-Abelian nature of QCD. That is, unlike the neutral photon which does not interact with itself, the gluons have color and can interact with themselves.
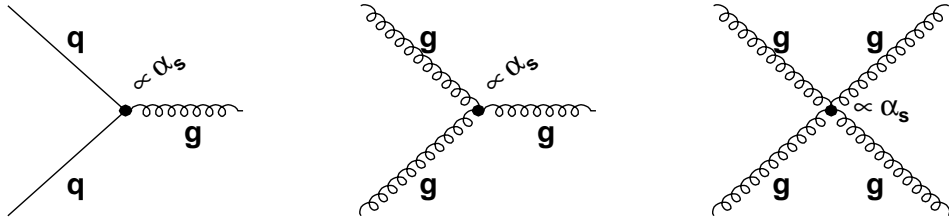
Figure 2.1   Two quark (left), three gluon (middle), and four gluon (right) vertices. In perturbative calculations these vertices are proportional to α_s.

Applying the Feynman diagram approach is useful only for a perturbative process. For any given interaction, there are infinitely many diagrams that can be written and calculated. Every vertex of every diagram is proportional to the coupling constant. If the coupling constant is small, then a converging power series can be written. Those diagrams with the fewest vertices dominate and are calculated. This process is known as perturbative QCD (pQCD). As was shown by Gross and Wilczek [1973] and Politzer [1973], QCD exhibits asymptotic freedom. That is, α_s is not constant but is a decreasing function of Q^2, the momentum transfer of the process.

$$\alpha_s\left(Q^2, \mu^2\right) = \frac{\alpha_s\left(\mu^2\right)}{1 + \frac{33 - 2n_f}{12\pi}\alpha_s\left(\mu^2\right)\ln\left(Q^2/\mu^2\right)} \tag{2.3}$$

In the above equation, n_f is the number of quark flavors, 6 in the standard model, and μ^2 is

the arbitrary renormalization scale. This renormalization scale defines the scale at which we lose information on the high-energy aspects of the theory. For a sufficiently high Q^2 process, the coupling constant, via Eqn 2.3, becomes small enough for a perturbative calculations. This has been measured from data. Fig. 2.2 is a compilation of the data revealing the decreasing coupling with increasing momentum transfer.
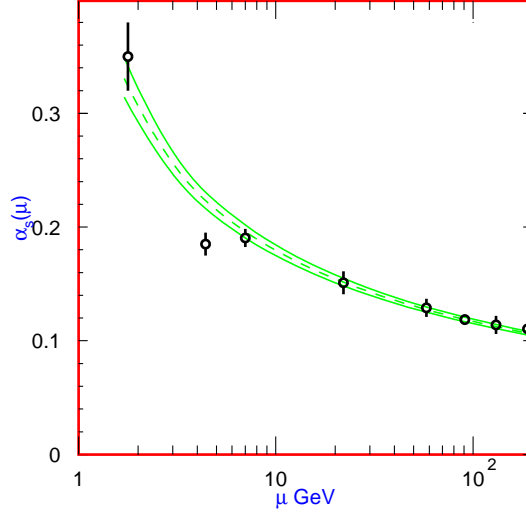
Figure 2.2 The QCD coupling constant as function of $\mu \equiv Q$ from measured data from $e^+ + e^-$ annihilations. There is a clear decrease as a function of increasing momentum transfer. (Compiled from Eidelman et al. [2004])

To gain further insight, the above result can be rewritten as

$$\alpha_S\left(Q^2\right) = \frac{12\pi}{(33 - 2n_f)\ln\left(\frac{Q^2}{\Lambda^2}\right)} \tag{2.4}$$

where Λ has the qualitative definition of being the momentum scale at which the QCD coupling constant is large and thus where the perturbation series does not converge. The value of Λ can be found from data on α_S vs Q^2, see Fig. 2.2. This value is around 100-200 MeV/c. If $Q^2 \gg \Lambda^2$, then the coupling is small and the process can be calculated perturbatively. Such processes are called hard processes. If $Q^2 \sim \Lambda^2$ then the process cannot be treated perturbatively. In

this thesis jets with energies of several to tens of GeV are considered. These processes are in the hard regime and the partonic interactions are calculable with pQCD.

The coupling constant of the theory, α_s, is not constant but depends on the momentum transfer of the process being measured, Q^2. By the uncertainty relation a process that is hard (i.e. with high-Q^2) probes short distance scales. For a soft (low-Q^2 process), the distance scale that is probed is large. Thus at short distance scales the partonic interactions can be considered without regard to their confinement within a hadron. This results in the seemingly paradoxical conclusion that quarks and gluons behave as free particles under hard processes. However, there is no evidence that they are free at smaller momentum scales. Soft processes create the hadrons that are measured by experiment from the free color charges.
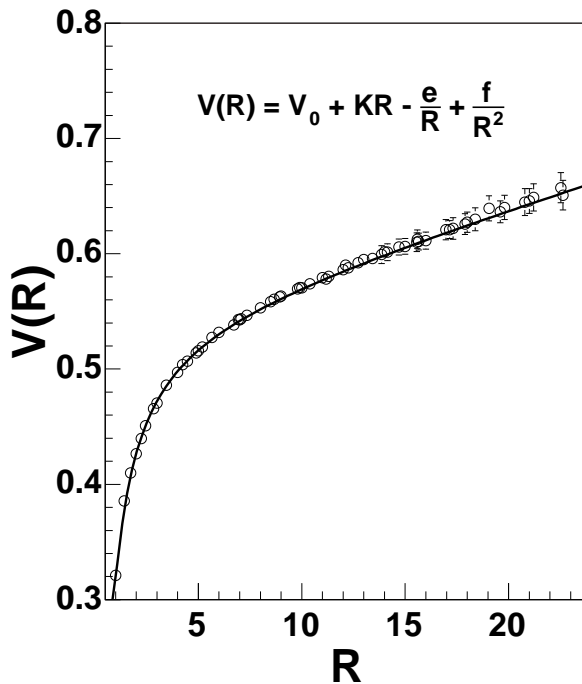
Figure 2.3   QCD potential (points) calculated from the lattice see Bali and Schilling [1993]. The solid line is a fit to the measured values with the form given.

This conclusion is further illuminated by results from lattice calculations. Such calculations of the QCD potential between two quarks [Bali and Schilling, 1993] is shown in Fig. 2.3. At large separation the potential is approximately linear. This implies a constant force rather

than a force diminishing with distance. As a pair of partons separate, the energy in the field increases to the point where there is enough energy to produce partons from the vacuum. This is one qualitative argument for the experimental result of confinement of partons within hadrons.
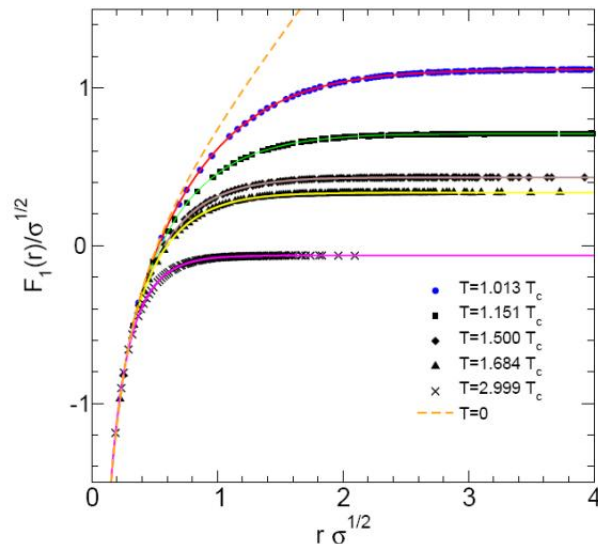
Figure 2.4   Free energy of a heavy quark pair as a function of the separation in lattice units calculated from the lattice at several different temperatures [Blaschke et al., 2005].

The potential shown in Fig. 2.3 is calculated at zero temperature. At high temperatures the potential is modified. Such a modification is shown in Fig. 2.4 where the free energy of a heavy quark pair is plotted as a function of separation for different temperatures. The dashed line indicates the free energy at zero temperature. As the temperature increases the asymptotic behavior begins to change. That is, the linear slope begins to decrease and turn over. At a temperature of about T_c the QCD potential at large distances has a zero slope resulting in a zero force between the heavy quark pair. Thus, they become asymptotically free at high temperature. This is entirely different than the linear rising potential and constant force resulting at zero temperature and causing confinement. What is truly remarkable is that lattice calculations indicate that the critical temperature is approximately 170 MeV, a temperature that is accessible to modern accelerators. The purpose of RHIC is to use nuclear

collisions to produce matter at a temperature above the T_c so as to study this phase transition.

2.2 Parton Model and Factorization

A brief history of QCD will aide in introducing several ideas that are important in jet production in heavy ion collisions. This history resulted in the experimental evidence for the structure of QCD. The history is not a temporal one but a systematic review of experimental results from the more simple systems and their theoretical implications as a background for studying jet production in nuclear collisions.

2.2.1 $e^+ + e^-$ Collisions
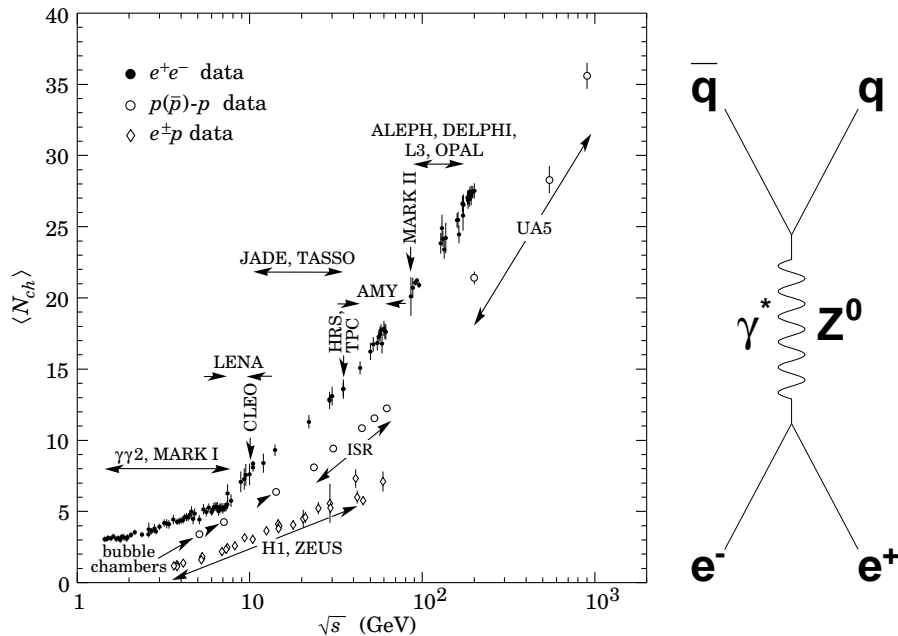
Figure 2.5   Event average charged particle multiplicity in $e^+ + e^-$, $e + p$, and $p + p(\bar{p})$ collisions (Compiled in Eidelman et al. [2004]).

The simplest collisions to study QCD are in electron-positron annihilation where the dominant Feynman diagram for hadron production is $e^+ + e^- \rightarrow q + \bar{q}$ (see Fig. 2.5) which is purely an electromagnetic or weak process depending on the center-of-mass energy and is calculable in perturbative QED or GWS (Glashow-Weinberg-Salam, eletroweak) theory. Because

of confinement the outgoing quarks are not detected but hadrons are produced from them. Fig. 2.5 shows the event-averaged charged particle multiplicity in $e^+ + e^-$ collisions. At none of the measured energies is the charged hadron multiplicity from $e^+ - e^-$ annihilation exactly 2. In fact, it is much larger than this. In leading order the two outgoing quarks produce many hadrons on average.

These charged hadrons are produced from the soft process responsible for quarks becoming hadrons, as discussed previously. Because it is a soft process, the resulting hadrons will have a very small transverse momentum with respect to the jet, i.e. nearly collinear with the jet. Therefore, the already back-to-back, quark-anti-quark pair produces many hadrons very close to themselves, resulting in a spray of back-to-back hadrons called di-jets. This process of the parent quark evolving into several hadrons is called fragmentation.
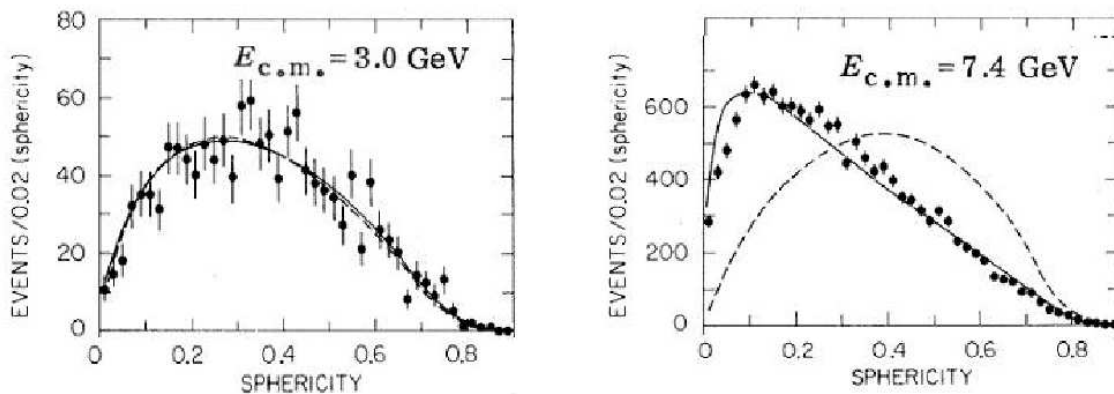
Figure 2.6   Sphericity (see text) of $e^+ + e^-$ events at SLAC [Hanson et al., 1975] for two different center of mass energies. The full line is a jet simulation and the dotted line is a phase space simulation.

The first evidence for di-jet events came from $e^+ + e^-$ collisions at $\sqrt{s} < 10$ GeV at SLAC in the mid 1970's. They defined a global event variable, the sphericity, as

$$S = \frac{3 \left(\sum_i p_{T,i}^2 \right)_{\min}}{2 \sum_i p_i^2} \tag{2.5}$$

where the sum is over all particles in the event. An axis is chosen to minimizes the transverse momentum of the particles with respect to that axis. This axis approximates the jet axis.
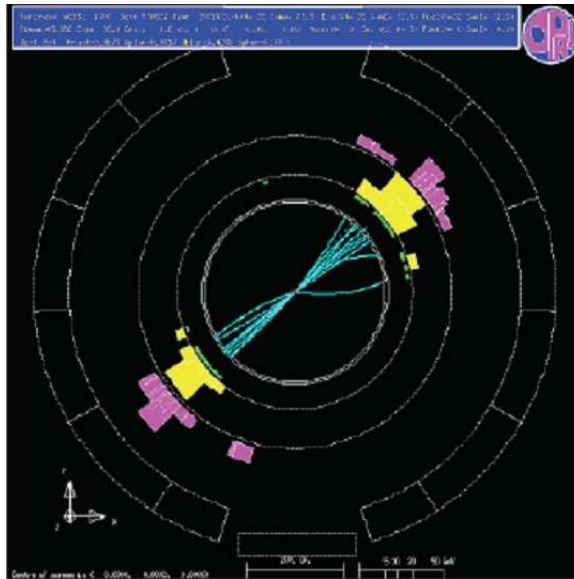
Figure 2.7   Event display from OPAL indicating two back-to-back sprays
of hadrons.

The sphericity quantifies how isotropic the event is with respect to the jet axis. If it is a completely isotropic, the sphericity is one. If there is a strong correlation with the measured axis, the sphericity tends to zero. Fig. 2.6 shows data from the SLAC-LBL collaboration at the SPEAR storage ring [Hanson et al., 1975]. At the lowest center-of-mass energy of the collision, the distribution favors a more uniform, random production of hadrons in the available phase space. At the higher center-of-mass energy, the data favors a more directed production along the jet axis.

As the center-of-mass of these collisions increases, clear di-jet signals become visible. Fig. 2.7 shows an event display from the OPAL collaboration at LEP where the center-of-mass energy is 91 GeV. There are clearly two back-to-back sprays of hadrons in this event.

Not only are event shapes measured in $e^+ + e^-$ collisions, but hadron cross-sections as well. These collisions are an especially clean environment to measure properties of jet production because all of the hadrons come from jets and the jet energy is exactly known. Since $e^+ - e^-$ is an annihilation process, all of the center-of-mass energy is converted into final state particle production. In the case of di-jets, because of momentum conservation, the jet energy is half of the center-of-mass energy ($\sqrt{s}/2$). Therefore, the production of particles of energy E_h can be
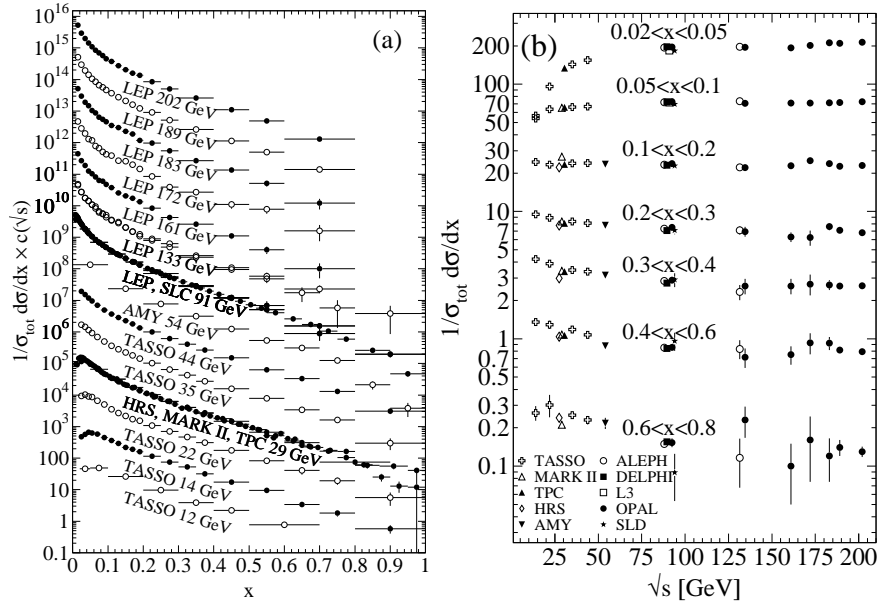
Figure 2.8   *Left:* Production of hadrons as a function of x, the fractional energy of the hadron with respect to the jet energy. There is a scale factor included in each of the center-of-mass energies. *Right:* Scaling of the fragmentation functions over a broad energy range. Data was compiled in Eidelman et al. [2004].

measured as a fraction of jet energy,

$$x = \frac{2E_h}{\sqrt{s}} \tag{2.6}$$

The measured hadronic cross-sections for a large range of center-of-mass energies is plotted in Fig. 2.8. These distributions cannot be calculated from first principles because fragmentation is a non-perturbative process. However since fragmentation is a long distance process as compared to the hard scattering, the cross-section factorizes as

$$\frac{1}{\sigma}\frac{d\sigma^h}{dx} = \sum_q \hat{\sigma}^q D_q^h(x) \tag{2.7}$$

That is, in leading order, the probability to produce a hadron h is determined by the cross-section to produce a quark q, $\hat{\sigma}^q$, and the probability for the quark, q, to fragment into hadron h with momentum fraction x of the parent quark, $D_q^h(x)$. The quark cross-section is determined by perturbative calculations. The test that fragmentation factorizes from the underlying

process is that these fragmentation functions can be applied universally in all collisions and not just $e^+ - e^-$ collisions. This universality is partly seen in the right panel of Fig. 2.8 where the $\sqrt{s}$ dependence of the hadronic cross sections are shown for different x-ranges. These distributions are nearly independent of $\sqrt{s}$.
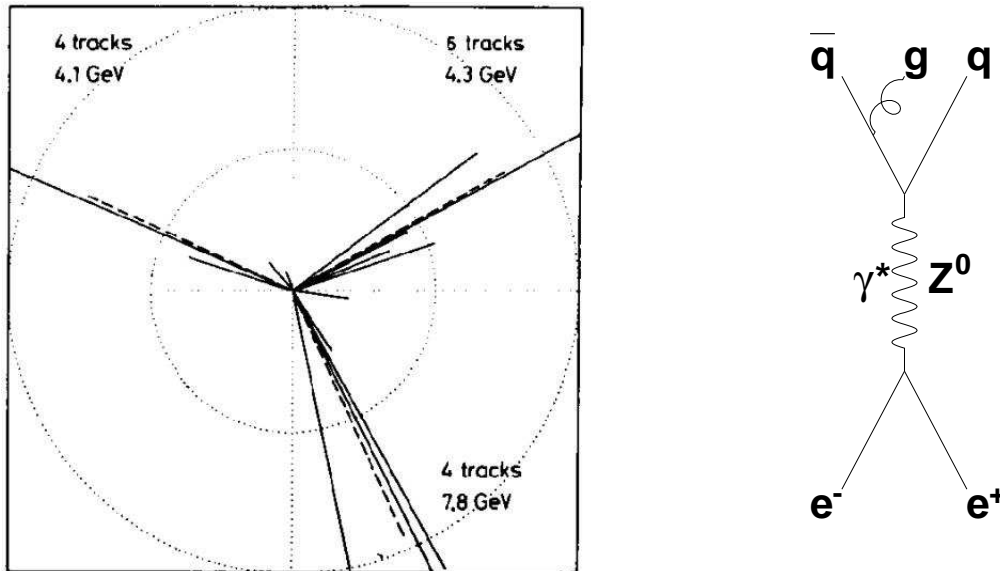
Figure 2.9   *Left:* An example of a beam view of a three jet event from TASSO at PETRA at DESY with $\sqrt{s}$ between 13 and 32 GeV [Brandelik et al., 1979; Barber et al., 1979]. *Right:* A third jet is due to a radiated hard gluon from one of the final state quarks.

Annihilations of electron and positions are also useful in studying higher-order QCD. The next-to-leading-order (NLO) pQCD diagrams involve a gluon being radiated from the final state or coupling the outgoing quark-anti-quark pair. If the radiated gluon is hard so that it does not interfere with the long range fragmentation and it is an external leg, it will fragment as well and produce a third jet of hadrons. Fig. 2.9 shows such an event in $e^+ + e^-$ collisions.

In calculations of the cross-section, perturbation theory only works when the gluons are hard. Any soft gluons will be collinear with the quark from which it is radiated. In leading order the cross-section for the gluon radiation is inversely proportional to the gluon momentum and so the cross-section is divergent for soft gluons. Such soft gluons are not distinguishable

from the fragmentation process. A scale is set for the gluons, the factorization scale, which defines the momentum scale that separates the short distance, hard, perturbative physics with the long distance, soft, non-perturbative physics.

2.2.2   Deep Inelastic Lepton-Hadron Collisions
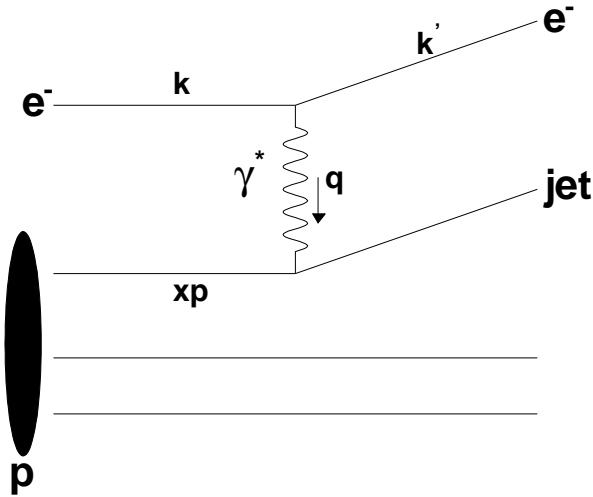
Figure 2.10   Schematic diagram of deep inelastic scattering of electrons off a proton. An electron with momentum k interacts with a parton in the proton with momentum fraction x of the proton and recoils with momentum k′. The struck parton produces a jet of hadrons.

The next simplest interaction where one can test QCD is deep-inelastic scattering of hadrons by leptons, Fig. 2.10. The focus in this section is on $e^- + p \rightarrow e^- + X$ collisions. The fundamental interaction is an elastic scattering of $e^- + q \rightarrow e^- + q$ where the scattered electron is detected and the liberated quark fragments into a jet. This is a direct measure of the proton interior since it is sensitive to the kinematics of the quark structure of the proton. The cross-section is dependent on, at most, the momentum transfer of the interaction

$$Q^2 = -q^2 = (k - k')^2 \tag{2.8}$$

and the fraction of the proton's momentum

$$x = \frac{p_q}{p} = \frac{Q^2}{2p \cdot q} \tag{2.9}$$

that the struck quark carries. The cross-section can be written in terms of the product of two tensors, one defining the leptonic vertex $e^- \rightarrow \gamma^* + e^-$ and the other in terms of the hadronic vertex $\gamma^* + p \rightarrow X$. The former tensor is determined from QED. By symmetry arguments and available vectors to create tensors, the later hadronic tensor is written in terms of at most two scalar functions (as coefficients of vector products) of x and Q^2 called structure functions, $F_1(x, Q^2)$ and $F_2(x, Q^2)$. These scalar functions define the partonic content of the proton.
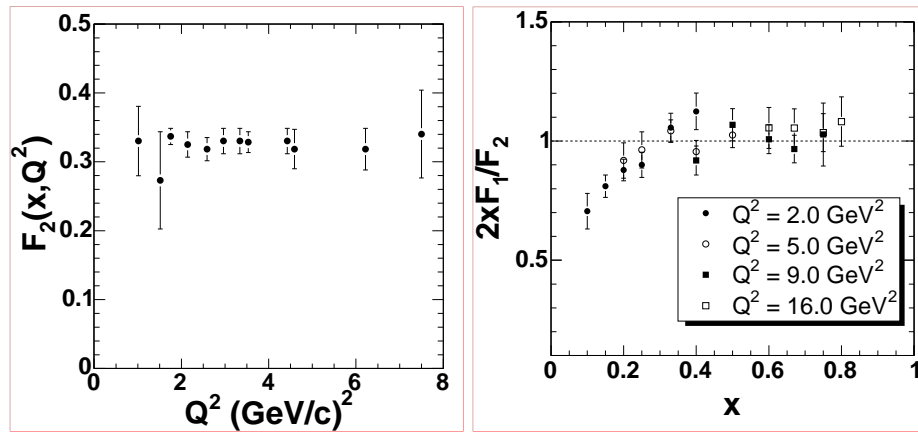
Figure 2.11   *Left:* F_2 structure function for different x values as a function of Q^2 [Friedman and Kendall, 1972]. Bjorken scaling is clearly seen. *Right:* Data from SLAC on the ratio of the two structure functions. The dashed line represents the Callan-Gross relationship. Data compiled from Bodek et al. [1979].

These experiments were first performed in SLAC in the late 1960's where the structure functions were extracted from the measured cross-sections [Bloom et al., 1969]. Bjorken had suggested if the proton substructure was point-like the structure functions would be independent of Q^2 [Bjorken, 1969]. This was shown from the SLAC data [Breidenbach et al., 1969]. Further, Callan and Gross showed that if the constituents are spin-1/2 particles the structure

functions are not independent [Callan and Gross, 1969].

$$F_2\left(x, Q^2\right) = 2xF_1\left(x, Q^2\right) \tag{2.10}$$

Fig. 2.11 shows the structure function $F_2(x, Q^2)$ for different ranges in x as a function of Q^2 [Friedman and Kendall, 1972] and the experimental observation of the Callan-Gross relationship [Bodek et al., 1979].

The structure function can be written as a sum of contributions of the different quarks. It is customary to define the parton distribution functions (PDFs) as $\phi_a^h\left(x, Q^2\right)$ which is the probability of finding a given parton a in hadron h. These distributions for a proton are shown in Fig. 2.12 for $Q^2 = 10$ GeV^2. At high-x the valence quarks, u and d, are dominant while at lower-x the gluons and the sea quarks become important.
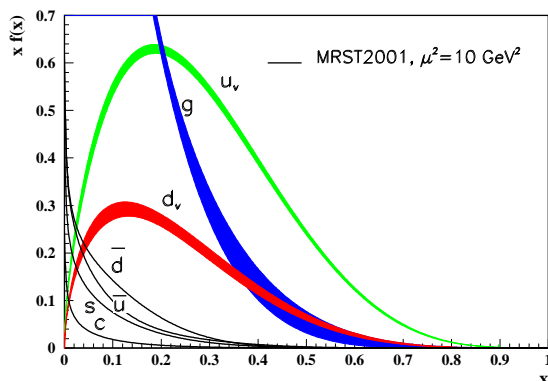
Figure 2.12   Parton distribution functions for several partons in the proton [Eidelman et al., 2004].

To describe these results Feynman Feynman [1969] and Bjorken Bjorken and Paschos [1969] independently proposed the parton model. This model provides a basis to calculate the cross-section for various quantities. For example, the total cross-section for electron-proton scattering can be written as

$$\sigma_{tot}^{ep} = \sum_a \int_0^1 dx \; \hat{\sigma}_{ea \to ea} \; \phi_a^p\left(x\right) \tag{2.11}$$

The total deep-inelastic scattering cross-section is expressed as the elastic scattering of an electron and parton a convoluted with the probability of finding parton a at a momentum fraction x of the proton. This formula factorizes the soft-QCD processes which are responsible for the partons being bound within the proton and the process of the hard scattering. Since the PDFs represent soft process, a long distance phenomena, due to confinement of the partons within the proton, they will factorize from the hard elastic electron-parton scattering, a short distance phenomenon.

2.2.3 Hadronic Collisions

The next collisions that can be studied are hadronic collisions. These are fundamentally different from the previous collisions because they will involve predominantly strong processes for particle production and these collisions will be sensitive to the gluon at leading order. One of the advantages of the previous collisions is precise information on the energy of the primary hard collisions. The $e^+ + e^-$ annihilation all of the beam and target energy goes into the final state. In $e^- + p$ collisions the recoiling electron can be measured to determine the Q^2. Because the hadrons are composed of constituent particles, hadron-anti-hadron collisions will not totally annihilate. In high-energy hadronic collisions one measures the results of parton-parton interactions with little information on the initial partons from the final state hadrons. Even so, the parton model can be used to evaluate cross-sections in hadronic collisions by assuming a factorization between the hard and soft processes. Namely,

$$\sigma^h = \sum_{a,b,c,d} \hat{\sigma}_{ab \to cd} \otimes \phi_a^p(x_a) \otimes \phi_b^p(x_b) \otimes D_c^h(z) \tag{2.12}$$

That is, the cross-section to produce a hadron h from a p+p collision is the probability that two partons a and b, one within each proton, produce a parton c that subsequently fragments into a hadron h. The hard process $\sigma_{ab \to cd}$ is a short distance process that does not interfere with either the PDFs or the fragmentation function.

The usefulness of the parton model is that the full QCD can factorize as well. One typically introduces a factorization scale that will define the boundary between soft and hard processes.

2.3   Jet Production in $(\bar{p})$p+p Collisions

For a complete discussion of the history of jet measurements and two-particle correlations in $(\bar{p})$p+p collisions in relationship to heavy ion collisions see a recent review talk by Tannenbaum [2005].

In the 1970's when the first high-energy ($\sqrt{s} > 5$ GeV) hadronic collisions were performed it was uncertain if the hadronic collisions were sensitive to strong partonic interactions instead of, for example, electromagnetic interactions. The prediction from the parton model, which persists today, was introduced by Feynman, Field, and Fox Feynman et al. [1978]. The picture is that of four jets from the hadronic collisions and is illustrated in Fig. 2.13. Two partons, a and b, one from each of the incoming hadrons, interact to produce two outgoing partons c and d. The probability of finding parton a in hadron A is given by the parton distribution function, $\phi_A^a (x_a, k_{Ta})$ (Eqn. 2.11) where k_{Ta} is the parton's transverse momentum with respect to the hadron momentum. The outgoing partons fragment with a fraction z of the parton's momentum via the universal fragmentation function, $D_c^h(z, j_T)$(Eqn. 2.7) where j_T is the fragments transverse momentum with respect to the jet axis. The remnants of the incoming hadrons break up into two other jets of hadrons with low transverse momentum.

The CERN Interacting Storage Ring (ISR) collided p+p with center-of-mass energies ranging from 23 - 63 GeV. The initial results from these collisions were single particle inclusive production (p+p→h+X, h is a particular hadron) cross-section at mid-rapidity, that is at 90° in the collision's center-of-mass. At low-p_T particle production is from soft processes which are not calculable from perturbative methods. What was observed was an exponential spectrum which indicated a "thermal"-like spectrum indicating that the particle production may be governed by statistical constraints. The mean-p_T of these spectra was found to be independent of the energy of the collision and have a value of approximately 0.350 GeV/c [Rossi et al., 1975]. This scale is near Λ from Eqn. 2.4, which is what it should be since it is a non-perturbative process.

At higher p_T the cross-section for π^0 [Busser et al., 1973] and $\pi^{\pm}$ [Alper et al., 1975] production becomes a power-law distribution instead of an exponential. Such a distribution was
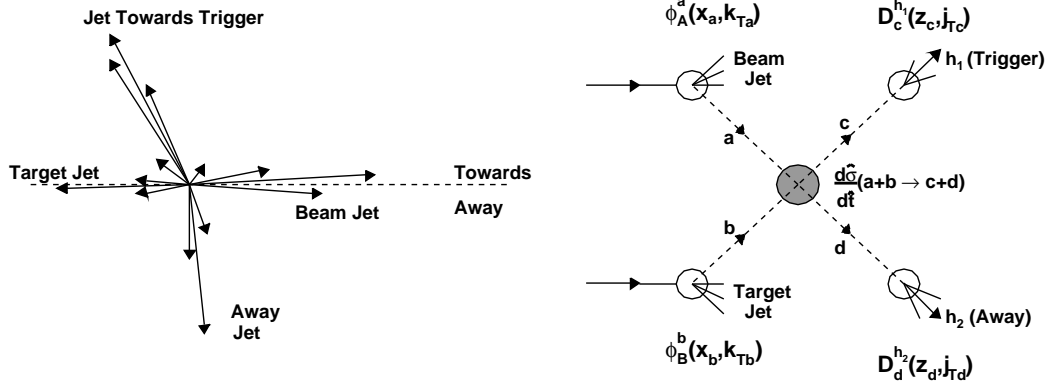
Figure 2.13　Parton model interpretation of high-p_T jet/particle production from Feynman, Field, and Fox Feynman et al. [1978]. The left panel is a center-of-mass reproduction of what the model assumes. That is, four jets are formed from an inelastic hadron-hadron collision. Two are from the hard scattering (towards and away) and two are from the break of the hadrons (beam and target). The right panel is a schematic of theoretical calculation.

predicted to occur from the parton model for high-p_T particle production but is independent of whether the underlying interaction is an electromagnetic or a strong process [Berman et al., 1971]. The data could be reliably reproduced with the form

$$E\frac{d^3\sigma}{d^3p} = p_T^{-n}f\left(x_T\right) \tag{2.13}$$

where $x_T = \frac{2p_T}{\sqrt{s}}$ is the fraction of transverse momentum to the total available energy. The data favored a power of approximately 8. This was not in keeping with the parton model which predicted a power of 4. When full QCD is employed to calculate the single particle production, this exponent varies with $\sqrt{s}$ and x_T. At higher-p_T particle production, this exponent is similar to that predicted from QCD [Angelis et al., 1978]. The QCD prediction was a variation of the exponent around 5-6 but not as high as 8 at the lower, high-p_T particle production.

This discrepancy could be reconciled once transverse momentum of the partons within the nucleon, known as k_T, was included. This k_T was initially ignored by Feynman, Field, and Fox

since, based solely on uncertainty arguments, the magnitude of k_T was expected to be only a few hundred MeV which is small compared to the momenta that was measured in the high-p_T spectra. Evidence for k_T much larger than this was found by the CCHK collaboration from measurements of two-particle correlations [Della Negra et al., 1977].

In the CCHK analysis only events with at least one charged track in the acceptance having p_T above 2 GeV/c were considered. The momentum vector of the highest p_T particle of the event defined the **trigger** or **towards** direction (see Fig. 2.13). In a simple picture of 2→2 scattering, the outgoing jets will have the same energy and be directed oppositely, i.e. coplanar jets. To test this simple picture they assumed that the trigger particle, which fragments at high-z, is approximately the jet p_T and direction. The **associated** jets were measured from distributions of particles produced at $180° \pm 40°$ in azimuth from the trigger direction, the **away-side**. The coplanarity of jet was quantified by defining p_{out}, the associated particle's p_T transverse to the trigger particle p_T.

$$p_{out} = \frac{|\vec{p}_{T,trig} \times \vec{p}_{T,assoc}|}{p_{T,trig}} \tag{2.14}$$

A low value of p_{out} would be expected from coplanary jets with only a small ($\sim \Lambda$) transverse momentum. To measure the fragmentation they defined x_E which is the fraction of the associated particle p_T along the trigger particle direction.

$$x_E = -\frac{\vec{p}_{T,trig} \cdot \vec{p}_{T,assoc}}{p_{T,trig}^2} \tag{2.15}$$

When the trigger jet approximates the jet energy, x_E approximates z of the associated particle.

Naively it was expected that the acoplanarity of the di-jets would be small, near $\langle |p_{out}| \rangle = \sqrt{\pi}\sqrt{\langle p_{out}^2 \rangle} = 0.3$ GeV/c, similar to the $\langle p_T \rangle$ of soft particle production. They found for particles with $x_E > 0.5$, $\langle |p_{out}| \rangle = 0.53 \pm 0.02$ GeV/c, significantly higher than expected. Further by Monte Carlo they showed that this is could be explained by the transverse momentum of the partons prior to the hard scattering. Utilizing a formula from Feynman et al. [1978], p_{out}

and x_E are approximately related by

$$\left\langle p_{out}^2 \right\rangle = x_E^2 \left(\left\langle j_{Ty}^2 \right\rangle + 2 \left\langle k_{Ty}^2 \right\rangle \right) + \left\langle j_{Ty}^2 \right\rangle \tag{2.16}$$

The y-subscripts indicate only one component of the two-dimensional vectors, $\vec{j}_T$ and $\vec{k}_T$. Also, $\vec{j}_T$ is the transverse momentum of a fragment with respect to the jet axis, which is expected to be near Λ as well. If $\left\langle j_{Ty}^2 \right\rangle$ is ignored the data indicate that the Gaussian RMS would be $\sqrt{\left\langle k_T^2 \right\rangle} \approx 1.3$ GeV/c. This is much larger than expected and of the same order as the measured high-p_T spectrum. This transverse momentum is large enough to smear the measured outgoing hadron spectrum such that the measured spectrum has an exponent from the x_T scaling is larger than 5-6.

Indirect evidence for jet production at ISR energies was observed by other correlation analyses similar to CCHK. The CCOR collaboration at the ISR whose spectrometer had full azimuthal coverage extended the work done by CCHK with both its coverage and p_T reach due to higher luminosities from ISR [Angelis et al., 1980].
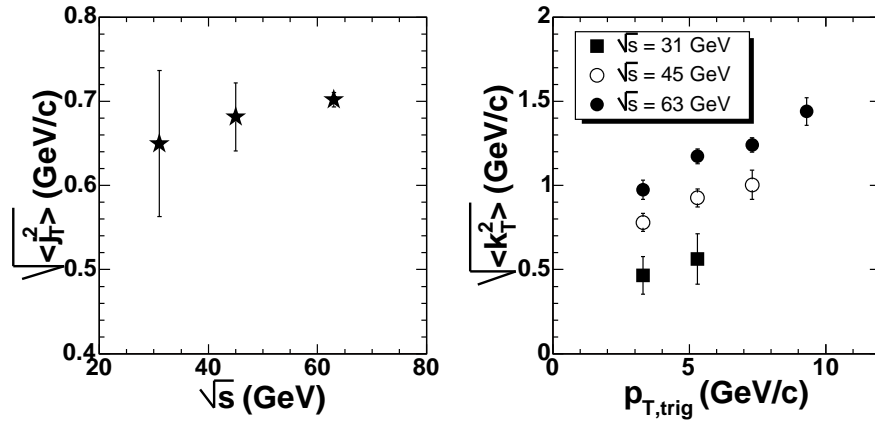
Figure 2.14   *Left:* Center-of-mass energy dependence of $\sqrt{\left\langle j_T^2 \right\rangle}$ from CCOR at the CERN ISR. *Right:* Trigger p_T and $\sqrt{s}$ dependence of $\sqrt{\left\langle k_T^2 \right\rangle}$.

Using high-p_T π^0 triggers from 3-11 GeV/c, both $\sqrt{\left\langle k_T^2 \right\rangle}$ and $\sqrt{\left\langle j_T^2 \right\rangle}$ were extracted via Eqn. 2.16 as a function of trigger p_T and as a function of $\sqrt{s}$. First, they found that $\sqrt{\left\langle j_T^2 \right\rangle}$ was independent of the trigger p_T and $\sqrt{s}$. This is expected since fragmentation is a universal

process independent of the underlying process to produce the partons which subsequently fragment. They also found that $\sqrt{\langle k_T^2 \rangle}$ is large and increases with increasing trigger p_T and increasing $\sqrt{s}$ (see Fig. 2.14).

Other evidence for jet-like structure of high-p_T events came from rapidity distributions of the away-side particles. The associated particle production is broad in rapidity but two peaks were observed one at the opposite rapidity to the trigger direction and one near the same rapidity of the trigger [Darriulat et al., 1976]. This is exactly what is expected for for jets which are tightly collimated in both ϕ and η. Still, it was not until the early 1980's when the CERN ISR $\bar{p}$+p collider running at a significantly higher $\sqrt{s}$ (=560 GeV/c) that unequivocal evidence for jet production in hadronic collisions was seen. An example of a jet event is given in Fig. 2.15.
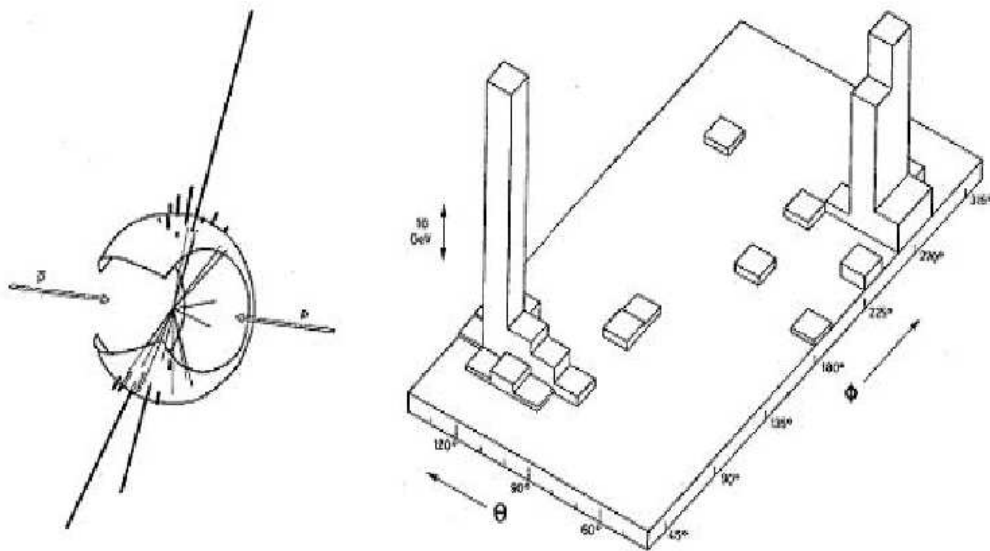
Figure 2.15   Event display from UA2 at the ISR $\bar{p}$+p collisions producing a pair of back-to-back jets [Banner et al., 1982].

Jet measurements in p($\bar{p}$)+p collisions have been made from $\sqrt{s}$ of 31 GeV up to 1.8 TeV at CERN ISR and at the Fermilab Tevatron [Affolder et al., 2001; Abe et al., 1996; Abbott et al., 2001]. Such measurements of jet production are used in global fits to constrain parton distribution functions. They are also used to probe physics beyond the standard model since

they represent the hardest probe available and thus probe the smallest distance scales. At the present time NLO pQCD is able to describe the single-jet cross-section at all energies (see Fig. 2.16).
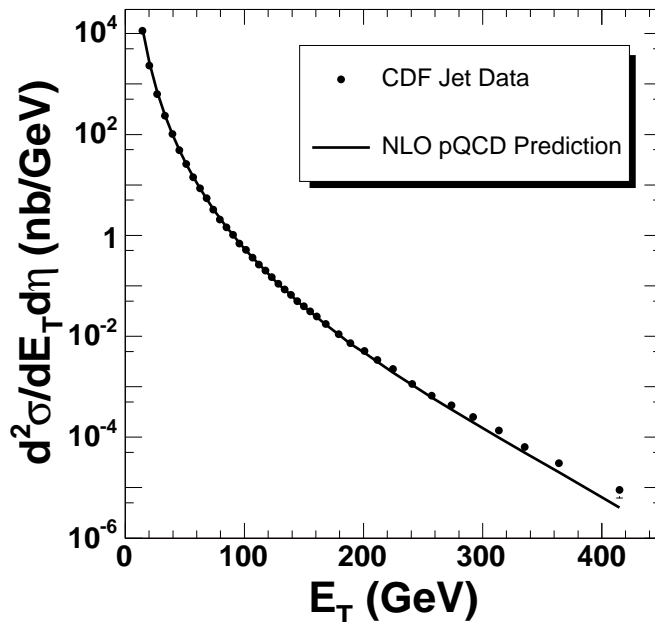
Figure 2.16   Inclusive jet production from CDF and a NLO calculation [Abe et al., 1996]. Errors on the data are statistical only. The difference between the data and theory are within the quoted systematic errors.

2.4   Jet Production in p+A Collisions

In parallel to early experiments at the ISR, Fermi National Accelerator Laboratory (Fermilab) produced proton beams for fixed target experiments. Studies of high-p_T particle production off nuclei were performed. Naively one would expect particle production to increase with A, the mass number of the nucleus. This would be true if the nucleus was an incoherent superposition of nucleons and no nuclear effects are present. The Chicago-Princeton collaboration measured the p_T dependence of high-p_T particle production in protons scattering off Beryllium, Titanium, and Tungsten targets [Cronin et al., 1975]. The cross-sections were fit

to

$$E\frac{d\sigma_{pA}}{d^3p} = E\frac{d\sigma_{pp}}{d^3p}A^{\alpha(p_T)} \tag{2.17}$$

The resulting exponents, α, for proton and positive pions are shown in Fig. 2.17. There are three important observations from this data 1) there is a difference between the particle production of pions (mesons) and protons (baryons), 2) at low p_T there is a suppression of particle production relative to the incoherent nucleon-nucleon collisions, and 3) at high p_T there is an enhanced particle production relative to the incoherent nucleon-nucleon collisions.
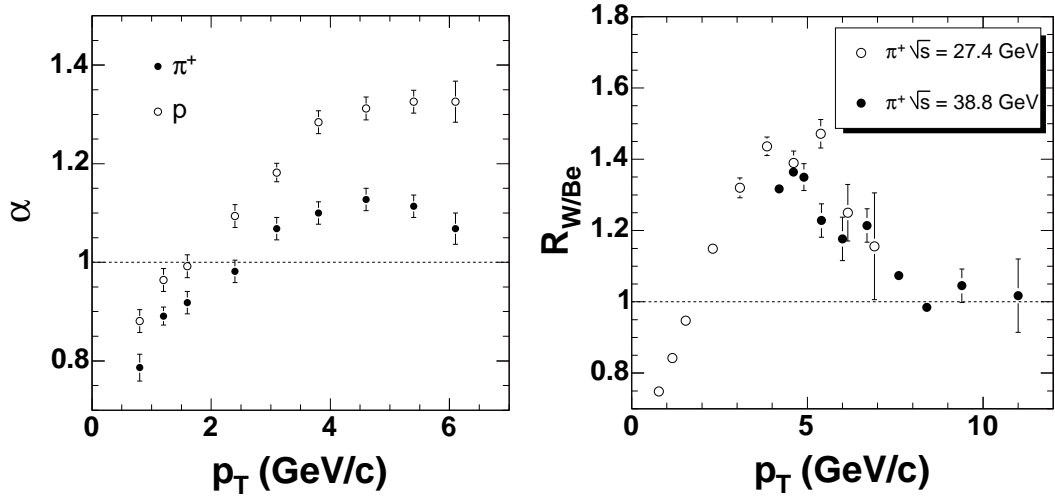
Figure 2.17   *Left:* Single particle production cross-section dependence on the atomic mass, A, from Eqn. 2.17 for single positive pions (closed circles) and protons (open circles) as a function of p_T. Data from Cronin et al. [1975]. *Right:* The ratio of positive pion cross-section per nucleon in a tungsten target compared to beryllium target. Data from Antreasyan et al. [1979] and Straub et al. [1992].

An alternative quantity that reveals the similar results is $R_{A/B}$ which is defined as the ratio of single particle cross-sections in p+A collisions to p+B collisions and normalized by the number of nucleons.

$$R_{A/B} = \frac{Ed\sigma^A/d^3p}{Ed\sigma^B/d^3p}\frac{A_B}{A_A} \tag{2.18}$$

Fig. 2.17 shows this ratio for tungsten and beryllium targets for two different center-or-mass energies. At the lowest p_T we see a suppression of particle production in p+W collisions

compared to p+Be. At mid-p_T the ratio is above one, implying an enhancement of particle production. At still further higher p_T the ratio decreases to unity.
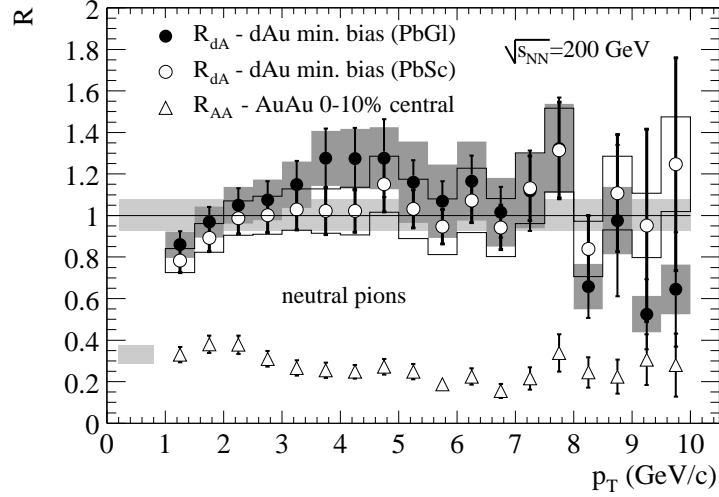
Figure 2.18   Comparison of ratio of single particle spectra in d+Au colli-
sions (open and close circles) and Au+Au collisions (triangles)
compared to binary-scaled p+p collisions.

This ratio has been measured at RHIC in d+Au collisions where the production of particles in d+Au is compared to p+p. This is plotted in Fig. 2.18. The ratio for π^0 production is consistent with this picture of a suppression at low p_T, enhancement at mid-p_T, and unity at high-p_T. From lower $\sqrt{s_{NN}}$ (center-of-mass of the nucleon-nucleon system) data there is a decrease of the peak of the ratio with increasing $\sqrt{s_{NN}}$ [Straub et al., 1992].

The enhancement of particle production at mid-p_T was reproduced in parton models by including multiple scattering of the *outgoing* partons within the nucleus [Kuhn, 1976]. This process is akin to a charged particle multiple scattering through a material. Multiple scattering will broaden the momentum distribution of the outgoing partons enhancing the mid-p_T spectrum. The effect decreases away at high p_T since the successive multiple scatterings are soft and the additional momentum is small compared to the initial momentum. This multiple scattering model was adapted to include the observed differences between pion and kaon enhancement, but not that difference with protons [Lev and Petersson, 1983]. It also predicted that the jets from which the high-p_T particles were produced would be more acoplanar. That

is, as the partons propagated through the medium the multiple scattering would increase the partons k_T.
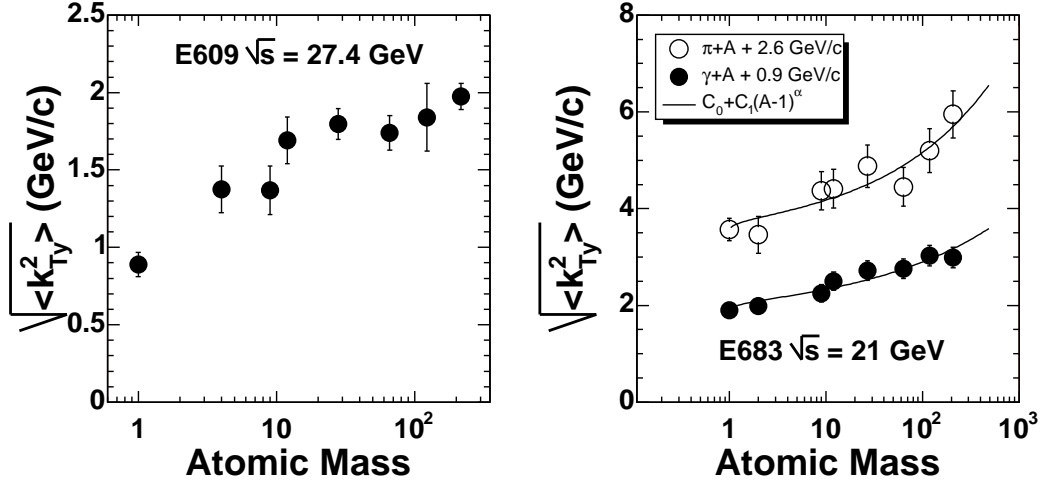
Figure 2.19   Plotted is extracted $\sqrt{\left\langle k_{Ty}^2 \right\rangle}$ from di-jets production in p+A collisions. E609(left) [Corcoran et al., 1991] measured jets in p+A collisions and E683 (right) [Naples et al., 1994] measured measured jets in γ+A and π+A collisions. The E683 data follows the curve for $\alpha = 0.32 \pm 0.08$ for the γ beam and $\alpha = 0.39 \pm 0.15$. Within errors this is consistent with $A^{1/3}$ dependence expected from multiple scattering.

Fermilab fixed target experiments began measuring jet production off of nuclear targets in the late 1980's and early 1990's. These experiments focused not only on the measurement of the jet cross-sections and α but also the planarity of the di-jets. The first such measurement to study the planarity of reconstructed jets from p+A collisions was the E557 collaboration [Stewart et al., 1990] using a proton beam of 800 GeV corresponding to a center-of-mass energy $\sqrt{s_{NN}} = 38.8$ GeV/c. They compared the relative azimuthal angle between di-jets in p+p, p+C, and p+Pb. They found a systematic broadening above the increasing background with the larger nuclei, hinting at a mechanism that increases the acoplanarity of the di-jets.

At lower beam energy two different experiments (E603, E683) measured jet production with γ, π, and proton beams [Corcoran et al., 1991; Naples et al., 1994]. Fig. 2.19 summarizes the results. These experiments found a substantial increase in $\sqrt{\left\langle k_{Ty}^2 \right\rangle}$ with atomic mass. The

E683 results for $\sqrt{\left\langle k_{Ty}^2 \right\rangle}$ are offset from the true value due to the identification of the jets. The jet identification is affected by the increased multiplicity of the underlying event. This offset was simulated to be independent of A but depends on the composition of the beam. The π-beam offset is ~ 3 GeV/c and γ-beam offset is ~ 1 GeV/c. When these offsets are taken into account, $\sqrt{\left\langle k_{Ty}^2 \right\rangle}$ are very similar between two different beams and the proton beam data from E609. Any extra $\sqrt{\left\langle k_{Ty}^2 \right\rangle}$ in γ+A collisions must be due to multiple scattering of the final state partons since the γ does not multiple scatter as it traverses the nucleus. Therefore, any increase in acoplanarity is due to interactions of partons in the final state. All three data sets being consistent with one another implies that the initial state has little to no effect on the increase of the measured k_{Ty}.

The data from the photon and pion beam was also fit to a functional form to determine the A dependence.

$$\sqrt{\left\langle k_{Ty}^2 \right\rangle} = C_0 + C_1 \left(A - 1\right)^\alpha \tag{2.19}$$

Here C_0 is $\sqrt{\left\langle k_{Ty}^2 \right\rangle}$ in p+p collisions and C_1 is the rate of change of $\sqrt{\left\langle k_{Ty}^2 \right\rangle}$ with A. The expected increase in $\sqrt{\left\langle k_{Ty}^2 \right\rangle}$ should be $A^{1/3}$ since the amount of multiple scattering is proportional to the length traversed in the nucleus. The fitted values of α are 0.32$\pm$0.08 for the photon beam and 0.39$\pm$0.15 for the pion beam. Both are consistent with an $A^{1/3}$ dependence expected from multiple scattering.

Renewed theoretical interest in the Cronin effect came with the advent of RHIC and LHC. Since, in heavy ion collisions multiple scattering from each of the partons from the hard scattering may be significant. A recent review [Accardi, 2002] summarized the theoretical developments in multiple scattering in the nucleus prior to the d+Au run at RHIC in 2003. The general result from several models was that there is an increase in k_T that is related to

$$
\begin{aligned}
\Delta \left\langle k_T^2 \right\rangle &= \left\langle k_T^2 \right\rangle_{p+A} - \left\langle k_T^2 \right\rangle_{p+p} \\
&= \sigma_{MS} \left(\sqrt{s_{NN}}\right) T\left(b\right)
\end{aligned}
\tag{2.20}
$$

where $T(b)$ is the nuclear thickness function of the overlapping nuclei with impact parameter b and σ_{MS} is the multiple scattering cross-section. This cross-section depends on the theoretical model. The expected $A^{1/3}$ dependence enters in $T(b)$ and the $\sqrt{s}$ dependence is in the cross-section. Further these models assume that it is in both the initial and final state that contributes to the increase in jet acoplanarity due to multiple scattering.

2.5   Jet Production in A+A Collisions

Heavy ion collisions have a long and interesting story [Baym, 2004]. Using heavy ion collisions to study a phase transition in QCD was first discussed some 30 years ago. Heavy ion collisions were first performed at the Berkeley Bevalac during the 1970's and 80's. These were fixed target experiments where the heavy ion beams were incident at about $\sqrt{s_{NN}}$ of 2 GeV/c. These experiments were focused primarily on determining the equation of state of QCD matter at extreme densities. This was motivated by astrophysical interest in the core structure of neutron stars where the energy density was about 1 GeV/fm^3 or about 4 times the normal nuclear matter energy density. Because of the energy and the goals of the collider, only soft, bulk properties (i.e. multiplicity, flow, and strangeness production) were measured. For a history of the results from the Bevalac to RHIC see Stock [2004].

Beginning in mid-80's the Alternate Gradient Synchrotron (AGS) at Brookhaven provided heavy ion beams for fixed target experiments. Soon after the CERN's Super Proton Synchrotron (SPS) began providing heavy ion beams for fixed target collisions as well. These accelerators produced center-of-mass energies that were < 20 GeV/nucleon and, at those energies, high-p_T particle cross-sections are still small. It was not until the mid-to-late 1990's that a measurement of high-p_T cross-sections was performed at the SPS. Even then, many measurements at the SPS and the AGS were focused on bulk properties of the final state matter in a quest to discover the QGP. As a result before RHIC there is little data on high-p_T particle production and no data on jet production from heavy ion collisions.

When no new final state interactions are present, A+A should reveal the same phenomena as p+A collisions, i.e. the Cronin effect. At sufficiently high temperature one expects a quark-

gluon plasma (QGP) to form. One of the earliest signatures of the formation of the quark-gluon plasma was that of jet energy loss [Bjorken, n.d.]. Initially this energy loss was predicted to be due to elastic scatterings within the medium. The multiple elastic scatterings in the medium have the natural consequence of increasing in the acoplanarity of di-jets [Appel, 1986; Blaizot and McLerran, 1986]. It was shown, however, that, because the energy loss due to elastic scattering is small, this acoplanarity may not be an ideal probe of the quark gluon plasma. Because of the soft background jet finding would be difficult and reasonable experimental cuts on finding jets would mask the signature [Rammerstorfer and Heinz, 1990].

By considering radiated gluon energy loss, that is bremsstrahlung of the parton through the medium, a larger suppression of high-p_T particle production was predicted [Gyulassy and Plumer, 1990] as well as a large acoplanarity of di-jets [Baier et al., 1999]. As an example from QED, the energy loss, ΔE, due to photon bremsstrahlung is proportional to the length that the charged particle traverses in the medium. However, in QCD the total energy loss is proportional to the square of the length traversed in the medium [Baier et al., 1997].

$$\Delta E \propto -\mu^2 L^2/\lambda = -\alpha_s \hat{q} L^2 \tag{2.21}$$

The different length dependence is due to the additional contribution in QCD due to the radiated gluon interacting with the medium. In Eqn. 2.21 $\lambda = 1/(\sigma_{el}\rho)$ is the mean free path of the parton in the medium where ρ is the medium's color-charge density, which is dominated by gluons, and σ_{el} is the elastic scattering cross-section of the parton with the medium.

It is useful to introduce the transport coefficient $\hat{q}$ which describes the opacity of the medium, a large $\hat{q}$ the medium is more opaque, less transparent. The transport coefficient is defined as $\hat{q} = \mu^2/\lambda$ where μ is the average momentum transfer in the parton-medium collision. Not only is $\hat{q}$ related to the energy loss but it is also related to the broadening of the di-jets in the nuclear medium. Because of multiple scattering in the medium, the acoplanarity of the jets will increase. This increase in the measured partonic k_T proportional to the length traversed and the transport coefficient.

$$\Delta \left\langle k_T^2 \right\rangle = \hat{q} L \tag{2.22}$$

Therefore, because of energy loss of a fast parton in the QGP, one expects a shift to lower values in the spectrum of high-p_T particles from the collision and an increase in k_T of the partons from back-to-back jets.
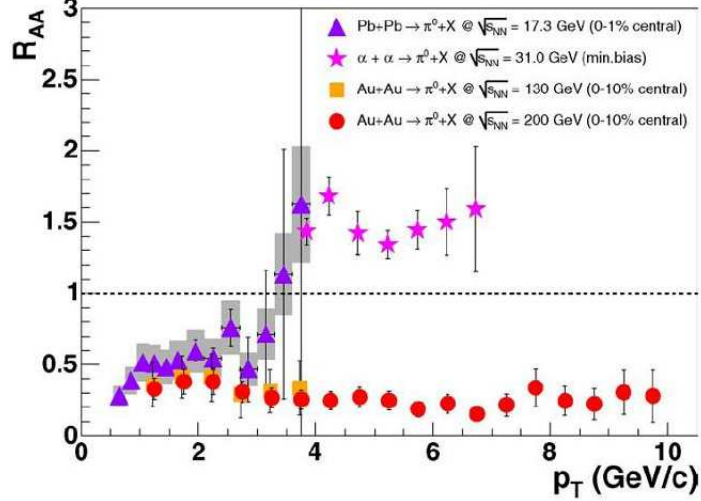
Figure 2.20   Comparison of R_{AA} (see Eqn. 1.3) from π^0 production in $\alpha+\alpha$ at ISR (stars) [Angelis et al., 1987], Pb+Pb at SPS (triangles) [Aggarwal et al., 2002], and Au+Au at RHIC (squares and circles) [Adcox et al., 2002; Adler et al., 2003b]. For the SPS data the p+p baseline spectrum was reanalyzed [d'Enterria, 2004].

The suppression of high-p_T particles as predicted by energy loss models was discovered at RHIC. The spectrum in Au+Au collisions was measured and compared to p+p collisions at the same energy by the nuclear modification factor, R_{AA}.

$$R_{AA} = \frac{\frac{1}{2\pi p_T N_{evt}} \frac{d^2 N_{A+A}}{dp_T dy}}{\langle N_{coll} \rangle \frac{1}{2\pi p_T N_{evt}} \frac{d^2 N_{p+p}}{dp_T dy}} \tag{2.23}$$

where $\langle N_{coll} \rangle$ is the number of binary nucleon-nucleon interactions there are for a given Au+Au event selection. This quantity is plotted in Fig. 2.20 for π^0 production from ISR [Angelis et al., 1987], SPS [Aggarwal et al., 2002], and RHIC [Adcox et al., 2002; Adler et al., 2003b]. In the $\alpha + \alpha$ collisions the ratio is above one, indicating an enhancement of particle production at moderate p_T which is the Cronin effect. At the CERN energies with Pb+Pb collisions a slight

suppression is seen but the ratio is near one at the highest p_T measured. As the center-of-mass energy (per nucleon) increases to RHIC energies a clear, persistent, suppression of π^0 production compared to binary-scaled p+p collisions is observed out to very high p_T.

One successful theory in predicting the single particle results at RHIC is reaction operator approach of Gyulassy, Levai, and Vitev (GLV) Gyulassy et al. [2000]; Gyulassy, Levai and Vitev [2001]. In this approach the energy loss is calculated as an expansion in the opacity of the medium where opacity is defined as $\chi = \mu/\lambda$. By varying the gluon density in the medium the measured R_{AA} from RHIC and SPS is reproduced (see Fig. 2.21).
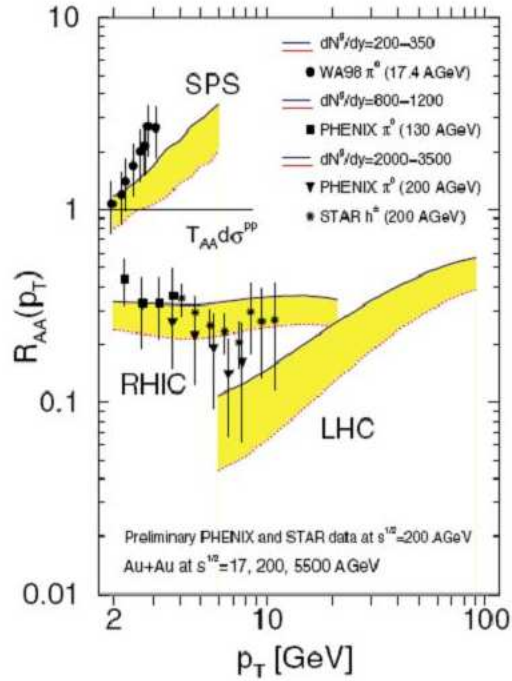
Figure 2.21   Comparison to the SPS and RHIC data from GLV [Vitev and Gyulassy, 2002] energy loss model for different gluon densities.

Further data on energy loss can be obtained in two-particle correlations, which is the subject of this thesis. In two particle correlations one measures the relative azimuth, $\Delta\phi$, to probe the physical correlations between pairs of particles. These correlation will be sensitive to jet correlations since jet pairs are found close in $\Delta\phi$ and di-jet pairs are offset by $180°$ in $\Delta\phi$. Another source of correlation include the harmonic correlation of particle production due

to a differential pressure gradient resulting from an asymmetric overlap region between the colliding nuclei (see Section 4.3 for complete details).
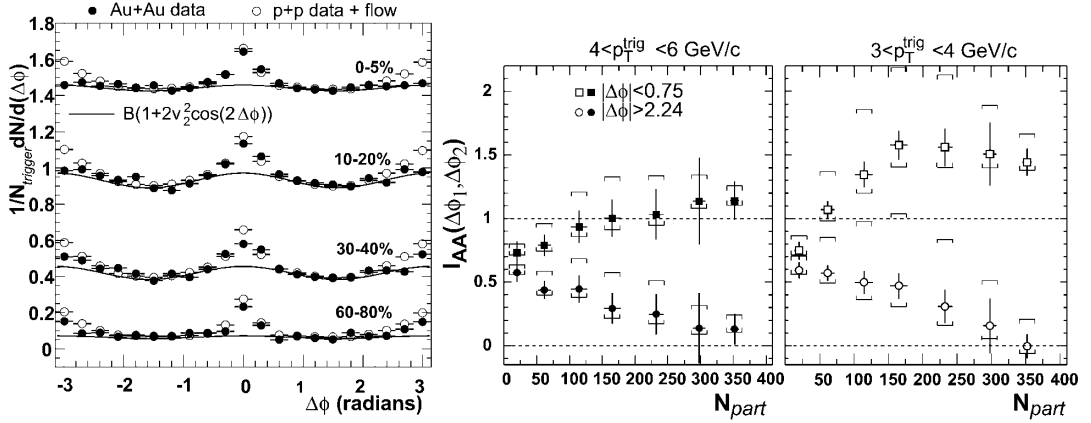
Figure 2.22   *Left:* Correlations of pairs of unidentified charged hadrons in two different momentum ranges in both p+p and Au+Au measured by the STAR experiment [Adler et al., 2003a]. The p+p is modulated by the measured elliptic flow in Au+Au collisions. *Right:* Ratio of near-($\Delta\phi \sim 0$) and far-side ($\Delta\phi \sim \pi$) pair per trigger yields in Au+Au compared to p+p (see Eqn. 2.24) as a function of Au+Au centrality as measured by the STAR collaboration [Adler et al., 2003a].

The STAR collaboration at RHIC measured these $\Delta\phi$ correlations between pairs of unidentified charged hadrons where one particle (the trigger) had p_T between 4 and 6 GeV/c and the other (the associated) had a p_T from 2 GeV/c up to the trigger p_T. These correlations were measured in both p+p and Au+Au collisions [Adler et al., 2003a] and are plotted in Fig. 2.22. From these correlations the number of pairs per trigger particle within a specified $\Delta\phi$ range is measured. Ranges were chosen to compare the yield within the jet, around $\Delta\phi = 0$, and within di-jets, around $\Delta\phi = \pi$, in both p+p and Au+Au collisions. The ratio of these data is plotted as I_{AA}.

$$I_{AA} = \frac{\frac{1}{N_{trig}} \frac{dN_{pair}^{Au+Au}}{dp_T}}{\frac{1}{N_{trig}} \frac{dN_{pair}^{p+p}}{dp_T}} \tag{2.24}$$

This quantity is plotted in Fig. 2.22 as a function of centrality for two different trigger momentum bins. In both trigger p_T ranges a suppression of the away side pairs per trigger and this

suppression increases with increasing centrality. The centrality is measured by the number of participating nucleons N_{part} in the overlap region.
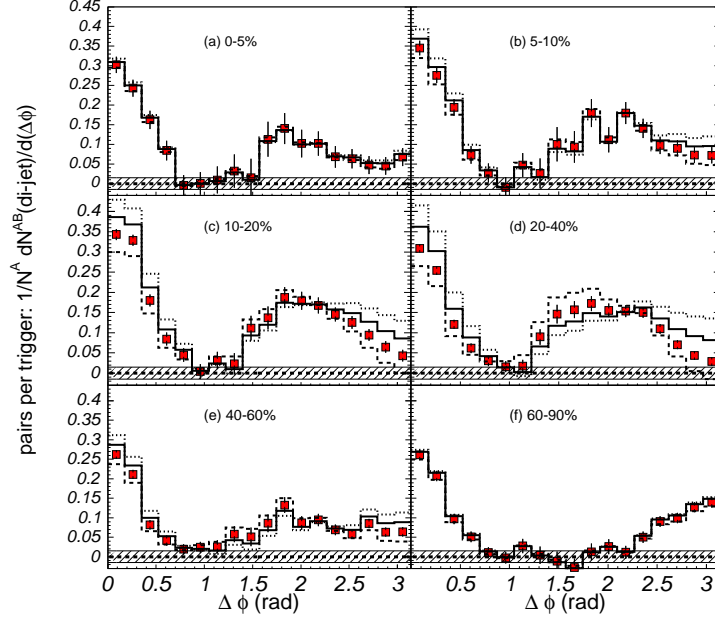
Figure 2.23   Pair per trigger $\Delta\phi$ distribution from pairs of unidentified charged hadrons in Au+Au collisions at different centralities. These distributions are shown after the subtraction of the flow component [Adler et al., 2005a].

Such correlations suffer from a "trigger bias" where the trigger particle is emitted near the surface of the overlap region and suffers little to no energy loss. The corresponding jet opposite to the trigger traverses most of the medium and can loose a significant amount of energy. The near-side yield is at (or above) the yield in p+p collisions while the away-side is suppressed due to energy loss.

Study of the shape of the away-side correlation should be sensitive to the multiple scattering due to this energy loss. The PHENIX collaboration has studied the shape of the far-side correlations at low to moderate p_T [Adler et al., 2005a]. These correlations showing only the jet contribution are plotted in Fig. 2.23 for different Au+Au centrality bins. The correlations are constructed from pairs of unidentified charged hadrons where the trigger is between 2.5-

4 GeV/c and the associated particle is between 1-2.5 GeV/c. In the far-side, the structure changes with centrality to a local minimum forming at $\Delta\phi = \pi$.

fragments from the away-side jet, which propagates through more of the medium than the near-side, are not back-to-back on average and not just broadened.
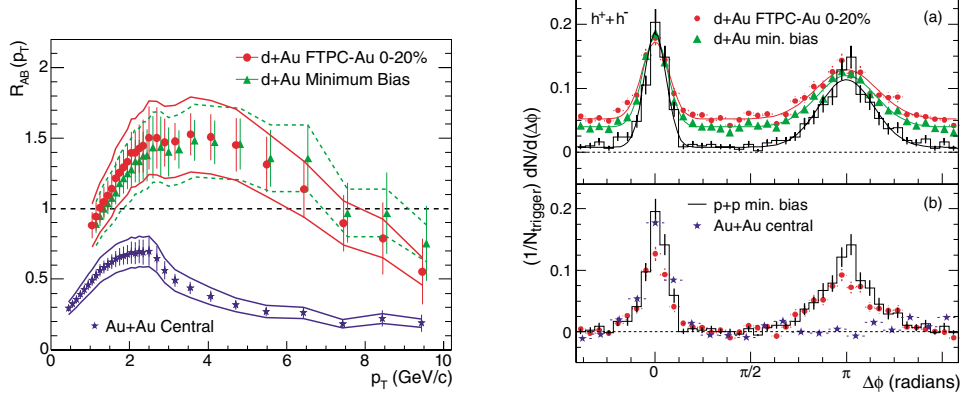
Figure 2.24   *Left:* Comparison of the single unidentified charged hadron spectrum in d+Au (circles and triangles) and Au+Au (stars) as compared to binary-scaled p+p collisions. *Right:* Comparison of unidentified charged hadron pair correlations in p+p, d+Au, and Au+Au collision. Data measured by the STAR collaboration [Adams et al., 2003]

Furthermore, these effects on the single particle suppression and the pair yields and correlation shape do not seem to be present in d+Au collisions [Adler et al., 2003c; Back et al., 2003a; Adams et al., 2003]. Fig. 2.24 shows an example of R_{AA} from Au+Au contrasted with that quantity in d+Au collisions. The d+Au ratio shows an enhancement at moderate p_T consistent with the Cronin enhancement seen at lower $\sqrt{s}$. This is in stark contrast to the observed Au+Au suppression. Further two-particle correlation measurements shown in the right panel of Fig. 2.24 show evidence for a clear far-side distribution that is similar to p+p. That is, it is neither suppressed nor a strongly modified as that in Au+Au. Taken together these data result in the conclusion that strong energy loss in Au+Au occurs in the final state at RHIC.

More information on jets in A+A collisions is found by examining high-p_T processes and requiring particle identification. Fig. 2.25 shows the proton-to-pion ratio as a function of p_T

for different Au+Au centrality bins [Adler et al., 2003d]. The proton-to-pion ratio increases with increasing centrality and in the most central Au+Au collisions, the ratio is at 1. There are as many protons as pions produced.
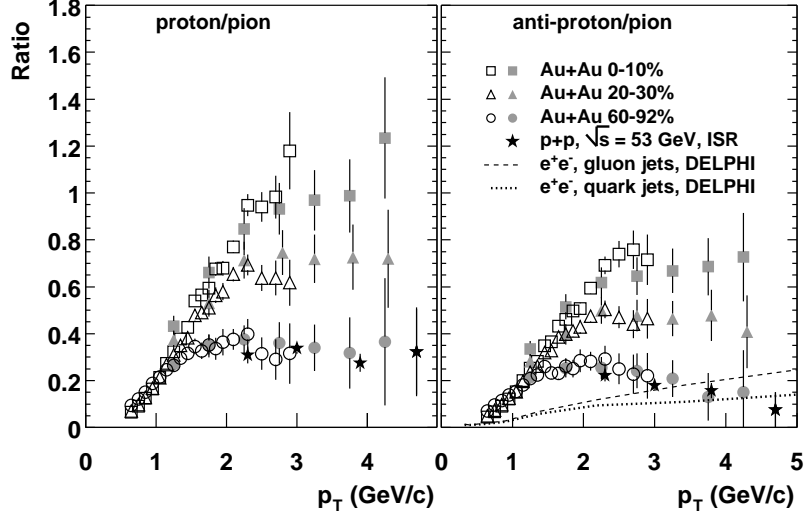
Figure 2.25   Ratio of protons to pions (anti-protons to negative pions on the right) as a function of p_T for different Au+Au centrality. Open points are results using the identified charged pions as the denominator. The filled points are results using neutral pion production as the denominator.

This result can be contrasted with $e^+ + e^-$ gluon and quark jets. In these jets, there is purely fragmentation in vacuum. The fragmentation favors pions (mesons) to protons (baryons). This can be understood by the breaking of the color field connecting the two outgoing quarks, the string. As the two partons move away from one another the increase of energy in the field (see Fig. 2.3) will more easily produce a $q\bar{q}$ pair instead of a di-quark pair. The former results in a two valence quark meson whereas the latter forms a three valence quark baryon. A proton-to-pion ration of about 0.2 is measured in $e^+ - e^-$ annihilation. The data show that in a central Au+Au collision the ratio is five times this value indicating another production mechanism is present which augments baryon production.

The leading model which provides a mechanism to explain the changing proton-to-pion

ratio [Fries et al., 2003] as well as the magnitude of the identified particle flow strength, v_2, is recombination [Molnar and Voloshin, 2003]. If partons are relatively close in phase space, they coalesce to form hadrons. Because of the copious production of particles in Au+Au collisions, finding partons near one another in phase space is more probable than in other collisions. To see how this explains the extra particle production at moderately high p_T consider a steeply falling spectra of partons. There is an interplay between two mechanisms to produce a given hadron at moderately high p_T. First is the fragmentation of a higher p_T parton to a lower p_T hadron. The second is the coalescence of two or three partons at lower p_T to produce a hadron with roughly $2p_T$ or $3p_T$. At moderate p_T, recombination will be important since the probability to find two partons at 2 GeV/c to produce a 4 GeV/c meson is similar to the probability of fragmenting a 6 GeV/c parton into a 4 GeV/c hadron. Further the difference between baryon and meson production is explained from recombination because three partons at 2 GeV/c will produce a proton at 6 GeV/c whereas it takes two partons at 3 GeV/c to produce a meson at 6 GeV/c. The probability to find three 2 GeV/c as compared to two 3 GeV/c partons is given by the steeply falling spectrum. At higher and higher p_T the effect of recombination will become smaller and smaller due to the steeply falling spectrum.

To summarize, there are many effects in high-p_T particle production that have been observed in RHIC, high-p_T suppression in Au+Au that is absent in d+Au collisions, suppression of away-side pair correlations in Au+Au that is not present in d+Au, and a baryon-meson production anomaly. All of these effect the interpretation of high-p_T particle production in A+A collisions.

2.6 Summary

The overall goal of this thesis is to present for the first time a systematic study of jet properties from p+p to d+Au to Au+Au collisions. As discussed the first jet measurements from nuclear collisions are available at RHIC. They pose a unique probe to study the matter produced in the nuclear collisions. The jets are readily produced in the collisions and interact strongly with the surrounding medium.

In the end hadronic fragments of the jet are measured in the detector, thus there are a non-perturbative effects in jet properties. These are taken care of by a study of p+p collisions which represents the absolute baseline for the study of jets from nuclear collisions. The jets from p+p collision will have, by definition, no modification and represent the vacuum fragmentation and vacuum acoplanarity.

For d+Au collisions one of the main goals is to test the multiple scattering model at higher $\sqrt{s}$. This is done by measured both the acoplanarity of jets to directly measure in the increase between p+p and d+Au collisions. This is also tested by measuring the x_E distribution of the away-side distribution. These distribution are related to the fragmentation function. It is possible that radiation due to the multiple scattering in medium could affect the measured fragmentation function. The final test is d+Au centrality dependent measurement of the acoplanarity. This will directly test the length dependence of the multiple scattering model. The d+Au data also provide a critical baseline for jet modification that are predicted to be present in A+A collisions at RHIC.

Finally, in Au+Au collisions, the resulting final state, whatever it may be, could produce further measurable effects on jets. A direct measurement of broadening of the away-side jet structure is made by pushing the data to the highest p_T available. This results in possibly measuring the away-side jet when it is not completely suppressed. The broadening is measured directly by measuring the width of the distribution and by measuring p_{out} distributions where p_{out} is the magnitude of the associated p_T perpendicular to the trigger p_T. This broadening can be compared directly to broadening in d+Au collisions to extract the contribution from Au+Au collisions directly. The conditional yield from the away-side is also measured to extend the p_T reach of previous measurements. The yields are measured from x_E distributions. The measurement of both the width and yields from the away-side distribution will put new constraints on energy loss models in Au+Au collisions.

CHAPTER 3.   PHENIX Experiment

This chapter introduces the PHENIX detector. Each subsystem relevant to this analysis is discussed in some detail. Global event characterization such as triggering on events from different collisions and the determination of the centrality or the impact parameter of the heavy ion collisions is explained.

The PHENIX detector is a large, multipurpose detector with several integrated subsystems used for event characterization, charged particle tracking, particle identification, electromagnetic calorimetry. These subsystems are arranged in two central spectrometer arms and two muon arms at forward and backward rapidity. The central arms cover a total azimuthal range of π radians and are located at pseudorapidity of $|\eta| \leq 0.35$. The forward spectrometer arms are located at each end of the central spectrometer. They cover 2π in azimuth and $|\eta|$ of 1.2-2.2 units. This analysis utilizes the central spectrometer arms and the subsystems which comprise these arms are covered in the following sections. Figure 3.1 is a beam view cross-section of the PHENIX central arms which were used in the analysis. A complete overview of the whole PHENIX detector is found in Adcox et al. [2003].

3.1   Global Detectors and Event Characterization

Event characterization is necessary for both p+p and heavy ion collisions to

1. Determine if a collision has occurred.

2. Determine if a collision should be triggered on.

3. Determine the initial time of the collision for time-of-flight (TOF) measurements.
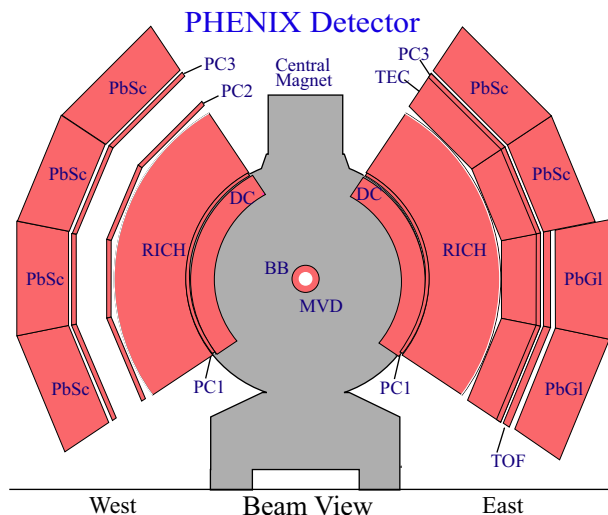
Figure 3.1   The two central spectrometer arms of the PHENIX experiment
used to collect the unidentified charged hadrons, electrons, and
photons.

4. Determine the collision point (in the case of PHENIX, the vertex point along the beam
   direction).

5. Determine the collision centrality in heavy ion reactions.

3.1.1   Beam-beam counters

In PHENIX the Beam-Beam Counters (BBCs) [Allen et al., 2003] are used in all aspects
of event characterization. The BBCs are sets of 64 Cherenkov counters symmetrically placed
144 cm along the beam line and cover 2π in azimuth and $3 < |\eta| < 3.9$ units of pseudorapidity.
The BBCs are part of the global level-1 trigger system which determines if a collisions has
occurred (see Section 3.1.6 and Section 3.1.7).

The BBCs determine the event vertex from the average time difference between leading
particles reaching each BBC. The inital time of the collision is necessary for time-of-flight
measurements for particle identification. The timing resolution of the BBC is 52 ± 4 ps for an
individual element, which results in 4σ separation of pions and kaons up to 2.4 GeV/c in the
TOF wall located 5 m from the beam line.

The multiplicity in the BBC is also useful in heavy ion reactions to aid in determining the centrality of the collisions. This is discussed later in Section 3.1.4 and Section 3.1.5.

3.1.2 Zero-degree calorimeters

The zero-degree calorimeter (ZDC) [Adler et al., 2001] is a common detector among all RHIC experiments in order to characterize nucleus-nucleus collisions. The ZDCs are located at the edge of each of the dipole magnets, which diverge the beams from the interaction region. Each ZDC covers 2π in azimuth and are $\pm$ 2 mrad from the beam line.

The ZDCs are hadronic calorimeters which measure very forward (spectator) neutrons from a collision. These neutrons are sensitive to peripheral heavy-ion collisions (see Section 3.1.5 and Section 3.1.7) and as a general luminosity monitor for RHIC itself. From the timing information one can determine the event vertex of the collision in a similar manner as the BBC.

3.1.3 Centrality Definition

In heavy ion collisions, the amount of overlap of the nuclei is quantified as the centrality of the collision. An example of a non-overlapping nuclear collision is shown in Fig. 3.2. In this figure the nuclei are assumed to be spherical (as is the case for the Au nucleus) and travelling in the direction into and out of the page.

Centrality can be related to the impact parameter, b, which is the vector connecting the center of the two nuclei. Centrality can also be quantified by the nucleons that participate in the overlapping, shaded area, N_{part}. These participating nucleons undergo several nucleon-nucleon collisions, N_{coll}, and centrality can be defined from this as well.

This last quantity, N_{coll}, can be calculated from the nuclear overlap function, $T_{AA}(b)$. If the nucleon-nucleon cross-section is σ_{NN}, then N_{coll} is related to $T_{AA}(b)$ as $\langle N_{coll} \rangle = \sigma_{NN} T_{AA}(b)$. To define $T_{AA}(b)$ more precisely it is necessary to define the nuclear thickness function, $T_A(b)$. This is the number of nucleons per unit area that a single nucleon interacts with as it traverses the nucleus. If the beam travels along the z direction into a nucleus A that has a number
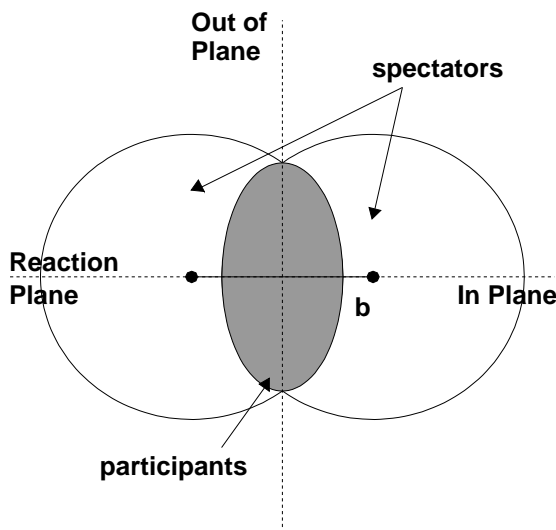
Figure 3.2   Schematic diagram of interacting nuclei. The overlap (shaded grey) region is where the nucleons which participate in the interaction are located. The remaining nucleons are labelled as spectators. The distance between the two nuclear centers is labelled, b, the impact parameter. The overlap region is typically denoted by a function $T_{AA}(b)$.

density, n_A, then

$$T_A(b) = \int dz \; n_A(\sqrt{b^2 + z^2}) \tag{3.1}$$

For p(d)+A collisions this function would define the "overlap" of the nuclei. For two heavy nuclei both thickness functions from each nuclei must be included. This nuclear overlap function between two nuclei is defined as

$$T_{AA}(b) = \int d^2\vec{s} T_A(\vec{s}) T_A(\vec{s} - \vec{b}) \tag{3.2}$$

where the vector $\vec{s}$ is centered on one of the two nuclei and the integration is over the overlap region.

All of these quantities, N_{part}, N_{coll}, $T_A(b)$, and $T_{AB}(b)$, can be determined from the Glauber model of high-energy collisions. In this model, the nucleons in a nucleus are have some distribution. The nucleons travel in straight line trajectories along the direction of the nucleus. It

assumes that the nucleon-nucleon cross-section is the same for nucleons in a nucleus as in free space and that these are not modified by the fact that a nucleon may have previously interacted. By making further assumptions about detector response it is the possible to determine the mapping of a detector to N_{part}, N_{coll}, $T_A(b)$, and $T_{AB}(b)$.

3.1.4   Centrality Determination in d+Au Collisions

Centrality selection in d+Au collisions is determined from the BBC in the direction that the Au nucleus travels. To determine the centrality, it is necessary to know the minimum bias trigger (see below) efficiency, which is 88.5%. This corresponds to the fraction of the total inelastic cross-section that the trigger is sensitive to. This was determined from the assumption that the BBC multiplicity in the Au-going direction is a weighted sum of negative binomial distributions (NBD) [Tannenbaum, 2001]. Each NBD represents the BBC multiplicity distribution for a given N_{part}. The weight is determined by the probability for a collision to have a certain N_{part} and is found by a Glauber model. The difference between the assumed form of the distribution and the measured form of the distribution is taken to be the efficiency. For more details see Milov et al. [2003].

The BBC multiplicity distribution is shown in Fig. 3.3. This distribution is broken up into bins corresponding to some percent of the distribution. The highest BBC multiplicity, the lowest fraction of the distribution, corresponds to the most central collisions. For each of the centrality selections the weighted average of the contribution from the different NBDs are known from the Glauber Monte Carlo. Therefore, one can determine the $\langle N_{coll} \rangle$ and $\langle T_A(b) \rangle$ which correspond to a given centrality bin. These values are given in Table. 3.1.

Percent σ_{inel}	$\langle N_{\mathrm{coll}} \rangle$	$\langle T_A(b) \rangle (\mathrm{mb}^{-1})$
0–20%	15.4 ± 1.0	0.367 ± 0.024
20–40%	10.6 ± 0.7	0.252 ± 0.017
40–88%	4.7 ± 0.3	0.112 ± 0.007

Table 3.1   Table of the mean number of collisions for d+Au, N_{coll}, versus the percentage of the total inelastic cross section and the nuclear overlap function $T_A(b)$.
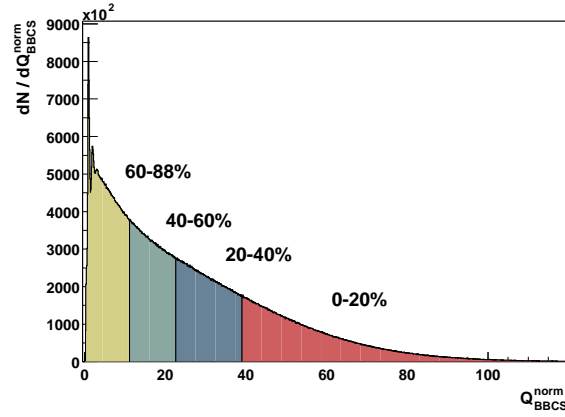
Figure 3.3   Total charge distribution on the Au-going side Beam-Beam Counter (BBC) for d+Au collisions and the centrality selection (see Table 3.1).

3.1.5   Centrality Determination in Au+Au Collisions

The determination of centrality in Au+Au utilizes the Beam-Beam Counters (BBCs, see Section 3.1.1) and the Zero-Degree Calorimeters (ZDCs, see Section 3.1.2). In peripheral Au+Au collisions there is little nuclear overlap and few neutrons are produced along the beam line since most of the spectators are heavy fragments swept away from the ZDC acceptance. For a central Au+Au collisions with large nuclear overlap, there are few spectator neutrons remaining from the collisions to deposit energy in the ZDC. In mid-central (or mid-peripheral) collisions there several spectator neutrons on the ZDC. As a function of centrality one expects a peak in the ZDC distribution at mid-central (mid-peripheral) collision. The multiplicity in the BBC is an increasing function of centrality as in d+Au collisions (see Fig. 3.3). A plot of the correlation between ZDC energy and BBC charge multiplicity is shown in Fig. 3.4. This distribution is then divided into centrality classes by the "clock" method. This method is illustrated in Fig. 3.4 where each of the slices of the distribution correspond to some fraction of the whole distribution. Similarly as for the d+Au centrality a Glauber model is then used to determine the average number of participating nucleons and the average number of binary collisions which correspond to a given centrality range. These values are given in table 3.2.
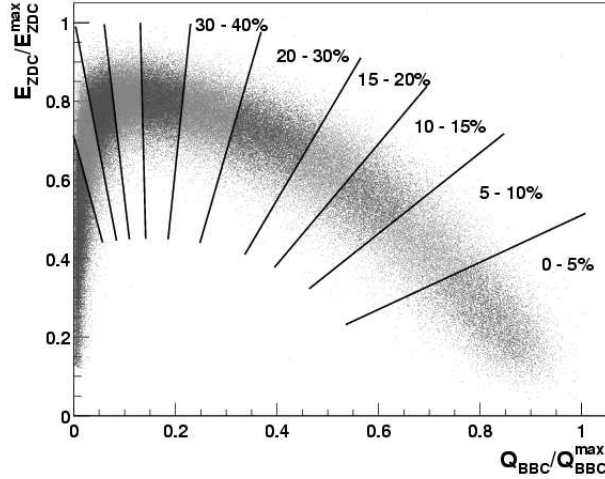
Figure 3.4   Correlation between deposited neutral charge in the Zero-Degree Calorimeters (ZDC) and charged particle multiplicity in the Beam-Beam Counters (BBCs) and the corresponding centrality slices.

Percent σ_{inel}	$\langle N_{\mathrm{part}} \rangle$	$\langle N_{\mathrm{coll}} \rangle$	$\langle T_{AA}(b) \rangle \, (\mathrm{mb}^{-1})$
0–20%	279.4 ± 4.0	779.2 ± 75.2	18.55 ± 1.27
20–40%	140.4 ± 4.9	296.8 ± 31.1	7.06 ± 0.58
40–60%	60.0 ± 3.6	90.6 ± 11.8	2.16 ± 0.26
60–92%	14.5 ± 2.5	14.5 ± 4.0	0.35 ± 0.10

Table 3.2   Table of the mean number of participating nucleons, N_{part}, binary collisions, N_{coll}, and the nuclear overlap function, $T_{AA}(b)$, versus the percentage of the total inelastic cross section in Au+Au collisions.

3.1.6   Level-1 Triggers in p+p and d+Au

The triggering in PHENIX was performed with several different Level-1 triggers in p+p and d+Au collisions. The minimum bias trigger, that trigger which requires little physics requirement except that a beam-beam interaction occurred, required at least one hit in each of the BBCs and that the collision vertex (computed online) satisfies $|z_{\mathrm{vertex}}| < 30$ cm. It was sensitive to 88.5% of the total inelastic d+Au cross section (see Section 3.1.4).

PHENIX also employed a series of Level-1 triggers to select electrons, photons and, with lower efficiency, high-p_T hadrons. These triggers are called the ERT triggers and they utilized the Ring Imaging Cerenkov (RICH) (see Section 3.4.1) for electron identification, together

with the Electromagnetic Calorimeter (EMC) (see Section 3.4.2). The RICH identifies charged particles within its fiducial volume by the cerenkov light the particles emit if they are travelling faster than the speed of light in the region. Cerenkov cones of light are reflected onto a series of photo-multiplier(PMTs) tubes for readout. The EMC has a long radiation length to absorb the energy from electromagnetic interactions within the material. The EMC is broken up into towers corresponding to a single PMT readout. The ERT triggers were produced by summing signals from tiles, where a tile was 4x5 photo-multipliers (PMTs) in the RICH and either 2x2 or 4x4 PMTs in the EMC.

The electron trigger was defined by the coincidence between the minimum bias trigger and the RICH and EMC 2x2 trigger. The threshold for the RICH tile was 3 photo-electrons and the EMC threshold varied between 400–800 MeV. Three different thresholds were available for the 4x4 photon triggers. These thresholds differed between the PbGl and PbSc and varied within and between the p+p and d+Au runs. The lowest threshold setting is about 1.4 GeV and was most sensitive to hadronic showers in the EMC.

3.1.7 Level-1 Triggers in Au+Au Collisions

Because of the exceptional performance of the PHENIX data acquisition system, PHENIX wrote out nearly all of the 2004 Au+Au data as minimum bias. The minimum bias trigger required at least two hits in each of the BBCs, a coincidence of signals in each ZDC, and a z-vertex as computed online of less than 30 cm from the center of the interaction region. The minimum bias trigger is sensitive to $92.2^{+2.5}_{-3.0}\%$ of the total inelastic cross-section [Adler et al., 2005c]. The central value was determined from a PISA (PHENIX Integrated Simulation Application) simulation of the BBC response to simulated Au+Au events from HIJING (Heavy Ion Jet Interaction Generator) [Wang and Gyulassy, 1991]. The error on this efficiency is a systematic error due to the response of the ZDC at peripheral collisions and the BBC at central collisions. In peripheral collisions, there are few neutrons that are not bound within a heavy fragments that are swept out of the ZDC acceptance. In peripheral collisions, there are small signals with large fluctuations in the ZDC. In the BBC, because of the multiplicity in central,

fully-overlapping, events, the BBC can become saturated. Small variations in the detector response becomes important.

3.2   PHENIX Central Magnetic Field

The PHENIX magnetic field [Aronson et al., 2003] is a combination of four different magnets, two for the central arms, and one for each of the muon arms. The muon magnets only slightly affect the central arm field and only at the edge of the central arm, thus the focus in this section is on the central arm magnets. To maximize the p_T sensitivity of PHENIX an axial field configuration was chosen, that is the field is along the beam line and any particle that is emitted radially bends in the azimuthal direction where the Drift Chamber (see Section 3.3.1) has excellent r-ϕ resolution. There are two different fields that can operate independently, an inner and outer coil. These have been run in the "++" and "+-" configuration where the "++" configuration results in the largest magnetic field of about 9 kG at the center of the interaction region, decreasing radially outward, and becoming negligible with a strength of a few hundred Gauss at about 2.2 m, the center of the Drift Chamber. The "+-" configuration results in a field that is zero at the center of the interaction region, peaking at 3.5 kG at around 1 m from the beam line, and decreasing until it is negligible at around 2.2 m.

3.3   Charge Particle Tracking

3.3.1   Drift Chamber

The Drift Chambers (DCH) [Mitchell et al., 2002] are located in both PHENIX central arms and cover the entire ϕ and η coverage of the central arm. They are located at a radial distance from 2.0 - 2.4 m from the beam line. At this position the DCH is almost entirely out of the PHENIX central magnet and only a residual field of about 0.6 kG exists at the front face of the detector with the field strength decreasing radially through the detector.

There are two planes of wires, X1 and X2, located along the beam direction (z-direction) which are used for r-ϕ determination of a track. Four other planes of wires, U1, U2, V1, and

V2, span the z direction but at ± 6° relative to the z-direction and yield information on the z-direction of the track.

Extensive simulation of the electric field was performed. The fine-tuned adjustments to the field result in single wire efficiency of 95%, singe wire resolution of 165 μm, and a two-track resolution of 2 mm.
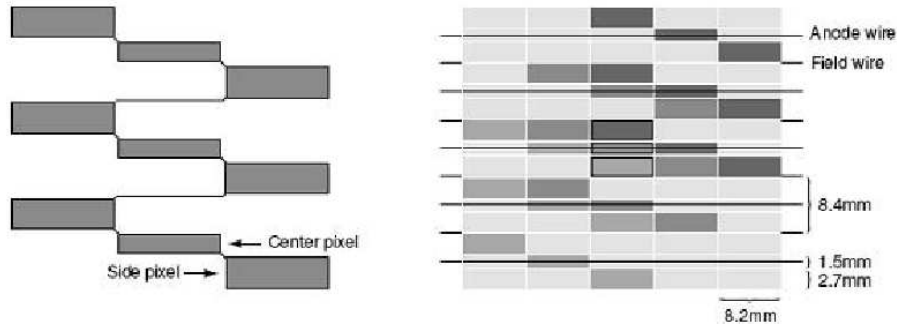
Figure 3.5   *Left:* Pixel arrangement of a pad. *Right:* Definition of a cell based on the pads. In both the z direction is left to right and the r-ϕ direction is up and down.

3.3.2   Pad Chambers

Tracking is also carried out with three different sets of multi-wire proportional chambers known as the pad chambers (PCs) [Mitchell et al., 2002]. They are labelled PC1 for the inner most located in both arms directly behind the DCH, PC2 for the intermediate chamber located only in the West Arm (see Figure 3.1) behind the RICH, and PC3 for the outer chambers located in both arms in front of the EMC. These detectors are have a single set of sense wires along the z-direction. These are segmented into pixels 8.2 mm along z by 8.4 mm in r-ϕ. A pad is formed by an the formation of pixels shown on the left panel of Fig. 3.5. A cell is formed by three adjacent pads, see the right panel of Fig. 3.5.

The resulting performance of the pad chambers are greater than 99.5% tracking efficiency in the high-multiplicity Au+Au environment and a z-resolution of 1.7 mm. The two-track resolution for PC1 and PC3 is 4 cm and 8 cm, respectively.

3.3.3 Track Reconstruction
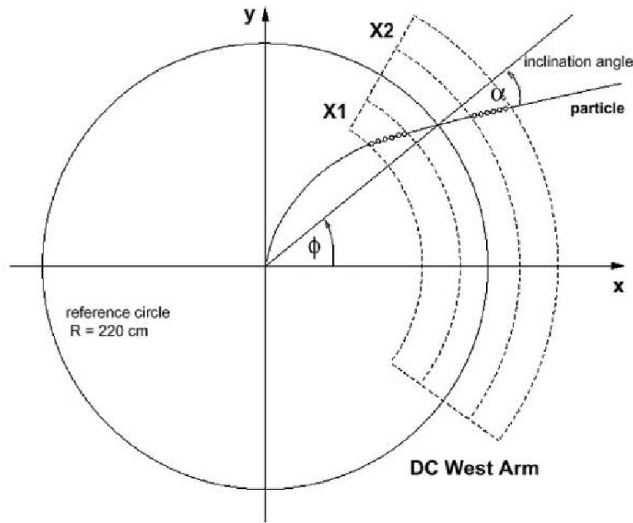
Figure 3.6   Circle defined by the DCH reference radius, 2.2 m which is the
center of the detector. The angle of inclination at the DCH
reference radius, α, is related to p_T of the track.

The PC1 and the DCH form the basis for the track model for PHENIX. The DCH measures azimuthal position of the track, while PC1 determines the polar angle, i.e. the z information. The algorithm for the charged particle tracking is the combinatorial Hough Transform [Mitchell et al., 2002]. Fig. 3.6 shows the relevant definitions of quantities used in the track model. The process is for each pair of hits in the DCH the azimuthal angle and the angle of inclination, α, of the straight line between the hits and a reference radius in the drift chamber is calculated and histogrammed. The angle of inclination is proportional to the p_T of the charged particle. Pairs of hits belonging to the same track cluster in ϕ-α space. Those hit pairs define a track. In the end the efficiency for track reconstruction is > 99%.

Track matching is done to the outer detectors, i.e. PC3. Part of the hits on the outer detectors are from electron conversion after the DCH or from decays of particles near the DCH. Therefore, requiring track matching between the DCH-PC1 track with an outer detector removes such background. This is discussed in detail in Section 5.1.2.1.

3.4 Electromagnetic Detection

3.4.1 Ring Imaging Cherenkov

The Ring Imaging Cherenkov detector [Aizawa et al., 2003] is a ethane-filled volume that detects charged particles that pass through with $\beta > 1$ in the medium. Electrons radiate above 18 MeV/c and pions radiate above 4.9 GeV/c. Particles above the threshold velocity emit a cherenkov cone with a half angle dependent on their velocity. This cherenkov light is reflected off of the back of the RICH by a set of mirrors that focus the light onto a series of PMTs to be read out. The fast readout of the PMTs allows the RICH to be part of the Level-1 triggering.

Electrons are determined by matching DCH-PC1 tracks to the outer detectors (PC2 and/or PC3), to the EMC (see the next section) cluster of an electromagnetic shower, and to a RICH cerenkov ring. Further rejection of background results from requiring the high momentum electron candidate have an energy-to-momentum ratio ~ 1. A similar procedure is employed for charged pion detection. A DCH-PC1 track matches to an outer detector hit and to a RICH ring. Further a match is made to a hadronic shower in the EMC.

3.4.2 Electromagnetic Calorimeter

The Electromagnetic Calorimeter (EMC) [Aphecetche et al., 2003], consists of 8 sectors, 6 of which are Lead-Scintillator (PbSc) sampling calorimeters and 2 are Lead-Glass (PbGl) Cherenkov counters.

The PbSc has alternating lead and scintillator tiles front to back. An electromagnetic interacting in the lead produces a spray of electrons and photons which scintillate in the scintillator and the resulting light is readout from PMTs. The PbSc has excellent timing resolution of about 100 ps for electrons and photons nearly independent of the incident energy. It's energy resolution from beam tests is $8.1\%\sqrt{E(\text{GeV})}\oplus2.1\%$.

The PbGl was commissioned and used successfully in the CERN SPS WA98 experiment. Light is read out by PMTs. The PbGl has excellent energy resolution of $5.9\%/\sqrt{E(\text{GeV})}\oplus0.8\%$ and has a timing resolution of about 300 ps.

Electromagnetic showers are primarily identified by time-of-flight (TOF) and shower shape. Because electrons are light and photons are massless, they are the first to arrive at the EMC. After correcting for the flight time from the interaction point to the EMC and the start time from the BBC, a peak at t=0 is seen for photons and electrons. Heavier hadrons show up as long tails at long times in the distribution.
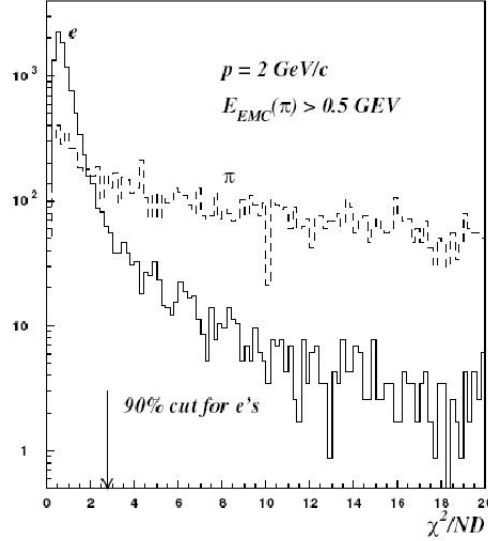
Figure 3.7   PbSc shower shape χ^2/NDF for 2 GeV/c electrons and pions.

In the PbSc, the shower shape is corrected for the impact angle and the energy of the photon. To quantify the shower shape in the PbSc the χ^2 variable is defined [David et al., 2000a],

$$\chi^2 = \sum_i \frac{(E_i^{\mathrm{meas}} - E_i^{\mathrm{pred}})^2}{\sigma_i^2} \tag{3.3}$$

where E_i^{meas} is the energy measured at tower i, E_i^{pred} is the predicted energy for an electromagnetic particle of total energy $\sum_i E_i^{\mathrm{meas}}$, and σ_i is the predicted fluctuation in energy in a tower i. This χ^2 value is useful for the discrimination of electromagnetic from hadron showers. A typically χ^2 cut of 3 corresponds to a S/B of 9/1 for electromagnetic/hadronic showers (see Fig. 3.7).

CHAPTER 4.   Experimental Measurement of Jets in Heavy Ion Collisions

This chapter details the experimental procedure in measuring jets. First, two-particle correlation function and the experimental method to measure these are given. The different sources of physical correlations in hadronic and heavy-ion collisions, namely elliptical flow and di-jet correlations are discussed. The chapter ends with a discussion of fundamental relationships that are used to quantify these sources of correlation from the correlation function.

4.1   Correlation Functions

In a typical high-energy experiment, the fact that jets are highly collimated in ϕ and η space is exploited and reconstruction of these jets are possible event-by-event. Typically there is a seed or trigger that indicates the presence of a jet in an event and a cone algorithm [Abe et al., 1992; Akers et al., 1994] or k_T algorithm [Catani et al., 1991] is used to build a jet from the shower of fragmented hadrons. Such methods are especially easy to implement in $e^+ + e^-$ where the jets are unambiguous even at relatively low energy (see Fig. 2.9). This method has also been successful at high-energy $p(\bar{p})$+p collisions. If the jet energy is low, the resulting fragments can become indistinguishable from the underlying background event. This background clouds the energy distribution within the jet.

In heavy ion collisions this underlying background is even larger because there are tens to hundreds of nucleons interacting in a given event. The resulting background level is tremendous. At $\sqrt{s_{NN}}$ of 200 GeV/c, the top RHIC energy, the mean multiplicity of particles (both charged and neutral) in p+p collisions is approximately 30 in the full 4π. The PHENIX detector has roughly one third of full coverage, thus an average multiplicity of 10 particles for a given p+p event is incident on PHENIX. At mid-rapidity the average number of particles for

a very peripheral Au+Au event is about 20 particles, whereas in the central event the average is about 600 particles [Adler et al., 2005c]. The multiplicities can easily swamp any low energy jet.

To measure jets at lower energies which is also useful for measuring jets in a high-multiplicity background, a technique was pioneered at the CERN Interacting Storage Ring (ISR) to statistically measure particles from jets. This technique relies on the fact that fragmentation products from the jet are tightly correlated in ϕ and in η. Therefore, if two particles fragment from the same jet, they will be near in $\Delta\phi$ and $\Delta\eta$, the relative ϕ and η of the pair of particles. If the hadrons fragment from two different jets in a 2→2 scattering, they will be back-to-back in ϕ and η. Because the partons from the beam and target have a distribution in longitudinal momentum, the spread in $\Delta\eta$ is rather large. At midrapidity in the center-of-mass of the beam-target collisions where the PHENIX detector is located, the partons will have roughly the same x, the fraction of longitudinal momentum fraction of the hadron carried by the parton. If there is a large difference in the x of the two partons, the system will be boosted along the longitudinal direction and the outgoing jets will not be back-to-back in η.

The method to statistically study jets is known as two-particle correlations [Wang, 1992, 1993]. If two particles produced in a given event, one at ϕ_A and η_A, and one at ϕ_B and η_B, the correlation between the two particles is written as

$$C\left(\Delta\phi, \Delta\eta\right) = \frac{\mathrm{Prob}\left(\phi_\mathrm{A}, \phi_\mathrm{B}, \eta_\mathrm{A}, \eta_\mathrm{B}\right)}{\mathrm{Prob}\left(\phi_\mathrm{A}, \eta_\mathrm{A}\right)\mathrm{Prob}\left(\phi_\mathrm{B}, \eta_\mathrm{B}\right)} \tag{4.1}$$

Prob($\phi_A, \phi_B, \eta_A, \eta_B$) is the probability of finding both particles in a given event. Prob(ϕ_A, η_A) and Prob(ϕ_B, η_B) are the probabilities of finding a particle at ϕ_A, η_A or finding a particle ϕ_B, η_B, respectively, in a given event. Under the assumption that detector effects are taken out, the resulting single particle distributions (Prob$\left(\phi, \eta\right)$) will be uniform in ϕ after averaging over many events. At midrapidity the η distribution is roughly flat in p+p [Alner et al., 1986], d+Au [Back et al., 2004], and Au+Au collisions [Back et al., 2003b], especially over the η coverage of PHENIX which is less than 0.35 units. The joint pair distribution (Prob$\left(\Delta\phi, \Delta\eta\right)$) does not have to be uniform in ϕ or η, and indeed will not be uniform in ϕ and η if jets are

present.

The advantage of the correlation function technique is it is independent of the rate of jet production and depends solely on the strength of the correlations of the jets.

4.2 Experimental Construction of the Correlation Function

The PHENIX detector does not have uniform azimuthal coverage, so the raw single particle distributions are not uniform in azimuth. Further, the raw joint pair distribution is not the true distribution since it also has acceptance is folded into it. These distributions must be corrected by the shape of the PHENIX acceptance in order to correct the distribution. Experimentally, one defines the correlation by

$$C\left(\Delta\phi, \Delta\eta\right) = \frac{\frac{\mathrm{d}^2 \mathrm{N}_{\mathrm{pair}}^{\mathrm{real}}}{\mathrm{d}\Delta\phi \mathrm{d}\Delta\eta}}{\frac{\mathrm{d}^2 \mathrm{N}_{\mathrm{pair}}^{\mathrm{mix}}}{\mathrm{d}\Delta\phi \mathrm{d}\Delta\eta}} \tag{4.2}$$

The numerator of Eqn. 4.2 is the raw joint pair distribution in the detector. The denominator is the raw mixed pair distribution, where each of the particles from the pair is taken from different events (see Section 4.2.1). Ideally the mixed pair distribution does not contain physical correlations, only information about the acceptance and the efficiency of the pairs. Constructing the correlation function in this way removes the acceptance and pair efficiency from the raw pair distribution. Therefore, the correlation function from Eqn. 4.2 is proportional real pair distribution.

$$C\left(\Delta\phi, \Delta\eta\right) \propto \frac{\mathrm{d}\mathrm{N}_{\mathrm{pair}}}{\mathrm{d}\Delta\phi \mathrm{d}\Delta\eta} \tag{4.3}$$

The one vital assumption that is made in Eqn. 4.3 is that the two-particle efficiency factorizes into the product of the two single particle efficiencies. Great care must be taken such that this is the case. That typically means that if a cut is applied to real pairs, i.e. detector resolution cuts, the same cut must be applied on the mixed pairs.

In correlation analyses, a range of momentum is defined for each particle. Typically the *trigger* particle is the particle in the highest momentum range and the *associated* particle is the particle in another lower momentum range. Any combination of ranges is possible since the pair distribution is symmetric with respect to the particles. **Fixed** correlations are defined

as both trigger and associated particle having the same p_T range. **Assorted** correlations are defined as both particles having different p_T ranges. Events can be further subdivided into centrality bins and reaction plane bins. So for all events that have a pair of particles, one in the trigger and one in the associated bin, and are in the centrality and reaction plane bin, the real joint pair distribution is filled. It is in this way that jets are not directly reconstructed but only statistical correlations of the fragmented particles produced by jets are measured.

4.2.1 Mixed Event Techniques

The purpose of the mixed event distribution is to completely remove all physical sources of correlation so that the only source of correlation is the pair acceptance and efficiency. There are several techniques that exist to reconstruct the mixed event background.

Regardless of the mixing technique, it is important that the events that are used to mix are a pure minimum bias sample, otherwise acceptance effects from, e.g. a preferential direction of the reaction plane, can bias your sample. A minimum bias event is saved in a trigger buffer if it has a trigger particle in it or it is saved in an associated buffer if an associated particle is in it. The event is saved in each of the buffers if it contains both a trigger and associated particle. If the event has neither a trigger nor an associated particle it is useless to use for an acceptance or efficiency estimation, and the events are discarded without a loss of information. Ideally the statistics in the mixed pair distribution should be no less than 10 times the statistics in the real pair distribution. This reduces the fluctuations in the mixed distributions such that the statistical error is not a dominant error in the final correlation function.

The technique that is employed in this thesis is known as the "rolling-buffer" technique. A list of N events are kept that have a similar acceptance. That is, they must be within some range of z-vertex of the collision and within some range of particle multiplicity. Both of these are important since the magnetic field can change the acceptance as a function of z-vertex and the multiplicity changes the single particle tracking efficiency. When both the trigger and associated buffer are full, then the top event from the trigger buffer is correlated with all similar events (i.e. those with similar z-vertex and multiplicity) from the associated buffer.

After this, the head event in both buffers are removed and the buffers are shifted to make room for the next event. This is the general method, but there are variations. For instance, the number of events in the buffer is not fixed and is typically guided by requiring a factor of 10 more statistic in the mixed distribution than the real distribution. The number of particles that are correlated from each mixed event is not fixed and can vary as well.

4.2.2 Normalization

The correct normalization of the correlation function is necessary in order to extract the correct yield of pairs. What has been done recently at RHIC is to report per trigger yields, where the correlation function is divided by the number of triggers and an appropriate normalization $\mathcal{N}$ is used. The normalization satisfies (where the subscript "pair" from is dropped now on)

$$\frac{1}{N_{trig}} \frac{d^2 N}{d\Delta\phi d\Delta\eta} = \mathcal{N} \mathrm{C}\left(\Delta\phi, \Delta\eta\right) \tag{4.4}$$

The normalization constant has been derived in [Jia, 2005]. After η integration the normalization is

$$\frac{1}{N_{trig}} \frac{dN}{d\Delta\phi} = \frac{R_{\Delta\eta}}{N'_{trig}} \frac{\int d\Delta\phi \frac{dN^{mix}}{d\Delta\phi} \frac{dN^{real}}{d\Delta\phi}}{\epsilon_{assoc} \Omega_{\Delta\phi} \frac{dN^{mix}}{d\Delta\phi}} \tag{4.5}$$

Here $R_{\Delta\eta}$ is the correction for the jet yield to an eta range of ± 1 unit. This is easily done in p+p and d+Au collisions since the jet widths are the same in $\Delta\phi$ and $\Delta\eta$. This is not included in Au+Au collisions because the jet on the near side has a ridge structure and not a peak in η [Adams et al., 2004a]. $\Omega_{\Delta\phi}$ is the azimuthal range of the correlation function which is either π or 2π depending on if the full range is folded. The associated single particle efficiency is ϵ_{assoc} and the number of measured triggers is N'_{trig}.

4.3 Sources of Correlations

Physical correlations in position and momentum space can occur from many sources including Hannbury-Brown-Twiss (HBT) correlations and decay. The HBT correlation is due to the wavefunction overlap of bosons. It is strongest at low transverse momentum near a few

hundred MeV where the relative momentum of the particles is low. In this analysis particles that have a transverse momentum above 1 GeV/c are considered where the HBT correlation is negligible.

Decay from both long and short lived particles introduce correlations as well. An example is the K_s^0 decay to two charged pions. Moderate p_T kaons decay into moderate p_T pions that exhibit a near angle, $\Delta\phi = 0$, correlation. The decay correlations in the near angle have been studied by simulation [Ogilvie and Rak, 2001] and directly by data from p+p collisions [Constantin, 2004]. At $p_T > 1.5$ GeV/c the contribution from decays is negligible.
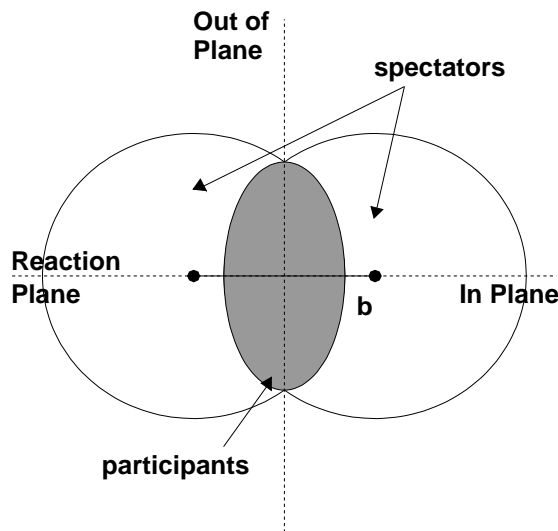
Figure 4.1   Schematic diagram of interacting nuclei. The grey-shaded, al-
mond-shaped overlap region results in a stronger pressure gra-
dient along the short axis, the reaction plane, compared to the
long axis. This difference results in elliptic flow.

In A+A collisions, a source of physical correlations arises due to elliptic flow. When two spherical nuclei undergo a non-central collision, the resulting overlap is an almond shape (see Fig. 4.1). In such collisions a reaction plane is formed by the beam direction and the impact parameter. A pressure exists within the almond-shaped overlap region and a larger pressure gradient is present along the reaction plane (in plane) as compared to the long side of the almond (out of plane).

The resulting particle distribution is not ϕ symmetric but depends on the orientation with respect to the reaction plane. Typically the azimuthal distribution of single particles is written as a Fourier series

$$\frac{dN}{d(\phi - \Psi)} = \frac{N_0}{2\pi} \left(1 + v_1 \cos(\phi - \Psi) + 2v_2 \cos\left(2(\phi - \Psi)\right) + \ldots\right) \tag{4.6}$$

where the v_n coefficients represent the strength of the correlation with respect to the reaction plane. By the symmetry of the overlap region (see Fig. 4.1) the dominant terms are the even coefficients. The most dominant of those even terms is the v_2 term, and it is known as elliptic flow [Adams et al., 2004c].

Since each of the particles in the event are correlated with the reaction plane, they will be correlated with one another in a very straightforward manner. This correlation can be seen by writing the definition of the two-particle correlation

$$\frac{dN}{d\Delta\phi} = \int_0^{2\pi} \int_0^{2\pi} d\phi_A d\phi_B \; \frac{dN}{d\phi_A} \frac{dN}{d\phi_B} \delta\left(\Delta\phi - \phi_A - \phi_B\right) \tag{4.7}$$

Substituting Eqn. 4.6 and gives

$$
\begin{aligned}
\frac{dN}{d\Delta\phi} &= \int_0^{2\pi} \int_0^{2\pi} d\phi_A d\phi_B \frac{N_A}{2\pi} \left(1 + 2v_2^A \cos\left(2(\phi_A - \Psi)\right)\right) \\
&\quad \frac{N_B}{2\pi} \left(1 + 2v_2^B \cos\left(2(\phi_B - \Psi)\right)\right) \delta\left(\Delta\phi - \phi_A - \phi_B\right) \\
&= \frac{N_A N_B}{(2\pi)^2} \int_0^{2\pi} d\phi_A [1 + 2v_2^A \cos(2(\phi_A - \Psi)) + 2v_2^B \cos(2(\phi_A - \Delta\phi - \Psi)) + \\
&\quad 4v_2^A v_2^B \cos\left(2(\phi_A - \Psi)\right) \cos\left(2(\phi_A - \Delta\phi - \Psi)\right)] \\
&= \frac{N_A N_B}{(2\pi)^2} [2\pi + 4v_2^A v_2^B \int_0^{2\pi} d\phi_A \; (\cos^2(2(\phi_A - \Psi)) \cos(2\Delta\phi) + \\
&\quad \cos(2(\phi_A - \Psi)) \sin(2(\phi_A - \Psi)) \sin(2\Delta\phi))] \\
&= \frac{N_A N_B}{2\pi} \left(1 + 2v_2^A v_2^B \cos(2\Delta\phi)\right) \tag{4.8}
\end{aligned}
$$

The resulting pair distribution which the same correlation shape as the single particle distribution with respect to the reaction plane but with the modification that the strength of the

modulation is the product of the single particle's v_2. The resulting distribution will peak at $\Delta\phi = 0$ and π, which is similar to the qualitative feature of the jet and di-jet correlations.

It is assumed that the correlation function has two sources. The first is from jets, with the accompanying underlying event. In p+p and d+Au collisions this background is *assumed* to be isotropic. In the case of A+A collisions, the elliptic flow introduces a harmonic $\cos(2\Delta\phi)$ shape on the background. In such a two source model, the correlation function, or more precisely the pair per trigger distribution, can be written as

$$\frac{1}{N_{trig}}\frac{dN}{d\Delta\phi} = B(1 + 2v_2^{trig}v_2^{assoc}\cos(2\Delta\phi)) + \mathcal{J}(\Delta\phi) \tag{4.9}$$

where B is the underlying isotropic background, v_2^{trig} and v_2^{assoc} are the trigger and associated particle's elliptical flow, and $\mathcal{J}(\Delta\phi)$ is the shape of the jet plus di-jet distribution. To determine the functional form for the jet distribution, we must introduce some fundamental ideas about fragmentation.

4.4 Fundamental Relationships

To study jets in depth, the model that that is used is an extension of that suggested by Feynman, Field, and Fox in a series of papers [Field and Feynman, 1977; Feynman et al., 1977, 1978] in the late 1970's which addressed the results from CERN Interacting Storage Ring (ISR) p+p experiments at high-p_T at midrapidity. Fig. 4.2 and Fig. 4.3 introduce the necessary variables that are accessible to two-particle correlations.

4.4.1 Near-angle Jet Correlations

Fig. 4.2 shows the transverse plane of a single event where two hadrons fragment from a single jet, $p_{T,trig}$ is in the trigger momentum range and $p_{T,assoc}$ is in the associated momentum range. The trigger hadron momentum is written for a single event as

$$p_{T,trig} = \sqrt{z_{trig}^2 q_T^2 + j_{Ty,trig}^2} \tag{4.10}$$
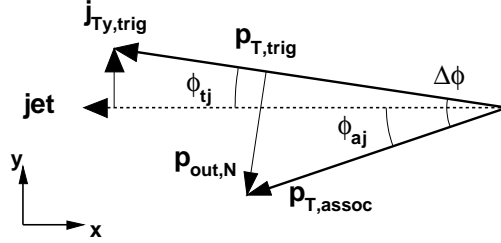
Figure 4.2   Schematic of an event where two fragmenting hadrons are pro-
duced in the p_T ranges of interest from the a single jet.

where the parent parton has momentum q_T, the fragment has some fraction z_{trig} along the parent parton direction, and the fragmented hadron has a component transverse to the jet direction known as $\vec{j}_T$. This $\vec{j}_T$ has components in the transverse and longitudinal directions. The transverse component is denoted as j_{Ty}. This j_{Ty} is empirically given a Gaussian distribution but has power-law tails at very large magnitude due to hard gluon radiation [Adler et al., 2005b]. Similarly, the associated particle momentum is written as

$$p_{T,assoc} = \sqrt{z_{assoc}^2 q_T^2 + j_{Ty,assoc}^2} \tag{4.11}$$

What is measured by two-particle correlations is the angle between the fragments, $\Delta\phi_N$. The subscript N is used here to denote the near angle correlation. This angle can be written in terms of the angles that each fragment makes with respect to the parent jet direction

$$\Delta\phi_N = \phi_{tj} + \phi_{aj} \tag{4.12}$$

The angles on the right-hand side of Eqn. 4.12 can be written in terms of the p_T and the j_{Ty}

of the fragments.

$$j_{Ty,assoc}^2 = p_{T,assoc}^2 \sin^2 \phi_{\mathrm{aj}} \tag{4.13}$$

$$j_{Ty,trig}^2 = p_{T,trig}^2 \sin^2 \phi_{\mathrm{tj}} \tag{4.14}$$

It is necessary to square the quantities because the event averages will eventually be taken and, in the case of a Gaussian distribution, the mean is zero but the root-mean-squared (RMS) is non-zero. Taking the sine of Eqn. 4.12 and multiplying by $p_{T,assoc}$ gives

$$p_{T,assoc} \sin(\Delta\phi_N) = p_{T,assoc} \sin(\phi_{tj}) \cos(\phi_{aj}) + p_{T,assoc} \sin(\phi_{aj}) \cos(\phi_{tj}) \tag{4.15}$$

Squaring and writing entirely in terms of sines so that Eqn. 4.13 can be used yields

$$
\begin{aligned}
p_{T,assoc}^2 \sin^2(\Delta\phi_N) &= p_{T,assoc}^2 \sin^2(\phi_{tj}) \cos^2(\phi_{aj}) + p_{T,assoc}^2 \sin^2(\phi_{aj}) \cos^2(\phi_{tj}) \\
&\quad + 2p_{T,assoc}^2 \sin(\phi_{aj}) \cos(\phi_{aj}) \sin(\phi_{tj}) \cos(\phi_{tj}) \\
&= p_{T,assoc}^2 \sin^2(\phi_{tj}) + p_{T,assoc}^2 \sin^2(\phi_{aj}) - 2p_{T,assoc}^2 \sin^2(\phi_{aj}) \sin^2(\phi_{tj}) \\
&\quad + \frac{1}{2} p_{T,assoc}^2 \sin(2\phi_{aj}) \sin(2\phi_{tj})
\end{aligned}
\tag{4.16}
$$

Taking the event average and substituting Eqn. 4.13 results in

$$
\begin{aligned}
\left\langle p_{T,assoc}^2 \sin^2(\Delta\phi_N) \right\rangle &= \left\langle p_{T,assoc}^2 \sin^2(\phi_{aj}) \right\rangle + \left\langle p_{T,assoc}^2 \sin^2(\phi_{tj}) \right\rangle \\
&\quad - 2 \left\langle p_{T,assoc}^2 \sin^2(\phi_{aj}) \sin^2(\phi_{tj}) \right\rangle + \frac{1}{2} \left\langle p_{T,assoc}^2 \sin(2\phi_{aj}) \sin(2\phi_{tj}) \right\rangle \\
&= \left\langle j_{Ty,assoc}^2 \right\rangle + \left\langle \frac{p_{T,assoc}^2}{p_{T,trig}^2} j_{Ty,trig}^2 \right\rangle - 2 \left\langle \frac{j_{Ty,assoc}^2 j_{Ty,trig}^2}{p_{T,trig}^2} \right\rangle \\
&\approx \left\langle j_{Ty}^2 \right\rangle + \left\langle x_h^2 j_{Ty}^2 \right\rangle
\end{aligned}
\tag{4.17}
$$

The terms of order $\left\langle j_{Ty}^4 \right\rangle$ have been neglected since $j_T \sim \Lambda \sim 0.4$ GeV/c. Further there is an assumption that the trigger and associated j_{Ty} after event averaging will be the same. The

notation

$$x_h = \frac{p_{T,assoc}}{p_{T,trig}} \tag{4.18}$$

has been introduced. Since the j_{Ty} distribution is approximately Gaussian, it follows from Eqn. 4.17 that $p_{T,assoc} \sin \Delta\phi \equiv p_{out,N}$ is Gaussian distributed. However, for small angles $\sin(\Delta\phi) \sim \Delta\phi$ and the angular distribution is approximately Gaussian. From the correlation function the RMS of the near angle Gaussian distribution is determined and related to the RMS of j_{Ty}. By making several approximations to Eqn. 4.17, it is found that

$$\sqrt{\left\langle j_{Ty}^2 \right\rangle} = \sigma_N \frac{\langle p_{T,assoc} \rangle \langle p_{T,trig} \rangle}{\sqrt{\langle p_{T,assoc} \rangle^2 + \langle p_{T,assoc} \rangle^2}} \tag{4.19}$$

where σ_N is the RMS of the near-angle $\Delta\phi$ distribution. The different approximations for Eqn. 4.19 are detailed in Appendix A.

4.4.2   Away-Side Jet Correlations
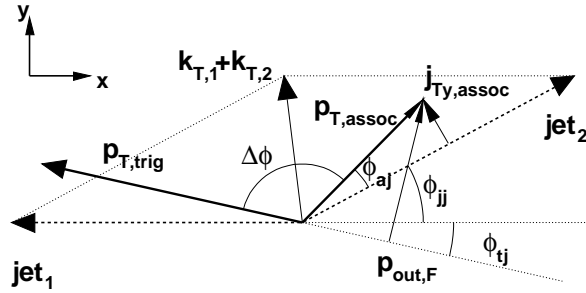
Figure 4.3   Schematic of a single event which produces one fragmented hadron from each pair from a di-jet.

The study of the away-side correlations is much complex. Initial state partons that par-

ticipate in the hard scattering are confined within the hadron and, by simple uncertainty arguments, have some distribution of transverse momentum in the center-of-mass frame of the hadron-hadron collision. In the frame in which the partons that participated in the hard scattering were collinear, the outgoing partons from the interaction will have the same momentum and be exactly back-to-back. However, the initial state transverse momentum of the partons boosts this system into the center-of-mass frame of the hadron-hadron collision, causing the outgoing parton momenta to be different and for the partons not to be back-to-back, i.e. they are acoplanar. This transverse momentum of the partons is called $\vec{k}_T$ and is entirely in the transverse plane (see Fig. 4.3). This partonic transverse momentum is assumed to be Gaussian. Similar to the analysis of the near angle, the far angle can be analyzed.

The first collaboration to systematically study away-side correlations in hadronic collisions was the CCHK collaboration at the ISR [Della Negra et al., 1977]. They introduced p_{out} to study away-side correlations. It is defined as (see Fig. 4.3)

$$p_{out,F} = p_{T,assoc} \sin(\Delta\phi_F) \tag{4.20}$$

This observable defines the associated particle's momentum transverse to the trigger direction and is directly related to the acoplanarity of the di-jets.

This observable can be used to determine the relationship between the far angle and k_T. This is seen by first writing the far angle in a given event as (see Fig. 4.3)

$$\Delta\phi_F = \phi_{jj} + \phi_{aj} + \phi_{tj} = \phi_{jj} + \Delta\phi_N \tag{4.21}$$

Squaring and taking the sine of this and following the mathematics, it is found that

$$
\begin{aligned}
\sin\Delta\phi_F &= \sin\phi_{jj}\cos\Delta\phi_N + \cos\phi_{jj}\sin\Delta\phi_N \\
p_{T,assoc}^2\sin^2\Delta\phi_F &= p_{T,assoc}^2\sin^2\phi_{jj}\cos^2\Delta\phi_N + p_{T,assoc}^2\cos^2\phi_{jj}\sin^2\Delta\phi_N \\
&\quad + \frac{1}{2}p_{T,assic}^2\sin(2\phi_{jj})\sin(2\Delta\phi_N) \\
\left\langle p_{out,F}^2 \right\rangle &= \left\langle p_{T,assoc}^2\sin^2\phi_{jj}(1 - \sin^2\Delta\phi_N) \right\rangle
\end{aligned}
$$

$$+ \left\langle p_{T,assoc}^2 (1 - \sin^2 \phi_{jj}) \sin \Delta\phi_N \right\rangle \qquad (4.22)$$

One component of the k_T vector is (see Fig. 4.3)

$$2k_{Ty} = q_{T,assoc} \sin \phi_{jj} \qquad (4.23)$$

where $q_{T,assoc}$ is the parent parton momentum of the **associated** particle. With this definition and Eqn. 4.17, it follows that

$$
\begin{aligned}
\left\langle p_{out,F}^2 \right\rangle &= \left\langle 2 \frac{p_{T,assoc}^2}{q_{T,assoc}^2} k_{Ty}^2 \right\rangle + \left\langle j_{Ty}^2 \right\rangle + \left\langle x_h^2 j_{Ty}^2 \right\rangle \\
&\quad - \left\langle \frac{4k_{Ty}^2}{q_{T,assoc}^2} \right\rangle (\left\langle j_{Ty}^2 \right\rangle + \left\langle x_h^2 j_{Ty}^2 \right\rangle) \\
&= \left\langle 2z_{assoc}^2 k_{Ty}^2 \right\rangle + \left\langle j_{Ty}^2 \right\rangle + \left\langle x_h^2 j_{Ty}^2 \right\rangle - \left\langle \frac{4z_{assoc}^2 k_{Ty}^2}{p_{T,assoc}^2} \right\rangle (\left\langle j_{Ty}^2 \right\rangle + \left\langle x_h^2 j_{Ty}^2 \right\rangle)(4.24)
\end{aligned}
$$

Inspecting the above result, $p_{out,F}$ is the quantity that is Gaussian distributed because j_T and k_T are Gaussian distributed. If the far-angle distribution is not very wide, the far-angle can be approximated as a Gaussian. To go further to relate the far-angle RMS to the RMS of k_{Ty} requires knowledge of $\langle z_{assoc} \rangle$.

Eqn 4.24 can be directly compared to the result of Feynman et al. [1978] in Eqn. 2.16. The result derived here is a more exact formulation. No approximations about the jet p_T being the same between the trigger and associated jets is made. With a large value of k_T low-p_T jets will not have the same p_T. The lack of approximation has the consequence that the associated fragmentation variable z_{assoc} must be determined which is a difficult. Further, there is a "cross-term" between $\left\langle j_{Ty}^2 \right\rangle$ and $\left\langle k_{Ty}^2 \right\rangle$ which is the result of not making any small angle approximations. This final term will contribute a fraction of the other second and third terms. The associated jet momentum must be not less than $2k_{Ty}$ for a given event. Therefore the term $\frac{4k_{Ty}^2}{q_{T,assoc}^2}$ is less than one. How much less than one depends on the magnitude of k_T.

To summarize, the jet function is approximately two Gaussian distributions, one centered at $\Delta\phi = 0$, the near side that is defined by j_{Ty} via Eqn. 4.19, and one at $\Delta\phi = \pi$, the far side

that is defined by the convolution of j_{Ty} and k_{Ty} via Eqn. 4.24.

$$\mathcal{J}(\Delta\phi) = \frac{S_N}{\sqrt{2\pi}\sigma_N} e^{-\frac{\Delta\phi^2}{2\sigma_N^2}} + \frac{S_F}{\sqrt{2\pi}\sigma_F} e^{-\frac{(\Delta\phi-\pi)^2}{2\sigma_F^2}} \tag{4.25}$$

4.4.3 Di-jet Acolpanarity

An alternative variable that can quantify the di-jet acoplanarity is the angle between the jets, ϕ_{jj}. Following the derivation as above the angle between the jets can be written in terms of the measured near and far angle relative azimuth, Eqn. 4.21. Taking the sine of both sides and squaring it is similar to removing the $p_{T,assoc}$ dependence from Eqn. 4.22. We have the following after squaring each side and taking the event average

$$\left\langle \sin^2 \Delta\phi_F \right\rangle = \left\langle \sin^2 \phi_{jj} \right\rangle + \left\langle \sin^2 \Delta\phi_N \right\rangle - 2\left\langle \sin^2 \phi_{jj} \right\rangle \left\langle \sin^2 \Delta\phi_N \right\rangle \tag{4.26}$$

This can be rearranged to find $\left\langle \sin^2 \phi_{jj} \right\rangle$

$$\left\langle \sin^2 \phi_{jj} \right\rangle = \frac{\left\langle \sin^2 \Delta\phi_F \right\rangle - \left\langle \sin^2 \Delta\phi_N \right\rangle}{1 - 2\left\langle \sin^2 \Delta\phi_N \right\rangle} \tag{4.27}$$

The left-hand side is a partonic quantity related to hadronic variables and contains all of the information about k_T. When the jets are nearly back-to-back, $\phi_{jj} \sim$ zero, so $\left\langle \sin^2 \phi_{jj} \right\rangle$ is near zero. As the di-jet distribution becomes more acoplanar $\left\langle \sin^2 \phi_{jj} \right\rangle$ increases. Because of j_T this quantity is never exactly zero.

To relate the quantities on the right-hand side of Eqn. 4.27 it is assumed that the angles are Gaussian distributed. This is not exactly true as was argued above but by inspection of the correlation functions this is a reasonable approximation. Quantitatively it is good to less that 2% (see Appendix A). Since the angles are small the sine term can be expanded.

$$\begin{aligned} \left\langle \sin^2 \Delta\phi \right\rangle &= \left\langle \left(\Delta\phi - \frac{1}{6}\Delta\phi^3 + \frac{1}{120}\Delta\phi^5 + \ldots \right)^2 \right\rangle \\ &= \left\langle \Delta\phi^2 \right\rangle - \frac{1}{3}\left\langle \Delta\phi^4 \right\rangle + \frac{2}{45}\left\langle \Delta\phi^6 \right\rangle + \ldots \end{aligned} \tag{4.28}$$

The first term, $\langle \Delta\phi^2 \rangle = \sigma^2$, is the square of the measured RMS. For a Gaussian distribution the higher even moments are related to the RMS by

$$\langle x^{2n} \rangle = (2n-1)!! \langle x^2 \rangle^n = (2n-1)!! \sigma^{2n} \tag{4.29}$$

In this case the higher powers are

$$\langle \Delta\phi^4 \rangle = 3 \langle \Delta\phi^2 \rangle^2 = 3\sigma^4 \tag{4.30}$$

$$\langle \Delta\phi^6 \rangle = 15 \langle \Delta\phi^2 \rangle^3 = 15\sigma^6 \tag{4.31}$$

These are substituted into Eqn. 4.28 and the expansion in terms of the Gaussian RMS of the angle is

$$\left\langle \sin^2 \Delta\phi \right\rangle = \sigma^2 - \sigma^4 + \frac{2}{3}\sigma^6 \tag{4.32}$$

This approximation is good to 2% for $\sigma < 0.5$ rad and 0.6% for $\sigma < 0.2$ rad. The final result is

$$\left\langle \sin^2 \phi_{jj} \right\rangle = \frac{\left(\sigma_F^2 - \sigma_F^4 + \frac{2}{3}\sigma_F^6 \right) - \left(\sigma_N^2 - \sigma_N^4 + \frac{2}{3}\sigma_N^6 \right)}{1 - 2\left(\sigma_N^2 - \sigma_N^4 + \frac{2}{3}\sigma_N^6 \right)} \tag{4.33}$$

In high-p_T p+p, d+Au, and Au+Au collisions the acoplanarity is quantified in terms of Eqn. 4.33.

4.4.4 Fragmentation Functions

The other that the CCHK collaboration at the ISR introduced is x_E [Della Negra et al., 1977] defined as

$$x_E = \frac{\vec{p}_{T,trig} \cdot \vec{p}_{T,assoc}}{|p_{T,trig}^2|} \tag{4.34}$$

which is the fractional momentum of the associated particle along the trigger direction. This observable is meant to substitute for z, the fraction of the fragment's momentum along the

parent parton direction. This x_E can be related to the z of each of the fragments

$$x_E = \frac{p_{T,assoc}\cos\Delta\phi_F}{p_{T,trig}} \approx \frac{z_{assoc}}{z_{trig}} \qquad (4.35)$$

This approximation is reasonable when k_T is not large enough to cause a large difference between the two parent parton momenta. Ideally the $D(z)$ could be measured by fixing z_{trig} and varying the associated momentum.

To see how the x_E distributions, that is the conditional yield as a function of x_E, are related to the fragmentation function it is instructive to see how the measured single particle spectrum can be related to the fragmentation function. To do so we must write the single particle spectrum similar to Eqn. 2.12.

First, the distribution of partons in the final state is defined as

$$f_q(q_T) \equiv \frac{1}{q_T}\frac{d\sigma_{hard}}{dq_T} \qquad (4.36)$$

This distribution represents the hard parton cross-section for all of the different channels which produce an outgoing parton at q_T. The fragmentation function is defined as usual

$$D(z) = \frac{d\sigma_{frag}}{dz} \qquad (4.37)$$

This fragmentation function is the effective fragmentation function which describes the probability of a parton to produce the single particle in question. The single particle distribution follows from these definitions.

$$
\begin{aligned}
d\sigma &= d\sigma_{hard}d\sigma_{frag} \\
&= q_T f_q(q_T)\,dq_T D(z)dz \\
&= \frac{p_T}{z}f_q\left(\frac{p_T}{z}\right)\frac{dp_T}{z}D(z)dz
\end{aligned}
\qquad (4.38)
$$

To find the p_T distribution the integral over z is performed. The lower limit of z is $x_T = 2p_T/\sqrt{s}$ since the parton cannot have a lower momentum than the fragment. The upper limit is 1, the

kinematical limit. Therefore, the single inclusive spectrum can be written as

$$\frac{1}{p_T}\frac{d\sigma}{dp_T} = \int_{x_T}^{1} \frac{dz}{z^2} f_q\left(\frac{p_T}{z}\right) D(z) \tag{4.39}$$

Assuming some form for the final state parton distribution, $f_q(q_T)$, a fit to the data extracts the fragmentation function.

Following the same arguments as above the pair cross-section, which is proportional to $1/N_{trig}dN/dp_{T,assoc}$, can be written as

$$
\begin{aligned}
d\sigma &= d\sigma_{hard}d\sigma_{frag,trig}d\sigma_{frag,assoc} \\[2mm]
&= q_T f_q(q_T)\, dq_T D(z_{trig})\, dz_{trig} D(z_{assoc})\, dz_{assoc} \\[2mm]
&= \frac{p_{T,trig}}{z_{trig}} f_q\left(\frac{p_{T,trig}}{z_{trig}}\right) \frac{dp_{T,trig}}{z_{trig}} D(z_{trig})\, dz_{trig} D\left(\frac{p_{T,assoc}}{p_{T,trig}} z_{trig}\right) \frac{dp_{T,assoc}}{p_{T,trig}} z_{trig} \tag{4.40}
\end{aligned}
$$

The last line follows when assuming that q_T is the jet momentum for both jets, that is, no k_T introduces any difference between the outgoing jet momentum. The integration over z_{trig} can be performed with the same limits as before yielding the pair cross-section.

$$\frac{d^2\sigma}{dp_{T,trig}dp_{T,assoc}} = \int_{x_{T,trig}}^{1} \frac{dz_{trig}}{z_{trig}} f_q\left(\frac{p_{T,trig}}{z_{trig}}\right) D(z_{trig}) D\left(\frac{p_{T,assoc}}{p_{T,trig}} z_{trig}\right) \tag{4.41}$$

In this distribution the interpretation of the f_q function changes to that distribution which produces two (azimuthally) back-to-back partons both with q_T. Each of the fragmentation functions represent the probability for a parton to fragment to the trigger and the associated particle. In principle they should not be the same function when dealing with different particle types for the trigger and associated particles.

Finally, this pair distribution proportional to $1/N_{trig}dN/dp_{T,assoc}$ can be related to the x_E distribution by relating $1/N_{trig}dN/dp_{T,assoc}$ to $1/N_{trig}dN/dx_E$. By the definition of x_E, Eqn. 4.34

$$x_E = \frac{p_{T,assoc}}{p_{T,trig}} \cos \Delta\phi_F$$

$$
\begin{aligned}
&= \frac{p_{T,assoc}}{p_{T,trig}} \left(\cos\phi_{jj} \cos\Delta\phi_N - \sin\phi_{jj} \sin\Delta\phi_N \right) \\
&\approx \frac{p_{T,assoc}}{p_{T,trig}} \cos\Delta\phi_N \\
&\approx \frac{p_{T,assoc}}{p_{T,trig}} \sqrt{1 - \sin^2\Delta\phi_N} \\
&\approx \frac{p_{T,assoc}}{p_{T,trig}} \sqrt{1 - \frac{j_{Ty}^2}{p_{T,assoc}^2}}
\end{aligned}
\tag{4.42}
$$

This is a good approximation only when k_T is small, which was also used in deriving the pair distribution. Therefore, the x_E distribution can be related to the $p_{T,assoc}$ distribution approximately as

$$
\frac{1}{N_{trig}} \frac{dN}{dx_E} \approx \frac{p_{T,trig}}{\sqrt{1 - j_{Ty}^2/p_{T,assoc}^2}} \frac{1}{N_{trig}} \frac{dN}{dp_{T,assoc}}
\tag{4.43}
$$

Therefore, the x_E and $p_{T,assoc}$ distributions are proportional to the pair cross-section in Eqn. 4.41. This means these distributions are proportional to an integral containing the product of the trigger and associated fragmentation functions. These were derived with the $k_T \approx 0$. Adding k_T is in principle possible but the effect of k_T should be in the $f_q(q_T)$ distribution.

CHAPTER 5.   Di-jets in p+p and d+Au Collisions

This chapter discusses the analysis of two-particle correlations in p+p and d+Au collisions at $\sqrt{s_{NN}} = 200$ GeV/c. These data were collected in consecutive runs under similar running conditions from December 2002 to May 2003. Jet properties from two-particle correlations and extracted quantities from these correlations are given. These results are reported in a recent publication [Adler et al., 2005b].

5.1   Experimental Method

5.1.1   Run Selection

In order to use the mixed event technique for the two-particle correlations, it is necessary to have a set of stable runs that do not have large fluctuations in acceptance. These runs have the most easily reproduced and stable acceptance. The acceptance depends on the types of particles that are correlated. In p+p collisions, neutral pions are used as triggers and unidentified charged hadrons are used as the associated particles. These correlations were also performed in d+Au collisions, along with correlations between pairs of charged hadrons. Since charged hadrons are used in all analyses, the acceptance of the charged particle tracking was studied. This was done by studying the run-by-run dependence of several quality assurance (QA) variables.

First, the difference in the mean number of tracks per event between the two central arms of PHENIX as a function of run number was chosen. This is plotted in Fig. 5.1 for tracks with $p_T > 1$ GeV/c in d+Au collisions. Most of the runs in the data set fall along a band near zero, but about a dozen runs show a large excursion from the typical set of runs. The reason for a fluctuation within a run is potentially due to a change in the drift chamber acceptance,
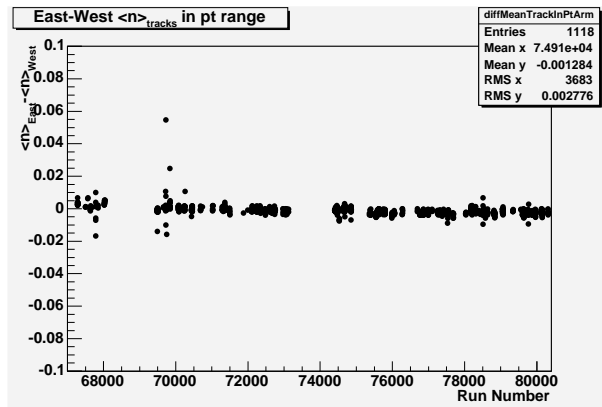
Figure 5.1 d+Au run-by-run dependence of the east-west difference in the mean number of tracks per event for tracks with reconstructed $p_T > 1$ GeV/c.

e.g. a section of the drift chamber having high voltage problems. Several high-voltage trips is one cause for stopping a run during data taking and would significantly change the charged particle tracking. This cause typically only affects the end of a run but we have removed the entire run to be conservative.

Choosing those runs that deviate significantly from the typical set of runs can be done systematically by projecting the distributions onto the y-axis to obtain a distribution of runs that fall at a given mean. For many runs, this distribution is Gaussian and a cut of several σ can be used. These will pick out the outliers above a given σ. Those runs that deviate by a large number of σ, are easily picked out by eye. This is what has been done in this analysis. Making a strict cut is not necessary since mixing only occurred within a single run and not across run boundaries where conditions can fluctuate more than within a single run.

Next, the average p_T of reconstructed charged tracks in both of the arms was studied. This is shown in Fig. 5.2 for the East and West arms for tracks with $p_T > 1$ GeV/c. Many of the runs lie along a line near 1.5 GeV/c, with only a handful of runs that deviate significantly. The result of many more or many fewer than usual high-p_T particles in the event could be caused by a problem in the magnetic field. Any run that deviated significantly was removed completely.

Another run QA check was the mean centrality for a given run. Fig. 5.3 shows this distri-
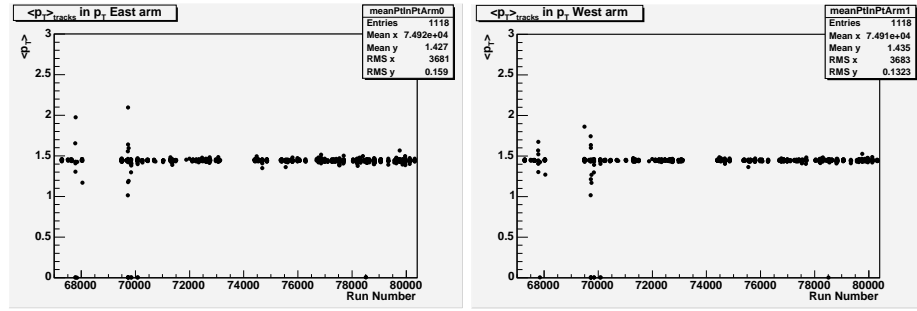
Figure 5.2   d+Au run-by-run dependence of the $\langle p_T \rangle$ with reconstructed tracks with $p_T > 1$ GeV/c in the East arm(left) and West arm(right).
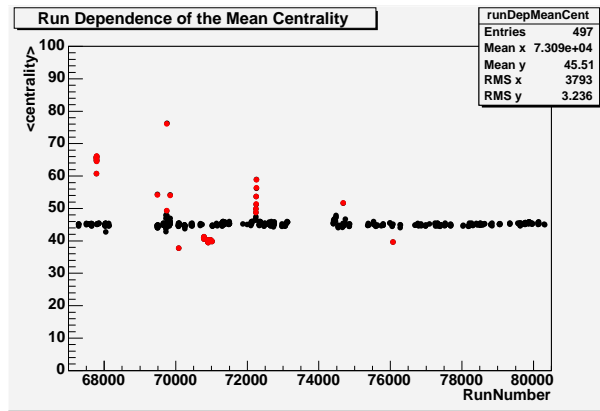
Figure 5.3   d+Au run-by-run dependence of the mean centrality for events with at least one reconstructed track with $p_T > 1$ GeV/c.

bution. There is a band of typical runs at a mean centrality of 44%. This is expected since the centrality should be a flat distribution between 0% and 88%. Several runs show a large deviation from the mean. Any problem with the measured centrality could be a problem with the BBC since it is the only subsystem that determines the centrality in d+Au (see Section 3.1.4). Any problem with the BBC could result in an incorrect determination of the z-vertex or t_0, both of which are important for detecting the photon decays from the π^0 triggers used. Those runs with a large deviation from the average are excluded.

During each of the p+p and d+Au runs there was a portion of the running period where additional thin material was placed in the central arms to convert photons into electrons for use as a background measure for single electron analysis. These runs have a reduced number

of reconstructed π^0 triggers since only the $\gamma\gamma$ decay channel is used. It also would introduces a large amount of background to the charged hadrons. As a result, these runs were removed from the analysis.

The data for the π^0-h correlations were collected using ERT triggers (see Section 3.1.6). These triggers were relatively stable during the d+Au and p+p runs, but there were some variation in gains and thresholds of the triggers. A detailed study of the ERT trigger performance was done by Bauer et al. [2003], and a list of runs that failed the study's QA tests are removed.

5.1.2 Single Particle Selections

The single particle selections are used to produce the highest quality input to the pairs as possible.

5.1.2.1 Charged Hadron Selections

Charged hadron selections are made on several levels from rejection of low-quality tracks to removal of remaining background by using additional information from other detectors. First the track model (see Section 3.3.3) is based on Drift Chamber (DCH) hits in a series of wires giving r-ϕ information (X wires) associated with z information from Pad Chamber 1 (PC1). The U and V plane wires in the DCH are used for confirmation of z information from PC1. A series of bits encode the planes of wires hit and the quality of the z information and is called the drift chamber quality.

The Drift Chamber Quality bit pattern is

- bit 0 - X1 plane used in the track model

- bit 1 - X2 plane used in the track model

- bit 2 - UV hits associated with a track

- bit 3 - unique UV hits in a track

- bit 4 - PC1 confirmation hit found

- bit 5 - unique PC1 confirmation hit found

The highest quality track has a value of 63, corresponding to all bits true. The next highest quality track is 31, which corresponds to all bits true except the final bit. For these tracks there is good z information, but the PC1 hit is ambiguous. The absolute minimum quality track is 7 which corresponds to both X1 and X2 used and a UV hit is found but it is not unique. That is, the z information is shared with at least one other track and no PC1 information can distinguish the z information. A cut on high quality tracks is made by requiring the DCH quality to be 63 or 31.
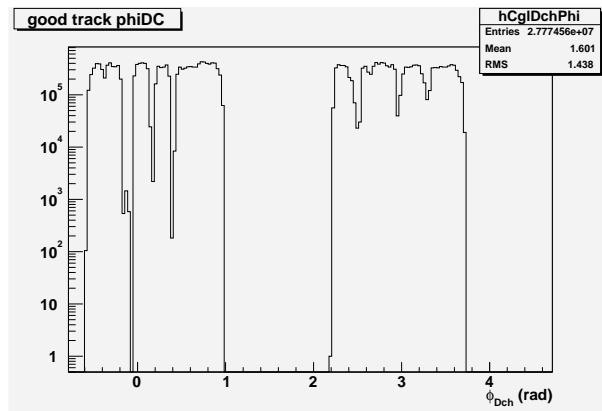
Figure 5.4   Example of azimuthal position of $p_T > 1$ GeV high-quality tracks in the DCH. In both arms there are gaps where fewer tracks are reconstructed.

To remove areas where the acceptance fluctuates, a fiducial cut on the ϕ at the DCH is made. The distribution is shown for high-quality tracks with $p_T > 1$ GeV/c in Fig. 5.4. Both East and West arms are visible with a nearly flat distribution of tracks. There are three gaps within each arm where there are very few tracks that are reconstructed. These areas correspond to intermittently dead areas of the drift chamber. These regions are not sampled in the analysis by requiring that tracks are outside these regions in the DCH. Specifically a track is kept if is is within the following ϕ ranges at the DCH: -0.55 < ϕ < -0.19 rad, -0.045 < ϕ < 0.013 rad, 0.2 < ϕ < 0.37 rad, 0.44 < ϕ < 0.95 rad, 2.21 < ϕ < 2.45 rad, 2.55 < ϕ < 2.93 rad, 3.01 < ϕ < 3.22 rad, 3.34 < ϕ < 3.7 rad.

The previous cuts were at the track level to remove low quality tracks from the analysis and

select a stable sample of charged tracks. The rest of the cuts remove remaining background to the unidentified charged hadrons and remove electrons from the sample of charged tracks. Since the DCH is almost entirely outside of the magnetic field high-p_T tracks in PHENIX have a nearly straight pattern of hits in the DCH. However, there can be straight tracks which are not true high-p_T charged tracks. The major backgrounds to high-p_T unidentified charged hadrons are photon conversions to e^+e^- pairs near the DCH, which result in two nearly straight tracks, and decay of strange mesons and hyperons near the DCH. Because of the proximity of conversion or decay of the daughters to the DCH, these charged particles produce a high quality straight tracks in the DCH having a large p_T. These backgrounds have been studied in great detail with simulation and real data [Adler et al., 2004]. The resulting measured signal-to-background (S/B) of high-p_T tracks is approximately 10 for 4-5 GeV/c tracks, approximately 2 for tracks between 5-7 GeV/c, and approximately 1 for tracks about 7 GeV/c. Only charged tracks below 5 GeV/c are considered as associated particles.

To remove large amounts of background below 5 GeV/c and to remove the electron (positron) tracks from the data, a cut on signals from the Ring Imaging Cherenkov (RICH) is made. If an electron traverses the active area of the RICH there is a corresponding cherenkov photon ring that is associated with the track. A cut requiring that a track does not have an associated RICH ring removes the electrons/positrons from the charged track sample. It is important to note that charged pions would begin to radiate cerenkov photons with the CO_2 gas in the RICH at a momentum of about 4.9 GeV/c. Therefore, this cut is only useful to remove electrons from charged tracks for $p_T < 5$ GeV, which is where the S/B for charged tracks is already reasonable.

To remove low momentum conversions and decays requires further information from the outer detectors in the PHENIX central arms. If a track is truly at lower momentum it multiple scatterings more through the material in the central arm than a true high-p_T track. This multiple scattering results in a larger separation between the track projected to the detector and the position of the hit associated with the tracks. These track residuals are calculated in the tracking algorithm by calculating the separation in ϕ and in z from the detector hits to

straight line projections of DCH/PC1 tracks. These distances are then recast as the number of Gaussian σ, where the σ is the detector resolution added in quadrature to the p_T-dependent multiple scattering through the material in the PHENIX central arm. In that way, requiring a 2σ matching cut on the residuals results in approximately 95% confidence that the track matches the outer detector hit. Any track that has a matching hit wider than that is likely a fake track that has an additional gaussian smearing due to the it being a low-p_T track. In the d+Au and p+p analysis a 2.5σ radial matching cut at PC3 is applied by

$$\sigma_{PC3} = \sqrt{\sigma_{z,PC3}^2 + \sigma_{\phi,PC3}^2} \leq 2.5 \tag{5.1}$$

The final background cut is a cut on z position at the DCH. At the outer edge of the DCH fiducial region are the supports for the DCH and the muon magnet. This material produces a large amount of charged particle background that are directed into the outer edges of the DCH. The DCH active region is symmetric about the center of the interaction region along the beam direction 80 cm on either side. Excluding tracks from the outer 5 cm removes this background.

All of these cuts are similar to those that are made for the single unidentified charged particle analysis. Therefore, the tracking efficiency and momentum resolution should be similar. The momentum resolution of these tracks is $\delta p/p = 0.7\% \oplus 1.0\% p$.

5.1.2.2 Photon Selections

Photons are detected in the Electromagnetic Calorimeter (EMC) which is comprised of both PbGl and PbSc technology. To determine high quality photons, a series of cuts based on the shower shape and the timing is used.

First, a total cluster energy cut is applied by requiring a cluster has more than 500 MeV. This is done because, for both calorimeters, the timing resolution is constant for deposited energy above 500 MeV. Further, those photons below 500 MeV do not contribute significantly to the yield of π^0 above 5 GeV/c, the minimum trigger p_T that is used in this analysis.

Using data those towers that were "hot", "warm", and "dead" were determined. Hot

towers are those with an unusually high number of hits per event. Those that are warm have an unusually high number of hits per event but not as much as the hot towers. Dead towers are those that have unusually low number of hits per event. Each tower has two 8-bit values containing the information on hot, warm, and dead towers called deadmap and warnmap. In the analysis if a cluster was dead, hot, or warm, it was excluded as a photon candidate.

To assess if a cluster in the EMC is an electromagnetic shower, a cut on χ^2 (see Section 3.4.2) is applied for PbSc clusters. This cut is based the shower-shape difference between electrons (photons) and hadrons in an electromagnetic calorimeter. Selecting clusters with $\chi^2 < 3$ produces an approximate electron(photon)-to-hadron signal-to-background of 9.
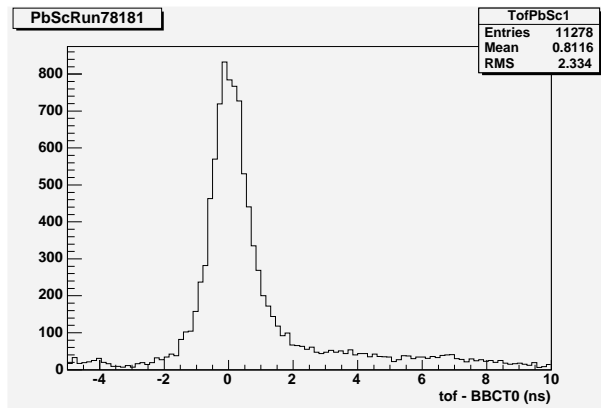
Figure 5.5   Example of time-of-flight (TOF) distribution for a single run in the EMC. This distribution has been corrected by the initial collision time as measured from the BBC and corrected for the flash point so that photons lie at TOF = 0 ns. A long tail in this distribution is the result of hadronic showers in the calorimeter.

The final selection to identify photons is the time-of-flight (TOF) cut. Photons are the first to reach the EMC and their arrival is reflected in the large "flash" peak in the timing distribution shown in Fig. 5.5. Run-by-run and sector-by-sector timing distributions were made and the flash peak was fitted with a Gaussian. These fitted mean and σ are stored for each run and sector. The TOF cut is made by requiring a TOF within 2σ of the fitted mean. This typically results in |TOF| < 2 ns.

Because the pair per trigger distributions are studied, it is not necessary to know he efficiency of these photon cuts. The reconstructed π^0 peak is a strong indication of the purity of

the sample.

5.1.3 π^0 Reconstruction

The π^0 triggers are measured via their $\gamma\gamma$ decay channel. All photons in a given event that pass the single particle cuts are paired and the invariant mass and the pair p_T are calculated. The only further cut for the photon pairs was a cut on the energy asymmetry

$$\alpha = \frac{|E_1 - E_2|}{E_1 + E_2} \tag{5.2}$$

This asymmetry is 0 when both photons share the energy of the parent π^0 equally and 1 when one of the photons decays with all of the parent π^0 momentum. The asymmetry distribution should be flat since the decay products have equal mass. An asymmetry $\alpha < 0.7$ in this analysis is applied in this analysis which is approximately where the distribution is uniform [David et al., 2000b]. The M_{inv} distributions for different pair p_T are plotted in Appendix B. A clear π^0 peak is present at the π^0 mass.

To determine the background to the invariant mass distribution, mixed events were constructed in the same way as they were constructed for the correlation functions. Photons from different events with similar conditions, *i.e.* centrality and z-vertex, were paired, and a separate invariant mass histogram was filled. The background was normalized to the real event invariant mass distribution by requiring that the integrals in the range from 0.200 GeV/c^2 to 0.300 GeV/c^2 of the two distributions were equal. This normalized background was then subtracted from the real distribution leaving the π^0 peak near $M_{inv} = 0.135$ GeV/c^2. In the data a small, linear, residual background is observed that decreases with increasing invariant mass. To account for this, the subtracted distribution is fitted with a Gaussian and a linear background term in the region near the π^0 mass peak.

To obtain the purest π^0 sample, all pairs of photons that reconstructed within 2σ of the fitted peak mass are selected as triggers. This was done by determining the peak and σ of the Gaussian π^0 peak as a function of p_T and centrality. The fitted peak and σ are shown in Fig. 5.6, where the peak$\pm 2\sigma$ as a function of pair p_T are plotted for different d+Au centralities. These
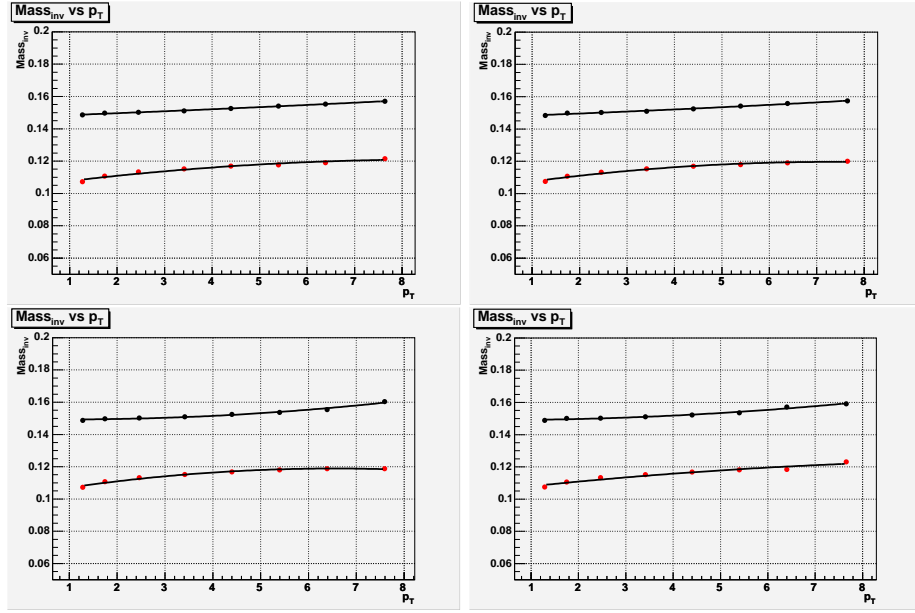
Figure 5.6   Peak $\pm 2\sigma$ of photon pairs. Upper left is for 0-20% central d+Au collisions, upper right is 20-40% central, lower left is 40-60% central, and lower right is 60-88% central. Pairs of photons within this invariant mass range bounded by the solid line are selected as π^0 triggers.

distributions are each parameterized by second order polynomials with different coefficients for each centrality bin. For a 2σ cut, the mass range is typically 0.100 GeV/c^2 to 0.150 GeV/c^2 and is nearly independent of centrality and p_T.

Not all photon pairs that fall within the mass region are real π^0 triggers. From the invariant mass distribution, the π^0 signal-to-background is determined. Fig. 5.7 shows the signal-to-background ratio as a function of pair p_T for different d+Au centrality classes. There is a steady rise as a function of momentum to a plateau and then a slight drop-off above 5 GeV/c. The drop off could possibly be due to the overlap of electromagnetic showers in the PbSc which becomes important around 6 GeV/c.

The background is from combinatoric pairs where each of the photon candidates likely come from two different hadronic, and mostly π^0, decays. Since the hadronic yield drops with p_T, so does the decay background. The decrease in the background is faster than the decrease in the signal since the background is two hadronic decays, as opposed to a single hadronic decay.
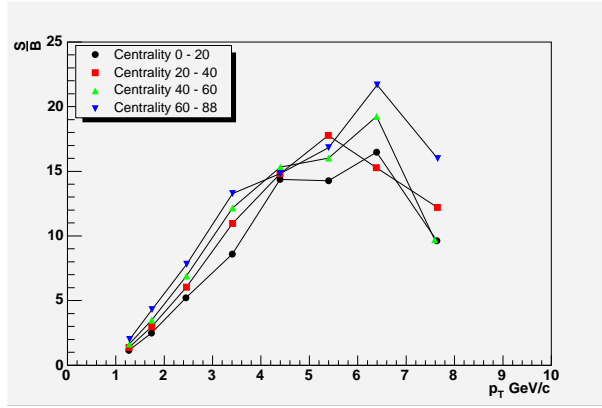
Figure 5.7   Signal-to-background within the π^0 mass window determined from the real and mixed event M_{inv} distributions as a function of pair p_T for different d+Au centrality classes.

Hence, the signal to background ratio increases with p_T.

There is a larger combinatoric background in the most central collisions than in the most peripheral collisions simply due to the higher $\langle N_{coll} \rangle$. This $\langle N_{coll} \rangle$ decreases with centrality and thus the combinatoric background decreases for peripheral collisions. The π^0 yield does not show a strong centrality dependence [Back et al., 2003a]. Therefore, the signal to background ratio for central collisions is lower than the most peripheral collisions.

5.1.4   Event Mixing

As discussed briefly in the previous chapter, when building a correlation function via the mixed event technique (Eqn. 4.2), it is important that the pair efficiency factorizes to cancel the product of the single particle efficiencies. This is accomplished by removing any effects that would ruin this factorization. Two types of problems that need to be removed are 1) temporal variation of central arm acceptance and 2) two-particle resolution effects at different detectors.

The first effect, temporal variation of the central arm acceptance, can be due to various detector failures within and between runs. These can be high-voltage problems, front-end electronics issues, etc. In the p+p and d+Au analysis mixing occurs only within a run and never across run boundaries. This eliminates variations between runs. To minimize effects

within runs, quality cuts are applied to the runs used (see Section 5.1.1) and the mixing buffer depth is chosen to minimize the variation within the run.

Choosing an event buffer depth is influenced by both statistics, *i.e.* having ten times the statistics in the mixed compared to the real distribution, and the length of real time that the buffered events cover. Ideally, the detector would not fluctuate on any time scale but detector failures can cause some acceptance changes on a several minute time scale. Consider 7 GeV/c π^0 production in p+p collisions from ERT triggers. These occurred at a rate of roughly 1 particle every 10000 triggered events. The event rate for the ERT triggers is roughly 1 kHz. Therefore, there is about 1 particle every 10 seconds. To fill a buffer with at least a few hundred particles corresponds to a few thousand seconds or a few 15 minute periods. Typically runs lasted about 1 to 2 hours. In general it is best not to mix with particles from the beginning of a run with those from the end of the run but a large amount of statistics in the mixed events is desirable. The temporal issue becomes more of a problem for rare correlations, such as high-p_T triggers. As a compromise, a buffer depth of 400 events has been chosen for π^0 triggers, hadron triggers, and associated hadron buffers. This depth is more than enough for the hadron buffers and is the lowest limit that should be considered for the highest π^0 trigger bin.

The second effect, the two-track resolution of the tracking detectors, only occurs when one of the particles affects the probability of measuring the other particle in the event. In this analysis the h-h correlations are affected by two-track resolution of the drift chamber. The π^0-h correlations which are measured in two separate detectors are not affected. The two-track resolutions are primarily due to the pattern recognition in high multiplicity environments and to the detector two-particle resolution. In events with very large multiplicity, that is several hundred tracks, separate tracks can merge or a single track can be split by the tracking algorithm. The latter are known as ghost tracks. This effect results in an enhancement of near-angle, $\Delta\phi{=}0$, correlation and must be removed. Ghost tracks from the drift chamber are found by looking at the ratio of real event pairs to mixed event pairs as a function of $\Delta\phi$ and Δzed at the DCH reference radius. One expects an enhancement at low $\Delta\phi$ and Δzed in the

mixed events compared to the real events since there is no ghosting effect in the mixed events. Because of the low multiplicity in p+p and d+Au, it is difficult to see this effect, whereas in Au+Au collisions it is much clearer. The same cuts determined from the 2002 Au+Au jet analyses are applied here. These were cuts on $\Delta\phi_{DCH} < 10$ mrad *and* $\Delta zed_{DCH} < 0.2$ cm.

Tracks from mixed events are not affected by the tracking inefficiencies due to ghosting, and therefore the pairs can be arbitrarily close in physical space. As such, event mixing will not accurately represent the real pair acceptance. To rectify this, the ghost cut is made on both the real and the mixed events. Operationally this cut is applied during the single track selections. If a pair of real tracks is determined to be ghosts, one track from that pair is randomly removed from the single track sample. This cut is applied when mixing by removing the pairs within the ghost cuts.
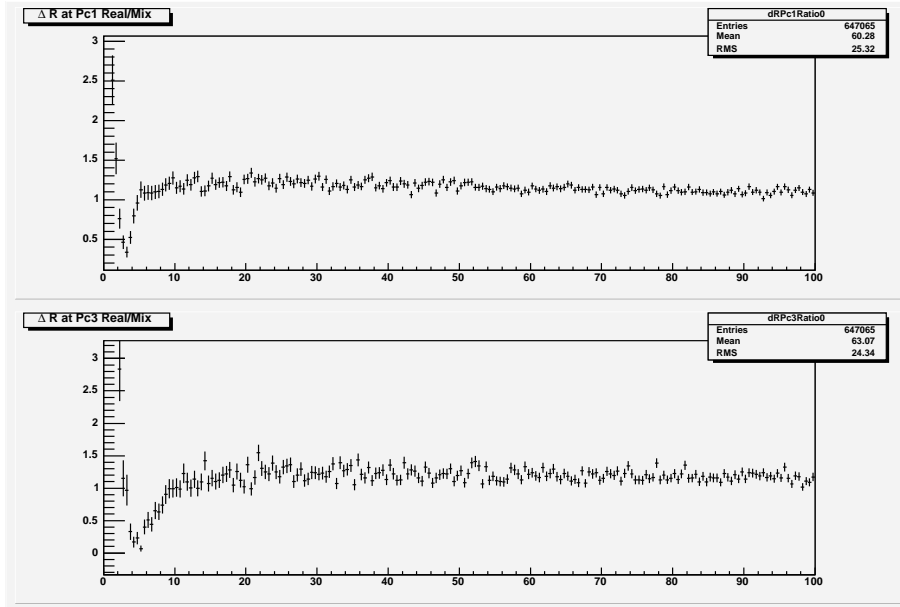
Figure 5.8   Real pair divided by mixed event pair ΔR_{PC} (see text) at PC1 (upper) and PC3(lower).

At PC1 and PC3 there are also two-track resolutions which must be taken into account. These resolutions can be seen by calculating the distance between pairs of tracks at that detector

$$\Delta R_{PC} = \sqrt{\Delta x_{PC}^2 + \Delta y_{PC}^2 + \Delta z_{PC}^2} \qquad (5.3)$$

where x_{PC}, y_{PC}, and z_{PC} are the hit coordinates at the detector. The real pair to mixed event pair distribution for ΔR_{PC} is plotted in Fig. 5.8. At low ΔR_{PC}, there is a large difference between the real and the mixed which is not present beyond $\Delta R_{PC1} > 10$ cm and $\Delta R_{PC3} > 15$ cm. These numbers are roughly a factor of two larger than the estimated two track resolution for these detectors. A cut requiring that track pairs satisfy $\Delta R_{PC1} > 10$ cm and $\Delta R_{PC3} > 15$ cm is applied to both real and mixed pairs.

For completeness the final details of the mixing technique are outlined here. Two buffers are kept, one for events with at least one trigger particle and one for events with at least one associated particle. Once both buffers are full, mixing begins. The first event of the trigger buffer is mixed with every event in the associated buffer. Mixed pair events are required to have their the z-vertices be within 3cm and be within the same centrality class in d+Au events. If the events pass these cuts, one particle from the trigger event is chosen randomly. There is typically only one trigger per event. The associated particle is chosen randomly from the associated event. At lower p_T there can be multiple associated particles.

By mixing only one particle from each event any possibility of auto-correlations resulting from correlations within an event are removed. Auto-correlations can result from a single trigger being correlated with multiple particles from an event. Since the multiple associated particles in an event are correlated with the reaction plane, correlation of all with the trigger particle results in a residual correlation. Since the trigger direction is effectively random, the effect will will decrease with N_{trig} that are mixed with the several associated particles in the event.

5.2 Fixed-p_T h$^\pm$-h$^\pm$ Correlations

By the techniques outlined in the previous sections, two-particle fixed-p_T h$^\pm$-h$^\pm$ correlations in d+Au collisions have been measured. These correlations have been studied between pairs of hadrons that are in the momentum ranges 1-1.5 GeV/c, or 1.5-2.0 GeV/c, or 2.0-3.0 GeV/c, or 3.0-4.0 GeV/c. The resulting conditional yield distributions (see Eqn. 4.5) are shown in Fig. 5.9. There is an evident near-angle, $\Delta\phi$=0, correlation due to pairs of fragments from

a single jet and a correlation at the away-side, $\Delta\phi = \pi$, due to fragments each from of a different jet. The transition from purely soft particle production to purely hard particle (jet) production is expected to be near 2-3 GeV/c, so there are different production mechanisms that are measured in these correlations that are not necessarily just 2→2 jets.
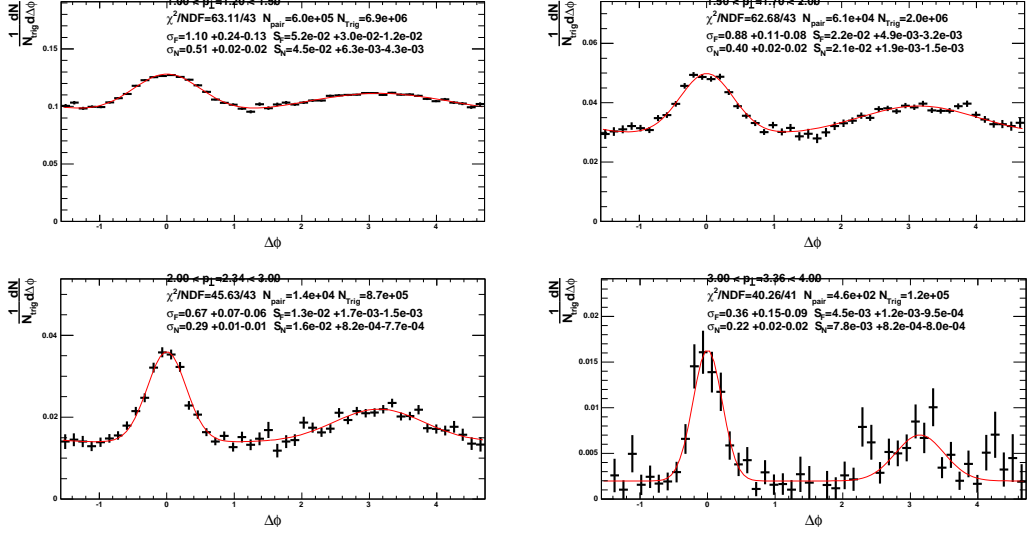
Figure 5.9   Fixed-p_T two-particle azimuthal $h^\pm$-$h^\pm$ correlations in minimum bias d+Au collisions.

To determine the conditional yield distribution it is necessary to determine the associated hadron efficiency. This efficiency has been evaluated for the single particle spectrum where the cuts used in the two analyses are similar. The p_T-dependent efficiencies of each arm have been fit by a smooth polynomial and valid for p_T from 0.4 GeV/c to 10 GeV/c [Reuter et al., 2004]

$$\text{Correction}_{\text{west}}\,(p_T) = \frac{1}{\epsilon_{\text{west}}} = 4.17/p_T + 20.56 - 0.34p_T + 0.015p_T^2$$

$$\text{Correction}_{\text{east}}\,(p_T) = \frac{1}{\epsilon_{\text{east}}} = 3.5/p_T + 18.47 - 0.147p_T - 0.0029p_T^2 \qquad (5.4)$$

The few differences in the cuts also give straightforward multiplicative factors which must be included. First, instead of $|zed| < 40$ cm used for the single particle analysis, a cut of $|zed| < 75$ cm is applied. This results in a factor of 0.53 to the Correction(p_T). The Correction(p_T) was determined for the the full range in azimuth, 2π rad, while the correlations are measured only

in the DCH acceptance, π rad. This results in a factor of 0.5 on the Correction(p_T). For this analysis, the Correction(p_T)'s from each arm are averaged resulting in the inverse efficiency used for obtaining the proper normalization for the conditional yields.

To extract information from these correlation functions, the final correlations function is assumed have a form outlined in Section 4.3 and 4.4, that is

$$\frac{1}{N_{trig}}\frac{dN}{d\Delta\phi} = B + \frac{S_N}{\sqrt{2\pi}\sigma_N}e^{-\frac{\Delta\phi^2}{2\sigma_N}} + \frac{S_F}{\sqrt{2\pi}\sigma_F}e^{-\frac{(\Delta\phi-\pi)^2}{2\sigma_F}} \qquad (5.5)$$

since there is no elliptical flow in p+p and d+Au collisions. For low-statistics data, it is best to fit with a log-likelihood routine instead of a χ^2-minimization routine. The log-likelihood method is useful when the errors are Poisson distributed. The real distribution fulfills this requirement since the bin contents are only counts. Therefore, we fit the real distribution by the following form

$$\frac{dN^{real}}{d\Delta\phi} = \left(B + \frac{S_N}{\sqrt{2\pi}\sigma_N}e^{-\frac{\Delta\phi^2}{2\sigma_N}} + \frac{S_F}{\sqrt{2\pi}\sigma_F}e^{-\frac{(\Delta\phi-\pi)^2}{2\sigma_F}} \right)\frac{dN^{mix}}{d\Delta\phi}/\mathcal{N} \qquad (5.6)$$

where $\mathcal{N}$ is the normalization from Section 4.2.2. In this fit function, there are 5 fit parameters: the overall background B, the yields S_N and S_F, and the widths σ_N and σ_F. The resulting RMS of the near- and far-angle widths are plotted in Fig. 5.10 and tabulated in Table 5.1.

$\langle p_T \rangle$ GeV/c	σ_N (rad)	σ_F (rad)	$\sqrt{\left\langle j_{Ty}^2 \right\rangle}$ (GeV/c)
1.20	$0.513^{+0.025+0.000}_{-0.021-0.013}$	$1.102^{+0.240+0.000}_{-0.134-0.060}$	$0.435^{+0.021+0.026}_{-0.018-0.037}$
1.70	$0.398^{+0.021+0.001}_{-0.019-0.019}$	$0.879^{+0.110+0.000}_{-0.083-0.046}$	$0.479^{+0.025+0.011}_{-0.023-0.032}$
2.34	$0.288^{+0.014+0.005}_{-0.013-0.014}$	$0.666^{+0.066+0.014}_{-0.058-0.044}$	$0.477^{+0.023+0.013}_{-0.022-0.028}$
3.36	$0.216^{+0.021+0.007}_{-0.020-0.000}$	$0.359^{+0.152+0.403}_{-0.092-0.088}$	$0.513^{+0.050+0.020}_{-0.048-0.004}$

Table 5.1   Extracted RMS of the near and far-angle fixed-p_T h$^{\pm}$-h$^{\pm}$ correlations from minimum bias d+Au collisions.

Systematic errors on the widths were determined based on variations of the widths when several cuts were changed in a reasonable, non-vital manner. The cut parameters were varied one-by-one to determine the variation of the correlation shape with these parameters. The
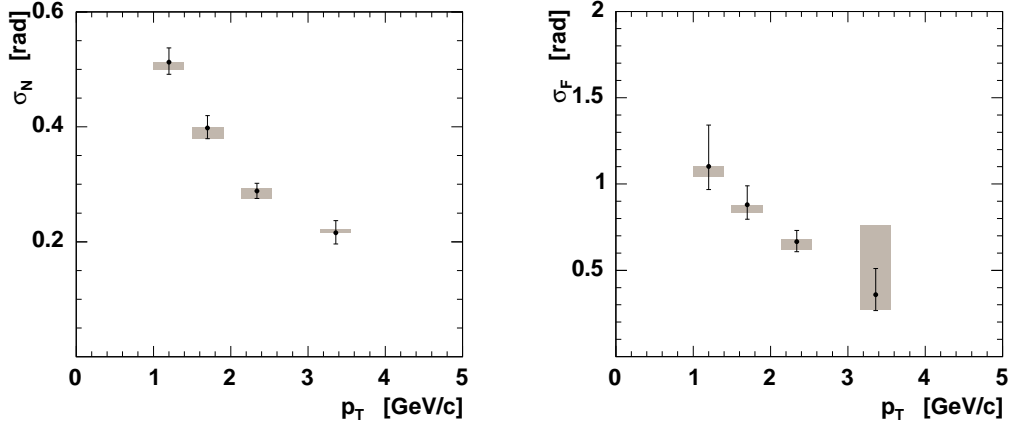
Figure 5.10   Extracted near-(left) and far-(right) angle widths from fixed-p_T h$^{\pm}$-h$^{\pm}$ correlations in minimum bias d+Au collisions. The bar represents the statistical errors from the fit. The grey band represents the systematic errors.

following cuts were changed: 1) the DCH fiducial cut was removed, 2) ghost tracks were not removed, and 3) $\Delta\phi$ and Δzed ghost cuts were not applied. These had little to no affect on the extracted correlation shapes except for the highest p_T far-angle width. The maximum variation is taken as an estimate for the maximum extent systematic error.

To extract jet information from these correlations the equations from Section 4.4 are applied. Because the p_T range is low, it is difficult to extract pure jet physics from the far angle. This is left for the higher-p_T correlations. From Eqn. 4.19 $\sqrt{\left\langle j_{Ty}^2 \right\rangle}$ is extracted from the fitted widths from the correlations. These are tabulated in the right column of Table 5.1. The systematic errors are the quadrature sum of the contributions from the systematic errors from the widths and the assumptions in the derivation. The latter systematic errors are outlined in Appendix A, Table A.1.

The results are plotted in Fig. 5.11. The $\sqrt{\left\langle j_{Ty}^2 \right\rangle}$ is independent of the momentum range. This is consistent with the previous results from the CERN ISR that showed that $\sqrt{\left\langle j_{Ty}^2 \right\rangle}$ is independent of $p_{T,trig}$ [Angelis et al., 1980]. This is understood as a signature of jets. Since fragmentation is a soft, non-perturbative process, the characteristic fragment p_T with respect to the jet will be of order Λ.
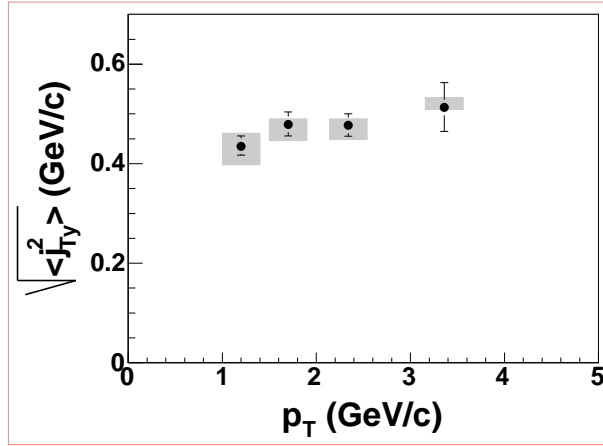
Figure 5.11 Extracted $\sqrt{\left\langle j_{Ty}^2 \right\rangle}$ from fixed-p_T d+Au collisions.

It is also important to note that j_T's independence of p_T implies the near-angle width of the correlation function decreases with increasing p_T in a very well-defined way. From Fig. 5.10 the far-angle width also decreases with increasing p_T. The far-angle is a convolution of the partonic k_T and the fragmentation j_T. Part of the decrease of the far angle width is due to j_T. At these low momentum where higher order processes other than 2→2 contribute to the correlations, it is difficult to extract a k_T value.

5.3 Assorted-p_T π^0-h$^{\pm}$ Correlations

The study of jet properties from two-particle azimuthal correlations can be extended to higher p_T by exploiting PHENIX's excellent capability of detecting π^0. From the p+p and d+Au runs the only limitation to the momentum range available was statistics. The ERT triggered data was used to enhance the yields of high-p_T π^0. The ratio between the raw p_T distributions from ERT triggered events to minimum bias events and normalized by the number of events is plotted in Fig. 5.12. There is a turn-on of the ERT trigger representing the efficiency of the trigger for identifying π^0 at a given p_T due to the energy threshold of the trigger. This ratio saturates above 5 GeV/c to about 80. Because of this turn-on π^0 triggers above 5 GeV/c have been chosen.

The two-particle correlations are broken up so that the associated- and trigger-p_T depen-
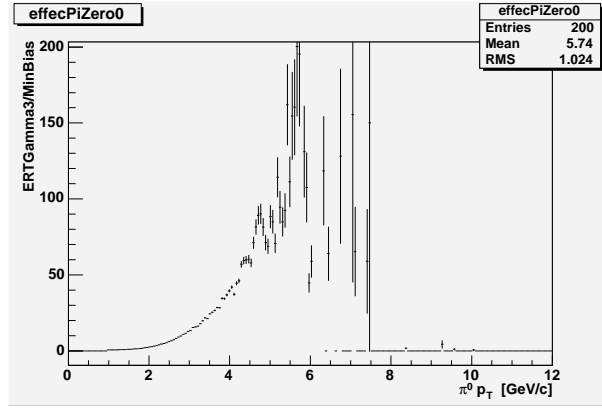
Figure 5.12   Ratio of raw π^0 p_T distributions for ERT events to minimum
bias events normalized by the number of events.

dence of the jet properties can be studied. This is done by measuring two sets of correlations. First, the trigger π^0 is kept at a constant range of 5-10 GeV/c while the associated hadron p_T range varies from 1 to 5 GeV/c. These correlations in p+p, centrality integrated (minimum bias) d+Au, and three different d+Au centrality ranges are compiled in Appendix C. An representative sample of these correlations are shown in Fig. 5.13. The correlations are also studied by fixing the associated hadron range from 2.5-5.0 GeV/c and varying the π^0 trigger range from 5-10 GeV/c and are compiled in Appendix C. The correlations have a qualitatively similar structure to those of the unidentified charged hadron correlations, *i.e.* a near- and far-angle Gaussian peak. These correlations are normalized and fit in the same manner as outlined for the unidentified hadron correlations. The resulting fits are tabulated in Appendix C.

type	$\delta\sigma_N$	$\delta\sigma_F$	δS_N	δS_F
Cut variation	4%	3%	3%	3%
S/B correction	1%	1%	1%	1-5%
normalization	N/A	N/A	10%	10%
total	4%	3%	10%	10-12%
type			$\delta\sqrt{\langle j_{Ty}^2 \rangle}$	$\delta\langle \sin^2\phi_{jj} \rangle$
Approximation to Eqns			6-0.7%	2%
total			7-4%	6-12%

Table 5.2   Breakdown of systematic Errors for π^0-h correlation fit results
for all d+Au centralities and p+p.
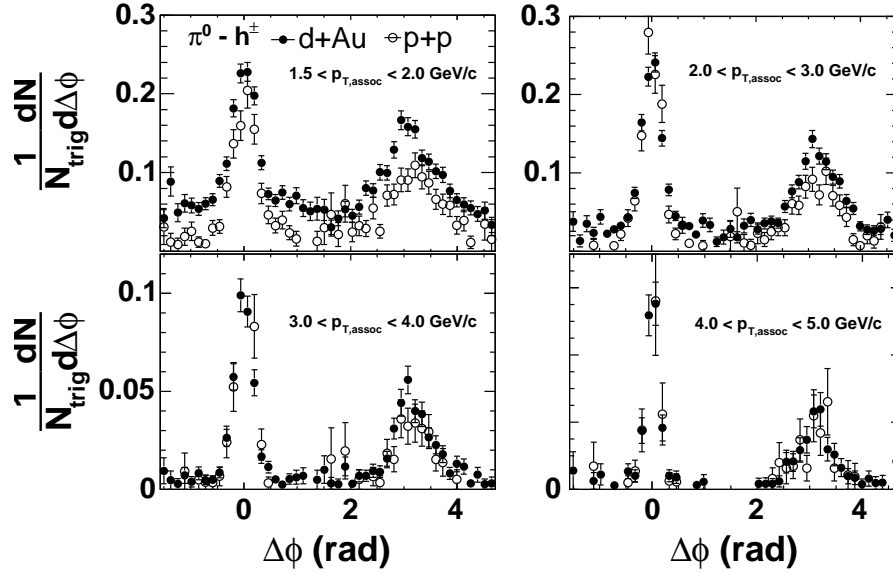
Figure 5.13 $\pi^0 - h$ correlations in p+p (open) and minimum bias d+Au (closed) for π^0 triggers from 5-10 GeV/c and several different hadron p_T ranges.

Systematic errors on the correlations are the result of several contributing factors. The detailed accounting of the systematic errors associated with the measurement is given in Table 5.2. As with the fixed-p_T h-h correlations some single particle cuts were reasonably varied to obtain an estimate of the error associated with the chosen cuts. The chosen cuts were varied independently and the largest deviation for any cut was taken as an estimate for the systematic error. The cuts were varied by 1) no ghost track removal in the unidentified charged hadrons, 2) no fiducial cut within the drift chamber acceptance however a fiducial edge cut was still applied, and 3) the photon pair asymmetry, Eqn. 5.2, was increased to 0.8. These cuts resulted in a 4% error on the near angle width, a 3% error on the far-angle widths, the near-angle yields, and far-angle yields independent of the trigger and associated p_T.

A further source of systematic error results from the signal-to-background. Within the π^0 mass window, not all photon pairs are real. It is necessary to remove the correlations due to the fake, combinatoric π^0 triggers. To determine the background contribution to the extracted jet properties, photon pairs outside of the π^0 mass region are selected as triggers and correlated with the hadrons. The mass ranges for the out-of-mass region were 0.05-0.10 GeV/c², 0.220-

0.300 GeV/c^2, and 0.300-0.400 GeV/c^2. These correlations were normalized and fitted in the same manner as the correlations triggered with photon pairs within the π^0 mass window.

To determine how the measured widths and yields with triggers outside the π^0 mass window are related to the width and yields of the background triggers in the π^0 mass range, a toy Monte Carlo simulation was written. In this Monte Carlo, several π^0's and hadrons were generated in each event with a two-Gaussian jet correlation. The π^0's were decayed and then reconstructed. With the Monte Carlo it was possible to tag which photon pairs reconstructed the generated π^0 and which reconstructed combinatoric pairs. From the Monte Carlo simple relationships were found between the signal and background widths and yields within the π^0 mass range.

$$\frac{S\sigma_{sig} + B\sigma_{bkg}}{S + B} = \sigma_{meas} \tag{5.7}$$

$$Y_{sig} + Y_{bkg} = Y_{meas} \tag{5.8}$$

To estimate the background widths and yields, the widths and yields as a function of photon pair mass in data revealed a linear relationship. An example of these data are shown in Fig. 5.14. Rather than performing the required subtraction to obtain the corrected widths and yields, Eqns. 5.7 was used to estimate the systematic error background widths and yields. This error is 1% for both near and far widths and the near angle yield and for the far angle yield it varies from 1-5%. This error is small because of the large signal-to-background of the π^0 peak.

The yields have a further source of systematic error due to the efficiency of the associated hadron. This efficiency and the associated systematic error was evaluated for the single particle d+Au spectrum [Adler et al., 2003c]. The efficiency has two sources of systematic error, the absolute normalization of the spectrum and the scale and the resolution of the particle momentum. The total normalization error is 10%.

The final source of systematic error is due to the formula assumptions. For the derivation of $\sqrt{\left\langle j_{Ty}^2 \right\rangle}$ the systematic errors are tabulated in Table A.1. The systematic error due to the derivation of $\left\langle \sin^2 \phi_{jj} \right\rangle$ is estimated by the assumption that ϕ_{jj} is Gaussian distributed. This introduces a 2% error for far angle widths less that 0.5 radians. A detailed study of these
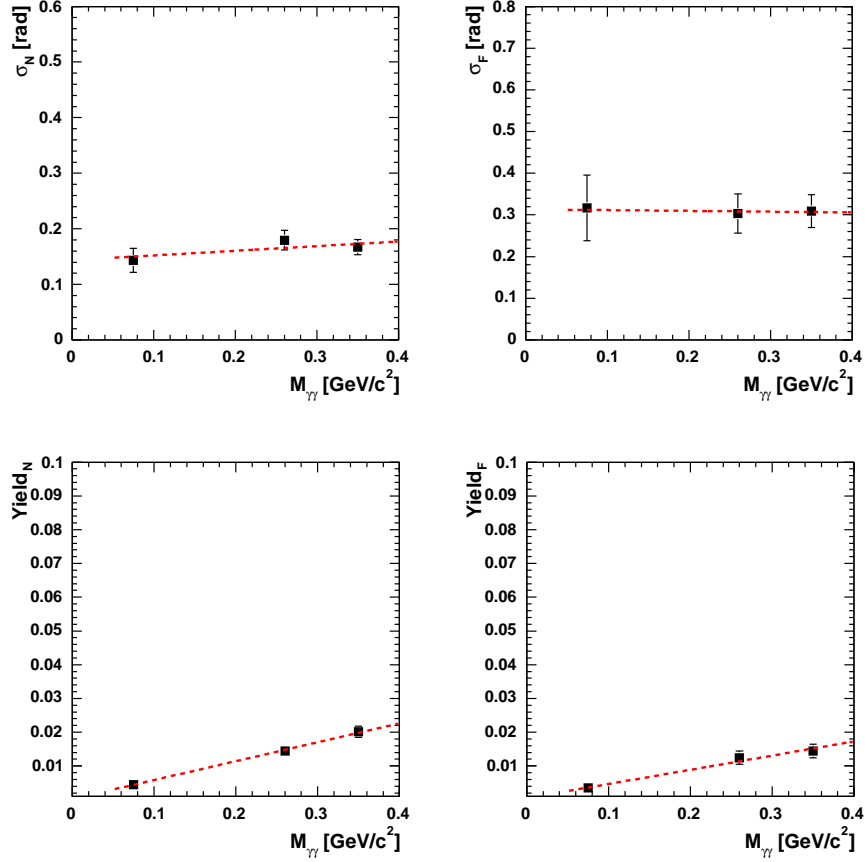
Figure 5.14   Example of the extraction of the background widths(top) and yields(bottom) using correlations with trigger photon pairs outside the π^0 mass bin. A linear fit was made to the data and the background values are evaluated at the π^0 mass of 0.130 GeV/c^2.

errors are given in Appendix A.

5.4 $\pi^\pm$-h Correlations

Another PHENIX analysis has performed correlations using charged pions as triggers. The technique is very similar between the two analyses and so here the focus is on the results. All of the details can be found in the relevant PHENIX internal analysis notes [Jia and Cole, 2004a,b,c]. Fig. 5.15 shows several different $\pi^\pm$-h correlations in p+p and d+Au collisions. They are constructed in the same way as the π^0-h Correlations.
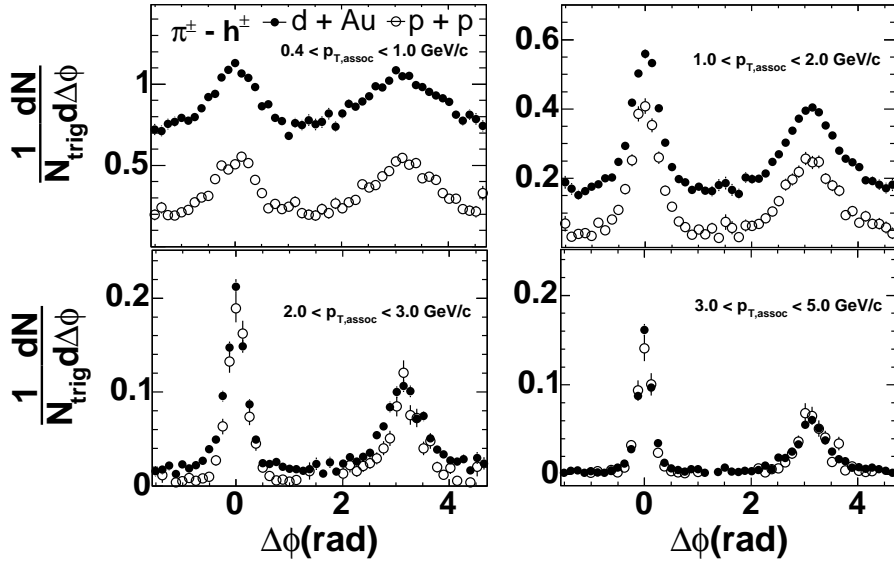
Figure 5.15   Example correlations between $\pi^{\pm}$ triggers from 5-10 GeV/c
with several different associated hadron p_T.

5.5   Jet Properties from p+p and d+Au Correlations

First, the π^0-h correlations are studied by fixing the trigger π^0 p_T and varying the associated hadron p_T. The resulting widths from the fit to the p+p and centrality integrated d+Au data are shown in Fig 5.16. In both the near- and far-angle there is the expected decrease with increasing p_T for both the p+p and the d+Au data. Both data sets also show that the far-angle width is larger than the near-angle widths for each p_T region. This is kinematically necessary since the far angle is a convolution of j_T and k_T whereas the near angle is j_T only. Little to no difference in the far-angle widths between p+p and d+Au collisions is observed. This is contrary to the expectation that multiple scattering prior to the hard parton-parton collisions will increase the acoplanarity of the outgoing jets.

To extract the jet properties from these widths Eqn. 4.19 is used to extract $\sqrt{\left\langle j_{Ty}^2 \right\rangle}$ and Eqn. 4.33 is used to extract $\langle \sin^2 \phi_{jj} \rangle$. These values are plotted in Fig. 5.16. The $\sqrt{\left\langle j_{Ty}^2 \right\rangle}$ is consistent between p+p and d+Au collisions and it shows a similar trend to the measured $\sqrt{\left\langle j_{Ty}^2 \right\rangle}$ from fixed-p_T h-h correlations. The $\langle \sin^2 \phi_{jj} \rangle$ is also consistent between p+p and d+Au. In fact, the d+Au is systematically lower than the p+p. This is the opposite trend

expected from multiple scattering which would tend to broaden the di-jet distribution.

To study these correlations further, the d+Au correlations have been divided into three centrality classes to determine the impact parameter dependence of the jet properties. Fig. 5.17 shows the near- and far-angle widths and the extracted $\sqrt{\left\langle j_{Ty}^2 \right\rangle}$ and $\langle \sin^2 \phi_{jj} \rangle$ for the different d+Au centrality. There is no statistical difference between the data nor is there any systematic trend as a function of centrality.

The conditional yields of associated hadrons per trigger π^0 in the near- and far-angle are studied as a function of $p_{T,assoc}$ and x_E. These distributions are shown in Fig. 5.18 and Fig. 5.19, respectively. The p_T distribution shows a drop of only a factor of 10-30 for $p_{T,assoc}$ between 1 and 5 GeV/c. This is a harder spectrum than the single particle spectrum which drops by a factor of 10000 [Adler et al., 2003c] over the same momentum range.

The far-angle p_T and x_E distributions can be roughly related to the product of two fragmentation functions (see Eqn. 4.41). It is instructive to compare the distributions from p+p and d+Au collisions to quantify the difference between the two distributions. This is done by taking the ratio of each of the d+Au centrality binned distributions to the p+p distribution as a function of p_T and x_E. These ratios are plotted in the lower panels of Fig. 5.18 and Fig. 5.19, respectively. The only systematic trends are that the near side is lower than unity while the ratio is higher than unity for the far side. These systematics are small and therefore, the fragmentation function in d+Au collisions do not change by more than 20% from p+p collisions.

The results from the two different triggers (π^0 and $\pi^{\pm}$) compare very well. Fig. 5.20 shows a comparison of the extracted widths. Because the widths are comparable the extracted $\sqrt{\left\langle j_{Ty}^2 \right\rangle}$ and $\langle sin^2 \phi_{jj} \rangle$ are comparable as well. As a further comparison the conditional yield distributions are compared. There is very good agreement between the two different trigger set both as a function of $p_{T,assoc}$ and x_E.

The π^0-h correlations have also been studied using a constant associated hadron momentum range of 2.5-5.0 GeV/c and binning the trigger π^0 in 5-6 GeV/c, 6-7 GeV/c, and 7-10 GeV/c bins. The resulting jet shapes and extracted properties are shown in Fig. 5.21 and Fig. 5.22.

The higher p_T triggers show a similar p_T dependence to the hadron associated p_T dependence. That is, the $\sqrt{\left\langle j_{Ty}^2 \right\rangle}$ is independent of p_T and shows no systematic centrality dependence. Also, the $\left\langle \sin^2 \phi_{jj} \right\rangle$ shows no difference between p+p and d+Au collisions nor a systematic dependence on d+Au centrality.

Other comparisons between jets in p+p collisions compared to jets in d+Au collisions come from the analysis using the $\pi^{\pm}$ triggers. The conditional yield x_E distributions have been constructed from correlations in p+p collisions and the comparison to d+Au is shown in upper panel of Fig. 5.23. No difference between the distributions is observed. The distributions of p_{out}, the component of the associated particle p_T perpendicular to the trigger p_T, is compared in the middle panel. The far side p_{out} is related to k_T (see Eqn. 4.24). Any difference seen would indicate a change in k_T. Multiple scattering models would predict a broadening in the the d+Au distribution compared to p+p. Qualitatively no broadening is seen between the p+p and d+Au distributions. The lowest panel shows the ratio of $p_{T,assoc}$ distributions for three different centrality selections of d+Au compared to p+p. The $p_{T,assoc}$ distributions are consistent with no difference within about 10%. This is also consistent with the π^0 triggered data. All results taken together show little to no modification of jets in d+Au collisions. This will be be discussed more quantitatively in Section 7.2.
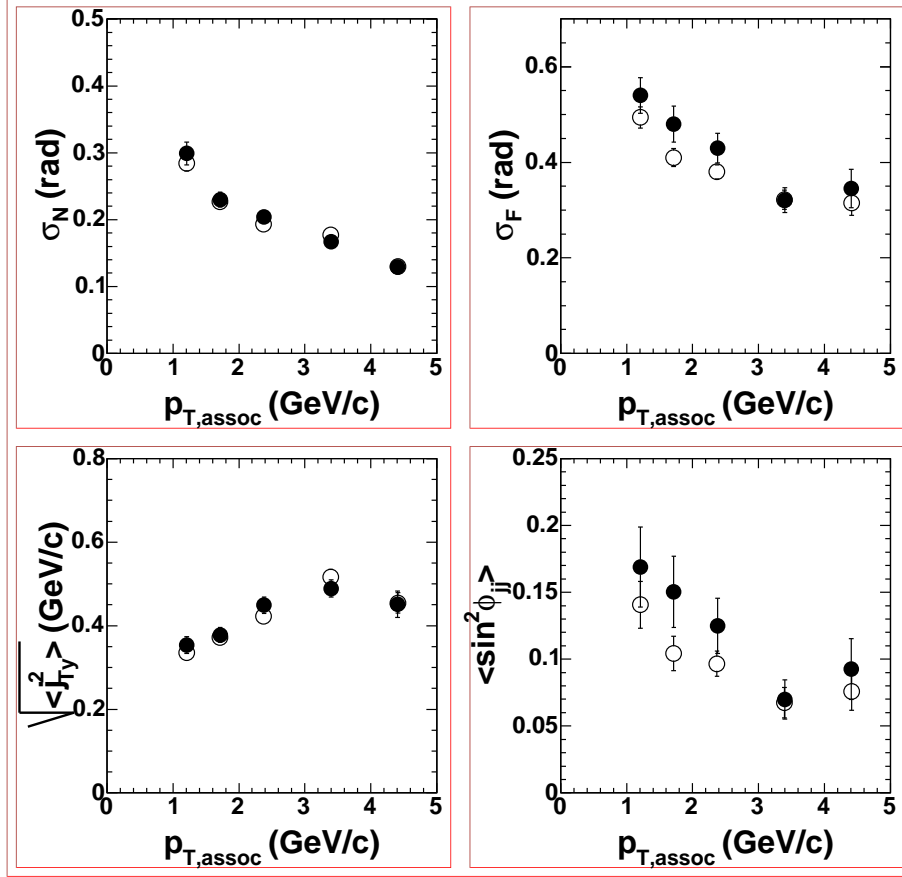
Figure 5.16   Near-(upper left) and far-(upper right) angle widths as a function of the associated hadron p_T from π^0-h correlations in p+p (closed) and centrality integrated, 0-88% d+Au collisions (open). The trigger π^0 is at 5-10 GeV/c for all correlations. The statistical error bars are smaller than some of the data points. The extracted $\sqrt{\langle j_{Ty}^2 \rangle}$ (lower left) and $\langle \sin^2 \phi_{jj} \rangle$ (upper right) are also shown.
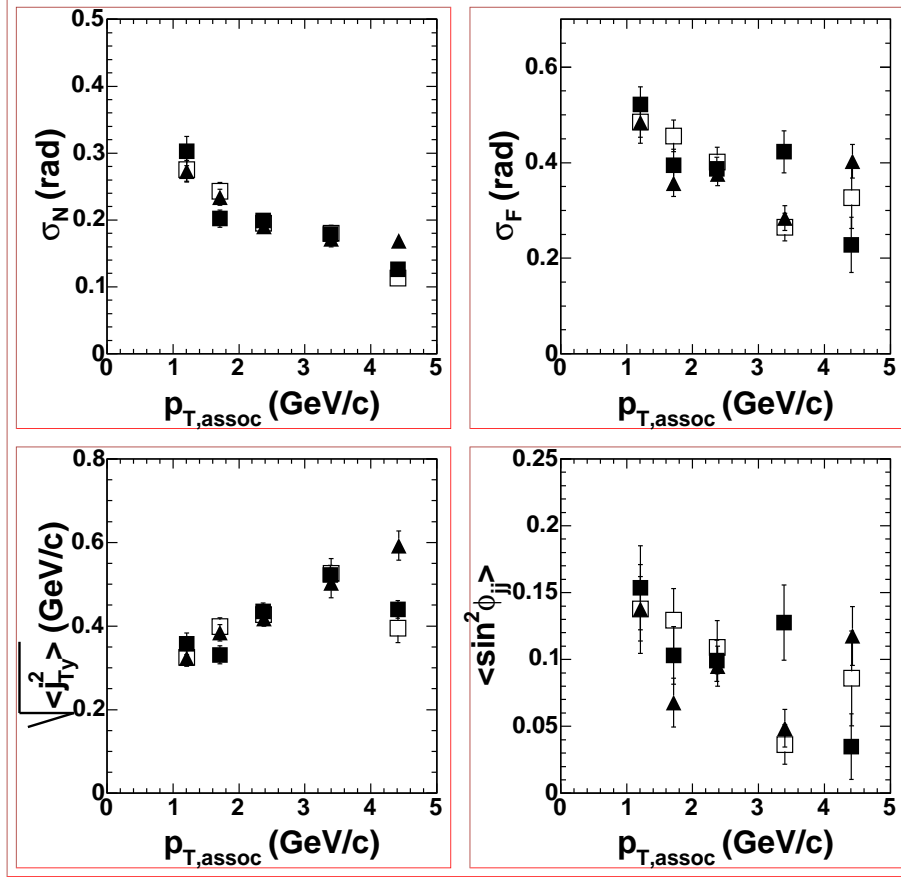
Figure 5.17   Near-(left) and far-(right) angle widths as a function of the associated hadron p_T from π^0-h correlations in centrality-binned d+Au collisions.   Filled squares are 0-20% central, open squares are 20-40% central, and triangles are 40-88% central. The trigger π^0 is at 5-10 GeV/c for all correlations. The statistical error bars are smaller than some of the data points. The extracted $\sqrt{\left\langle j_{Ty}^2 \right\rangle}$ (lower left) and $\langle \sin^2 \phi_{jj} \rangle$ (lower right) are also shown.
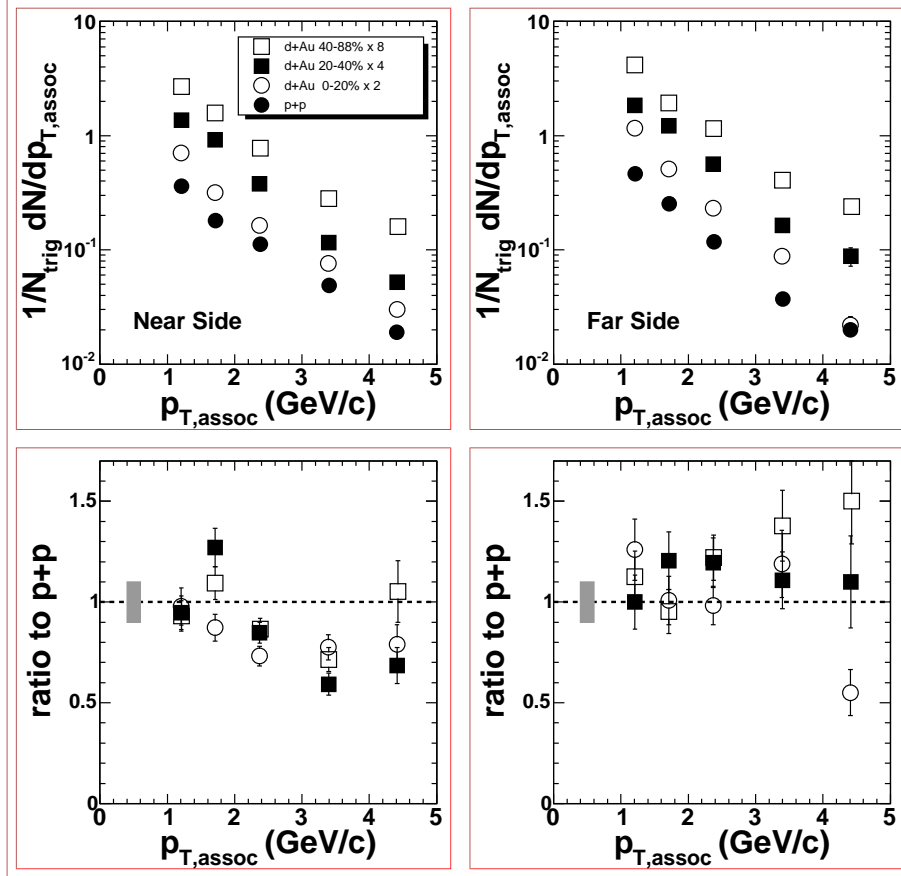
Figure 5.18 The jet conditional yield distribution as a function of associate particle p_T for the near-side (upper left) and the far-side (upper right) in p+p and three centralities in d+Au. The lower panels are the ratio of different d+Au centrality distributions to the p+p distribution. The error bars are statistical. The band at 1 on the lower panel is the 10% normalization error from the associated particle efficiency.
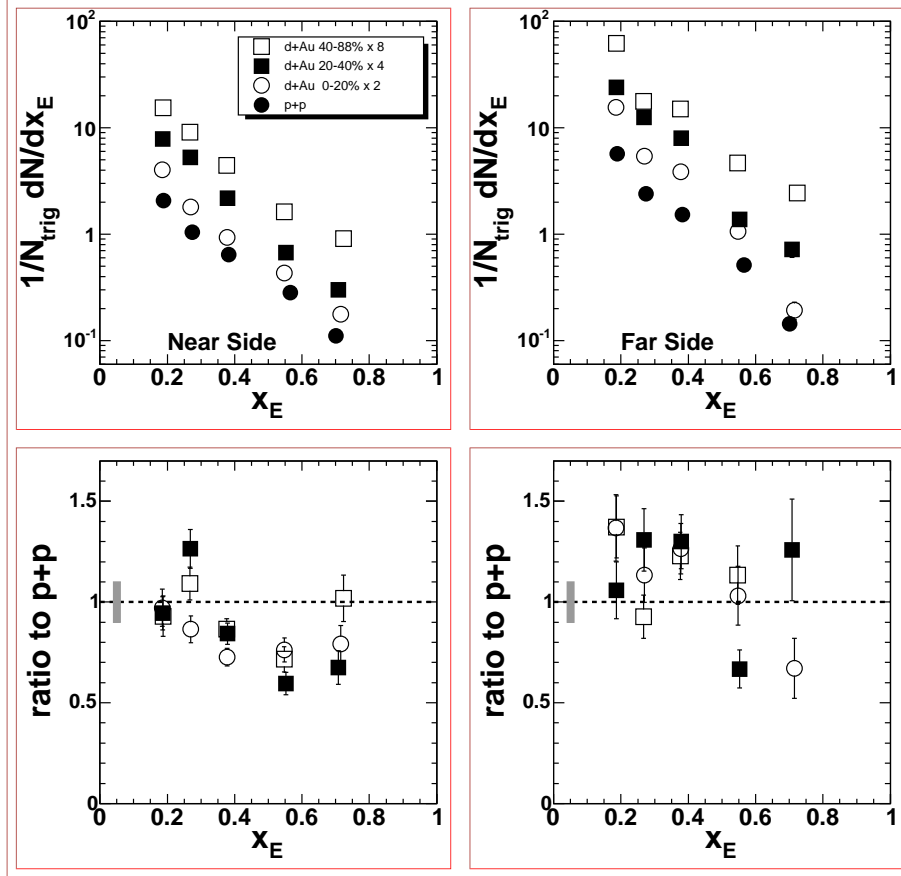
Figure 5.19   The jet conditional yield distribution as a function of x_E for the near-side (upper left) and the far-side (upper right) for p+p and three centralities in d+Au. The lower panels are the ratio of different d+Au centrality distributions to the p+p distribution. The error bars are statistical. The band at 1 on the lower panel is the 10% normalization error from the associated particle efficiency.
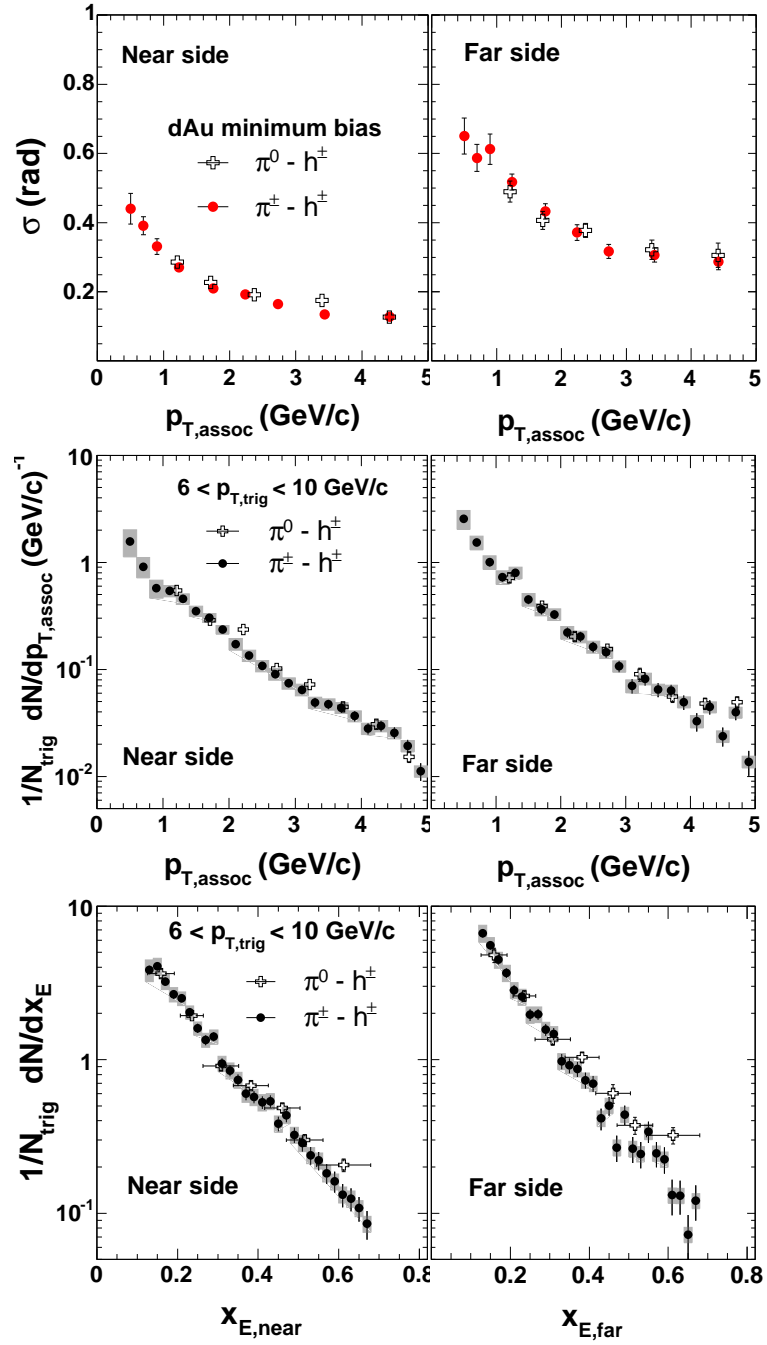
Figure 5.20 *Upper:* Comparison of extracted widths from correlations using 5-10 GeV/c π^0 triggers (crosses) and $\pi^{\pm}$ triggers (circles). *Middle:* Comparison of the conditional yield distribution as a function of $p_{T,assoc}$. *Lower:* Comparison of the conditional yield distribution as a function of x_E.
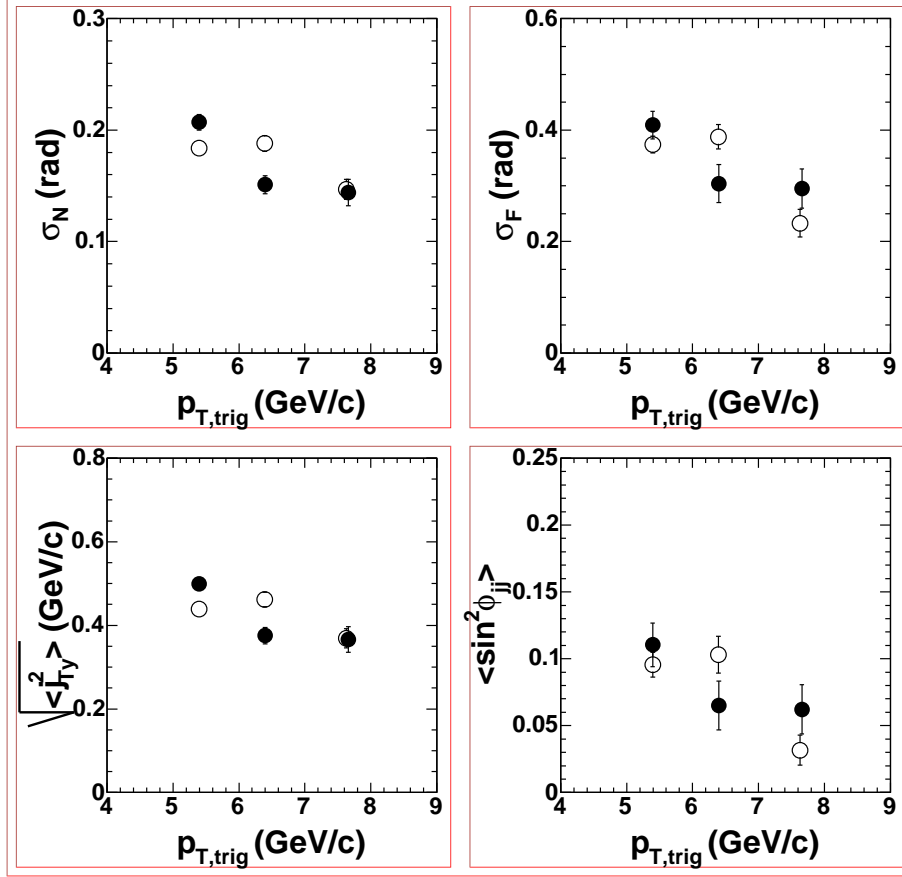
Figure 5.21 Near-(upper left) and far-(upper right) angle widths as a function of the trigger π^0 p_T from π^0-h correlations in p+p (closed) and centrality integrated, 0-88%, d+Au collisions (open). The associated hadron is at 2.5-5 GeV/c for all correlations. The statistical error bars are smaller than some of the data points. The extracted $\sqrt{\left\langle j_{Ty}^2 \right\rangle}$ (lower left) and $\langle \sin^2 \phi_{jj} \rangle$ (upper right) are also shown.
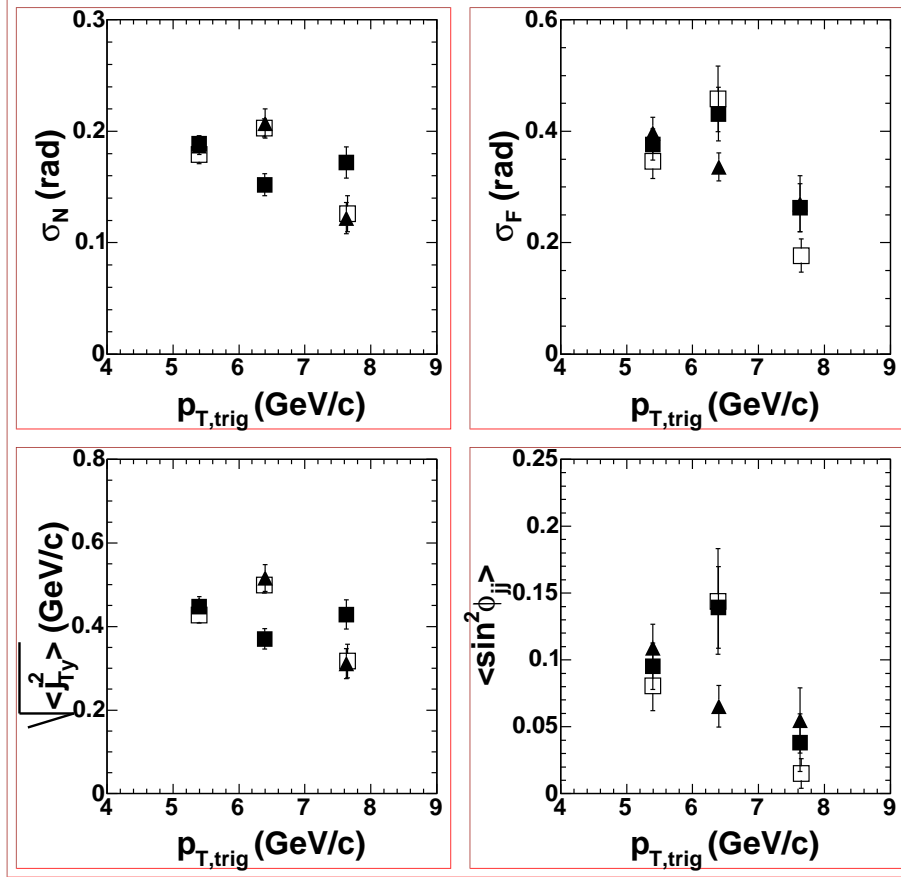
Figure 5.22 Near-(left) and far-(right) angle widths as a function of the trigger π^0 p_T from π^0-h correlations in centrality-binned d+Au collisions. Filled squares are 0-20% central, open squares are 20-40% central, and triangles are 40-88% central. The associated hadron is at 2.5-5 GeV/c for all correlations. The statistical error bars are smaller than some of the data points. The extracted $\sqrt{\langle j_{Ty}^2 \rangle}$ (left) and $\langle \sin^2 \phi_{jj} \rangle$ are also shown.
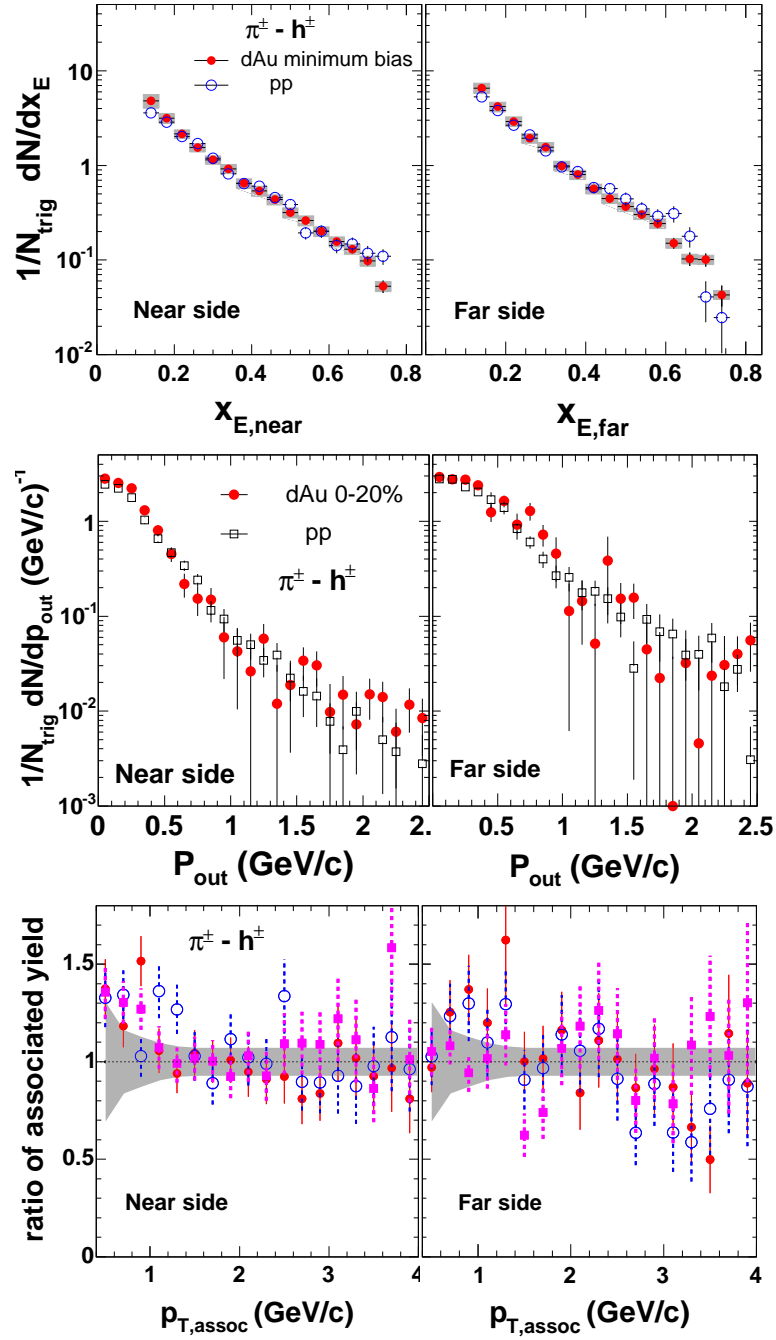
Figure 5.23 Comparison of several distributions in p+p and d+Au using $\pi^{\pm}$ triggered correlations. The upper are x_E distributions, the middle are p_{out} distributions, and the lower are ratios of $p_{T,assoc}$ distributions in several d+Au centrality bins compared to p+p. In the bottom figure the closed circles are 0-20% central, the open circles are 20-40% central, and the squares are 40-88% central.

CHAPTER 6.   Di-jets in Au+Au Collisions

This chapter outlines the analysis of data from the Au+Au run at RHIC from January-May 2004. The correlations between π^0 triggers and unidentified charged hadrons are discussed. The removal of the elliptic flow from correlations is presented. Finally, the jet properties from the correlations are presented including a discussion of the statistical subtraction method to measure the x_E and p_{out} distributions due to jet correlations.

There was significant coordination between the correlation analyses from this Au+Au run. Some systematic checks were done and used throughout all analyses. As a result these checks and cuts are fully documented elsewhere [Jia et al., 2005] and are presented here for completeness.

6.1   Run Selection

As in the case for the p+p and d+Au analysis, a stable set of runs that are representative of the PHENIX acceptance and pair efficiency is crucial for correlations analyses since fluctuations of these can result in unphysical correlations. Therefore, a thorough investigation of run-by-run dependent quantities sensitive to both the acceptance and pair efficiency of the whole detector has been done. Runs used in the analysis were obtained after rejection of bad runs based on several different quality assurance (QA) checks. They can be divided into three categories: broad run QA, single-particle QA, and pair QA.

In the first category, runs were removed for several general reasons. First, runs with fewer than 0.5 million events are removed. These runs resulted from a few tens of minutes as opposed to the more typical 1-2 hour running. Such runs were often stopped short for high voltage trips in some section of the detector or unexpected beam dumps. This would result in potentially

large acceptance and multiplicity fluctuations at the end of the run. Runs that did not have a reasonable reaction plane defined for the events were discarded since some analyses binned in reaction plane. Finally, any converter runs where additional thin material was added in the fiducial region of the central arms was excluded. After removal of these runs a total of 940 million minimum bias events corresponding to roughly 90% of the total number of minimum bias triggered events recorded by PHENIX are analyzed.

The single particle QA was used PHENIX wide. The single particle QA focused on three variables. The first is the $\langle p_T \rangle$ of tracks in the Drift Chamber (DCH). This is sensitive to variations in the magnetic field. The second is the fraction of tracks that are matched to a Pad Chamber 3 (PC3) hit within a 3σ window in z and ϕ (see Eqn. 5.1). This is sensitive to a change in the PC3 acceptance. Finally the average number of tracks per event in the DCH is checked which is sensitive to fluctuations in the DCH acceptance. Runs that show a significant deviation from the average were excluded from the analysis.

An extensive pair QA is necessary in order to obtain a stable set of runs for mixed distributions. These mixed distributions ideally should have little to no relative fluctuation. However, small fluctuations are possible and it is important to check that these fluctuations are smaller than the signal being measured. It is known from the 2002 Au+Au jet analyses that the signal-to-background of jets in correlations is on the order of a few percent when the trigger and associated particle are below ~ 4 GeV/c [Adler et al., 2005d,a]. The pair QA has focused on building very high-quality mixed event samples from low-p_T, i.e. around 1 GeV/c, hadron pairs and studying the run-by-run shape variation.

One method of quantifying this run-by-run dependence is the ratio of the mixed distribution in two different $\Delta\phi$ regions. If this ratio for a particular run varies considerably, that is many σ from the mean, compared to the majority of the runs, it is removed. The ratio between the mixed distribution in $\pi/2 < \Delta\phi < \pi$ to $0 < \Delta\phi < \pi/2$ reveals the relative pair acceptance between the two arms. Only 0.5% of the runs were removed with this cut.

Another quantity that has been studied is the χ^2/NDF comparison of the mixed events

for every pair of runs. The χ^2/NDF is defined as

$$\chi^2/NDF = \frac{1}{N_{bins}} \sum_i \frac{\left(dN_{mix}^j/d\Delta\phi_i - dN_{mix}^k/d\Delta\phi_i\right)^2}{dN_{mix}^j/d\Delta\phi_i + dN_{mix}^k/d\Delta\phi_i} \tag{6.1}$$

The sum is over the bins of the two different mixed distributions j and k each representing a run. The mixed distributions were normalized relative to one another such that the integrals of the distributions were equal. Given a particular χ^2/NDF maximum value, a distribution of the number of times a run resulted in a χ^2/NDF above the maximum. A cut on this distribution is made. This cut was sensitive to broad, general shape changes of the mixed event distribution. Only 1% of the runs were removed by this cut.

Finally, the centrality dependence of the mixed event background was studied. In principle the acceptance should not change with centrality. However, the occupancy correction due to track multiplicity is centrality dependent. By dividing the measured mixed distributions into centrality classes and comparing the most peripheral bin (60-92%) with the most central bin (0-5%) a 5% maximal variation was found in the regions around $\pi/2$ radians while $< 1\%$ variation was found near 0 and π radians. The pairs in the region at $\pi/2$ rad result from a pair of tracks each at the top edge of the DCH in each arm. Therefore, it is reasonable to use the most central mixed distribution for the mixed distribution for all centralities so long as the jet signal to be measured is above a few percent of the background.

6.2 Single Particle Selection

In Au+Au only π^0-h correlations are measured. Many of the cuts from the previous chapter are repeated here. For completeness the cuts are briefly listed. Any modification to what has been done in the p+p and d+Au analysis is detailed.

To increase the speed of the analysis a special set of data files were produced during the production of the whole data set. A software trigger was applied which kept hadrons with $p_T > 1$ GeV/c and Electromagnetic Calorimeter (EMC) clusters with energy > 1.5 GeV/c for a given event. From this sub-sample of data further cuts were applied.

6.2.1 Single Hadron Cuts

The single hadron cuts for the correlations are similar to those used in the p+p and d+Au analysis.

1. DCH quality of 63 or 31

2. PC3 radial matching, $\sigma < 2$ (see Eqn. 5.1)

3. For hadron $p_T > 5$ GeV/c, EMC radial matching, $\sigma < 3$

4. For hadron $p_T > 5$ GeV/c, EMC cluster energy (GeV) > 0.3 GeV $+ 0.2 \times p_T$(GeV)

A tighter PC3 matching cut is applied in Au+Au because of the higher multiplicity in Au+Au events. A wider matching cut produces a smaller signal-to-background for real high-p_T hadrons. In these correlations hadrons above 5 GeV/c were used as associated particles. These required additional cuts not necessary in the p+p and d+Au analysis. The single particle analyses decided on the above cuts to select clean hadrons using the EMC [Messer and Jia, 2002].

6.2.2 Photon and π^0 Single Particle Cuts

The photon cuts are also similar to those from the previous chapter. The cuts made were

1. PbSc $\chi^2 < 3$ or PbGl dispersion cut which is similar to the χ^2 cut for the PbSc.

2. Dead/Warm map cut based on the tower-by-tower information.

There was no time-of-flight cut or rejection of a cluster to which a track points.

The photons which passed the cuts were paired to reconstruct π^0 candidates. Those pairs with an invariant mass of 0.120-0.150 GeV/c^2 and an energy asymmetry (see Eqn. 5.2) of $\alpha < 0.7$ were taken as π^0 triggers. The resulting π^0 invariant mass distributions are given in Appendix B. A clear π^0 peak is seen in the data even at the most central collisions. The peak is fitted with a Gaussian and a second order polynomial to determine the mass, width, and signal-to-background of the peak.
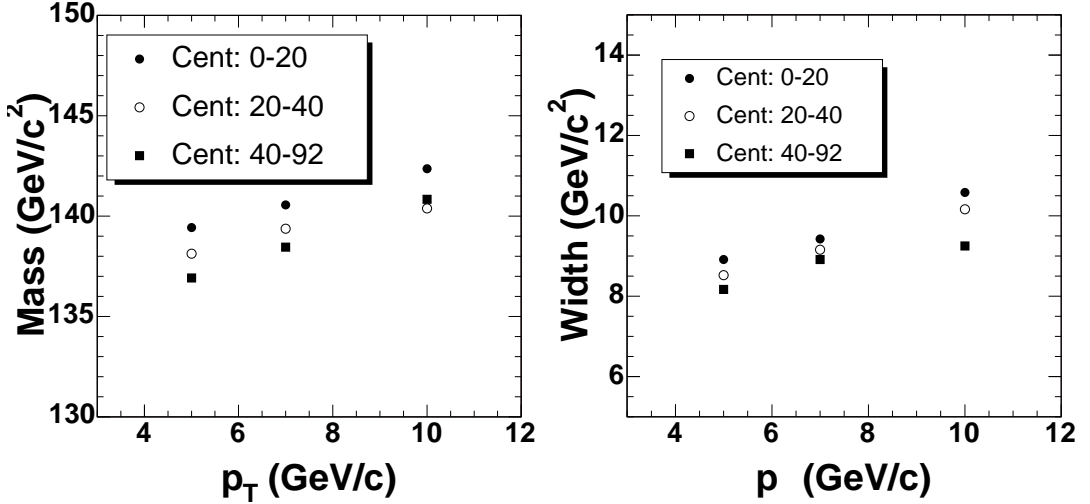
Figure 6.1 *Left:* The fitted π^0 mass as a function of pair p_T and central-
ity. *Right:* The fitted π^0 peak width as a function of p_T and
centrality.

The results for the mass and width are plotted in Fig. 6.1. The fixed mass window is wide
enough to cover just more than 1σ of π^0 width. Fig. 6.2 shows the signal-to-background in
the π^0 peak. The signal-to-background is quite large despite the larger combinatoric back-
ground from Au+Au events compared to p+p and d+Au. There is a decrease in the signal-to-
background as a function of centrality due to the increase in combinatoric background level in
the more central collisions. These signal-to-background ratios are used to estimate a systematic
error due to combinatoric photon pairs in the π^0 trigger range.

6.3 π^0-h$^\pm$ Correlations

All correlations are given in Appendix D but a representative sample is shown in Fig. 6.3.
The trigger π^0 correlations were measured by varying both the trigger and associated p_T ranges.
The trigger bins are 5-7, 7-10, and 10-20 GeV/c while the associated hadrons are binned from
1-2, 2-3, 3-5, and 5-10 GeV/c. Every trigger bin is correlated with every associated bin. The
data is also binned in three different centrality classes, 0-20%, 20-40%, and 40-92%.
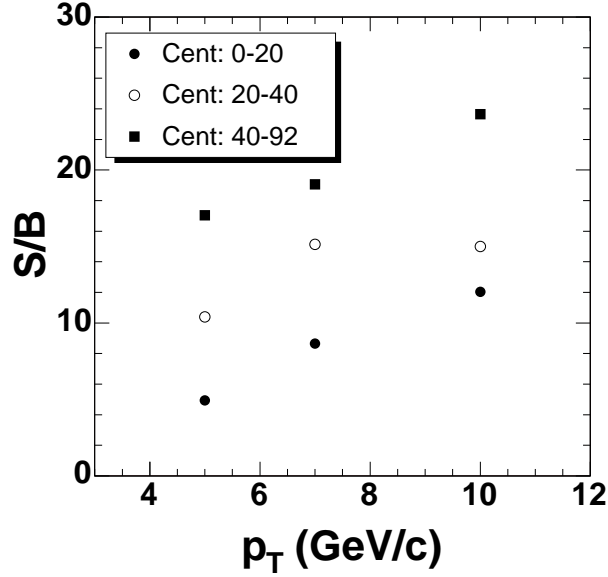
Figure 6.2 Centrality and p_T dependence of the fitted π^0 peak signal-to-background.

6.3.1 Mixed Events

The mixing technique employed for the Au+Au collisions is slightly different than that for p+p and d+Au. The buffers are binned in both z-vertex and centrality. The z-vertex bins are 3 cm wide from -30 to +30 cm. The centrality is binned in 10% bins from 0-100%. Events within a given z-vertex and centrality bin are mixed. Rather than choosing a single trigger and single associated particle from each of the two different trigger and associated events, all pairs between the events are made. This introduces auto-correlations as argued in the previous chapter, however, these correlations decrease as $1/N_{trig}$ where N_{trig} is the number of triggers used to mix. There were approximately 100 times the number of pairs in the mixed as in the real events for these correlations. This reduced the error due to auto-correlations to the percent level which is less that the signal that is measured. All pairs were chosen to maximize the statistics in the mixed events which is essential for rare triggers.

When producing the correlation functions (see Eqn. 4.2) the normalization was made on the mixed event background by weighting each entry by the number of pairs that were mixed for that event. This resulted in the background level of the correlations to be approximately
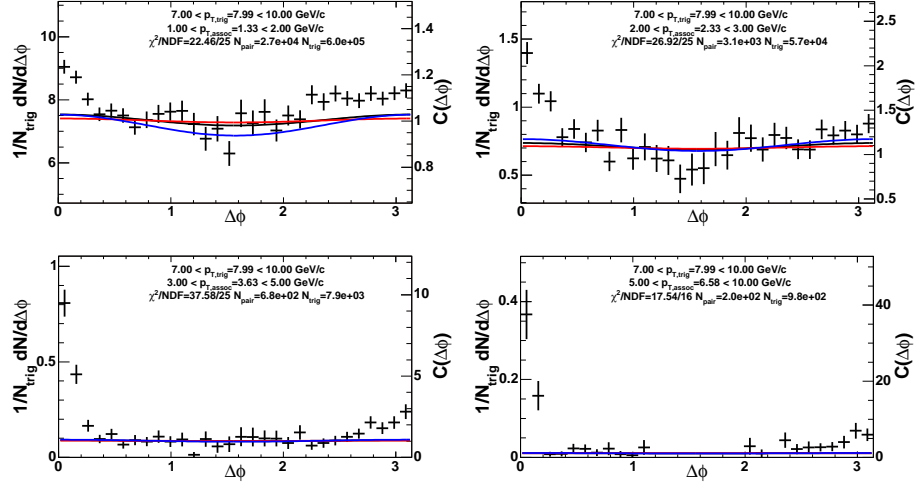
Figure 6.3   Shown are correlations in 20-40% Au+Au collisions using π^0 triggers from 7-10 GeV/c and several different associated hadron p_T bins. The lines indicate the systematic error due to the elliptic flow contribution to these correlations.

1. As such, the correlation strength is roughly equivalent to the signal-to-background of the jet pairs compared to other pairs. As seen from the correlation functions in Appendix D, the away-side correlations strength is less than 2 for many of the correlations, i.e. S/B < 1.

6.3.2   Normalization

It is important to note that the above normalization for the correlation function does not exactly produce a combinatoric background at 1 because of finite binning in centrality. The correlation function will be at a level of $1+\xi$, where ξ is defined as the strength of the residual correlation due to the finite binning of centrality and is proportional to the square of the ratio of the bin width to the mean of the bin [Stankus, 2005]. Determining the exact value of ξ is not necessary in this analysis because the physical correlations are above this background level.

The normalization to convert these correlations into pair-per-trigger azimuthal distributions

is slightly different from p+p and d+Au (Eqn. 4.5).

$$\frac{1}{N_{trig}}\frac{dN}{d\Delta\phi} = \frac{Occ\,(cent)}{N'_{trig}}\frac{\int d\Delta\phi \,\frac{dN^{mix}}{d\Delta\phi}\frac{dN^{real}}{d\Delta\phi}}{\epsilon_{assoc}\Omega_{\Delta\phi}\frac{dN^{mix}}{d\Delta\phi}} \tag{6.2}$$

In this normalization the extrapolation to a larger $\Delta\eta$ range than the PHENIX acceptance is not applied, i.e. the term $R_{\Delta\eta}$ is dropped. The single particle efficiency is modified by including an occupancy correction. In high multiplicity events, merging of tracks results in an efficiency loss. This occupancy correction is dependent on the multiplicity of the tracks in the events. It is found by embedding simulated tracks into real events and determining the probability for reconstructing the embedded track [Reuter et al., 2004]. The occupancy correction is given in Table 6.1.

The single particle efficiency is also slightly different in Au+Au compared to d+Au. The correction function was determined the same way for the Au+Au as d+Au for the single particle analysis [Reuter et al., 2004]

$$\text{Correction}\,(p_T) = \frac{1}{\epsilon_{\text{assoc}}} = \frac{4.017}{p_T} + 23.52 - 0.3135 p_T - 0.0108 p_T^2 \tag{6.3}$$

There are factors of 0.53 and 0.5 that are multiplied to the correction function. The first factor is for a smaller range in the drift chamber zed used in single particle analysis compared to this analysis. The second factor is the difference in the azimuthal range of the single particle analysis compared to this analysis. See Section 5.2 for more details.

Centrality	Occupancy Correction	Normalization Error
Min. Bias	0.950	3.5%
0-20%	0.875	5.0%
20-40%	0.950	4.0%
40-92%	0.978	3.0%

Table 6.1　Occupancy corrections and the contribution to the normalization systematic error as a function of Au+Au centrality, see [Reuter et al., 2004].
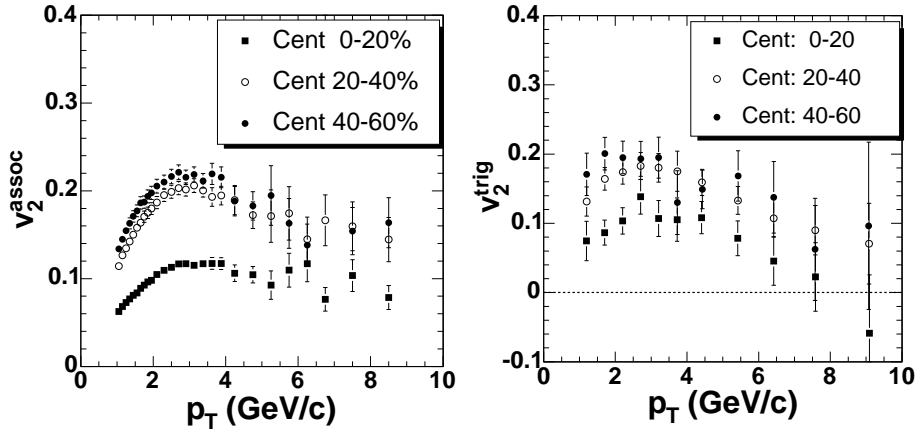
Figure 6.4   Hadron (left) and π^0 (right) v_2 values from independent reaction
plane analyses [Jia et al., 2005; Winter et al., 2005]

6.3.3   Elliptic Flow

The correlation functions are fitted with the form of the two-source model (see Eqn. 4.9 and Eqn. 4.25).

$$\frac{1}{N_{trig}}\frac{dN}{d\Delta\phi} = B(1 + 2v_2^{trig}v_2^{assoc}\cos(2\Delta\phi)) + \frac{S_N}{\sqrt{2\pi}\sigma_N}e^{-\frac{\Delta\phi^2}{2\sigma_N}} + \frac{S_F}{\sqrt{2\pi}\sigma_F}e^{-\frac{(\Delta\phi-\pi)^2}{2\sigma_F}} \qquad (6.4)$$

In this function there are 8 parameters to specify the elliptic flow and the near- and far-angle jets. The harmonic contributions from elliptic flow can be difficult to distinguish from the far-angle jet when the RMS of the distribution is relatively large [?]. Because of this the two parameters for the elliptic flow, v_2^{trig} and v_2^{assoc}, are fixed. The values are obtained independently from single particle studies as a function of reaction plane for hadrons [Jia et al., 2005] and for π^0 [Winter et al., 2005]. The values from these independent analyses are plotted in Fig. 6.4. The values of v_2 and their errors used in this analysis were interpolated at the mean trigger and associated p_T from those in Fig. 6.4. The errors used are also interpolated from the measured statistical and systematic errors. These interpolated values are tabulated in Table 6.2 and Table 6.3.

It should be pointed out that in the derivation of the elliptical flow correlation between two particles in Section 4.3 that the coefficient on $\cos(2\Delta\phi)$ (Eqn. 4.8) is $\left\langle v_2^{trig}v_2^{assoc}\right\rangle$. It has

$p_{T,trig}$	0-20%	20-40%	40-92%
5-7 GeV/c	0.070±0.028	0.126±0.022	0.136±0.054
7-10 GeV/c	0.001±0.059	0.085±0.042	0.101±0.121
10-20 GeV/c	-0.054±0.082	0.072±0.057	0.050±0.168

Table 6.2   Trigger π^0 v_2 from [Winter et al., 2005]. The values are interpolated at the $\langle p_T \rangle$ of the trigger bin.

$p_{T,assoc}$	0-20%	20-40%	40-92%
1-2 GeV/c	0.076±0.003	0.140±0.005	0.158±0.009
2-3 GeV/c	0.110±0.005	0.196±0.007	0.205±0.011
3-5 GeV/c	0.117±0.007	0.194±0.011	0.202±0.014
5-10 GeV/c	0.089±0.016	0.160±0.028	0.356±0.064

Table 6.3   Associated hadron v_2 from [Jia et al., 2005]. The values are interpolated at the $\langle p_T \rangle$ of the associated bin.

been assumed then that $\left\langle v_2^{trig} v_2^{assoc} \right\rangle = \left\langle v_2^{trig} \right\rangle \left\langle v_2^{assoc} \right\rangle$. At lower p_T this has been shown to be a reasonable assumption [Adler et al., 2005a].

The fit to the correlation function is performed three times. The first fit fixes both trigger and associated v_2 to their central values. This is the nominal fit to the data and the central value of all extracted quantities are the result of this fit. In the correlation functions this nominal fit is the black line. The second fit fixes the v_2 values at the one σ of the quadrature sum of the statistical and systematic error above the central value. This fit is shown in red on the correlation functions. The last fit fixes the v_2 values at one σ of the quadrature sum of the statistical and systematic error below the central value. This fit is shown in blue on the correlation functions. The fit results from the variation of the v_2 values from the final two fits are one component of the systematic error. This error is quite large (40-50%) at the lowest p_T where the elliptic flow is a significant fraction of the total correlation. See Section 6.3.5 for further details.

6.3.4   Robust Far-Angle Correlations

By subtracting off the contribution from the background and the elliptic flow from the correlation function, the resulting distribution is the jet function, that is, the correlation due
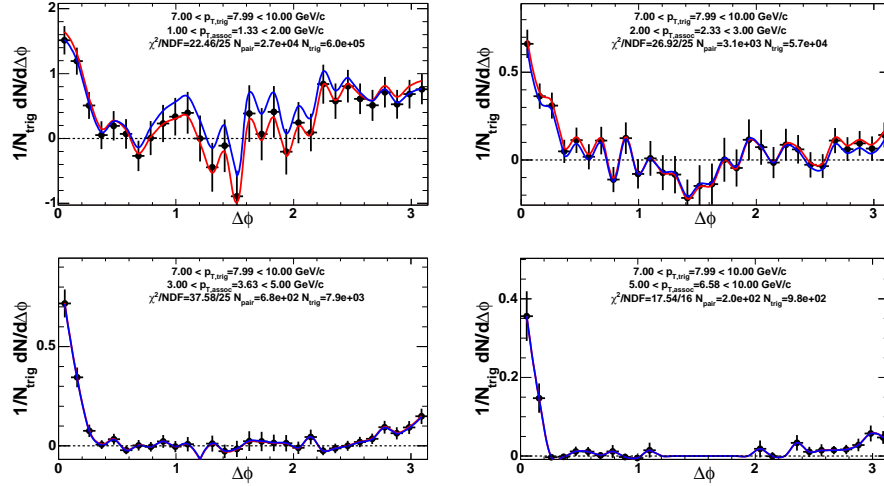
Figure 6.5   Shown are jet functions, the correlations after subtraction of the background and elliptic flow, in 20-40% Au+Au collisions using π^0 triggers from 7-10 GeV/c and several different associated hadron p_T bins. The lines indicate the systematic error due to the elliptic flow contribution to these correlations.

to jets. Fig. 6.5 shows the resulting jet functions for the corresponding correlations in Fig. 6.3. The lines indicate the systematic error due to the subtraction of the elliptic flow. It is a goal of this thesis to study the correlations to determine if the modification of the away-side shape and yields present at lower p_T persists at higher-p_T.

To maximize the physics impact and the robustness of the away-side structure, the correlations must exhibit a statistically significant structure. To test the statistical significance of the far-angle structure a likelihood ratio test was performed on all of the correlations. The procedure is to fit the same correlation function with two different fit functions, one with n parameters and the other with $n+m$ parameters. The test compares the resulting χ^2 to determine if the extra m parameters are relevant in describing the data. The difference in χ^2 from the different fits, $\Delta\chi^2 \equiv \chi_n^2 - \chi_{n+m}^2$, is itself a sample of a χ^2 distribution with m degrees of freedom. Therefore, a given $\Delta\chi^2$ corresponds to a confidence limit.

The fit function with $n+m$ parameters was the nominal fit function Eqn. 6.2. For the likelihood ratio test the same form without the far-angle Gaussian was chosen. In this way the relevance of the far-angle Gaussian is directly tested. The difference between the number of

parameters in the two fits is two, one for the far-angle yield and one for the far-angle width. If the far-angle structure is present at or above the 2σ confidence level, then $\Delta\chi^2$ should be larger than 6.2. Tables 6.4-6.6 gives the $\Delta\chi^2$ values as well as the χ^2/NDF of the nominal fit for the different trigger-associated-centrality bins chosen for this analysis.

$p_{T,assoc}$	Min. Bias	0-20%	20-40%	40-92%
1-2 GeV/c	30.3 (24.1/25)	6.2 (24.3/25)	20.4 (23.0/25)	60.9 (42.2/25)
2-3 GeV/c	20.5 (25.3/25)	8.4 (15.1/25)	3.1 (39.6/25)	52.6 (27.7/25)
3-5 GeV/c	47.2 (43.2/25)	11.5 (30.0/25)	22.5 (30.6/25)	65.0 (26.8/25)
5-10 GeV/c	51.5 (37.6/25)	9.6 (31.7/25)	32.5 (18.8/24)	27.8 (9.7/18)

Table 6.4   Table of $\Delta\chi^2$ values for correlations between a π^0 trigger from 5-7 GeV/c with several different associated charged hadron and centrality bins. The χ^2/NDF from the nominal fit is given in parentheses.

$p_{T,assoc}$	Min. Bias	0-20%	20-40%	40-92%
1-2 GeV/c	35.5 (26.8/25)	6.6 (28.6/25)	27.8 (22.5/25)	48.7 (31.7/25)
2-3 GeV/c	25.2 (21.1/25)	13.9 (19.6/25)	5.1 (26.9/25)	14.8 (46.4/25)
3-5 GeV/c	41.0 (30.5/25)	1.9 (28.0/25)	31.5 (37.6/25)	28.5 (17.4/19)
5-10 GeV/c	31.5 (24.6/25)	3.9 (19.9/25)	16.0 (16.5/16)	5.0 (7.7/ 8)

Table 6.5   Table of $\Delta\chi^2$ values for correlations between a π^0 trigger from 7-10 GeV/c with several different associated charged hadron and centrality bins. The χ^2/NDF from the nominal fit is given in parentheses.

$p_{T,assoc}$	Min. Bias	0-20%	20-40%	40-92%
1-2 GeV/c	13.8 (34.0/25)	2.5 (18.8/25)	12.2 (53.6/25)	10.3 (16.0/25)
2-3 GeV/c	35.2 (24.8/25)	12.6 (27.2/25)	14.1 (22.2/25)	13.8 (24.9/21)
3-5 GeV/c	40.0 (15.1/23)	10.9 (29.1/21)	8.6 (6.5/17)	9.3 (4.5/16)
5-10 GeV/c	1.4 (20.9/14)	1.4 (8.2/11)	-4.1 (6.6/ 5)	1.4 (2.9/ 2)

Table 6.6   Table of $\Delta\chi^2$ values for correlations between a π^0 trigger from 10-20 GeV/c with several different associated charged hadron and centrality bins. The χ^2/NDF from the nominal fit is given in parentheses.

As seen from the tables, 10 of the 48 fits have a $\Delta\chi^2$ below 6.2 meaning the far-angle structure is not a statistically significant in those p_T and centrality bins at the 2σ level. There

is no distinct pattern to those correlations whose fits do not pass the tests except for the fits of the 10-20 GeV/c trigger with the 5-10 GeV/c associated which fail for all centrality bins. These correlations are the most statistics limited of all of the correlations. In what follows, far-angle jet shapes are not extracted from these correlations. However, since the background and near-angle width can still be reasonably determined, the near-angle jet properties are still extracted and the statistical subtraction (see Section 6.5) is still performed on these bins.
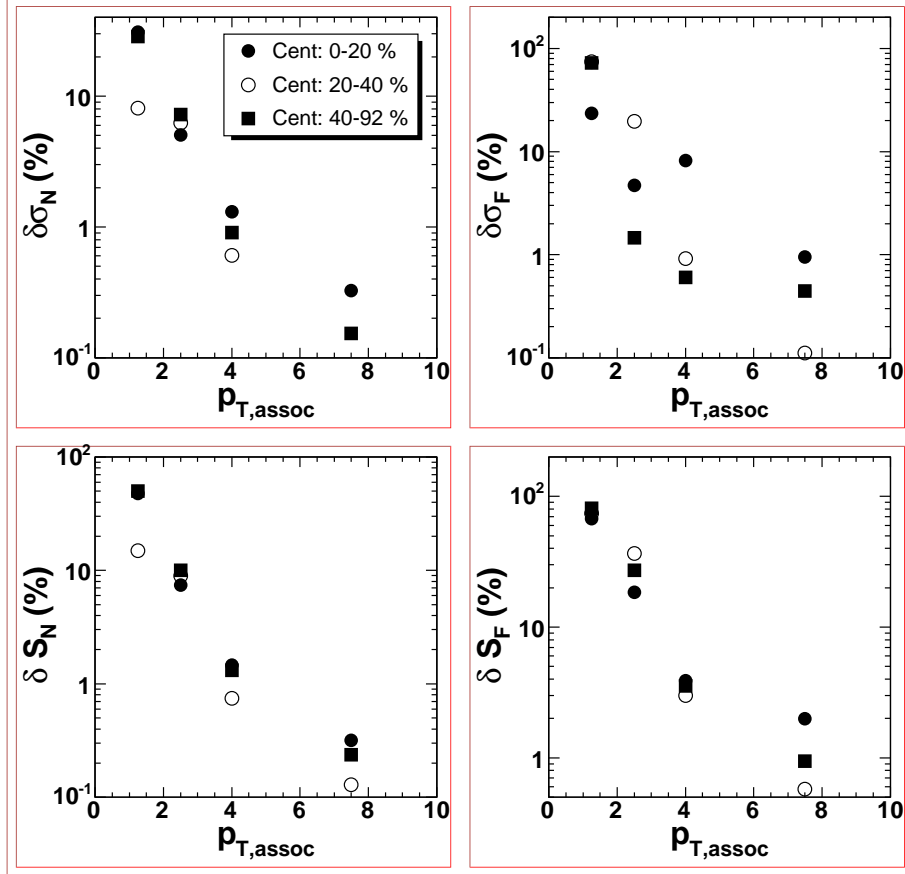
Figure 6.6   The relative error on the near angle width (upper left), far angle width (upper right), near angle yield (lower left), and far angle yield (lower right) as a function of associated p_T and centrality for a trigger p_T of 7-10 GeV/c.

6.3.5 Systematic Errors

There are several systematic errors in this analysis. The first is due to the variation of the input v_2 values. At low p_T the resulting errors can be 40-50%. As the p_T is increased these errors reduce rather dramatically to the few percent level. An example of the relative error due to the v_2 variation is given in Fig. 6.6. Another source of error is the extraction of jet properties, $\sqrt{\langle j_{Ty}^2 \rangle}$ and $\langle \sin^2 \phi_{jj} \rangle$. These errors are outlined in Appendix A. A further source of error is due to the signal-to-background within the π^0 mass peak. The signal-to-background in the π^0 mass range is slightly worse than p+p and d+Au collisions. The resulting systematic errors on the p+p and d+Au widths and yields vary from 1-5%. In this analysis the error due to the signal-to-background is conservatively estimated to be 5% on all extracted quantities and independent of p_T and centrality. A further source of systematic error that was performed in the p+p and d+Au analysis was the variation of some of the single particle cuts and checking the effect on the extracted quantities. A detailed study of these effects have not been performed in Au+Au but they are estimated to be slightly larger than the d+Au errors and a conservative systematic error of 5% is assigned to all quantities, independent of p_T and centrality. The final contribution to the systematic error is due to the normalization of the associated particle distribution. This error is a quadrature sum of the error on the correction function which is 10% and the error on the occupancy correction which is between 3-5% and is tabulated in Table 6.1. A summary of all of the contributions to the systematic error is presented in Table 6.7.

6.4   Centrality Dependence of Jet Properties

The correlations are fit using Eqn. 6.4 and fixing the trigger and associated v_2 values. The resulting fitted widths and extracted jet shapes, $\sqrt{\langle j_{Ty}^2 \rangle}$ and $\langle \sin^2 \phi_{jj} \rangle$, are plotted in Fig. 6.7-6.9. Each figure is a single trigger π^0 bin: 5-7 GeV/c, 7-10 GeV/c, and 10-20 GeV/c. The quantities are plotted as a function of the associated hadron p_T. The different symbols represent the different centralities: closed circles 0-20%, open circles 20-40%, and closed squares 40-92%. The expected shape of the near- and far-angle widths as a function of $p_{T,assoc}$ is seen, i.e. a

type	$\delta\sigma_N$	$\delta\sigma_F$	$\delta\mathrm{Y}_N$	$\delta\mathrm{Y}_F$
Cut variation	5%	5%	5%	5%
S/B Correction	5%	5%	5%	5%
normalization	N/A	N/A	11%-10.5%	11%-10.5%
v_2 variation	30%-0.5%	30%-0.5%	30%-0.5%	30%-1%
total	30%-7%	30%-7%	33%-13%	33%-13%
type			$\delta\sqrt{\left\langle j_{Ty}^2\right\rangle}$	$\delta\left\langle\sin^2\phi_{jj}\right\rangle$
Approximations to Eqn.			6%-0.7%	2%
total			30%-7%	30%-2%

Table 6.7   Summary of the systematic errors on the various results. The v_2 variations dominates over the other errors. This error is strongly p_T-dependent. As the p_T of both particles increases the resulting error decreases dramatically.

decrease with increasing $p_{T,assoc}$. The extracted $\sqrt{\left\langle j_{Ty}^2\right\rangle}$ is constant for all of the different trigger for associated p_T above 2 GeV/c. For each trigger and centrality bin the weighted average of the $\sqrt{\left\langle j_{Ty}^2\right\rangle}$ is found. These values are tabulated in Table 6.8. No centrality or $p_{T,trig}$ dependence is seen. These data are also consistent with the $\sqrt{\left\langle j_{Ty}^2\right\rangle}$ measured in p+p and d+Au collisions tabulated in Table 5.1 and in Appendix C.

$p_{T,trig}$	0-20%	20-40%	40-92%
5-7 GeV/c	0.415±0.017±0.019	0.406±0.017±0.018	0.434±0.017±0.018
7-10 GeV/c	0.415±0.026±0.018	0.437±0.027±0.019	0.416±0.022±0.019
10-20 GeV/c	0.421±0.038±0.018	0.490±0.040±0.020	0.325±0.033±0.015

Table 6.8   Table of asymptotic $\sqrt{\left\langle j_{Ty}^2\right\rangle}$ values in GeV/c for the different trigger and centrality bins. The values are averaged over the $p_{T,assoc}$ bins outside of the seagull region, that is above 2.0 GeV/c.

From energy loss models which describe the measured single particle suppression, a broadening of the di-jets is predicted [Vitev, 2005]. This broadening should be seen as an increase in the far-angle jet widths. To study this effect, the far-angle widths are plotted as a function of centrality for a fixed associated p_T range. This is shown in Fig. 6.10 where each symbol is a different trigger p_T bins. There is no systematic trend in any of the p_T ranges as a function

of centrality. In particular, the far-angle jet widths are not inconsistent with constant as a function of centrality, contrary to the expectation from energy loss models.

The conditional yields are also studied as a function of centrality. A suppression of the away-side yield has been observed at lower p_T (see Fig. 2.22) which has been interpreted as the result of energy loss of the away-side jet. To further test the energy loss the far-angle conditional yields as a function of x_E are constructed. These data extend the p_T reach of the previous analysis.

These x_E distributions are constructed by the same method employed for p+p and d+Au analysis. For a given trigger and associated p_T range there is a distribution of x_E. This distribution is fitted with a Gaussian to extract the mean of the peak. The yield is plotted at the mean from the Gaussian. The width of the Gaussian peak is also shown in the distributions to indicate the approximate bin width of the distribution. The x_E bin used is $\Delta x_E = \Delta p_{T,assoc}/p_{T,trig}$.

The x_E distributions are plotted in Fig. 6.11 for each centrality with all of the different trigger p_T ranges overlayed. For each centrality these data lie along a universal curve indicative of the universal similar to what was observed in p+p and d+Au. All of the data for a given centrality are then fit with an exponential distribution

$$\frac{1}{N_{trig}}\frac{dN}{dx_E} = A\exp\left(-\frac{x_E}{\langle x_E\rangle}\right) \tag{6.5}$$

The fitted slopes, $1/\langle x_E\rangle$, are shown in the plot along with the χ^2/NDF for the fit. The horizontal error bars are not used in the fit. Even though the most central data has a much higher slope than the peripheral, no systematic trend of increasing slope is seen in the data.

6.5 Statistical Subtraction Method for Pair Variables

To maximize the available statistics, conditional yield distributions have been constructed by the statistical subtraction method [Jia and Cole, 2004c]. As an introduction to the method consider the construction of the correlation function. Typically, the correlation function is

defined as the real pair distribution divided by the mixed event distribution to remove detector acceptance and efficiency. Using the proper normalization the conditional yield distribution, the number of pairs per trigger as a function of $\Delta\phi$, is obtained.

$$\frac{1}{N_{trig}}\frac{dN}{d\Delta\phi} = \frac{Occ(cent)}{N'_{trig}}\frac{\int d\Delta\phi\ Mix\left(\Delta\phi\right)}{\epsilon_{assoc}\Omega_{\Delta\phi}}\frac{Real\left(\Delta\phi\right)}{Mix\left(\Delta\phi\right)} \tag{6.6}$$

Alternatively it is possible to fill the real distribution with a weight equal to the properly normalized mixed distribution.

$$w\left(\Delta\phi\right) = \frac{Occ(cent)}{N'_{trig}}\frac{\int d\Delta\phi\ Mix\left(\Delta\phi\right)}{\epsilon_{assoc}\Omega_{\Delta\phi}}\frac{1}{Mix\left(\Delta\phi\right)} \tag{6.7}$$

In this way the conditional yield is simply

$$\frac{1}{N_{trig}}\frac{dN}{d\Delta\phi} = Real\left(\Delta\phi; w\left(\Delta\phi\right)\right) \tag{6.8}$$

where the second argument implies that a weighting is applied to each entry of the distribution. This results in a properly normalized and corrected distribution. Still present is the overall combinatoric background level, $1+\xi$, modulated by the elliptic flow. This $1+\xi$ background can be found by fitting the correlation function.

The elliptic flow can be removed by weighting the mixed distribution with the elliptic flow as well.

$$w_{mix}\left(\Delta\phi\right) = w\left(\Delta\phi\right)\left(1 + 2v_2^t v_2^a \cos\left(2\Delta\phi\right)\right) \tag{6.9}$$

The trigger and associated particle's v_2 is fixed from Table 6.2 and Table 6.3 respectively. In fact, the mixed distribution with a weight as in Eqn. 6.9 would be a flat line by construction. To summarize to obtain the **jet** conditional yield distribution is

$$\frac{1}{N_{trig}}\frac{dN^{jet}}{d\Delta\phi} = Real\left(\Delta\phi; w\left(\Delta\phi\right)\right) - \left(1 + \xi\right)Mix\left(\Delta\phi; w_{mix}\left(\Delta\phi\right)\right) \tag{6.10}$$

One advantage of this method is that distributions combine data from different $p_{T,trig}$ and

$p_{T,assoc}$ ranges to exploit the full statistics. A second advantage is that this method is useful for *any* pair variable. For example, x_E distributions

$$\frac{1}{N_{trig}}\frac{dN^{jet}}{dx_E} = Real\left(x_E; w\left(\Delta\phi\right)\right) - \left(1+\xi\right)Mix\left(x_E; w_{mix}\left(\Delta\phi\right)\right) \tag{6.11}$$

and p_{out} distributions

$$\frac{1}{N_{trig}}\frac{dN^{jet}}{dp_{out}} = Real\left(p_{out}; w\left(\Delta\phi\right)\right) - \left(1+\xi\right)Mix\left(p_{out}; w_{mix}\left(\Delta\phi\right)\right) \tag{6.12}$$

are measured. Recall that p_{out} is the component of the associated p_T perpendicular to the trigger p_T. The advantage of these distributions above the statistical power of the method is that they contain the information which is sensitive to the energy loss, i.e. p_{out} is sensitive to di-jet broadening and the x_E distributions are sensitive to the yield suppression.

The x_E distributions are outlined here with the focus on the details of the method. First, a pass through the data must be made to build the correlation functions and the mixed distributions. These mixed distributions are then used in the second pass through the data as an input the weights of the real and mixed distributions. An example of the resulting weighted distributions is shown in Fig. 6.12. The mixed distribution is scaled by $1+\xi$ as well. This factor comes from the background fit to the conditional yield distributions, *i.e. B* in Eqn. 6.4, and scaled by the normalization factor in Eqn. 6.3. The difference between these two distributions is the x_E distribution due to jet correlations only. The distributions are calculated separately for each trigger and associated p_T ranges since the background that is subtracted in the distribution is a very different fraction of the total distribution. Taking a large associated bin would require a large bin-shift correction to the background.

Next, the difference is taken between the weighted and scaled distributions in each of the trigger and associated and centrality bins. These distributions, which are the jet x_E distribution for a given trigger, associated, and centrality bin. An example is shown in Fig. 6.13. It is should be noted that, by the definition of x_E, the maximum x_E for each trigger-associated bin is $p_{T,assoc}/p_{T,trig}$. Within a given bin there is a distribution of x_E. Hence, the different

trigger-associated bins populate different ranges of x_E.

Finally, the different distributions are summed to give the final x_E distribution for a given trigger and centrality bin. These are shown for all centrality and trigger bins in Fig. 6.14-Fig. 6.16. By combining the data from different associated ranges all of the available statistics are maximally used permitting a finely binned distribution. As a result a clear shape is seen.

By taking a ratio of the distribution in the central bins to the most peripheral bin, the difference between these distributions can be seen in detail. Fig. 6.17-Fig. 6.19 plot the quantity I_{cp} defined as (c.f. Eqn. 2.24)

$$I_{cp} = \frac{\frac{1}{N_{trig}}\frac{dN^{central}}{dx_E}}{\frac{1}{N_{trig}}\frac{dN^{peripheral}}{dx_E}} \tag{6.13}$$

If there is no change between the two distributions, I_{cp} would be unity. This is not the case for the data as a whole, the ratio is systematically below unity. This indicates a suppression of the associated yield in the central bins compared to the peripheral bin. By assuming that the ratio is constant as a function of x_E, the average value for each trigger and centrality bin is computed. These values are all below unity. There is also a systematic trend that the 0-20% data has a lower average I_{cp} than the 20-40% data. This is seen by plotting the average I_{cp} as a function of $p_{T,trig}$ for both centrality bins.

I_{cp} is sensitive to the differential energy loss between the trigger and the associated particle. To see this consider two separate cases. First, if the trigger is emitted at the skin of the overlap region, the corona, it will not suffer energy loss. If a pair is not counted in the conditional yield it is entirely due to the energy loss of the associated particle. In this case the suppression of the pairs would be similar to the suppression of single particle, $I_{cp} \sim R_{cp}$. In the second case, consider both particles emitted at the center of the interaction region and losing the same amount of energy. It could be possible, if the energy is high enough, that both the pair and the trigger are not counted in the correlation. In this case I_{AA} is about unity. Therefore, a value of I_{cp} between R_{cp} and 1 would indicate a differential energy loss between the trigger and associated particle. From the single particle hadron analysis [Adler et al., 2004] R_{cp} a constant value of 0.4 above 5 GeV/c for 0-20%/40-92% and 0.6 above 5 GeV/c for 20-40%/40-92%. The measured I_{cp} are systematically above these R_{cp} values (see Fig. 6.20) indicating that there

may be differential energy loss between the trigger and associated particles.

The p_{out} distributions have also been measured. This observable is defined as the component of the associated particle p_T perpendicular to the trigger p_T. It is of interest since the far-side p_{out} is directly related to k_T (see Eqn. 4.24). In the energy loss models which reproduce the single particle suppression, a large broadening of the away-side jet distribution is predicted [Vitev, 2005]. Therefore, the expectation is that the p_{out} distribution should broaden as well.

These p_{out} distributions are constructed using the same method for constructing the x_E distributions. Fig. 6.21-Fig. 6.23 show the p_{out} distribution for the different trigger particle ranges and the different centrality bins. All distributions are approximately Gaussian which is expected since p_{out} is directly related to k_T. A Gaussian fit has been made of each of these distributions to extract the RMS $\sqrt{\langle p_{out}^2 \rangle}$. The measured RMS values as a function of centrality are shown in Fig. 6.24. These values are not inconsistent with a constant value as a function of centrality and as a function of $p_{T,trig}$. A broadening of at most 30% may be indicated in the most central bin compared to the more peripheral bins.

Taking the data as a whole we see that the $\sqrt{\langle j_{Ty}^2 \rangle}$ is consistent with p+p and d+Au. The far-angle widths within the statistic show little to no broadening as a function of centrality. The p_{out} distributions indicate $\sqrt{\langle p_{out}^2 \rangle}$ not inconsistent with being independent of centrality but could possibly indicate an increase of 30% in the most central bin. The yields show a suppression. That is, I_{cp} is less than unity between central and peripheral collisions. These are interesting results because the suppression that was observed at lower p_T persists to higher p_T and the away-side jet distribution can be quantified. The last result is crucial for testing energy loss models in Au+Au collisions at RHIC.
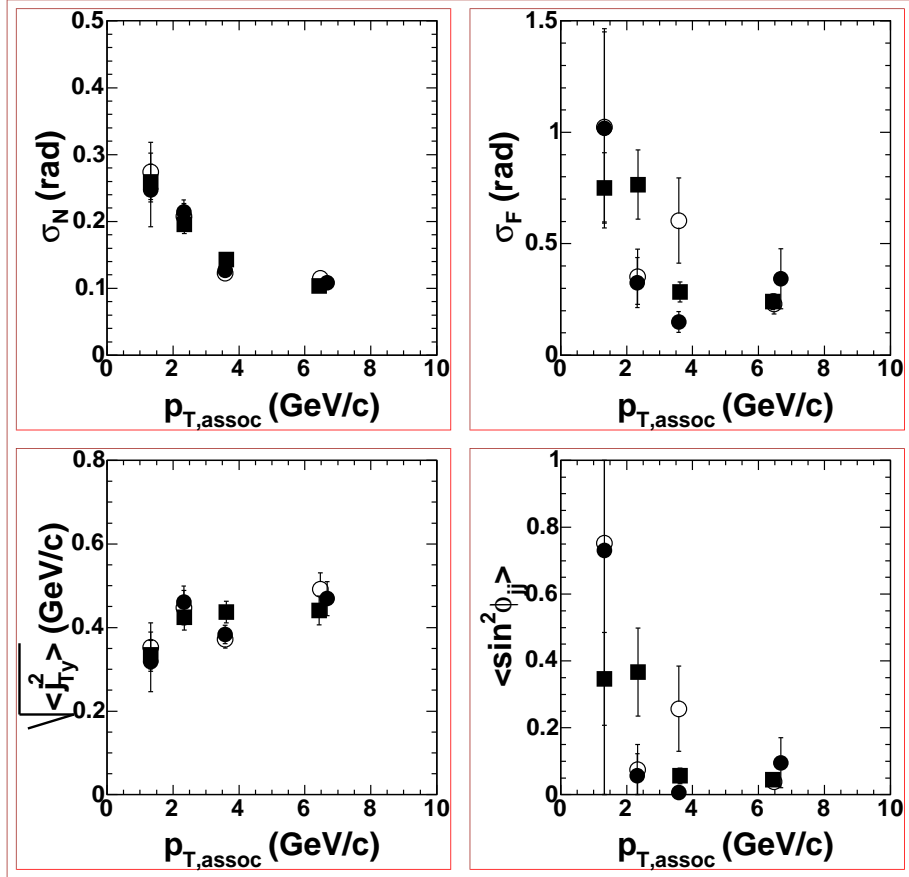
Figure 6.7   *Upper Left:* Near-angle widths as a function of $p_{T,assoc}$ for 5-7
GeV/c π^0 triggers. Closed circles are 0-20% central, open cir-
cles are 20-40% central, and closed squares are 40-92% central.
Upper Right: Far-angle widths as a function of $p_{T,assoc}$. *Bottom
Left:* Extracted $\sqrt{\left\langle j_{Ty}^2 \right\rangle}$ as a function of $p_{T,assoc}$. *Bottom Left:*
Extracted $\left\langle \sin^2 \phi_{jj} \right\rangle$ as a function of $p_{T,assoc}$.
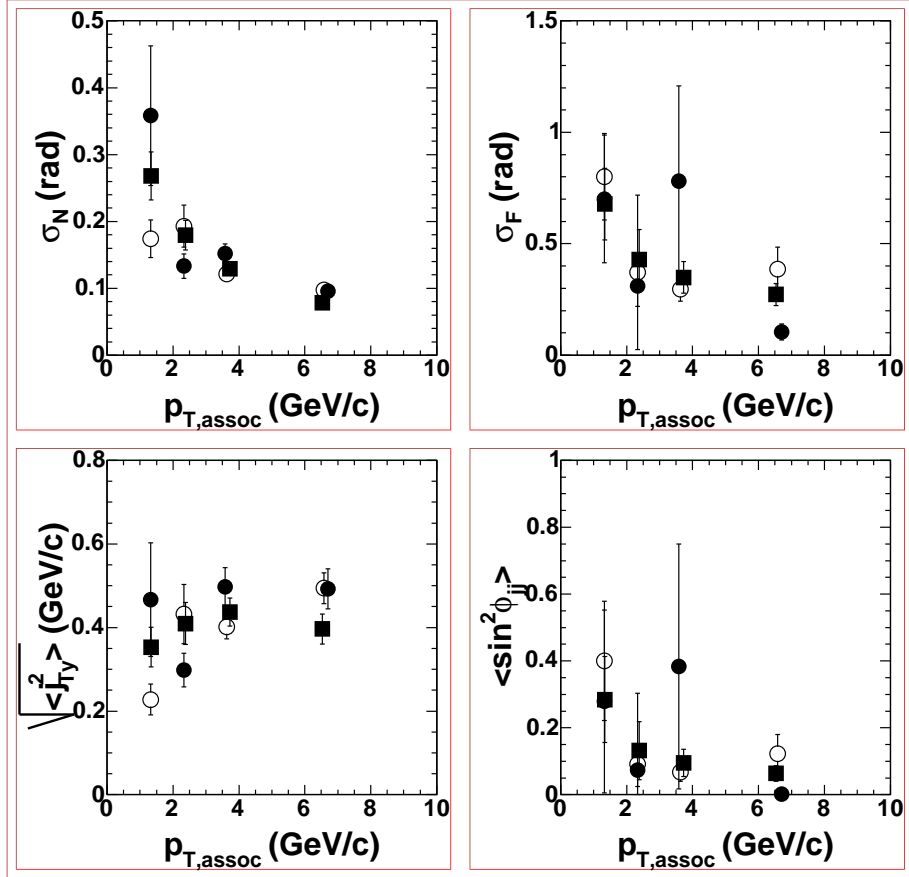
Figure 6.8   *Upper Left:* Near-angle widths as a function of $p_{T,assoc}$ for 7-10 GeV/c π^0 triggers. Closed circles are 0-20% central, open circles are 20-40% central, and closed squares are 40-92% central. *Upper Right:* Far-angle widths as a function of $p_{T,assoc}$. *Bottom Left:* Extracted $\sqrt{\left\langle j_{Ty}^2 \right\rangle}$ as a function of $p_{T,assoc}$. *Bottom Left:* Extracted $\left\langle \sin^2 \phi_{jj} \right\rangle$ as a function of $p_{T,assoc}$.
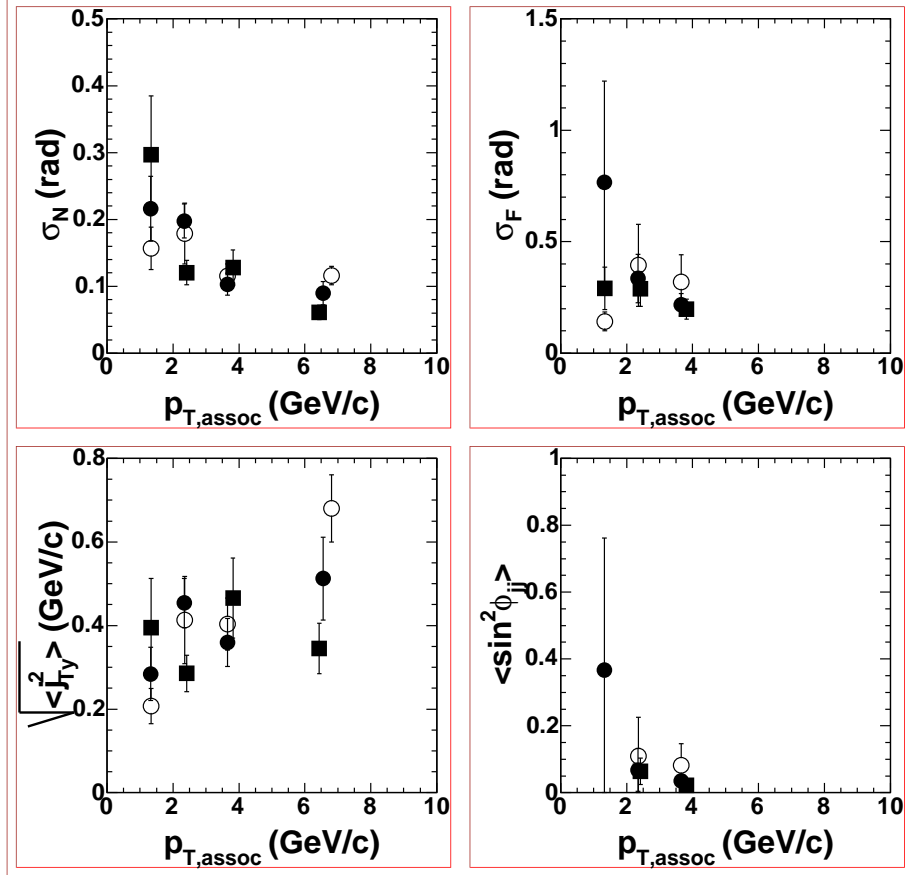
Figure 6.9   *Upper Left:* Near-angle widths as a function of $p_{T,assoc}$ for 10-20 GeV/c π^0 triggers. Closed circles are 0-20% central, open circles are 20-40% central, and closed squares are 40-92% central. *Upper Right:* Far-angle widths as a function of $p_{T,assoc}$. *Bottom Left:* Extracted $\sqrt{\left\langle j_{Ty}^2 \right\rangle}$ as a function of $p_{T,assoc}$. *Bottom Left:* Extracted $\left\langle \sin^2 \phi_{jj} \right\rangle$ as a function of $p_{T,assoc}$.
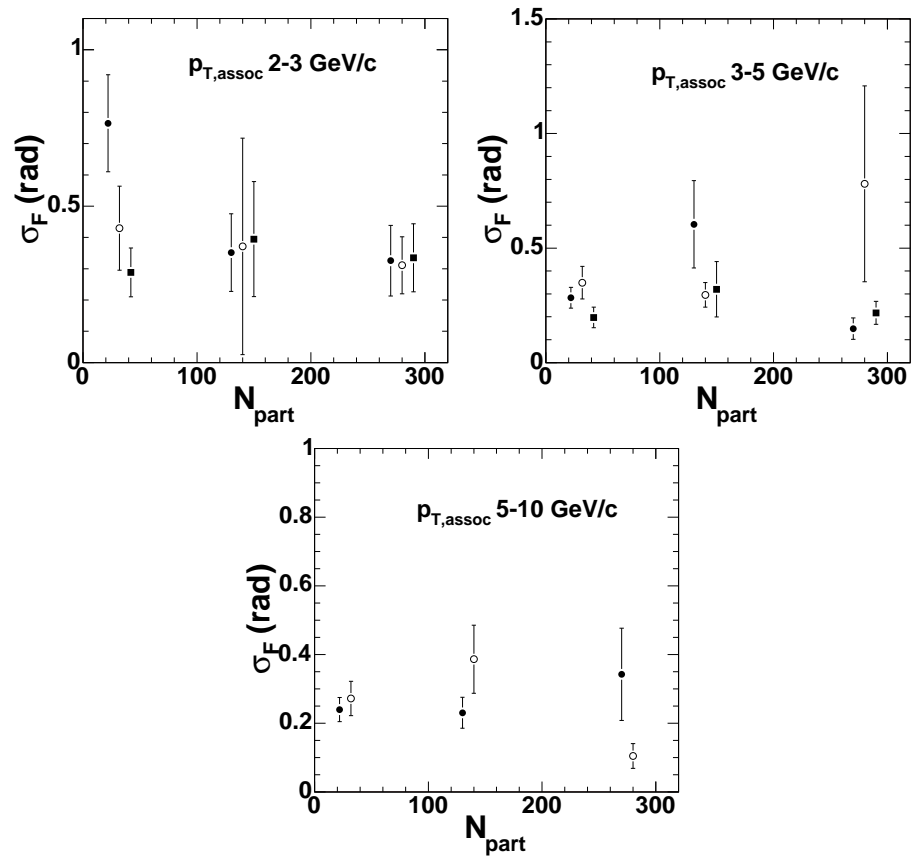
Figure 6.10   Fitted σ_F as a function of centrality for associated hadron p_T range from 2-3 GeV/c (upper left), 3-5 GeV/c (upper right), and 5-10 GeV/c (bottom). Each symbol represents a different trigger p_T. Closed circles are 5-7 GeV/c, open circles are 7-10 GeV/c, and closed squared are 10-20 GeV/c.
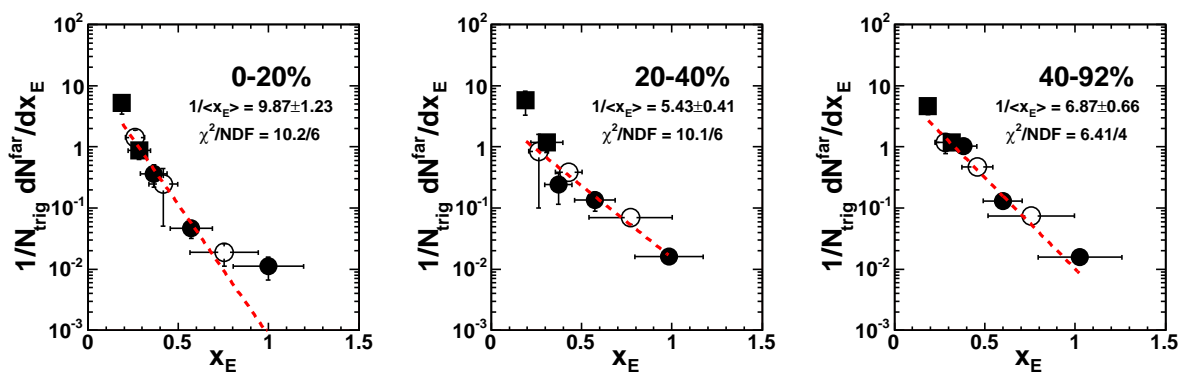
Figure 6.11   Conditional yield x_E distributions. The different symbols represent different trigger ranges: 5-7 GeV/c, closed circles, 7-10 open circles, and 10-20 GeV/c, closed squares. The dashed line is an exponential fit to the data.
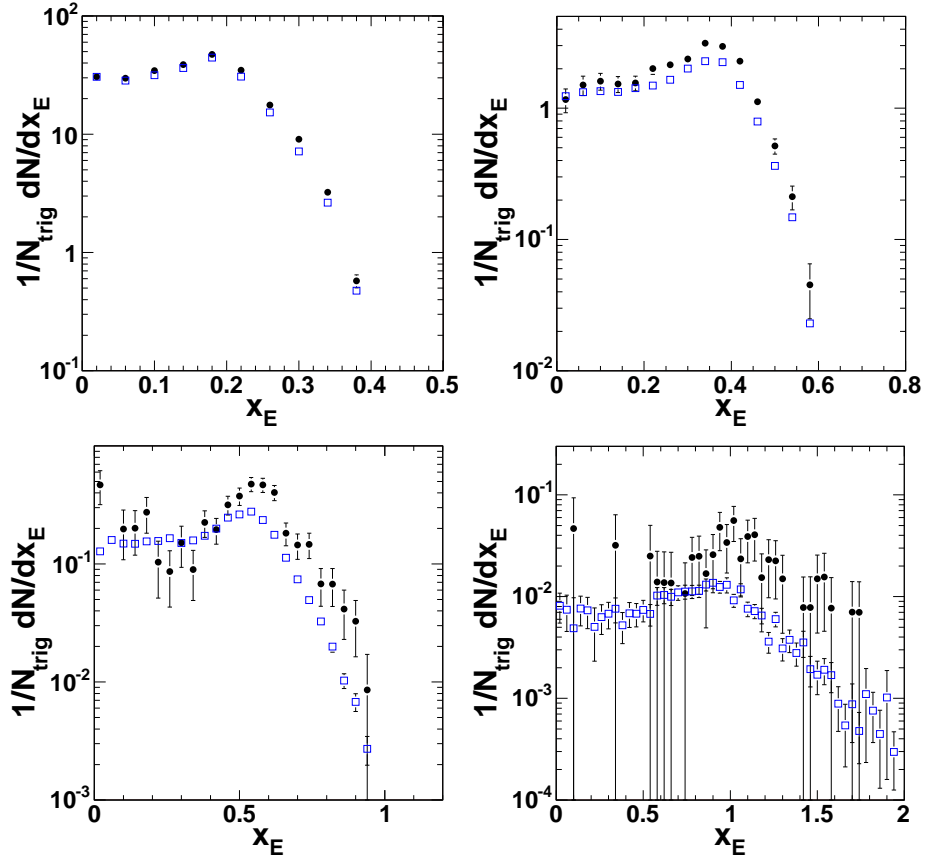
Figure 6.12 The x_E distribution from real pairs (circles) weighted by the acceptance (Eqn. 6.7). and mixed pairs (squares) weighted by the acceptance (Eqn. 6.9) and scaled by $1+\xi$ background. All distributions are for 40-92% Au+Au collisions with π^0 triggers from 5-7 GeV/c. Each different panel is a different associated hadron p_T range: 1-2 GeV/c (upper left), 2-3 GeV/c (upper right), 3-5 GeV/c (lower left), and 5-10 GeV/c (lower right).
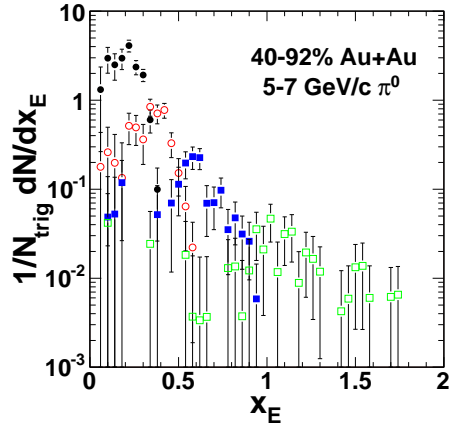
Figure 6.13   The resulting difference between the real and mixed distributions from Fig. 6.12 for each of the associated bins overlayed on one another.
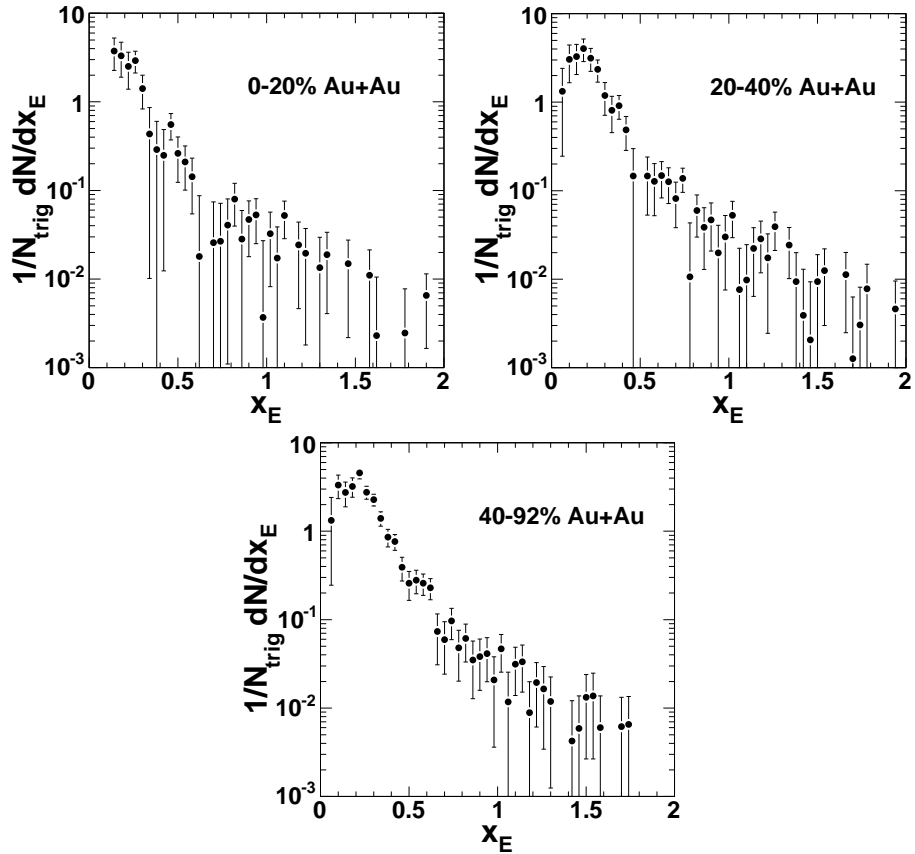
Figure 6.14   Jet x_E distributions with π^0 triggers from 5-7 GeV/c and associated hadrons from 1-10 GeV/c.
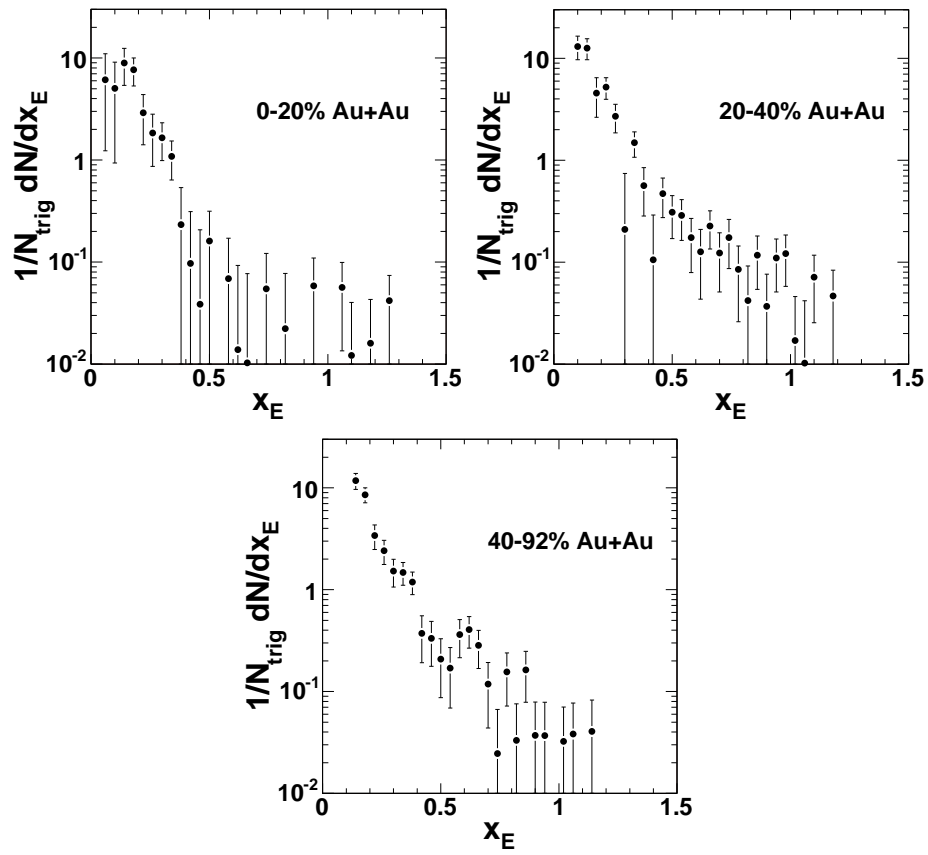
Figure 6.15   Jet x_E distributions with π^0 triggers from 7-10 GeV/c and associated hadrons from 1-10 GeV/c.
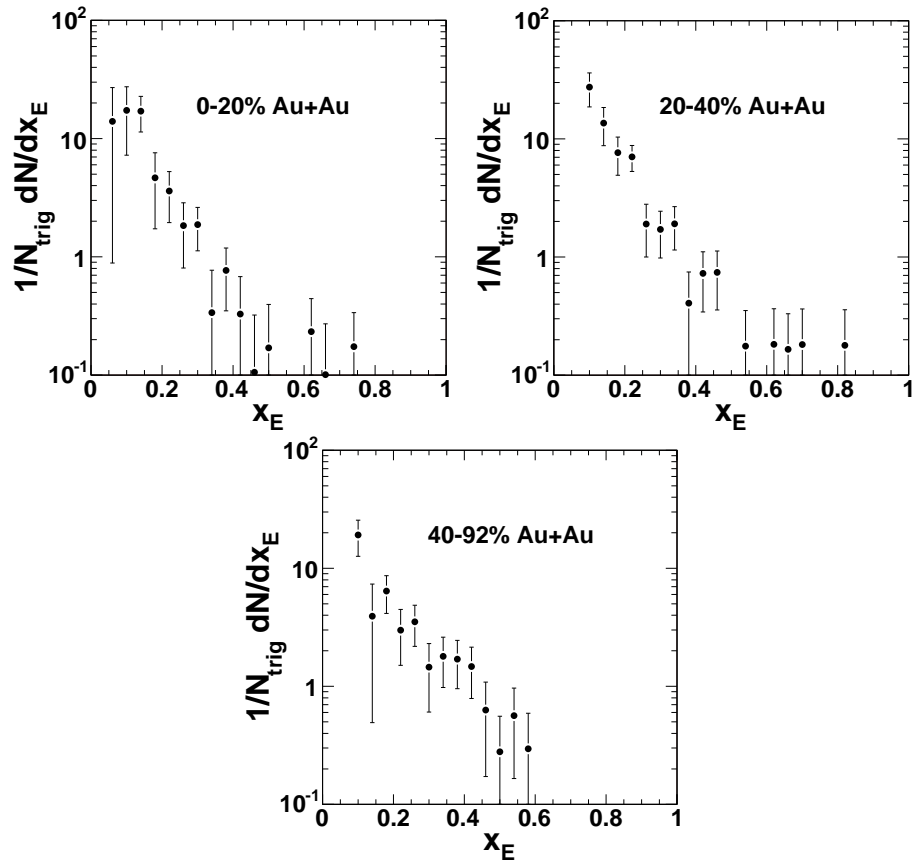
Figure 6.16   Jet x_E distributions with π^0 triggers from 10-20 GeV/c and associated hadrons from 1-10 GeV/c.
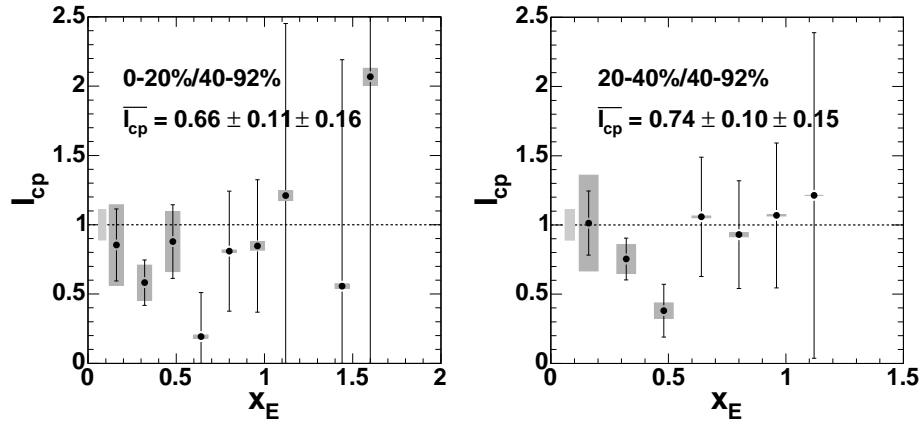
Figure 6.17   Ratio of the two most central jet x_E distributions to the most peripheral distribution using π^0 triggers from 5-7 GeV/c. The weighted average of the data is given. The shaded band at one is the normalization error on the yields. The shaded band at each point are the point-to-point systematic error due to the variation of v_2.
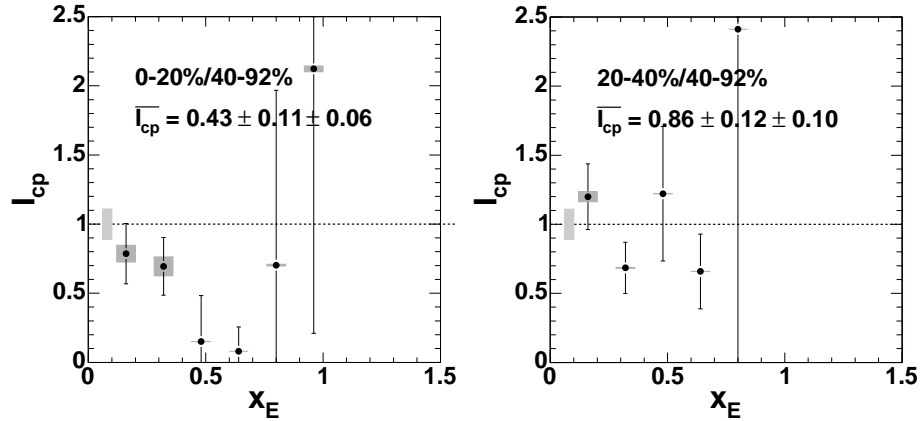
Figure 6.18   Ratio of the two most central jet x_E distributions to the most peripheral distribution using π^0 triggers from 7-10 GeV/c. The weighted average of the data is given. The shaded band at one is the normalization error on the yields. The shaded band at each point are the point-to-point systematic error due to the variation of v_2.
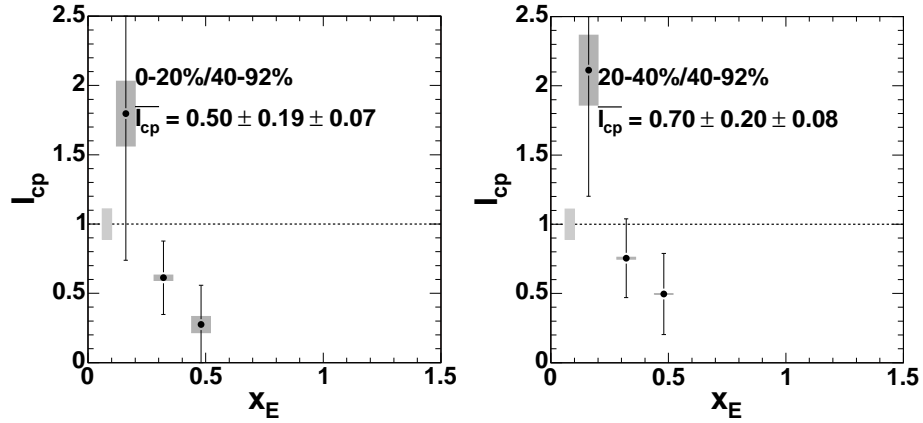
Figure 6.19   Ratio of the two most central jet x_E distributions to the most peripheral distribution using π^0 triggers from 10-20 GeV/c. The weighted average of the data is given. The shaded band at one is the normalization error on the yields. The shaded band at each point are the point-to-point systematic error due to the variation of v_2.
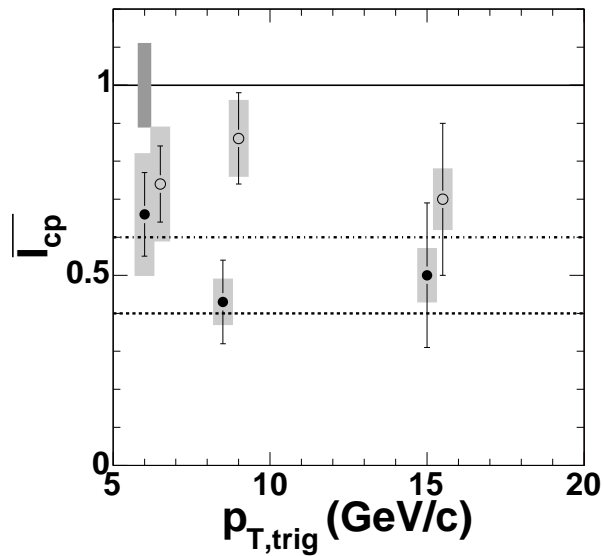
Figure 6.20 $\bar{I}_{CP}$ as a function of trigger p_T for 0-20%/40-92% central Au+Au collisions (closed) and 20-40%/40-92% central Au+Au (open). The dashed line is the approximate value of R_{cp} corresponding to 0-20%/40-92% Au+Au and the dot-dashed line corresponds 20-40%/40-92% Au+Au collisions.
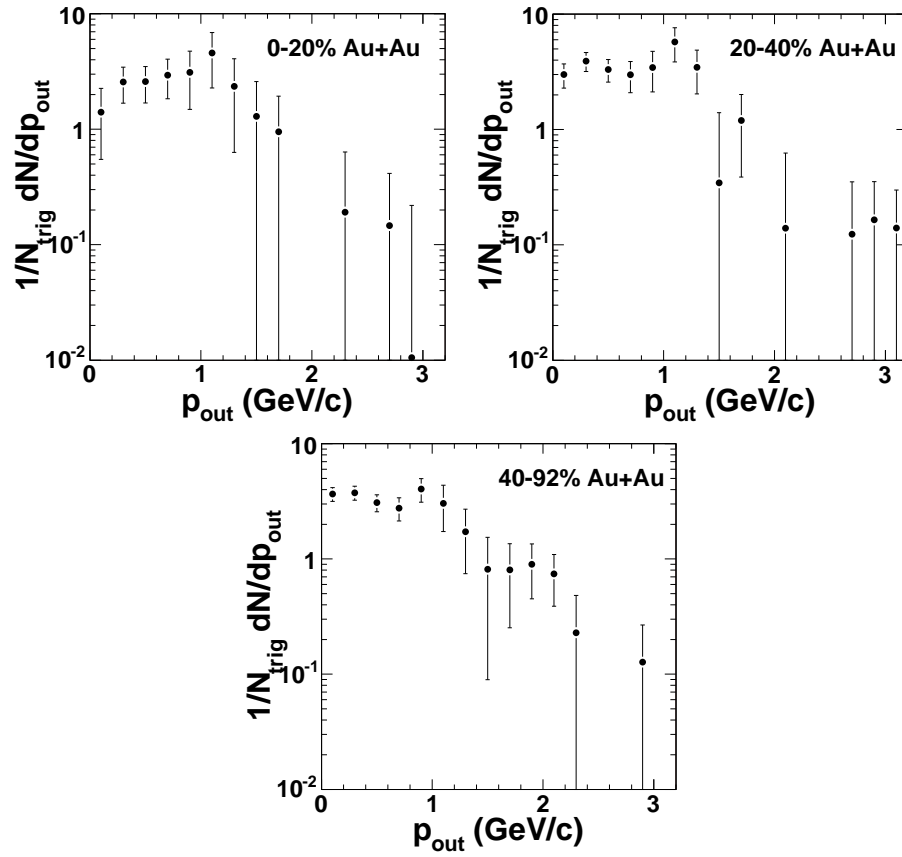
Figure 6.21   Jet p_{out} distributions for π^0 triggers from 5-7 GeV/c and associated hadrons from 1-10 GeV/c.
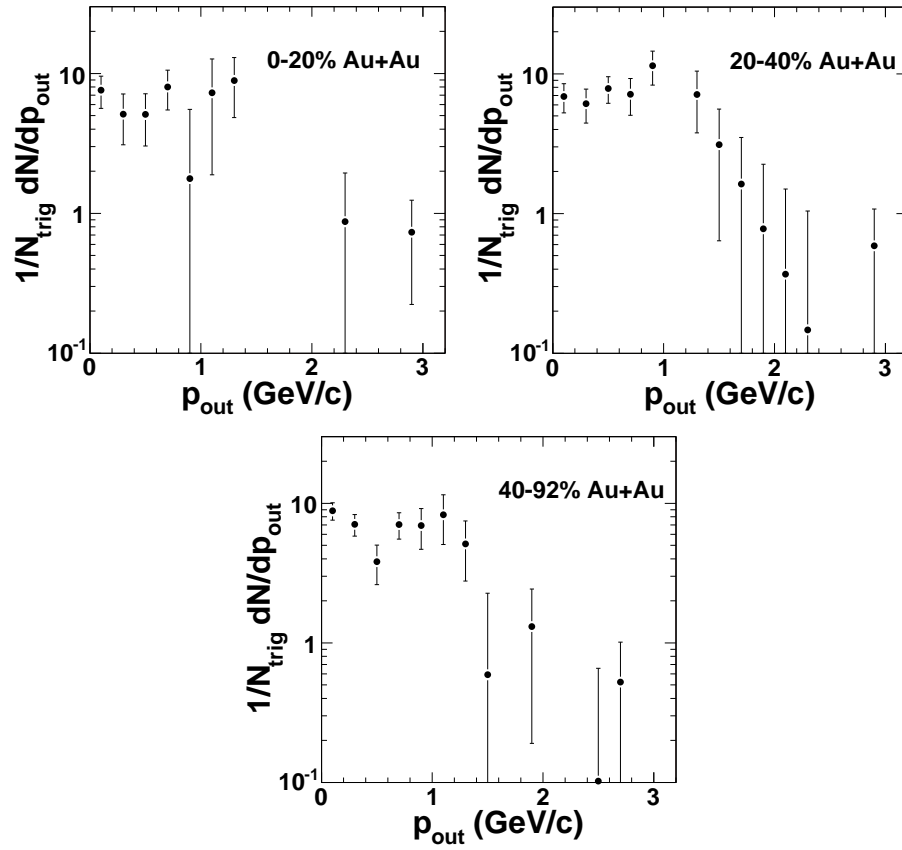
Figure 6.22   Jet p_{out} distributions for π^0 triggers from 7-10 GeV/c and associated hadrons from 1-10 GeV/c.
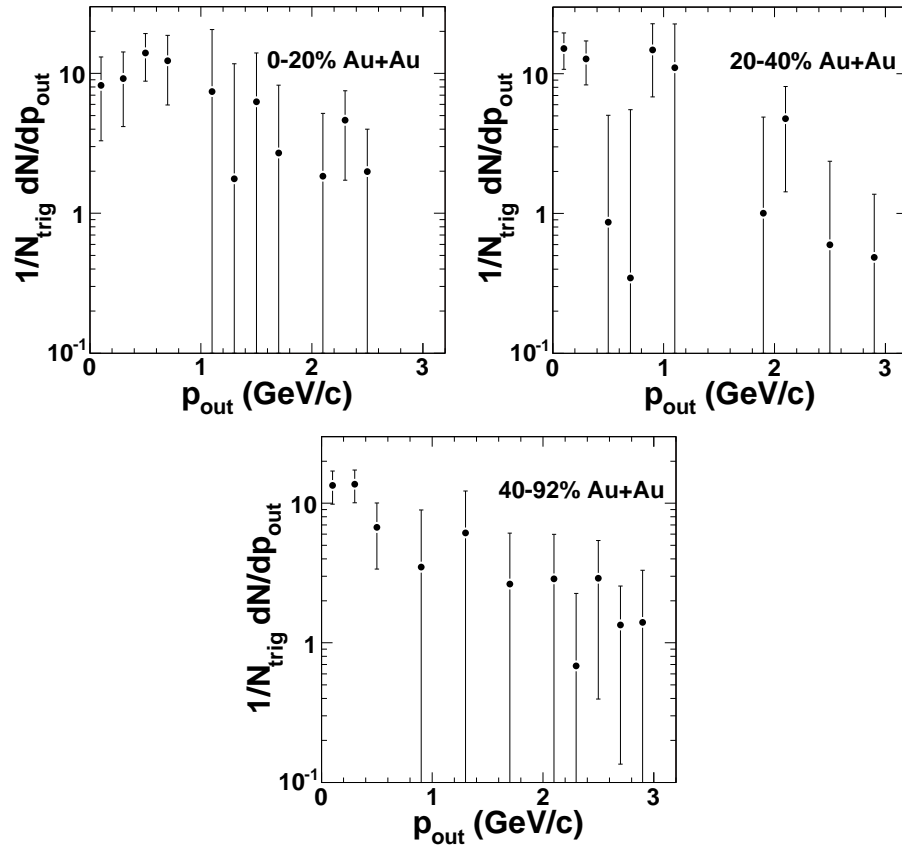
Figure 6.23   Jet p_{out} distributions for π^0 triggers from 10-20 GeV/c and associated hadrons from 1-10 GeV/c.
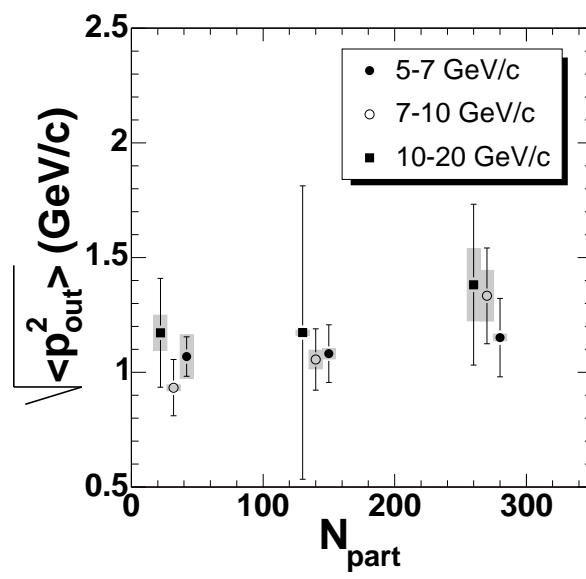
Figure 6.24   Fitted Gaussian RMS of the p_{out} distributions as a function of centrality. Each symbol represents a different trigger π^0 range.

CHAPTER 7.   Discussion

This chapter discusses the data presented in this thesis in comparison to other data and theoretical models in an attempt to understand jet modification in nuclear collisions.

7.1   Baseline Correlations

It is typically stated that jet production, which is a useful probe of the quark-gluon plasma, can be understood from perturbative QCD (pQCD). In fact, next-to-leading order (NLO) pQCD has been successful at predicting single π^0 particle production [Adler et al., 2003e] and single, direct (isolated) γ production [Sakaguchi, 2005; Gordon and Vogelsang, 1993] in p+p collisions at RHIC. The NLO calculations involve processes such as 2→3 or 3→2, where a parton is radiated in the final or initial state, respectively. Such initial state radiation breaks the collinearity of the incoming partons, that is they will have some transverse momentum. The final state radiation will give a random kick to each of the outgoing partons resulting in further transverse momentum of the pair of outgoing partons. These calculations in general do not include other sources of k_T beyond NLO diagrams, i.e. k_T due to confinement. The fact that the NLO pQCD calculations reproduce the single particle distribution suggests that 1) the semi-hard gluon radiation in both the initial and final state dominates the "intrinsic" k_T resulting from confinement, and 2) the rates for jet production are calculable. The shape of these events, which is explicitly measured in correlation functions, is not calculable in pQCD. The correlation functions include the fragmentation of each of the partons, which is a non-perturbative effect. Even though pQCD calculations can reproduce single particle spectra by using fragmentation functions, it is not possible for pQCD to reproduce p+p correlation functions (see, however, di-hadron fragmentation functions from Majumder and Wang [2004]).

In light of this, the discussion of the results focuses on the comparison of correlation results in heavy ion collisions to those measured in p+p collisions.

7.2 Cold Nuclear Medium Jet Modification

The jet properties extracted from p+p and d+Au collisions (see Section 5.5) should be sensitive to and provide a handle on the cold nuclear medium modifications of jets in the nuclear environment at RHIC energies. Fixed target experiments at Fermilab of lower energy p+A collisions measured a strong enhancement of di-jet acoplanarity (see Fig. 2.19). The data show that the $\sqrt{\left\langle k_{Ty}^2 \right\rangle}$ doubles from x+p collisions to x+Pb collisions from 1 GeV/c to 2 GeV/c for x=γ, π, and p. It is important to note that the increased broadening in γ+A collisions must be due to the multiple scattering of the final state partons from the collisions since the γ does not strongly multiple scatter in the nucleus prior to the hard collision. Since the p+A and π+A data show the same trend with A and the same magnitude of $\sqrt{\left\langle k_{Ty}^2 \right\rangle}$, one would conclude that the broadening in those collisions would be due entirely to the final state.

This conclusion is, in fact, in contrast to Drell-Yan data in p+A collisions. The Drell-Yan process is $q + \bar{q} \rightarrow \ell^+ + \ell^-$. The pair p_T of the outgoing lepton pair is equal to the sum of k_T of the incoming quarks. Since the outgoing leptons do not strongly multiple scatter in the nuclear medium, any p_T broadening measured in Drell-Yan pairs is purely from the initial state multiple scattering of the partons. Indeed, p_T broadening of Drell-Yan pairs is measured in p+A collisions.

It is not clear from lower energy data if there is a coherent understanding of multiple scattering, i.e. the origin of the Cronin effect. That is, some data indicate that the origin is from the initial state while other data suggest it is from the final state. It is clear, however, that all models reproducing the lower energy Cronin effect include multiple scattering as the source. At RHIC energies, modification of jet properties in p(d)+A collisions should be sensitive to the combined effect of the initial and final state interactions. The data indicate that there is an enhancement in the d+Au single particle spectrum consistent with the Cronin effect. This enhancement is in stark contrast to the strong suppression measured in Au+Au collisions at

the same energy. Because of the large difference between effects in Au+Au compared to d+Au, disentangling the initial and final state effects in d+Au collisions is perhaps not critical.

7.2.1   Transverse Fragmentation of a Jet
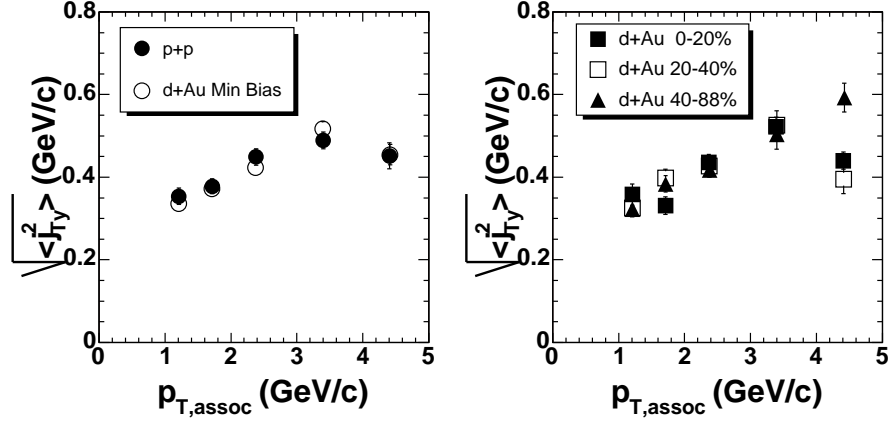
Figure 7.1   *Left:* Comparison of $\sqrt{\left\langle j_{Ty}^2 \right\rangle}$ between p+p and minimum bis d+Au. *Right:* Comparison of $\sqrt{\left\langle j_{Ty}^2 \right\rangle}$ for different d+Au centrality bins.

A jet property that could potentially be affected only by final state interactions is $\sqrt{\left\langle j_{Ty}^2 \right\rangle}$, the transverse momentum of fragment with respect to the parent parton. The j_T distribution is a result of fragmentation which occurs only in the final state. Depending on when the parton begins to fragment, it could take place within the nucleus. This time can be estimated by the time it takes for j_T to develop [Wiedemann, 2004].

$$\ell \sim \frac{q_T}{j_T^2} \tag{7.1}$$

For the jets considered in this thesis, $q_T = 10$ GeV and $j_T = 0.5$ GeV, the approximate formation length is $\ell \sim 8$ fm. This is longer than the Au radius. Therefore, little interaction of the final state fragments with the nuclear medium should be expected.

The data indicate no significant change in $\sqrt{\left\langle j_{Ty}^2 \right\rangle}$, see Fig. 7.1. This quantity is very similar between p+p and d+Au collisions, and there is no obvious dependence on the centrality. No

indication of modification due to the final state is observed.
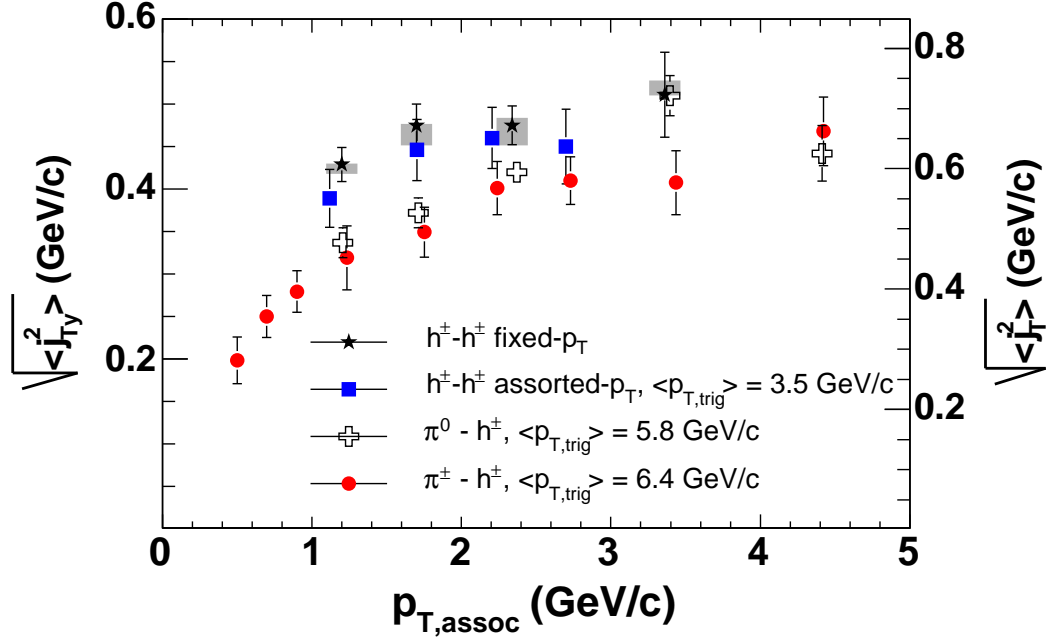
Figure 7.2   Compilation of d+Au minimum bias $\sqrt{\left\langle j_{Ty}^2 \right\rangle}$ from different correlation analyses from PHENIX [Adler et al., 2005b]. The stars and crosses are from this thesis.

Other PHENIX analyses have shown a similar result for $\sqrt{\left\langle j_{Ty}^2 \right\rangle}$. The compilation is plotted in Fig. 7.2. The data are for minimum bias d+Au collisions for fixed-p_T h-h (stars), assorted h-h (squares), assorted π^0-h (crosses), and assorted $\pi^{\pm}$-h (circles) correlations. The data for the fixed-p_T h-h and π^0-h correlations are from this thesis. All data are consistent with one another.

The data also indicate that j_T is independent of both the trigger and associated momentum, at least above about 1.5 GeV/c. The "turn-on" of the data at low $p_{T,assoc}$ is due to a simple kinematic constraint that j_T cannot be larger than the p_T of the particle. This is known as the "Seagull effect" [van Apeldoorn et al., 1975; Agababyan et al., 1994]. When calculating the average of $\sqrt{\left\langle j_{Ty}^2 \right\rangle}$ from the data, only those data above 2 GeV/c are used. This average is $\sqrt{\left\langle j_{Ty}^2 \right\rangle} = 0.45 \pm 0.01 \pm 0.03$ GeV/c. This value can be compared with the value extracted by the CCOR collaboration at the CERN ISR [Angelis et al., 1980]. They extracted a value of $\sqrt{\left\langle j_{Ty}^2 \right\rangle}$

= 0.493±0.009 GeV/c at $\sqrt{s}$=31-63 GeV. These values are also consistent with another ISR collaboration which measured $\sqrt{\left\langle j_{Ty}^2 \right\rangle}$ = 0.44±0.04 GeV/c at $\sqrt{s}$=31-63 GeV [Clark et al., 1979]. All of these data show that $\sqrt{\left\langle j_{Ty}^2 \right\rangle}$ is independent of $\sqrt{s}$. This is indicative of the universality of fragmentation.

7.2.2 Di-jet Acoplanarity
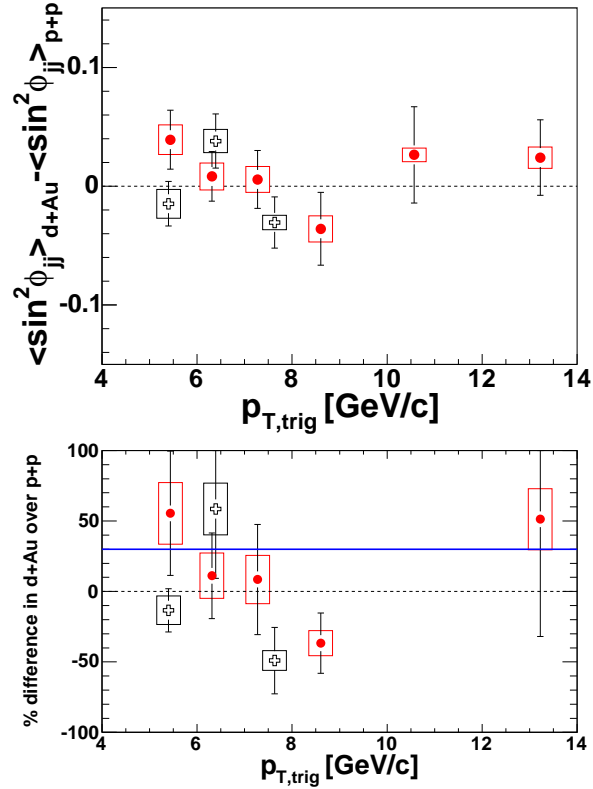
Figure 7.3 *Top:* Absolute difference of $\left\langle \sin^2 \phi_{jj} \right\rangle$ between d+Au and p+p collisions. Crosses are π^0-h correlations from this analysis. The circles are $\pi^\pm$-h correlation results. The average of the data is consistent with no difference between p+p and d+Au. *Bottom:* Percent difference in d+Au compared to p+p. The solid line is a prediction from a multiple scattering model [Qiu and Vitev, 2003]

To probe the effect of multiple scattering, the acoplanarity of the outgoing jets is studied. It is measured via the sin of the angle between the jet axes, $\left\langle \sin^2 \phi_{jj} \right\rangle$ (see Fig. 4.3). As the parton which participates in the hard collision multiple scatters, it picks up extra transverse

momentum resulting in the broadening of the outgoing di-jet distribution. This broadening, from both initial and final state interactions, should be observable as an increase in $\langle \sin^2 \phi_{jj} \rangle$.

The acoplanarity increase is measured by the difference between $\langle \sin^2 \phi_{jj} \rangle$ in p+p and minimum bias d+Au collisions. This quantity is plotted in Fig. 7.3. The absolute difference is consistent with no change between p+p and d+Au collisions. Separately, the weighted average of the difference is -0.005±0.012±0.003 for π^0 triggers from this analysis and 0.011±0.011±0.010 for $\pi^{\pm}$ triggers, both consistent with zero. Combined, the weighted average of the difference is 0.004±0.008±0.009. In all of these quantities, the first error is statistical and the second error is systematic.

This difference can be compared with a prediction from J. Qiu and I. Vitev based on multiple scattering of the partons in both the initial and final state [Qiu and Vitev, 2003]. They predicted a 25-30% increase in acoplanarity in d+Au collisions compared to p+p. This can be tested by recasting the absolute difference as a percent difference of $\langle \sin^2 \phi_{jj} \rangle$ in d+Au compared to p+p. This is plotted in the lower panel of Fig. 7.3. The weighted average of the percent difference for all data is -13%±10%±15%. The quadrature sum of the errors is 18% which is approximately 1.5σ from the prediction, i.e. the prediction is not inconsistent with the data.

Another prediction of the modification of jet properties in p+p compared to d+Au collisions was from Hwa and Yang [2004a] based on a recombination model. In this model the hadronization process of fragmentation is augmented by soft partons from the underlying event combining with partons from the fragmentation process. This model is able to reproduce the single, identified particle spectra. The enhancement in intermediate p_T production is due to the addition of parton momentum from recombination and not from multiple scattering in the nucleus. Therefore, this model predicted no increase of the acoplanarity of jets. They also predicted a factor of two increase in the near-side conditional yield [Hwa and Yang, 2004b].
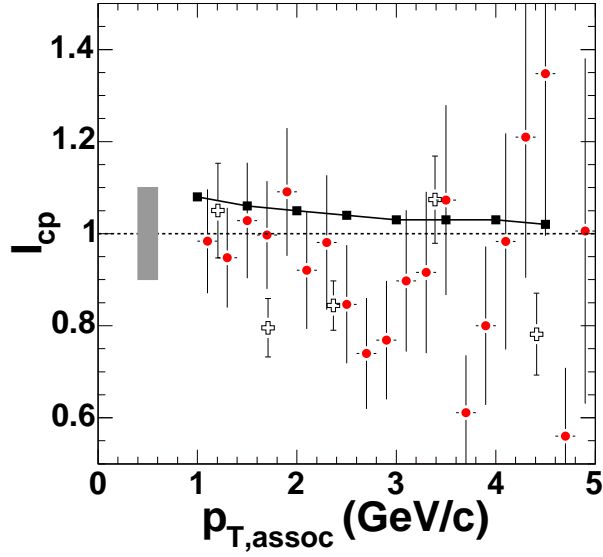
Figure 7.4   Central to peripheral ratio of near-side yields from the recombination model (closed squares) of Hwa and Tan [2005]. The d+Au data are from $\pi^\pm$ triggers (closed circles) and π^0 triggers (open crosses).

7.2.3   Near-angle Yields

The data on the ratio of the near-side yield in d+Au to p+p is shown in Fig. 5.18 and Fig. 5.23. This ratio is approximately 1, not consistent a predicted factor of 2. Because of this data Hwa and Tan [2005] revisited the result. What was initially calculated, which gave a factor of 2, was

$$\frac{1}{N_{trig}}\frac{dN}{dp_{T,assoc}} = \int_{p_{T,trig}^{Low}}^{p_{T,trig}^{High}} \frac{\frac{d^2\sigma}{dp_{T,assoc}dp_{T,trig}}}{\frac{d\sigma}{dp_{T,trig}}} \tag{7.2}$$

where the correlations are measured in a trigger p_T range between $p_{T,trig}^{Low}$ and $p_{T,trig}^{High}$. What is actually measured is the ratio of the integrals.

$$\frac{1}{N_{trig}}\frac{dN}{dp_{T,assoc}} = \frac{\int_{p_{T,trig}^{Low}}^{p_{T,trig}^{High}} \frac{d^2\sigma}{dp_{T,assoc}dp_{T,trig}}}{\int_{p_{T,trig}^{Low}}^{p_{T,trig}^{High}} \frac{d\sigma}{dp_{T,trig}}} \tag{7.3}$$

Using Eqn. 7.3 the ratio of the conditional yields of central collisions(0-20%) to peripheral collisions (60-80%) is compared to the d+Au results from PHENIX in Fig. 7.4. The model is

now consistent with the data.

7.2.4 Far-side Yields
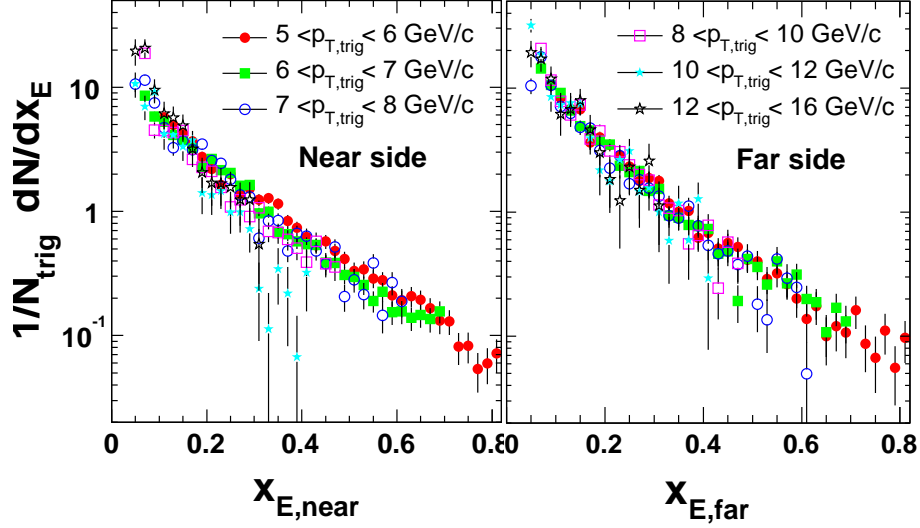
Figure 7.5 Jet x_E distributions from $\pi^\pm$ triggers for several different trigger ranges in minimum bias d+Au collisions.

A comparison of the far-side yields completes the study of jet properties in d+Au collisions. These yields are best studied as x_E distributions. The far-side x_E distributions are related to the product of the trigger and associated particle fragmentation functions (Eqn. 4.40). It may be possible that the effective fragmentation function changes in d+Au since additional soft gluon radiation could lead to a softening of the measured fragmentation function.

Hadron x_E distributions have been constructed in both p+p and d+Au for several $p_{T,trig}$ bins. These distributions using $\pi^\pm$ triggers in d+Au collisions are shown in Fig. 7.5. To check the scaling of these distributions, the data is replotted as a function of $p_{T,trig}$ for several different x_E ranges. These distributions from p+p and d+Au collisions are shown in Fig. 7.6. The scaling is measured by a linear fit as a function of p_T for each x_E range. That is, the distribution is assumed to have the form

$$\frac{1}{N_{trig}}\frac{dN}{dx_E} = \frac{1}{N_{trig}}\frac{dN}{dx_E}_0 \left(1 + \beta p_T\right) \tag{7.4}$$

where $\frac{1}{N_{trig}}\frac{dN}{dx_E}{}_0$ is the overall level of the x_E distribution and β represents the fractional change in the distribution as a function of trigger p_T. These fitted values are shown in Fig. 7.7. Point to point there are no systematic differences between the p+p and d+Au. Therefore, there are no measurable differences in the x_E distributions in d+Au compared to p+p.
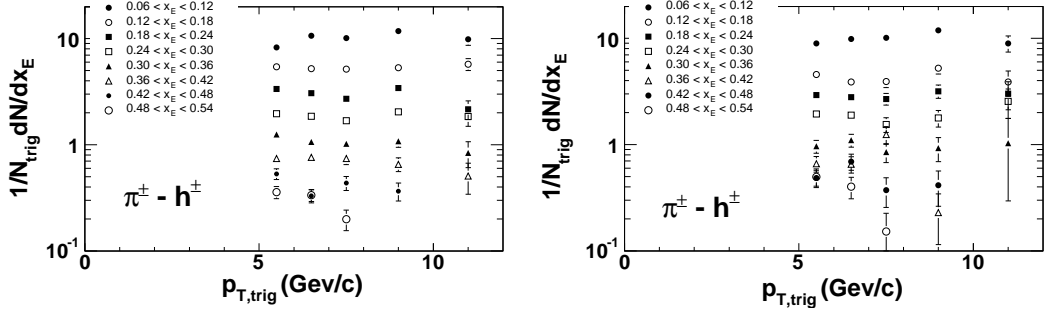
Figure 7.6   Jet x_E distributions as a function of $p_{T,trig}$ for different x_E ranges in minimum bias d+Au (left) and p+p (right).
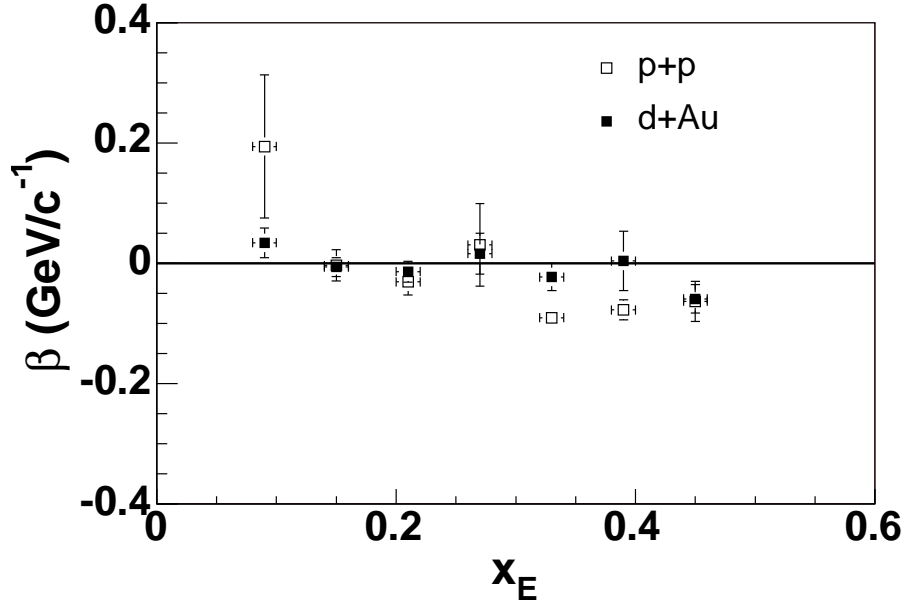
Figure 7.7   The fractional change of the x_E distribution per unit trigger p_T (see Eqn. 7.4) as a function of x_E for p+p (open) and d+Au (closed) collisions.

7.2.5 Summary of Cold Nuclear Medium Modification

Several observables have been measured in order to fully quantify any differences between jet properties in p+p and d+Au collisions. The extracted $\sqrt{\left\langle j_{Ty}^2 \right\rangle}$ shows no statistically significant difference between p+p and d+Au. This implies that the fragmentation process is not affected by the medium.

The di-jet acoplanarity difference between p+p and d+Au is not statistically significant. The difference in $\left\langle \sin^2 \phi_{jj} \right\rangle$ is zero within the statistical errors. Both a multiple scattering model from Qiu and Vitev [2003] and a recombination model from Hwa and Yang [2004b] predicted no increase in the di-jet acoplanarity. The data is not inconsistent with either prediction. The lack of difference seen in the acoplanarity and the observation that the measured p+p spectrum is well described by NLO pQCD seem to indicated that the k_T measured by these correlations are dominated by hard gluon radiation in the initial and final state. This hard radiation seems to dominate any k_T increase due to soft multiple scattering. The observation of a dramatic increase in k_T at lower $\sqrt{s_{NN}}$ may be due to the $\sqrt{s_{NN}}$ dependence of the gluon radiation. That is, at lower $\sqrt{s_{NN}}$ the gluon radiation may not dominate the multiple scattering.

The near-side jet yields show little centrality dependence. The data is not inconsistent with an increase in the yield predicted by the recombination model [Hwa and Tan, 2005]. The far-side jet yields as a function of x_E also show no significant difference between p+p and d+Au collisions. These distributions are independent of $p_{T,trig}$ in both cases. The scaling of the two distributions are similar as well.

Taken together, these data build a strong case that jet properties in d+Au collisions are very similar to p+p collisions. These data are consistent with both the multiple scattering models and a recombination model. At the current level of statistics, the data cannot distinguish between these models because nearly all of the predictions are similar between them. However, a robust result is that either p+p or d+Au can be reliably used as a baseline for Au+Au collisions at RHIC since no large cold nuclear medium effects are indicated by the data.
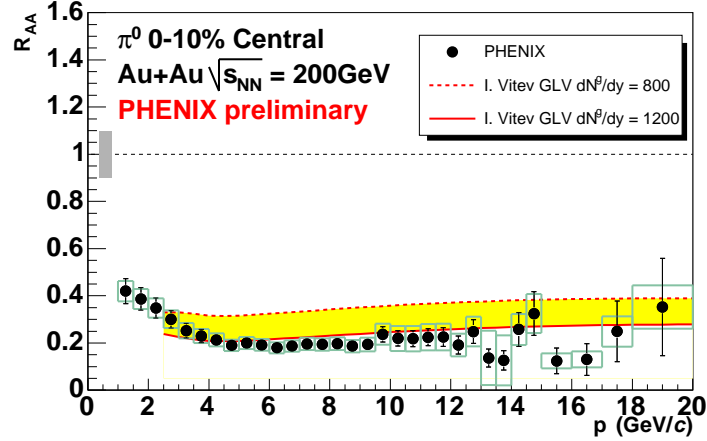
Figure 7.8   Nuclear modification factor for π^0 production in 0-10% central
Au+Au compared with binary-scaled p+p collisions [Shimo-
mura, 2005]. The data is compared with the energy loss model
from Gyulassy-Levai-Vitev (GLV) [Gyulassy et al., 2000].

7.3   Hot, Dense Nuclear Medium Jet Modification

Before the most recent Au+Au run at RHIC in 2004, several observables indicated that a
strong energy loss mechanism is present in central Au+Au collisions. The initial observation of
strong suppression of high-p_T single particles was discovered at $\sqrt{s_{NN}} = 130$ GeV data [Adcox
et al., 2002] and extended to higher p_T in the $\sqrt{s_{NN}} = 200$ GeV Au+Au collisions [Adler
et al., 2003b]. This measurement on π^0 production has been further extended to 20 GeV/c
in the most recent Au+Au run [Shimomura, 2005]. The nuclear modification factor is plotted
in Fig. 7.8 with a comparison to the prediction from the Gyulassy-Levai-Vitev (GLV) model
of energy loss [Gyulassy et al., 2000]. The agreement is reasonable although the data may
indicate a slightly higher gluon density than what is plotted. The strong suppression persists
in the data out to 10-20 GeV/c. This range corresponds to the highest p_T triggers that are
used in this analysis.

The other observable previously measured is the suppression of the away-side jet associated
yield in central Au+Au collisions. This suppression is shown in Fig. 7.9 from the STAR
experiment [Adler et al., 2003a] for two different trigger ranges. The associated particle ranges
from 2 GeV/c to the trigger p_T. In the away-side, a clear suppression is observed in the data
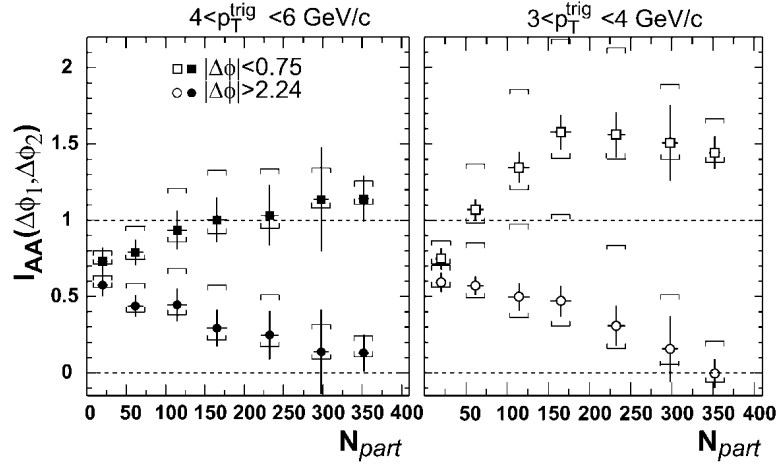
Figure 7.9   Conditional yield in Au+Au compared to p+p collisions as a function of Au+Au centrality for two different trigger ranges [Adler et al., 2003*a*].

for both trigger p_T ranges.

The crucial piece that is missing from these data is the widths of the away-side distribution. This is mostly to the suppression of the distribution to the point of not having a clear away-side distribution above the measured background.

7.3.1   Broadening of the Di-jet Distribution

Because of the factor of ten increase in statistics in the 2004 Au+Au run, both the statistical precision of the correlation functions and the p_T reach have increased. The former makes it more possible to disentangle the elliptic flow from the away-side jet. The latter increases the signal-to-background of the jet pairs in the whole correlations, which also aids in disentangling the flow from the jets. A clear away-side shape is present in the data and the RMS of the away-side distribution has been extracted. Fig. 7.10 shows a compilation of results from STAR [Magestro, 2005] and this thesis on the shape of the away-side distribution. The upper left panel is data from p+p, d+Au, and Au+Au from this thesis for two different trigger ranges: 5-7 GeV/c (closed points) and 7-10 GeV/c (open points). The associated hadrons range from 2.5-5 GeV/c in the p+p and d+Au data and from 3-5 GeV/c for the Au+Au data. The peripheral Au+Au data is consistent with p+p and d+Au. At higher centrality, no systematic

broadening is seen in the data. The STAR data on conditional yields in the upper right panel is for a fixed hadron trigger p_T of 8-15 GeV/c. The associated hadron varies from the top of the plot to the bottom of the plot. The centrality varies left to right. All of the distributions seem to indicate the width is independent of centrality to a high degree of statistical accuracy. The PHENIX data is consistent with this conclusion, but with less statistical accuracy.
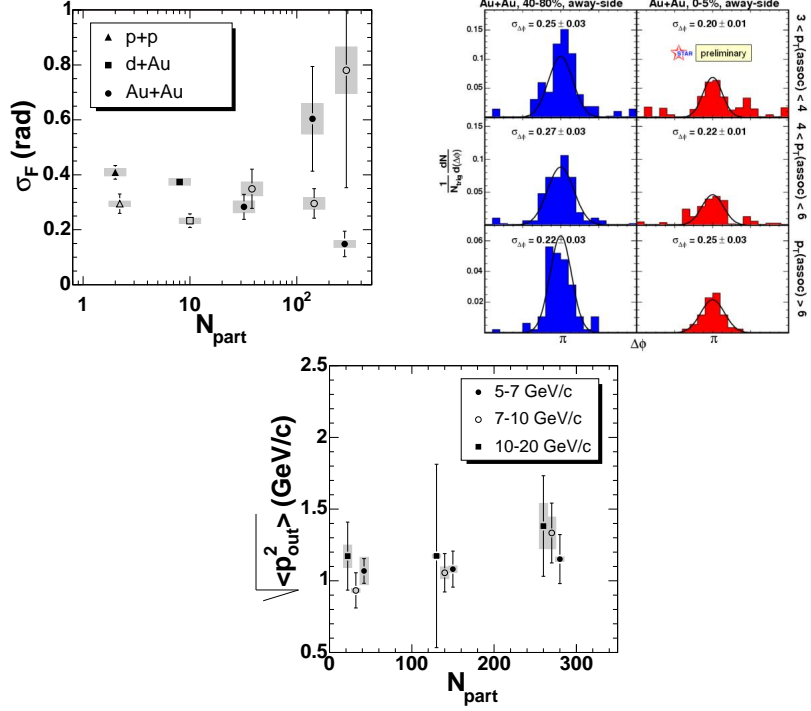
Figure 7.10   *Upper Left:* Far-angle widths as a function of N_{part} for p+p, d+Au, and Au+Au collisions. The p+p and d+Au data are for 5-6 GeV/c (closed) and 7-10 GeV/c (open) triggers and 2.5-5 GeV/c associated hadrons. The Au+Au data are for 5-7 GeV/c triggers (closed) and 7-10 GeV/c triggers (open) with 3-5 GeV/c associated hadrons. *Upper Right:* Away-side conditional yield distributions for 8-15 GeV/c hadron triggers with different associated p_T ranges for peripheral (left) and central (right) Au+Au collisions from STAR [Magestro, 2005]. *Lower:* Fitted Gaussian RMS of the p_{out} distributions as a function of centrality. Each symbol represents a different trigger π^0 range.

To maximize the available statistics p_{out} distributions are measured. The fitted Gaussian RMS of the p_{out} distributions are shown in the bottom panel of Fig. 7.10. The data are

not inconsistent with being independent of centrality. An increase of approximately 30% in $\sqrt{\langle p_{out}^2 \rangle}$ in the central collisions compared to the peripheral collisions is also not excluded by this data. A direct comparison between the values in Au+Au collisions to those in p+p and d+Au collisions is not yet possible since the p_T ranges used in the p+p and d+Au analysis were lower than those in this analysis. As such the distributions are necessarily narrower.
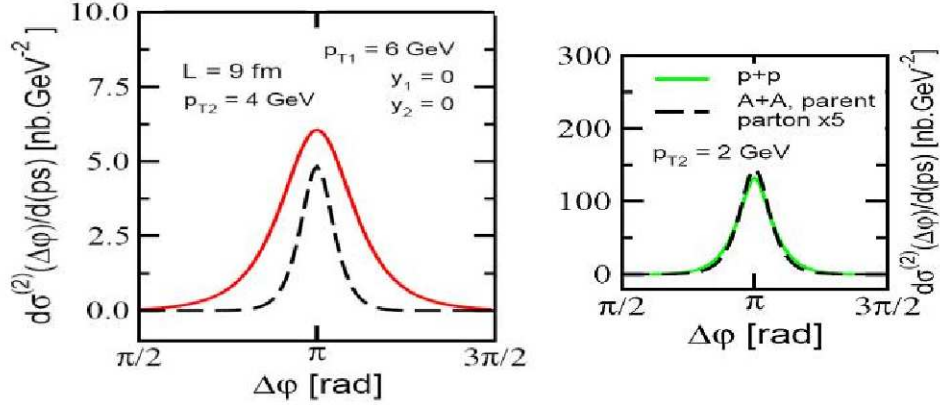
Figure 7.11   Prediction from Vitev [2005] of the expected broadening from the radiative gluons (left, solid line) compared to the attenuated parent parton (left, dashed line). The attenuated parent parton has a distribution similar to p+p (right).

The lack of large broadening in σ_F and $\sqrt{\langle p_{out}^2 \rangle}$ are in contrast to the prediction that the gluons from radiative energy loss broaden the away-side distribution [Vitev, 2005]. This prediction is shown in Fig. 7.11 for a fixed length calculation where the trigger is 6 GeV/c and the associated particle is 4 GeV/c which corresponds approximately to the trigger-associated bin in the left panel of Fig. 7.10. The solid line represents the distribution of radiated gluons from energy loss of a parton. The parent parton distribution is shown as the dashed line. This parent parton distribution is consistent with p+p collisions as shown in the right panel. Such a strong broadening of a factor of 2-3 is not seen in the data. It is possible that a fixed length calculation is not useful for comparison to correlation results. The lengths that partons traverse in medium can have a very wide distribution. In 0-10% central Au+Au collisions the average path length is closer to 4 fm and not 9 fm [Dainese et al., 2005].

7.3.2 Yield Suppression in Hot, Dense Nuclear Matter
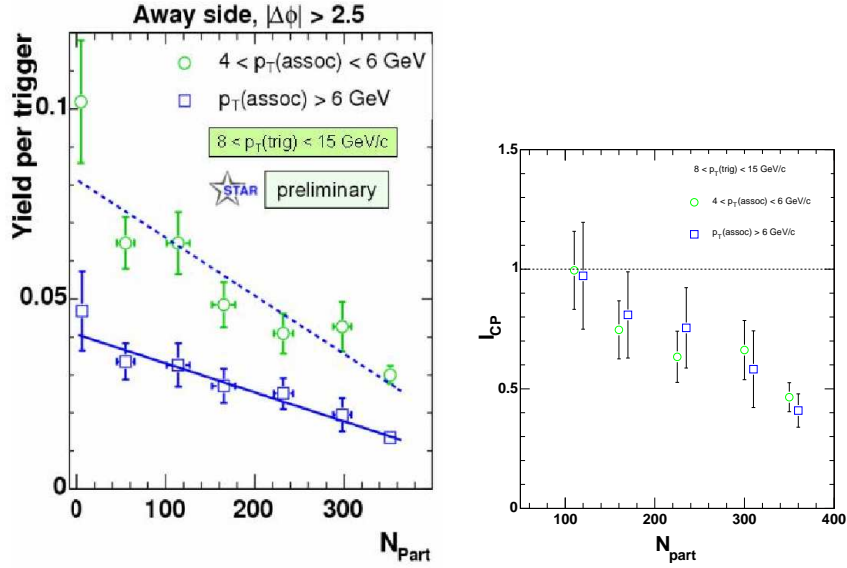
Figure 7.12   *Left:*Far-side conditional yields as a function of centrality. The solid line is a fit to the associated p_T above 6 GeV/c. The dashed line is the fit scaled by a factor of two. *Right:* I_{cp} as a function of centrality for this data.

What is apparent in the STAR data in Fig. 7.10 is that for a given $p_{T,assoc}$ range, the conditional yield is suppressed from peripheral to central collisions. The suppression can be seen by plotting the away-side conditional yield as a function of centrality and is shown in Fig. 7.12. From d+Au to the most central data the yield decreases by nearly a factor of 5. This is quantitatively similar to R_{AA}.

The data can be replotted as I_{cp} to compare with the data in this thesis. This is shown in the right panel of Fig. 7.12. At the most central collisions, the yield drops by a factor of 2 compared to the most peripheral collisions. This is quantitatively similar to the suppression that is seen in the measured hadron x_E distributions in Fig. 7.13. The x_E distributions have an average I_{cp} values of 0.66±0.11±0.16 for 5-7 GeV/c triggers, 0.43±0.11±0.06 for 7-10 GeV/c triggers, and 0.50±0.19±0.07 for 10-20 GeV/c triggers. The data indicate that the yield of the away-side is suppressed.
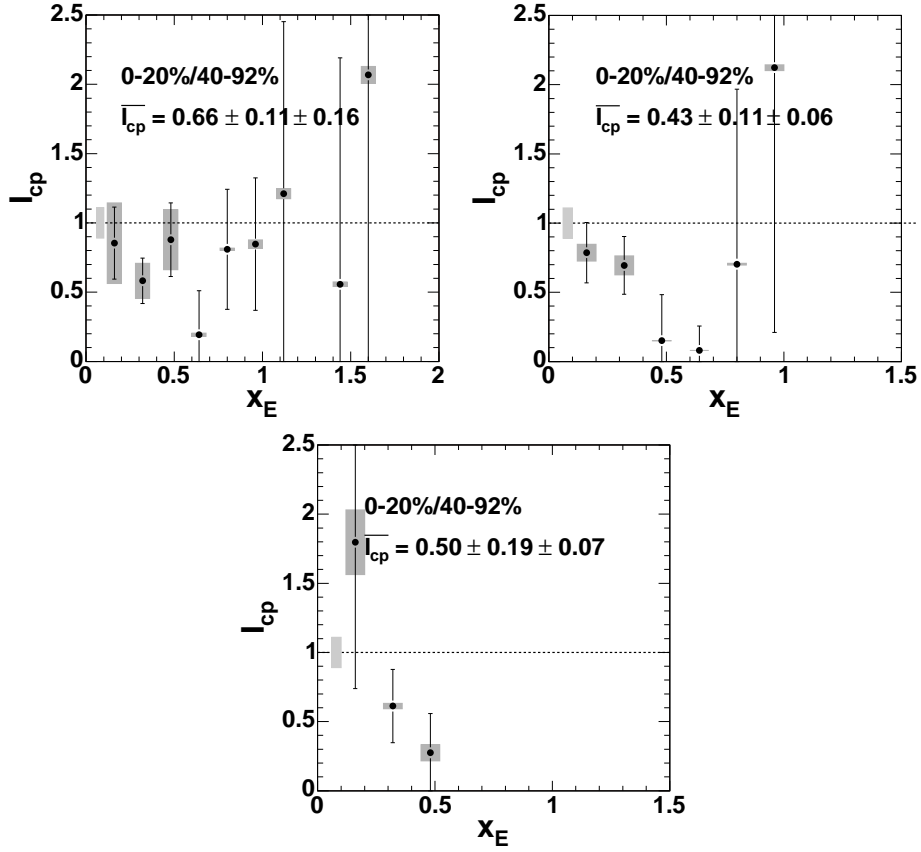
Figure 7.13   Ratio of jet x_E distributions in 0-20% central collisions compared to 40-92% peripheral collisions for 5-7 GeV/c π^0 triggers (upper left), 7-10 GeV/c triggers (upper right), and 10-20 GeV/c triggers (lower). The average value of I_{cp} is given.

7.3.3   Length Dependence of Energy Loss and v_2 at High-p_T

Radiative gluon energy loss is sensitive to the parton's path length in medium and the predicted energy loss is $\Delta E \propto L^2$. One consequence of this is that the energy loss is less for particles in-plane, along the reaction plane, than out-of-plane, perpendicular to the reaction plane. The STAR collaboration has measured correlations by requiring that the trigger have some specified orientation to the reaction plane, *i.e.* in-plane and out-of-plane [Adams et al., 2004b]. These are shown in Fig. 7.14. For the correlations out-of-plane (circles) the away-side correlation is almost completely suppressed. When the trigger is in-plane (squares) the away-side survives but is still slightly suppressed. This is the first indication that the energy loss is
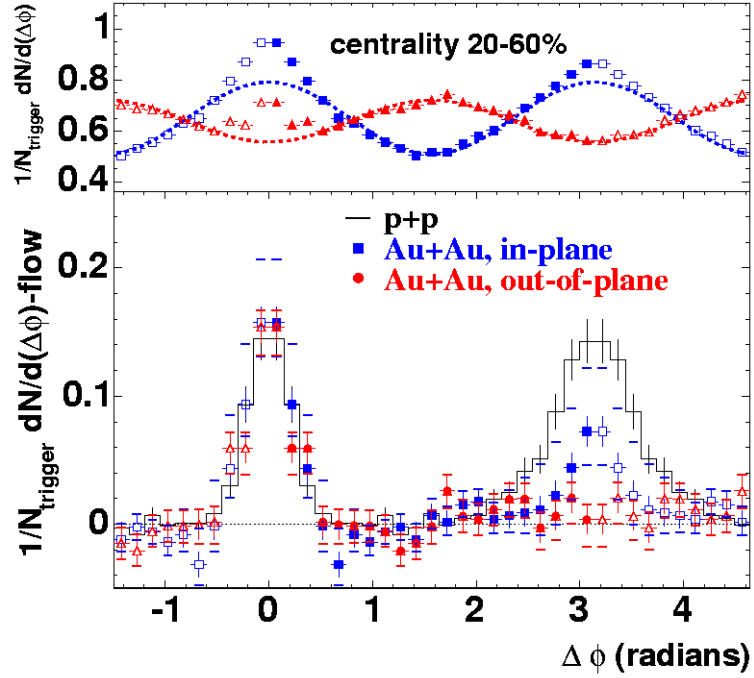
Figure 7.14   Correlation functions in 20-60% Au+Au in two different re-
action plane bins compared to p+p correlations. Squares are
correlations where the trigger particle is required to be within
0-45° of the measured reaction plane (in-plane). Circles are
correlations where the trigger is between 45-90° from the re-
action plane (out-of-plane).

dependent on the path length.

A further consequence of the path-length dependence of energy loss is the prediction that
the resulting differential energy loss with respect to the reaction plane will be observable as
a component of v_2 at high-p_T [Gyulassy, Vitev and Wang, 2001]. Fig. 7.15 is the prediction
of high-p_T v_2 based on the Gyulassy-Levai-Vitev (GLV) energy loss model. The prediction
was a slow decrease at high p_T. Measurements of high-p_T v_2 first indicated a large plateau
at intermediate p_T between 2-6 GeV/c. With the most recent statistics of the 2004 Au+Au
run, the data [Winter, 2005] indicate that the v_2 finally decreases near 6-7 GeV/c to a level
consistent with energy loss models [Dainese et al., 2005; Arnold et al., 2003]. One reason for
a large v_2 at intermediate p_T (2-6 GeV/c) is due to recombination. The resulting meson v_2
$\approx 2v_{2,quark}$ and baryon $v_2 \approx 3v_{2,quark}$ [Fries et al., 2003].
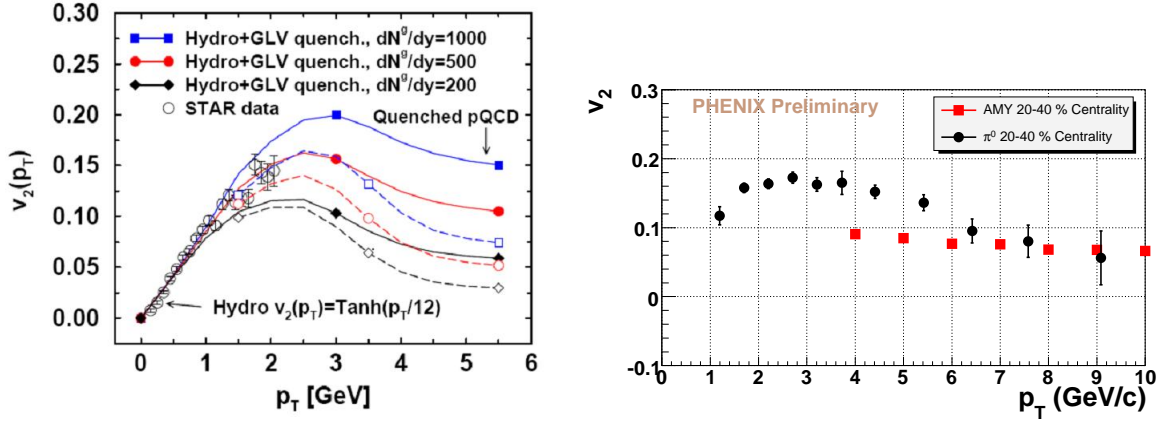
Figure 7.15   *Left:* Predicted shape of v_2 based on hydrodynamical flow at low p_T (< 2 GeV/c) and GLV energy loss at high-p_T [Gyulassy, Vitev and Wang, 2001]. *Right:* Measured π^0 v_2 in 20-40% Au+Au collisions at high-p_T [Winter, 2005]. The boxes are a prediction from an energy loss calculation [Arnold et al., 2003].

Since the v_2 at high-p_T should at least in part be the result of the differential energy loss with respect to the reaction plane, calculations have been made which attempt to reproduce R_{AA}, I_{AA}, and v_2 simultaneously. Fig. 7.16 is one such example. As seen in the figure, when R_{AA} and I_{AA} (in the figure this is labelled D_{AA}) are reproduced, the v_2 is largely underpredicted. The data that the model is comparing to is π^0 data at 4.5 GeV/c from PHENIX and hadrons at 6 GeV/c from STAR. At these p_T recombination effects are predicted to be small since the the h-to-π ratio in Au+Au decreases to the value it has in p+p collisions. Therefore, there must be another mechanism that increases v_2.

The data from this thesis and from STAR will further constrain these models. Not only must the models reproduce the single particle, pair suppression, and v_2, they will also reproduce the away-side distribution from the correlations widths and $\sqrt{\langle p_{out}^2 \rangle}$.

7.3.4   Summary of Modification in Hot, Dense Nuclear Matter

The picture that is emerging from high-p_T is a combination of at least four related quantities. The first is the single particle suppression. The nuclear modification factor for π^0 above 7 GeV/c for both Cu+Cu and Au+Au collisions are shown in Fig. 7.17 as a function of cen-
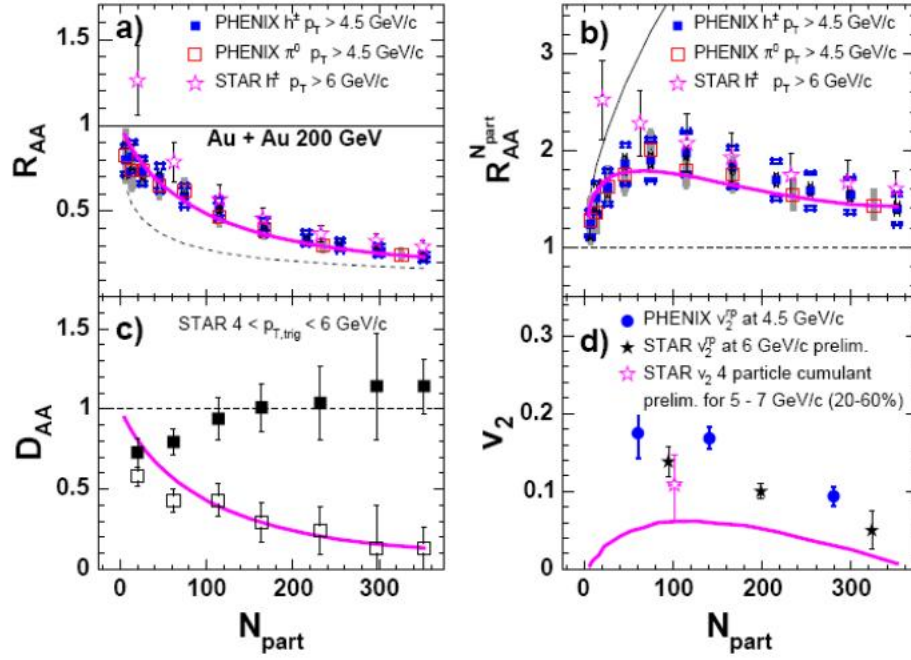
Figure 7.16   Calculation from Drees et al. [2005] of R_{AA} (upper left and
upper right), I_{AA} (here called D_{AA} in lower left) and v_2 (lower
right) all as a function of centrality. In the lower left plot all the
points are STAR data. The closed points are the near-angle
yield and the open points are the far-angle yield.

trality. A strong suppression is observed that sets in at peripheral collisions and flattens out

at more central collisions. This can be contrasted with the centrality dependence of the second

observable, I_{AA}, from the STAR data, i.e. the conditional yield compared to d+Au collisions

from Fig. 7.12. This is shown in the right panel of Fig. 7.17. A suppression is weakly present

in the most peripheral collisions but the strong suppression does not set in until the most

central collisions. These results can be compared with the centrality dependence of the third

observable, the away-side jet widths or p_{out}. There is little to no centrality dependence of the

measured far-side widths and p_{out}. The final observable, the magnitude and p_T dependence of

single particle v_2 at high-p_T, must be reconciled in this picture.

At this time there is no coherent picture of energy loss which can describe all four observ-

ables related to energy loss: single particle suppression, conditional yield suppression, little to
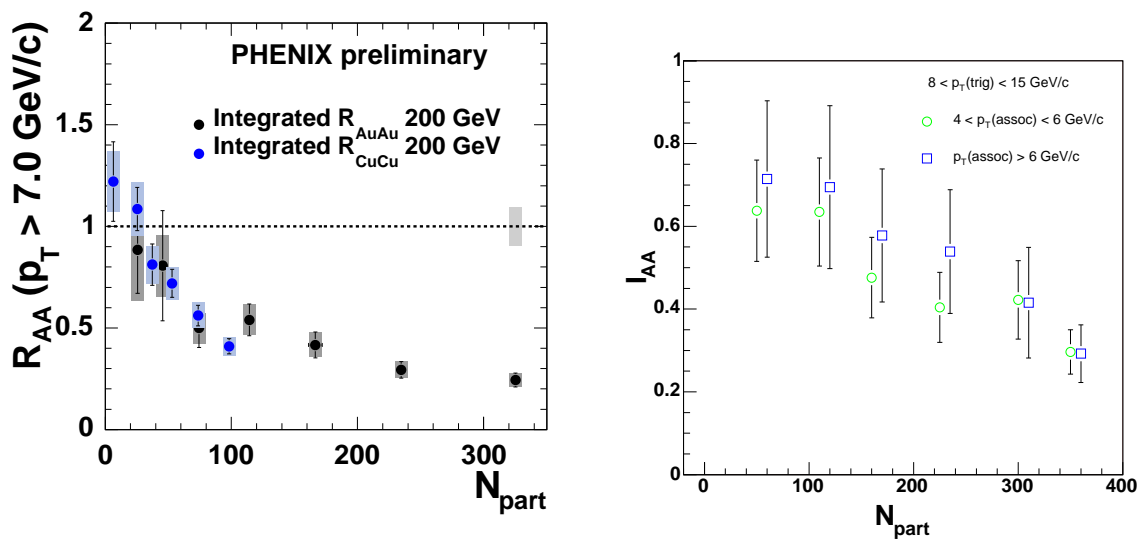
Figure 7.17   *Left:* Centrality dependence of the integrated R_{AA} of π^0 above 7 GeV/c in Au+Au and Cu+Cu collisions. *Right:* Centrality dependence of I_{AA} from Fig. 7.12 using the d+Au yield as the denominator.

no broadening of the away-side distribution, and high-p_T v_2. This serves as a challenge to both theorists and experimentalists to search for new avenues to gain insight to energy loss. These new avenues may possibly lead to insights on properties of the plasma itself.

APPENDIX A. Systematic Errors on Jet Formula

Systematic Errors on the Formulation of $\sqrt{\left\langle j_{Ty}^2 \right\rangle}$

In this appendix, the different approximations necessary to relate the gaussian RMS from the near-angle $\Delta\phi$ distribution to the RMS of j_{Ty} are outlined.

Begin from Eqn. 4.17 a succession of approximations are made.

$$
\begin{aligned}
\left\langle p_{T,assoc}^2 \sin^2(\Delta\phi) \right\rangle &= \left\langle j_{Ty}^2 \right\rangle + \left\langle x_h^2 j_{Ty}^2 \right\rangle \\
&\approx \left\langle j_{Ty}^2 \right\rangle \left(1 + \left\langle x_h^2 \right\rangle\right) \\
\left\langle j_{Ty}^2 \right\rangle &\approx \frac{\left\langle p_{T,assoc}^2 \right\rangle \left\langle \sin^2(\Delta\phi) \right\rangle}{1 + \left\langle x_h^2 \right\rangle} \\
&\approx \left\langle \sin^2(\Delta\phi) \right\rangle \frac{\left\langle p_{T,assoc}^2 \right\rangle \left\langle p_{T,trig}^2 \right\rangle}{\left\langle p_{T,assoc}^2 \right\rangle + \left\langle p_{T,trig}^2 \right\rangle} \\
&\approx \left\langle \sin^2(\Delta\phi) \right\rangle \frac{\left\langle p_{T,assoc} \right\rangle^2 \left\langle p_{T,trig} \right\rangle^2}{\left\langle p_{T,assoc} \right\rangle^2 + \left\langle p_{T,trig} \right\rangle^2} \\
&\approx \left\langle \sin(\Delta\phi^2) \right\rangle \frac{\left\langle p_{T,assoc} \right\rangle^2 \left\langle p_{T,trig} \right\rangle^2}{\left\langle p_{T,assoc} \right\rangle^2 + \left\langle p_{T,trig} \right\rangle^2} \\
&\approx \sin(\left\langle \Delta\phi^2 \right\rangle) \frac{\left\langle p_{T,assoc} \right\rangle^2 \left\langle p_{T,trig} \right\rangle^2}{\left\langle p_{T,assoc} \right\rangle^2 + \left\langle p_{T,trig} \right\rangle^2} \\
&\approx \left\langle \Delta\phi^2 \right\rangle \frac{\left\langle p_{T,assoc} \right\rangle^2 \left\langle p_{T,trig} \right\rangle^2}{\left\langle p_{T,assoc} \right\rangle^2 + \left\langle p_{T,trig} \right\rangle^2} \\
&\approx \sigma_N^2 \frac{\left\langle p_{T,assoc} \right\rangle^2 \left\langle p_{T,trig} \right\rangle^2}{\left\langle p_{T,assoc} \right\rangle^2 + \left\langle p_{T,trig} \right\rangle^2} \\
\sqrt{\left\langle j_{Ty}^2 \right\rangle} &\approx \sigma_N \frac{\left\langle p_{T,assoc} \right\rangle \left\langle p_{T,trig} \right\rangle}{\sqrt{\left\langle p_{T,assoc} \right\rangle^2 + \left\langle p_{T,trig} \right\rangle^2}}
\end{aligned}
\tag{A.1}
$$

There are many approximations that are made with the above result including taking the mean of the product as the product of the means, taking the mean-squared as the square of

the mean, and many sine manipulations. These can be evaluated with a simple Monte Carlo where the p_T is fixed before addition of the j_{Ty}, a j_{Ty} is generated according to some Gaussian distribution, these are added in quadrature to get p_{Ta}, and the angle ϕ_{aj} us evaluated. With the Monte Carlo the appropriate distributions can be filled and Eqn. 4.19 can be checked to see if it holds. For $p_{Ta} = 1.0$ GeV, there is a 3% error. For $p_{Ta} = 3$ GeV/c, the error is 0.5%. Table A.1 outlines the p_T-dependent systematic errors associated with the approximations in the formula.

p_T (GeV/c)	error for averaging	error for sin approx.	tot error
1.0	5%	3%	6%
1.5	2%	1%	2%
2.0	1%	0.5%	1%
>3.0	0.5%	0.5%	0.7%

Table A.1   Table of systematic errors due to formula approximations for the evaluation of the RMS of j_{Ty}.

Systematic Error on the formulation of $\left\langle \sin^2 \phi_{jj} \right\rangle$

It was argued in Section 4.4.2 that the correct quantity that is more approximately a gaussian distribution is the $p_{out,F}$. This is defined event-by-event as $p_{out,F} = p_{T,assoc} \sin \Delta\phi$. The far angle distribution can be written in terms of $p_{out,F}$ instead.

$$
\begin{aligned}
\frac{1}{N_{trig}} \frac{dN}{d\Delta\phi} &= \frac{1}{N_{trig}} \frac{dN}{dp_{out,F}} \frac{dp_{out,F}}{d\Delta\phi} \\
&= p_{T,assoc} \cos \Delta\phi \frac{1}{N_{trig}} \frac{dN}{dp_{out,F}} \\
&= p_{T,assoc} \cos \Delta\phi \, \exp\left(\frac{-\mathrm{p}_{\mathrm{out,F}}^2}{2 \left\langle \mathrm{p}_{\mathrm{out,F}}^2 \right\rangle} \right) \\
&= p_{T,assoc} \cos \Delta\phi \, \exp\left(\frac{-\mathrm{p}_{\mathrm{T,assoc}} \sin \Delta\phi}{2 \left\langle \mathrm{p}_{\mathrm{out,F}}^2 \right\rangle} \right) \quad\quad \text{(A.2)}
\end{aligned}
$$

The comparison of this form with the other forms is shown in Fig. A.1. The form used in this analysis is the Taylor expansion (see Eqn. 4.32). This is good to 2% for away-side widths less

that 0.4 rad, which is true for all of the π^0-h correlations in this analysis. Therefore, it is taken as the systematic error.
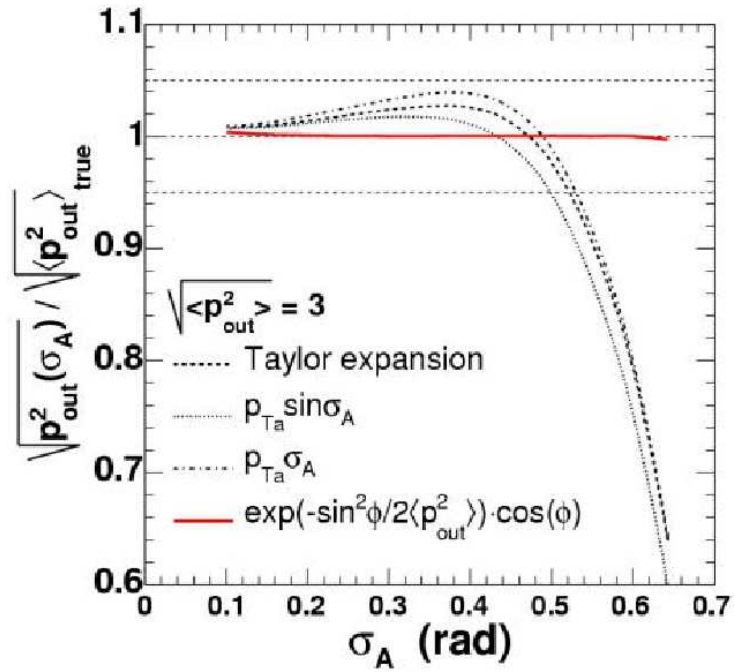
Figure A.1   Monte Carlo [Rak and Tannenbaum, 2005] comparison of the $p_{out,F}$ RMS for different assumptions of the relationship to the measured away-side width. The one used in this analysis is the Taylor expansion, the dashed line.

APPENDIX B. π^0 Reconstruction

This appendix contains all the $\gamma\gamma$ invariant mass distributions.

π^0 in d+Au Collisions
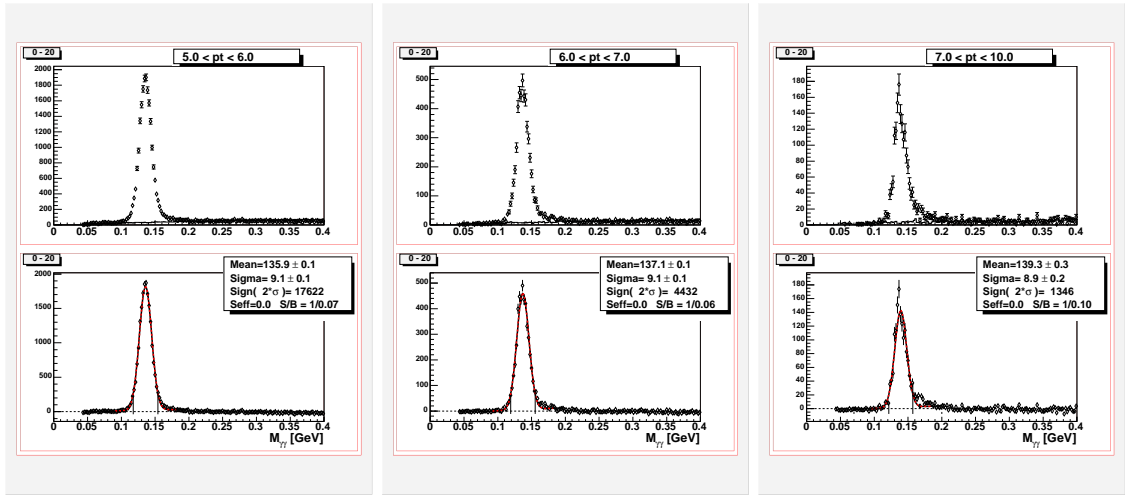
Figure B.1 Di-photon M_{inv} distributions for different pair p_T for 0-20% central d+Au collisions. Upper plots are the signal and the normalized mixed event background. The lower plots are the background subtracted distribution. The peak is fitted with a Gaussian and a first order polynomial.
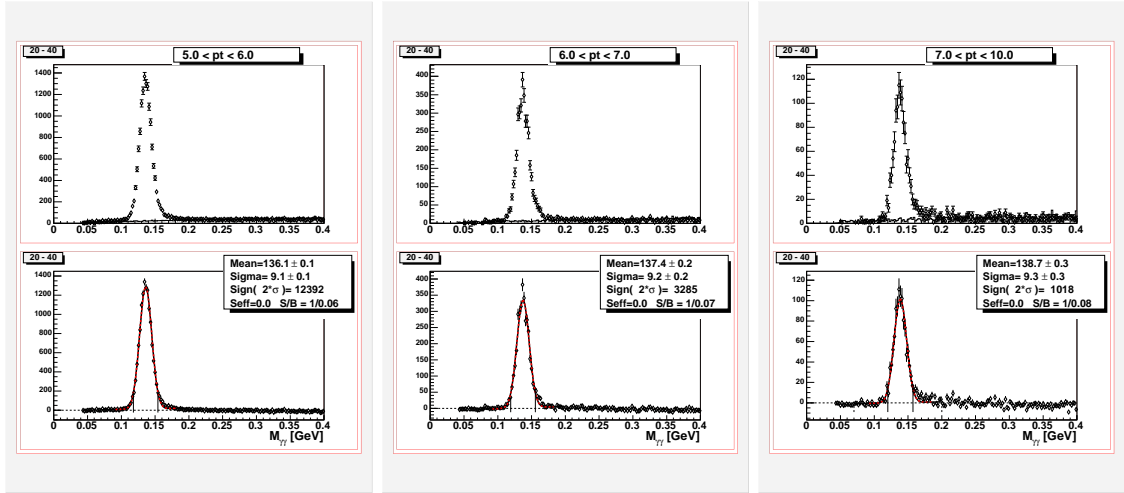
Figure B.2 Di-photon M_{inv} distributions for different pair p_T for 20-40% central d+Au collisions. Upper plots are the signal and the normalized mixed event background. The lower plots are the background subtracted distribution. The peak is fitted with a Gaussian and a first order polynomial.
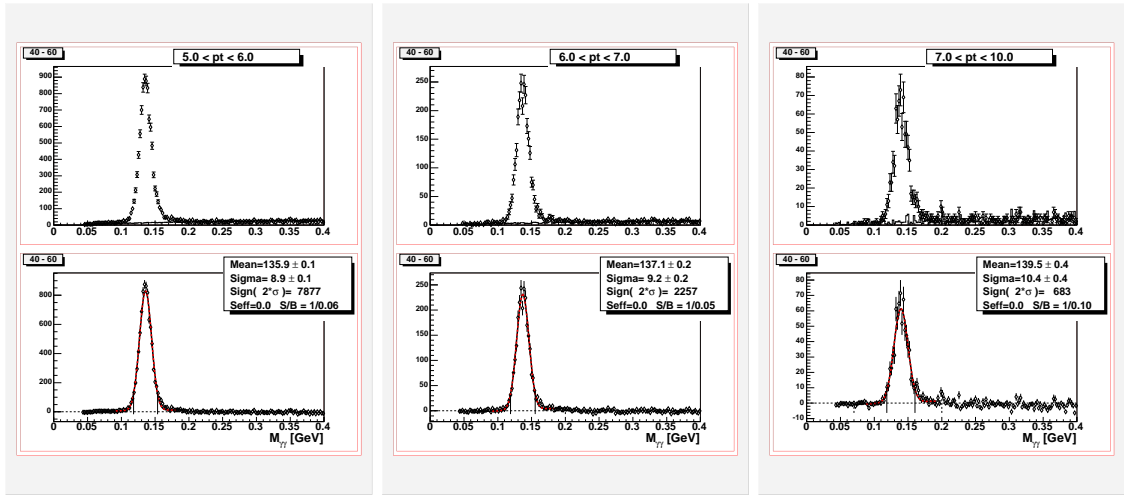
Figure B.3 Di-photon M_{inv} distributions for different pair p_T for 40-60% central d+Au collisions. Upper plots are the signal and the normalized mixed event background. The lower plots are the background subtracted distribution. The peak is fitted with a Gaussian and a first order polynomial.
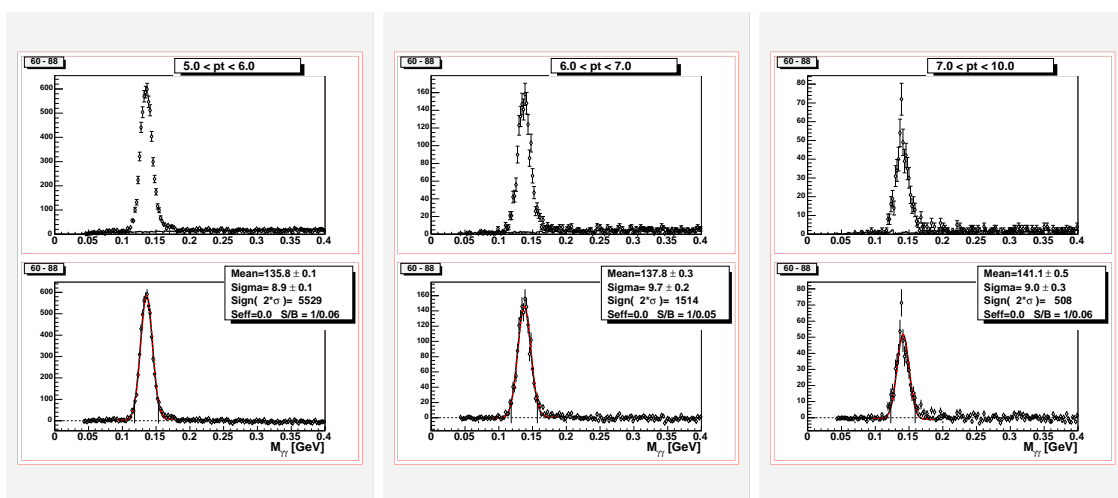
Figure B.4 Di-photon M_{inv} distributions for different pair p_T for 60-88% central d+Au collisions. Upper plots are the signal and the normalized mixed event background. The lower plots are the background subtracted distribution. The peak is fitted with a Gaussian and a first order polynomial.

π^0 **in Au+Au Collisions**
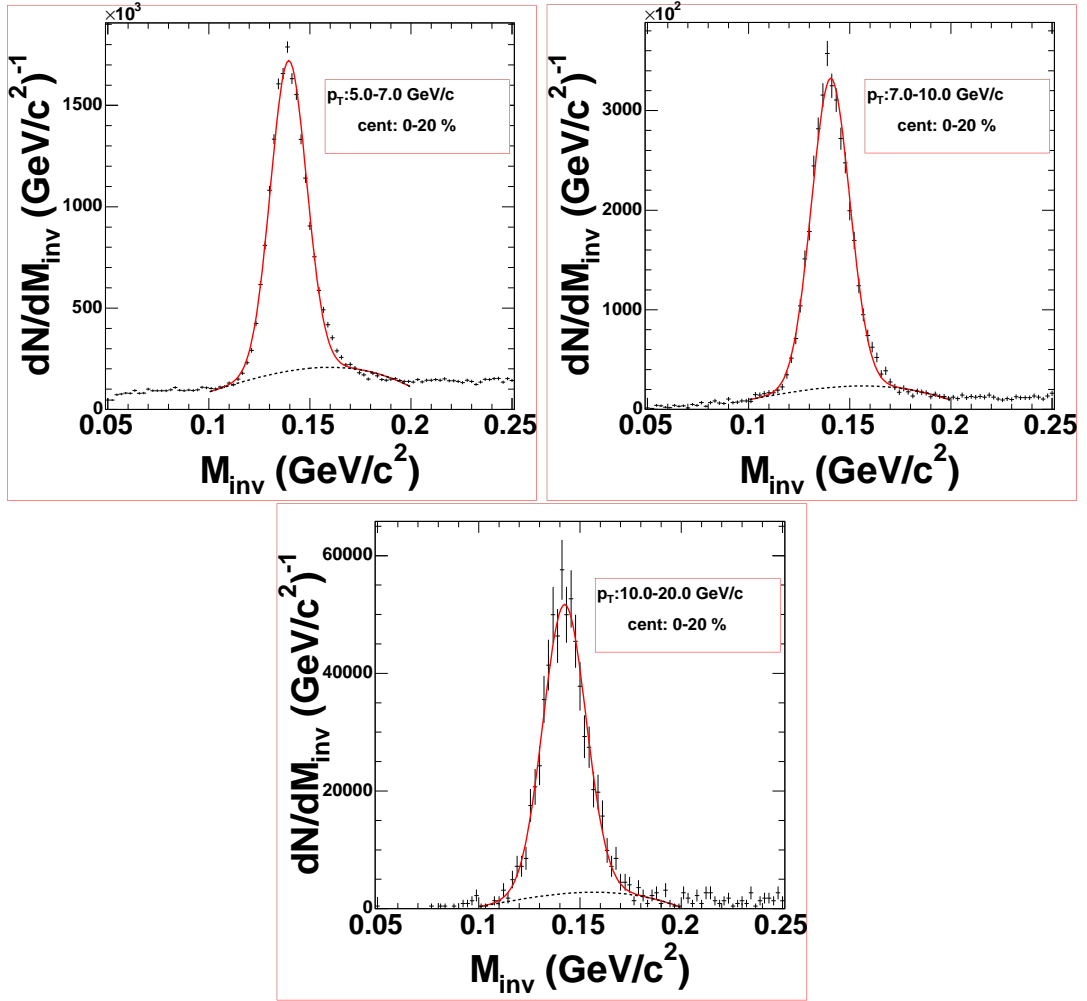
Figure B.5   Di-photon M_{inv} distributions for different pair p_T for 0-20% central Au+Au collisions. The peak is fitted with a Gaussian and a second order polynomial to extract a mean and width and signal-to-background.
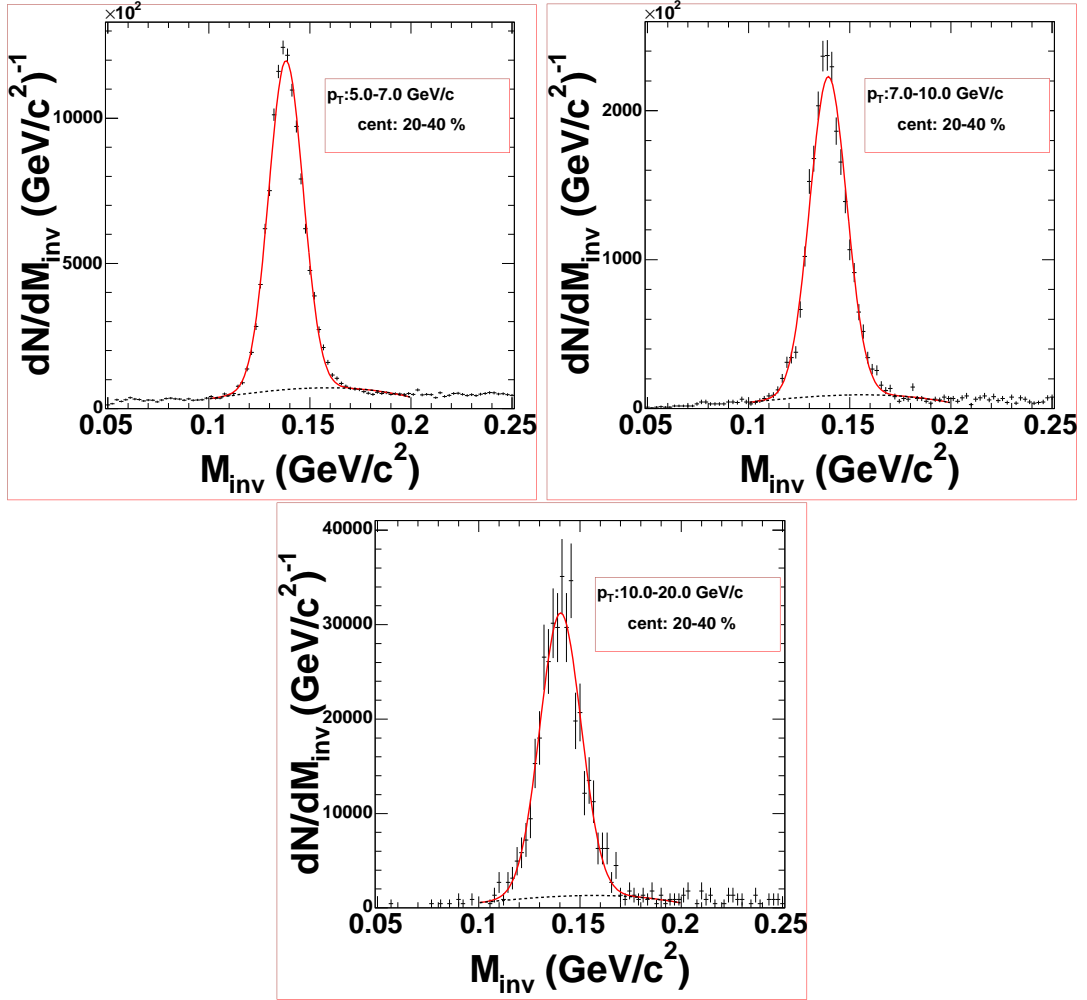
Figure B.6   Di-photon M_{inv} distributions for different pair p_T for 20-40%
central Au+Au collisions. The peak is fitted with a Gaussian
and a second order polynomial to extract a mean and width
and signal-to-background.
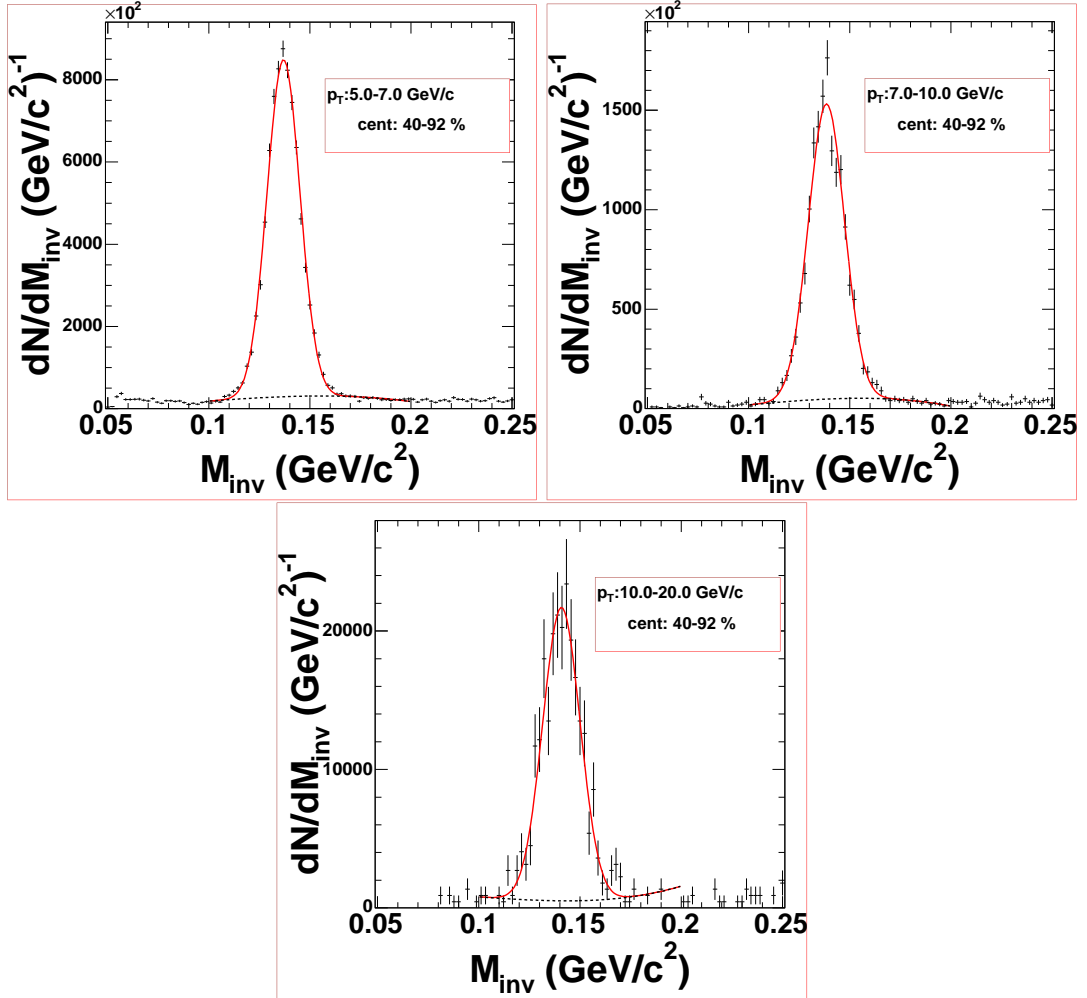
Figure B.7 Di-photon M_{inv} distributions for different pair p_T for 40-92% central Au+Au collisions. The peak is fitted with a Gaussian and a second order polynomial to extract a mean and width and signal-to-background.

APPENDIX C. π^0-h Correlations in p+p and d+Au Collisions

This appendix contains the correlation functions and the x_E histograms for π^0-h correlations in p+p and d+Au collisions. Tables of fitted widths and yields as well as other extracted quantities are given as well.

Constant Trigger π^0 p_T Correlations

The following correlations are for π^0 triggers in a constant range from 5-10 GeV/c. The associated charged hadrons are varied from 1-1.5-2-3-4-5 GeV/c.
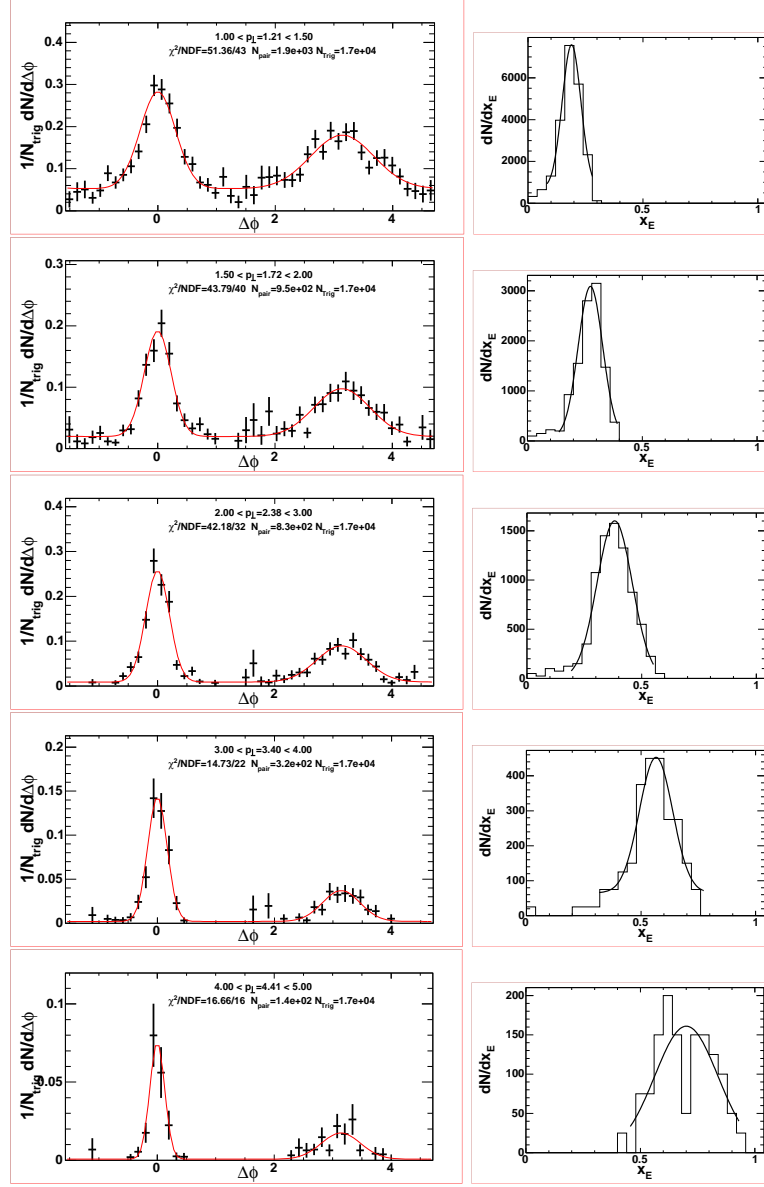
Figure C.1   The left panels are two particle azimuthal correlations in p+p
collisions with a trigger π^0 from 5-10 GeV/c with varied as-
sociated hadron p_T ranges from top to bottom: 1-1.5 GeV/c,
1.5-2.0 GeV/c, 2.0-3.0 GeV/c, 3.0-4.0 GeV/c, 4.0-5.0 GeV/c.
The right panels are the corresponding x_E distribution for the
given trigger and associated range. Fit results and extracted
values are tabulated in Table C.1 and Table C.2.
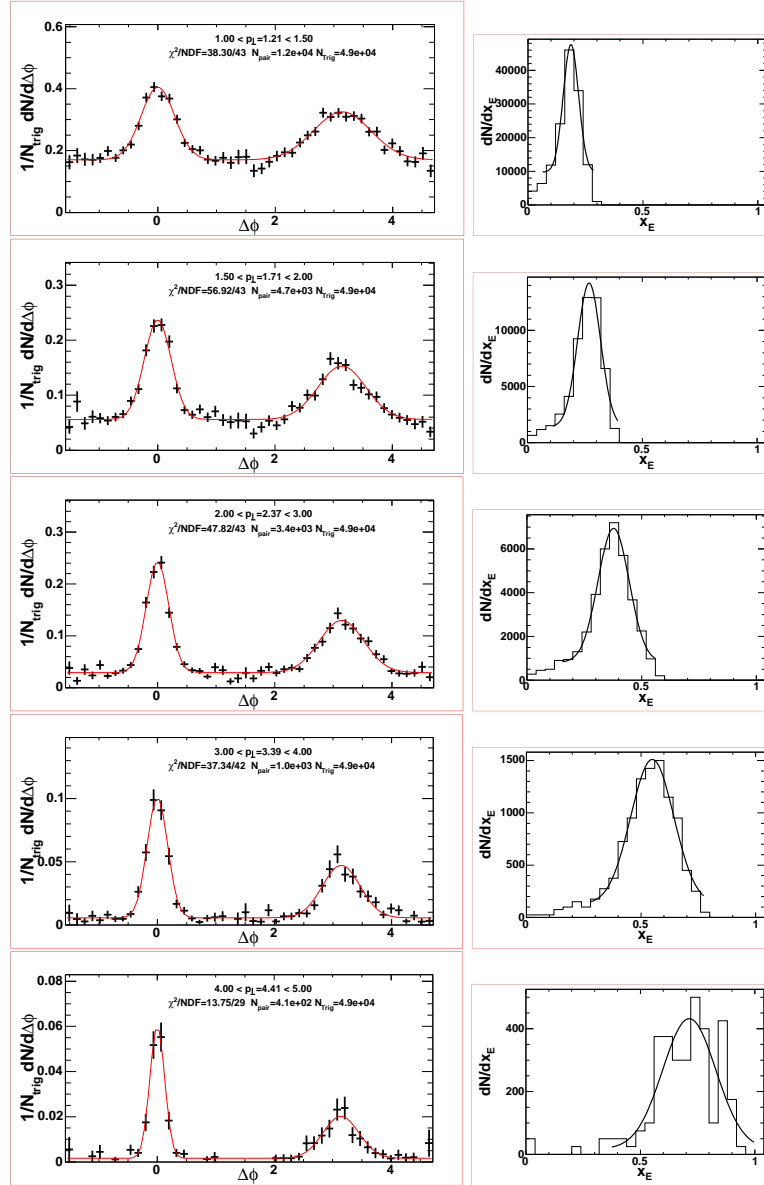
Figure C.2   The left panels are two particle azimuthal correlations in centrality integrated (0-88%) d+Au collisions with a trigger π^0 from 5-10 GeV/c with varied associated hadron p_T ranges from top to bottom: 1-1.5 GeV/c, 1.5-2.0 GeV/c, 2.0-3.0 GeV/c, 3.0-4.0 GeV/c, 4.0-5.0 GeV/c. The right panels are the corresponding x_E distribution for the given trigger and associated range. Fit results and extracted values are tabulated in Table C.3 and Table C.4.
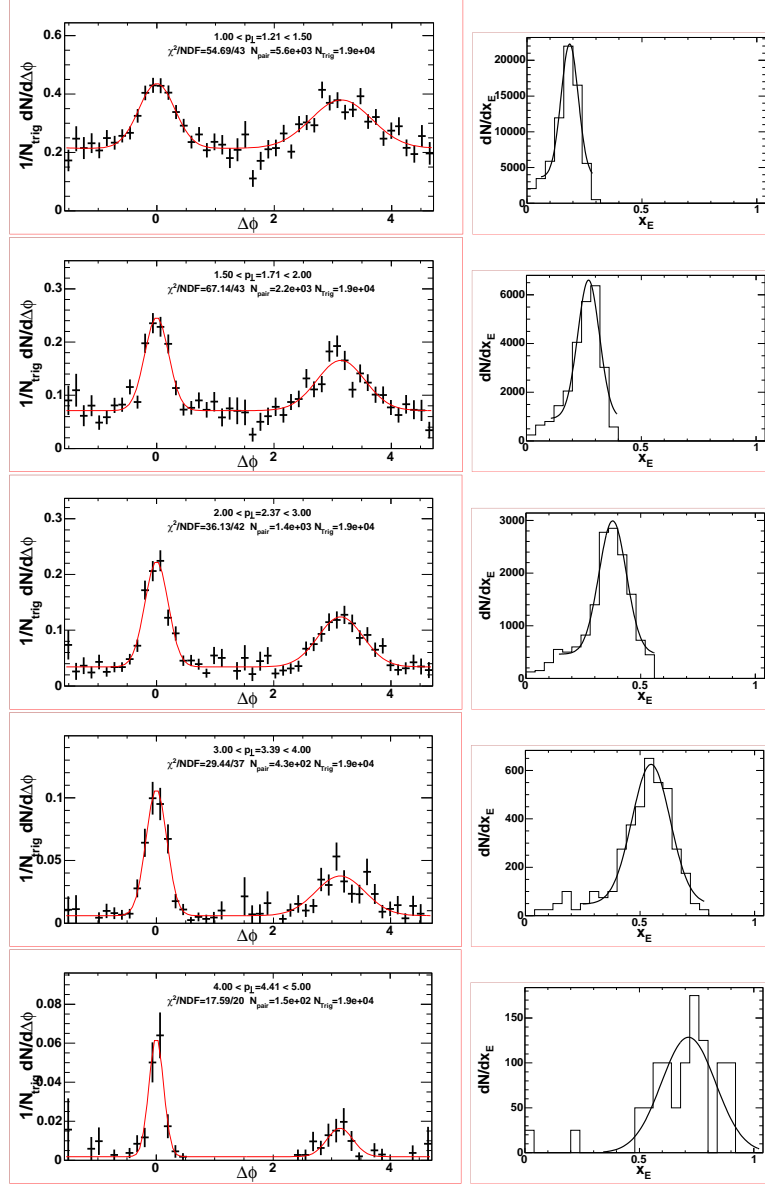
Figure C.3   The left panels are two particle azimuthal correlations in 0-20% central d+Au collisions with a trigger π^0 from 5-10 GeV/c with varied associated hadron p_T ranges from top to bottom: 1-1.5 GeV/c, 1.5-2.0 GeV/c, 2.0-3.0 GeV/c, 3.0-4.0 GeV/c, 4.0-5.0 GeV/c. The right panels are the corresponding x_E distribution for the given trigger and associated range. Fit results and extracted values are tabulated in Table C.5 and Table C.6.
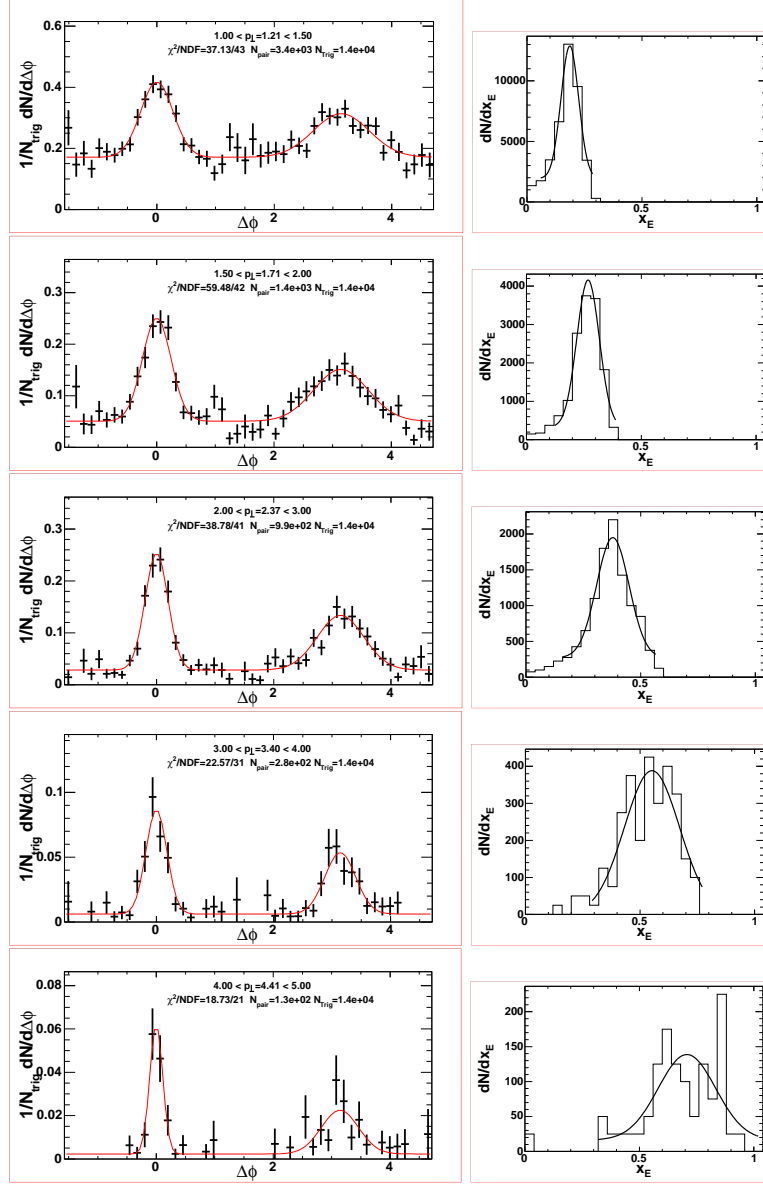
Figure C.4   The left panels are two particle azimuthal correlations in 20-40% central d+Au collisions with a trigger π^0 from 5-10 GeV/c with varied associated hadron p_T ranges from top to bottom: 1-1.5 GeV/c, 1.5-2.0 GeV/c, 2.0-3.0 GeV/c, 3.0-4.0 GeV/c, 4.0-5.0 GeV/c. The right panels are the corresponding x_E distribution for the given trigger and associated range. Fit results and extracted values are tabulated in Table C.7 and Table C.8.
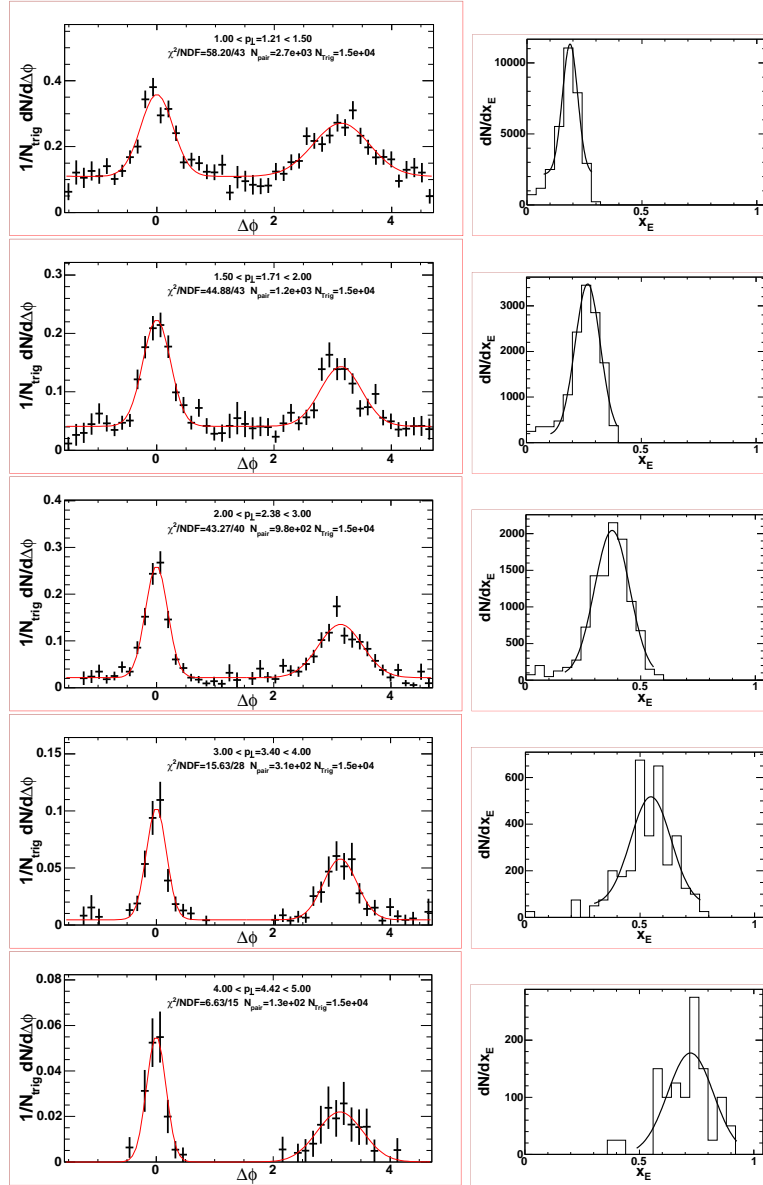
Figure C.5   The left panels are two particle azimuthal correlations in 40-88% central d+Au collisions with a trigger π^0 from 5-10 GeV/c with varied associated hadron p_T ranges from top to bottom: 1-1.5 GeV/c, 1.5-2.0 GeV/c, 2.0-3.0 GeV/c, 3.0-4.0 GeV/c, 4.0-5.0 GeV/c. The right panels are the corresponding x_E distribution for the given trigger and associated range. Fit results and extracted values are tabulated in Table C.9 and Table C.10.

$p_{T,assoc}$	$\sigma_N(rad)$	$\sigma_F(rad)$	$\sqrt{\langle j_{Ty}^2 \rangle}$	$\langle \sin^2 \phi_{jj} \rangle$
1.209	0.299 ± 0.017	0.540 ± 0.037	0.354 ± 0.020	0.169 ± 0.030
1.715	0.230 ± 0.011	0.480 ± 0.038	0.378 ± 0.018	0.150 ± 0.027
2.382	0.204 ± 0.009	0.430 ± 0.031	0.449 ± 0.020	0.125 ± 0.021
3.401	0.167 ± 0.007	0.321 ± 0.026	0.489 ± 0.020	0.070 ± 0.016
4.405	0.129 ± 0.009	0.345 ± 0.040	0.451 ± 0.031	0.092 ± 0.023

Table C.1   Near- and far-angle widths extracted from p+p $\pi^0 - h$ correlations with a constant π^0 p_T of 5-10 GeV/c. ($\langle p_{T,trig} \rangle = 5.756$ GeV/c) The errors are statistical only.

$p_{T,assoc}$	x_E	S_N	S_F
1.209	0.189 ± 0.041	0.180 ± 0.020	0.231 ± 0.019
1.715	0.274 ± 0.053	0.098 ± 0.010	0.127 ± 0.010
2.382	0.382 ± 0.077	0.112 ± 0.005	0.118 ± 0.008
3.401	0.565 ± 0.073	0.049 ± 0.003	0.037 ± 0.003
4.405	0.701 ± 0.138	0.019 ± 0.002	0.020 ± 0.002

Table C.2   Near- (S_N) and far-(S_F) yields and x_E extracted from p+p $\pi^0 - h$ correlations with a constant π^0 p_T of 5-10 GeV/c. ($\langle p_{T,trig} \rangle = 5.756$ GeV/c) Errors are statistical only.

$p_{T,assoc}$	$\sigma_N(rad)$	$\sigma_F(rad)$	$\sqrt{\left\langle j_{Ty}^2\right\rangle}$	$\left\langle \sin^2\phi_{jj}\right\rangle$
1.208	0.284 ± 0.011	0.494 ± 0.022	0.336 ± 0.013	0.140 ± 0.017
1.711	0.227 ± 0.007	0.410 ± 0.019	0.372 ± 0.011	0.104 ± 0.013
2.371	0.193 ± 0.005	0.380 ± 0.015	0.423 ± 0.011	0.097 ± 0.009
3.394	0.177 ± 0.006	0.322 ± 0.020	0.517 ± 0.017	0.067 ± 0.011
4.414	0.130 ± 0.007	0.315 ± 0.026	0.455 ± 0.024	0.076 ± 0.014

Table C.3   Near- and far-angle widths extracted from centrality integrated, 0-88% d+Au $\pi^0 - h$ correlations with a constant π^0 p_T of 5-10 GeV/c. ($\langle p_{T,trig}\rangle = 5.729$ GeV/c) The errors are statistical only.

$p_{T,assoc}$	x_E	S_N	S_F
1.208	0.187 ± 0.033	0.169 ± 0.006	0.256 ± 0.014
1.711	0.268 ± 0.050	0.095 ± 0.003	0.130 ± 0.006
2.371	0.378 ± 0.068	0.088 ± 0.002	0.128 ± 0.005
3.394	0.549 ± 0.094	0.035 ± 0.001	0.044 ± 0.003
4.414	0.713 ± 0.116	0.015 ± 0.001	0.020 ± 0.002

Table C.4   Near- (S_N) and far-(S_F) yields and x_E extracted from centrality integrated, 0-88% d+Au $\pi^0 - h$ correlations with a constant π^0 p_T of 5-10 GeV/c. ($\langle p_{T,trig}\rangle = 5.729$ GeV/c) The errors are statistical only.

$p_{T,assoc}$	$\sigma_N(rad)$	$\sigma_F(rad)$	$\sqrt{\left\langle j_{Ty}^2\right\rangle}$	$\left\langle \sin^2\phi_{jj}\right\rangle$
1.207	0.303 ± 0.022	0.522 ± 0.037	0.358 ± 0.026	0.154 ± 0.031
1.711	0.202 ± 0.013	0.395 ± 0.033	0.331 ± 0.021	0.103 ± 0.022
2.368	0.199 ± 0.009	0.387 ± 0.024	0.436 ± 0.020	0.099 ± 0.015
3.389	0.179 ± 0.009	0.423 ± 0.044	0.522 ± 0.023	0.128 ± 0.028
4.410	0.126 ± 0.012	0.228 ± 0.058	0.440 ± 0.021	0.035 ± 0.025

Table C.5   Near- and far-angle widths extracted from 0-20% central d+Au $\pi^0 - h$ correlations with a constant π^0 p_T of 5-10 GeV/c. ($\langle p_{T,trig}\rangle = 5.717$ GeV/c) The errors are statistical only.

$p_{T,assoc}$	x_E	S_N	S_F
1.207	0.185 ± 0.037	0.176 ± 0.014	0.291 ± 0.026
1.711	0.270 ± 0.047	0.079 ± 0.005	0.128 ± 0.012
2.368	0.378 ± 0.060	0.082 ± 0.004	0.116 ± 0.008
3.389	0.548 ± 0.083	0.038 ± 0.002	0.044 ± 0.005
4.410	0.715 ± 0.118	0.015 ± 0.001	0.011 ± 0.002

Table C.6 Near- (S_N) and far-(S_F) yields and x_E extracted from 0-20% central d+Au $\pi^0 - h$ correlations with a constant π^0 p_T of 5-10 GeV/c. ($\langle p_{T,trig} \rangle = 5.717$ GeV/c) The errors are statistical only.

$p_{T,assoc}$	$\sigma_N(rad)$	$\sigma_F(rad)$	$\sqrt{\langle j_{Ty}^2 \rangle}$	$\langle \sin^2 \phi_{jj} \rangle$
1.208	0.275 ± 0.017	0.485 ± 0.044	0.325 ± 0.020	0.138 ± 0.033
1.711	0.243 ± 0.013	0.456 ± 0.033	0.398 ± 0.021	0.129 ± 0.024
2.372	0.195 ± 0.009	0.401 ± 0.031	0.427 ± 0.020	0.109 ± 0.020
3.398	0.180 ± 0.012	0.265 ± 0.029	0.526 ± 0.035	0.036 ± 0.015
4.411	0.113 ± 0.010	0.327 ± 0.065	0.395 ± 0.035	0.086 ± 0.035

Table C.7 Near- and far-angle widths extracted from 20-40% central d+Au $\pi^0 - h$ correlations with a constant π^0 p_T of 5-10 GeV/c. ($\langle p_{T,trig} \rangle = 5.728$ GeV/c) The errors are statistical only.

$p_{T,assoc}$	x_E	S_N	S_F
1.208	0.186 ± 0.038	0.170 ± 0.012	0.231 ± 0.024
1.711	0.268 ± 0.049	0.115 ± 0.006	0.153 ± 0.014
2.372	0.379 ± 0.071	0.095 ± 0.004	0.141 ± 0.011
3.398	0.552 ± 0.120	0.029 ± 0.002	0.041 ± 0.004
4.411	0.708 ± 0.125	0.013 ± 0.001	0.022 ± 0.004

Table C.8 Near- (S_N) and far-(S_F) yields and x_E extracted from 20-40% central d+Au $\pi^0 - h$ correlations with a constant π^0 p_T of 5-10 GeV/c. ($\langle p_{T,trig} \rangle = 5.728$ GeV/c) The errors are statistical only.

$p_{T,assoc}$	$\sigma_N(rad)$	$\sigma_F(rad)$	$\sqrt{\left\langle j_{Ty}^2 \right\rangle}$	$\langle \sin^2 \phi_{jj} \rangle$
1.208	0.273 ± 0.016	0.484 ± 0.031	0.323 ± 0.019	0.138 ± 0.024
1.712	0.234 ± 0.012	0.357 ± 0.028	0.384 ± 0.020	0.068 ± 0.018
2.378	0.190 ± 0.008	0.376 ± 0.024	0.331 ± 0.015	1.027 ± 0.084
3.399	0.172 ± 0.012	0.284 ± 0.026	0.503 ± 0.035	0.049 ± 0.014
4.424	0.169 ± 0.010	0.403 ± 0.035	0.592 ± 0.035	0.118 ± 0.022

Table C.9   Near- and far-angle widths extracted from 40-88% central d+Au $\pi^0 - h$ correlations with a constant π^0 p_T of 5-10 GeV/c. ($\langle p_{T,trig} \rangle = 5.746$ GeV/c) The errors are statistical only.

$p_{T,assoc}$	x_E	S_N	S_F
1.208	0.187 ± 0.033	0.168 ± 0.010	0.520 ± 0.040
1.712	0.267 ± 0.055	0.099 ± 0.003	0.121 ± 0.010
2.378	0.376 ± 0.076	0.097 ± 0.004	0.144 ± 0.009
3.399	0.547 ± 0.088	0.035 ± 0.002	0.051 ± 0.005
4.424	0.723 ± 0.100	0.020 ± 0.002	0.030 ± 0.003

Table C.10   Near- (S_N) and far-(S_F) yields and x_E extracted from 40-88% central d+Au $\pi^0 - h$ correlations with a constant π^0 p_T of 5-10 GeV/c. ($\langle p_{T,trig} \rangle = 5.746$ GeV/c) The errors are statistical only.

Constant Associated $h^\pm$ p_T Correlations

The following correlations are for associated charged hadrons in a constant range from 2.5-5 GeV/c. The π^0 triggers are varied from 5-6-7-10 GeV/c.

Figure C.6   The left panels are two particle azimuthal correlations in p+p collisions with associated hadrons from 2.5-5.0 GeV/c with varied trigger π^0 p_T ranges from top to bottom: 5.0-6.0 GeV/c, 6.0-7.0 GeV/c, 7.0-10.0 GeV/c. The right panels are the corresponding x_E distribution for the given trigger and associated range.
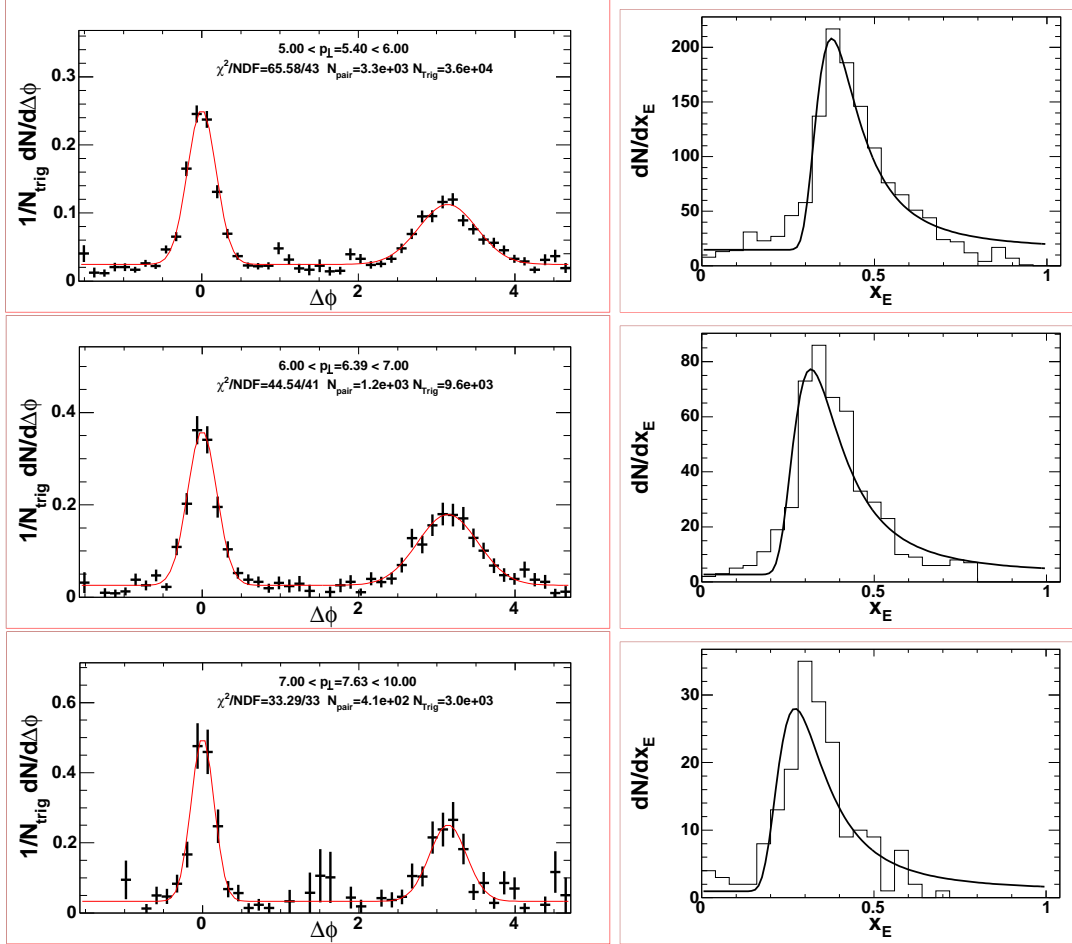
Figure C.7 The left panels are two particle azimuthal correlations in centrality integrated (0-88%) d+Au collisions with associated hadrons from 2.5-5.0 GeV/c with varied trigger π^0 p_T ranges from top to bottom: 5.0-6.0 GeV/c, 6.0-7.0 GeV/c, 7.0-10.0 GeV/c. The right panels are the corresponding x_E distribution for the given trigger and associated range.
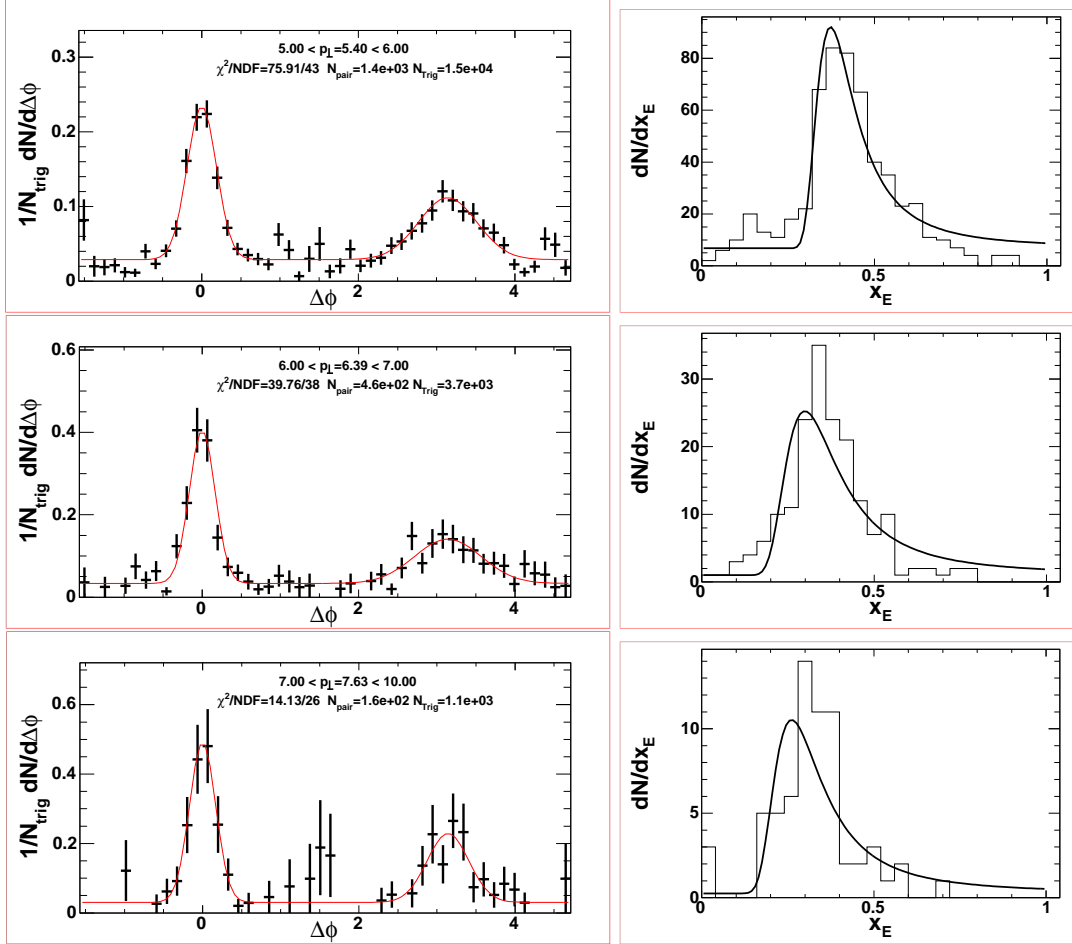
Figure C.8   The left panels are two particle azimuthal correlations in 0-20% central d+Au collisions with associated hadrons from 2.5-5.0 GeV/c with varied trigger π^0 p_T ranges from top to bottom: 5.0-6.0 GeV/c, 6.0-7.0 GeV/c, 7.0-10.0 GeV/c. The right panels are the corresponding x_E distribution for the given trigger and associated range.
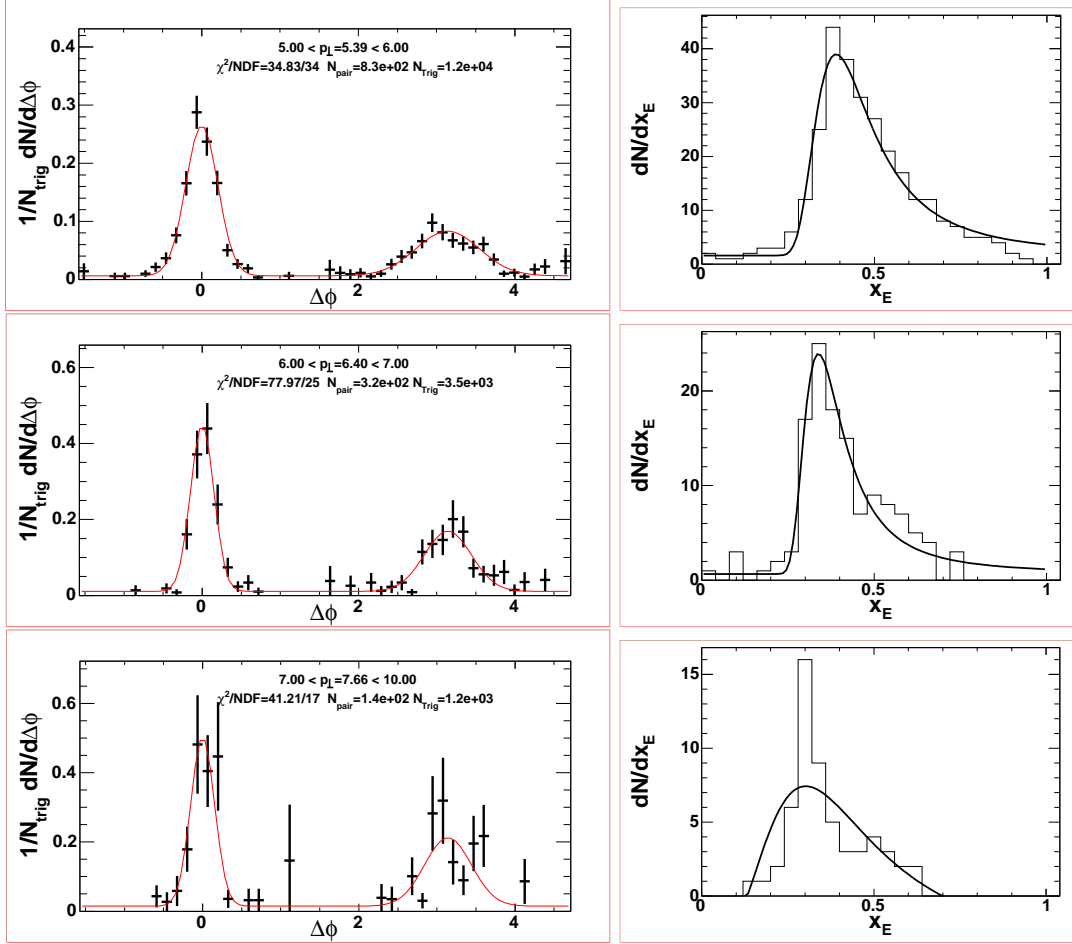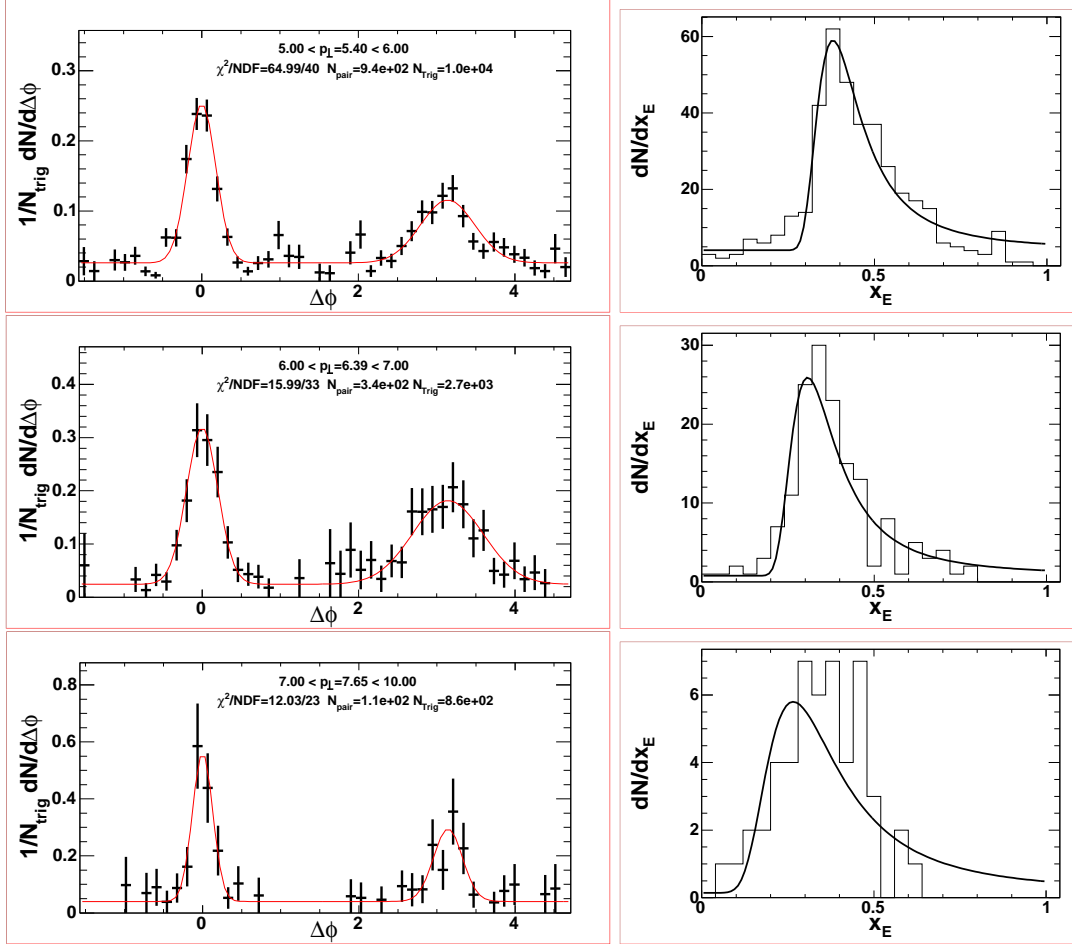
Figure C.9   The left panels are two particle azimuthal correlations in 20-40% central d+Au collisions with associated hadrons from 2.5-5.0 GeV/c with varied trigger π^0 p_T ranges from top to bottom: 5.0-6.0 GeV/c, 6.0-7.0 GeV/c, 7.0-10.0 GeV/c. The right panels are the corresponding x_E distribution for the given trigger and associated range.

Figure C.10   The left panels are two particle azimuthal correlations in 40-88% central d+Au collisions with associated hadrons from 2.5-5.0 GeV/c with varied trigger π^0 p_T ranges from top to bottom: 5.0-6.0 GeV/c, 6.0-7.0 GeV/c, 7.0-10.0 GeV/c. The right panels are the corresponding x_E distribution for the given trigger and associated range.
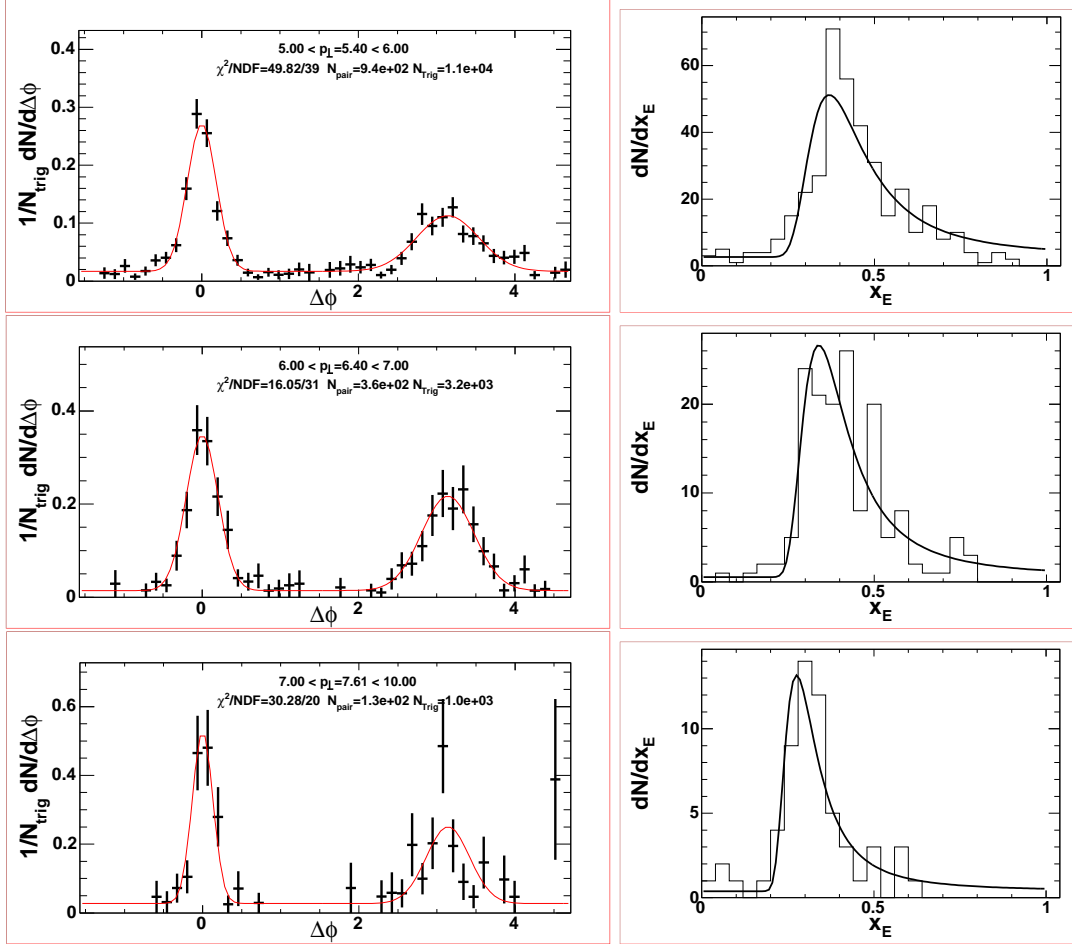
$p_{T,trig}$	$\sigma_N(rad)$	$\sigma_F(rad)$	$\sqrt{\left\langle j_{Ty}^2 \right\rangle}$	$\langle \sin^2 \phi_{jj} \rangle$
5.394	0.207 ± 0.007	0.409 ± 0.025	0.499 ± 0.017	0.110 ± 0.016
6.398	0.151 ± 0.008	0.304 ± 0.034	0.375 ± 0.020	0.065 ± 0.018
7.658	0.144 ± 0.012	0.295 ± 0.035	0.366 ± 0.031	0.062 ± 0.018

Table C.11   Near- and far-angle widths extracted from p+p $\pi^0 - h$ correlations with a constant hadron p_T of 2.5-5 GeV/c. ($\langle p_{T,assoc} \rangle = 2.697$ GeV/c) The errors are statistical only.

$p_{T,trig}$	$\sigma_N(rad)$	$\sigma_F(rad)$	$\sqrt{\left\langle j_{Ty}^2 \right\rangle}$	$\langle \sin^2 \phi_{jj} \rangle$
5.398	0.184 ± 0.004	0.374 ± 0.015	0.439 ± 0.010	0.096 ± 0.009
6.391	0.188 ± 0.007	0.388 ± 0.022	0.462 ± 0.017	0.103 ± 0.014
7.631	0.147 ± 0.009	0.233 ± 0.025	0.369 ± 0.023	0.032 ± 0.011

Table C.12   Near- and far-angle widths extracted from centrality integrated, 0-88% d+Au π^0-h correlations with a constant hadron p_T of 2.5-5 GeV/c ($\langle p_{T,assoc} \rangle = 2.659$ GeV/c). The errors are statistical only.

$p_{T,trig}$	$\sigma_N(rad)$	$\sigma_F(rad)$	$\sqrt{\left\langle j_{Ty}^2 \right\rangle}$	$\langle \sin^2 \phi_{jj} \rangle$
5.398	0.189 ± 0.007	0.376 ± 0.023	0.448 ± 0.017	0.095 ± 0.017
6.390	0.152 ± 0.010	0.431 ± 0.048	0.370 ± 0.024	0.139 ± 0.030
7.634	0.172 ± 0.014	0.263 ± 0.043	0.429 ± 0.035	0.038 ± 0.021

Table C.13   Near- and far-angle widths extracted from 0-20% d+Au π^0-h correlations with a constant hadron p_T of 2.5-5 GeV/c ($\langle p_{T,assoc} \rangle = 2.636$ GeV/c). The errors are statistical only.

$p_{T,trig}$	$\sigma_N(rad)$	$\sigma_F(rad)$	$\sqrt{\left\langle j_{Ty}^2 \right\rangle}$	$\left\langle \sin^2 \phi_{jj} \right\rangle$
5.395	0.179 ± 0.008	0.346 ± 0.031	0.428 ± 0.019	0.080 ± 0.018
6.387	0.203 ± 0.016	0.458 ± 0.059	0.499 ± 0.020	0.144 ± 0.039
7.650	0.126 ± 0.016	0.177 ± 0.030	0.317 ± 0.040	0.015 ± 0.011

Table C.14   Near- and far-angle widths extracted from 20-40% d+Au π^0-h correlations with a constant hadron p_T of 2.5-5 GeV/c ($\langle p_{T,assoc} \rangle = 2.666$ GeV/c). The errors are statistical only.

$p_{T,trig}$	$\sigma_N(rad)$	$\sigma_F(rad)$	$\sqrt{\left\langle j_{Ty}^2 \right\rangle}$	$\left\langle \sin^2 \phi_{jj} \right\rangle$
5.399	0.187 ± 0.008	0.397 ± 0.028	0.453 ± 0.019	0.109 ± 0.018
6.396	0.207 ± 0.013	0.336 ± 0.025	0.516 ± 0.032	0.065 ± 0.016
7.613	0.122 ± 0.014	0.270 ± 0.050	0.311 ± 0.036	0.055 ± 0.024

Table C.15   Near- and far-angle widths extracted from 40-88% d+Au π^0-h correlations with a constant hadron p_T of 2.5-5 GeV/c ($\langle p_{T,assoc} \rangle = 2.707$ GeV/c). The errors are statistical only.

APPENDIX D. π^0-h Correlations in Au+Au Collisions

This appendix contains the π^0-h correlations functions and jet functions from Au+Au collisions.
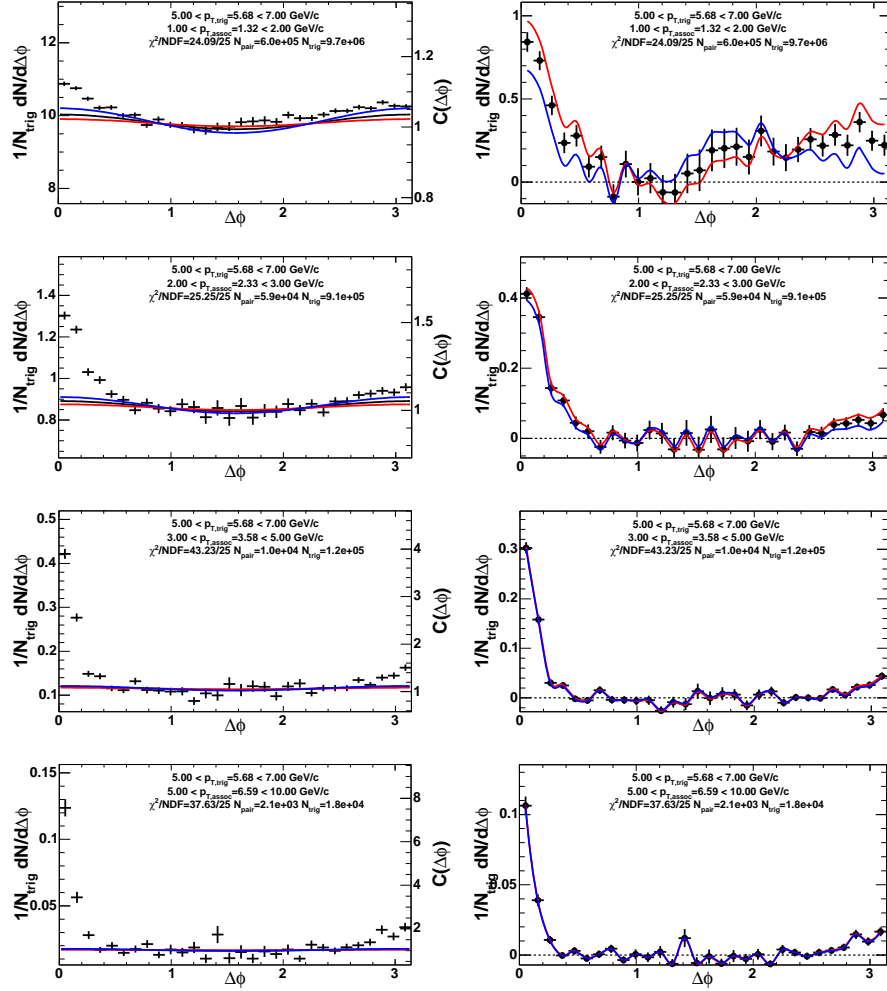
Correlation and Jet Functions

Figure D.1   The left panels are correlations in minimum bias Au+Au us-
ing π^0 triggers from 5-7 GeV/c and several different associated
hadron p_T bins. The right panels are the resulting jet correla-
tions where the background and elliptic flow have subtracted.
The blue and red lines are the systematic error due to the sub-
traction of the elliptic flow component.

Figure D.2   The left panels are correlations in 0-20% Au+Au using π^0 triggers from 5-7 GeV/c and several different associated hadron p_T bins. The right panels are the resulting jet correlations where the background and elliptic flow have subtracted. The blue and red lines are the systematic error due to the subtraction of the elliptic flow component.

Figure D.3   The left panels are correlations in 20-40% Au+Au using π^0 triggers from 5-7 GeV/c and several different associated hadron p_T bins. The right panels are the resulting jet correlations where the background and elliptic flow have subtracted. The blue and red lines are the systematic error due to the subtraction of the elliptic flow component.
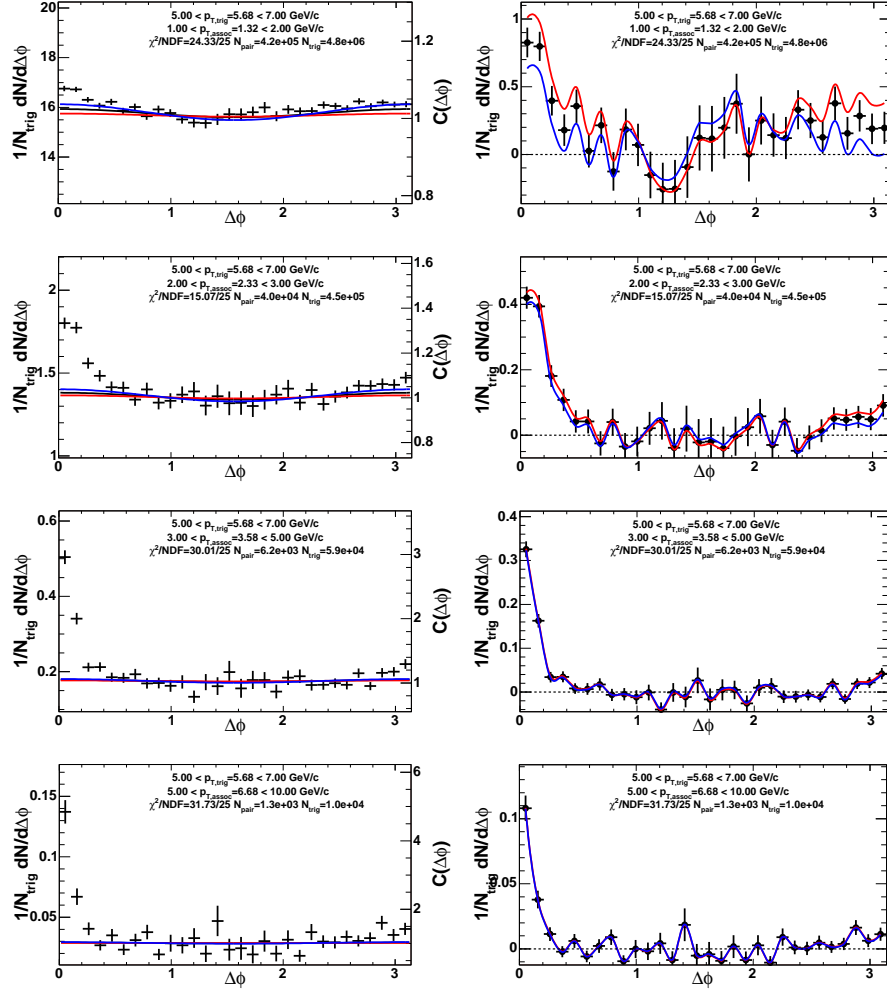
Figure D.4   The left panels are correlations in 40-92% Au+Au using π^0 triggers from 5-7 GeV/c and several different associated hadron p_T bins. The right panels are the resulting jet correlations where the background and elliptic flow have subtracted. The blue and red lines are the systematic error due to the subtraction of the elliptic flow component.
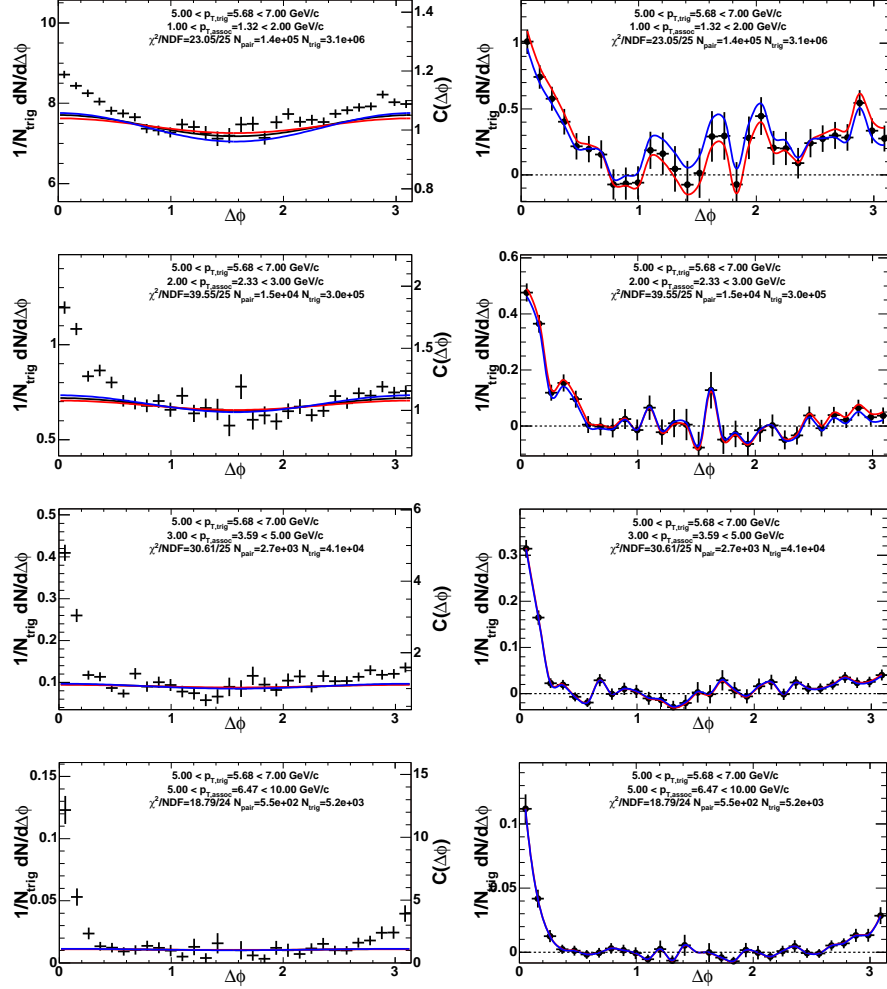
Figure D.5   The left panels are correlations in minimum bias Au+Au using
π^0 triggers from 7-10 GeV/c and several different associated
hadron p_T bins. The right panels are the resulting jet correla-
tions where the background and elliptic flow have subtracted.
The blue and red lines are the systematic error due to the sub-
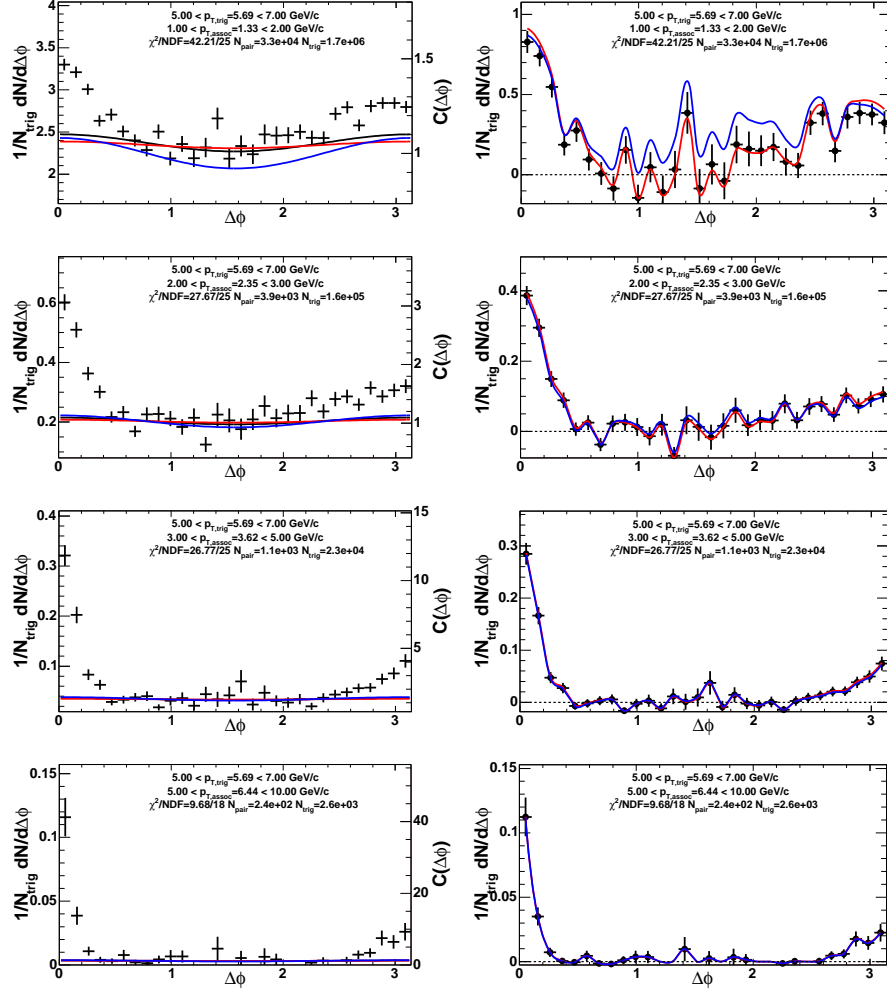traction of the elliptic flow component.

Figure D.6   The left panels are correlations in 0-20% Au+Au using π^0 triggers from 7-10 GeV/c and several different associated hadron p_T bins. The right panels are the resulting jet correlations where the background and elliptic flow have subtracted. The blue and red lines are the systematic error due to the subtraction of the elliptic flow component.
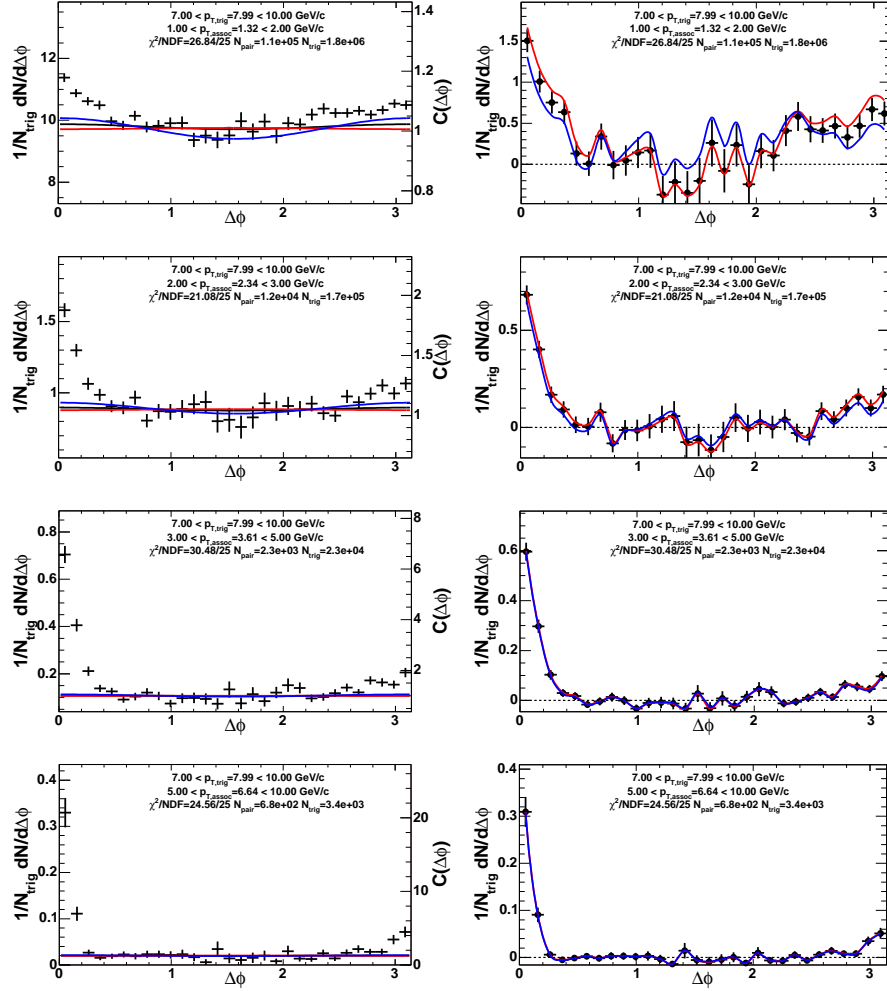
Figure D.7 The left panels are correlations in 20-40% Au+Au using π^0 triggers from 7-10 GeV/c and several different associated hadron p_T bins. The right panels are the resulting jet correlations where the background and elliptic flow have subtracted. The blue and red lines are the systematic error due to the subtraction of the elliptic flow component.
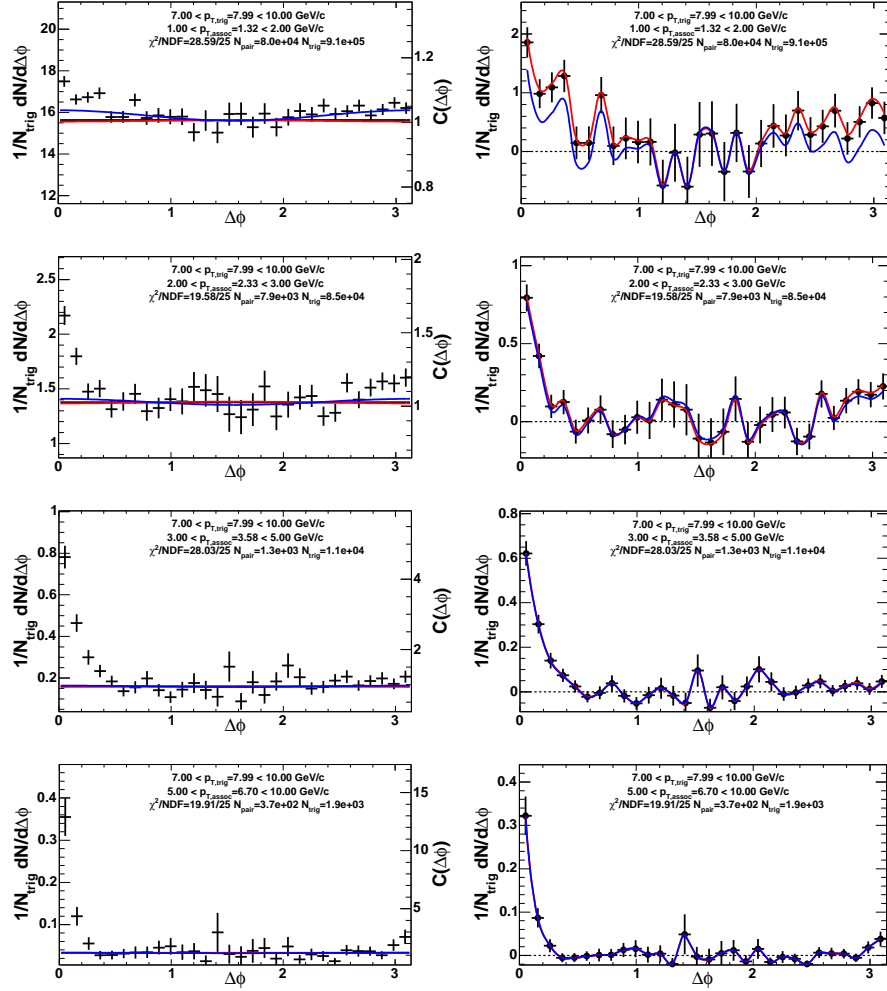
Figure D.8   The left panels are correlations in 40-92% Au+Au using π^0 triggers from 7-10 GeV/c and several different associated hadron p_T bins. The right panels are the resulting jet correlations where the background and elliptic flow have subtracted. The blue and red lines are the systematic error due to the subtraction of the elliptic flow component.

Figure D.9   The left panels are correlations in minimum bias Au+Au using
π^0 triggers from 10-20 GeV/c and several different associated
hadron p_T bins. The right panels are the resulting jet correla-
tions where the background and elliptic flow have subtracted.
The blue and red lines are the systematic error due to the sub-
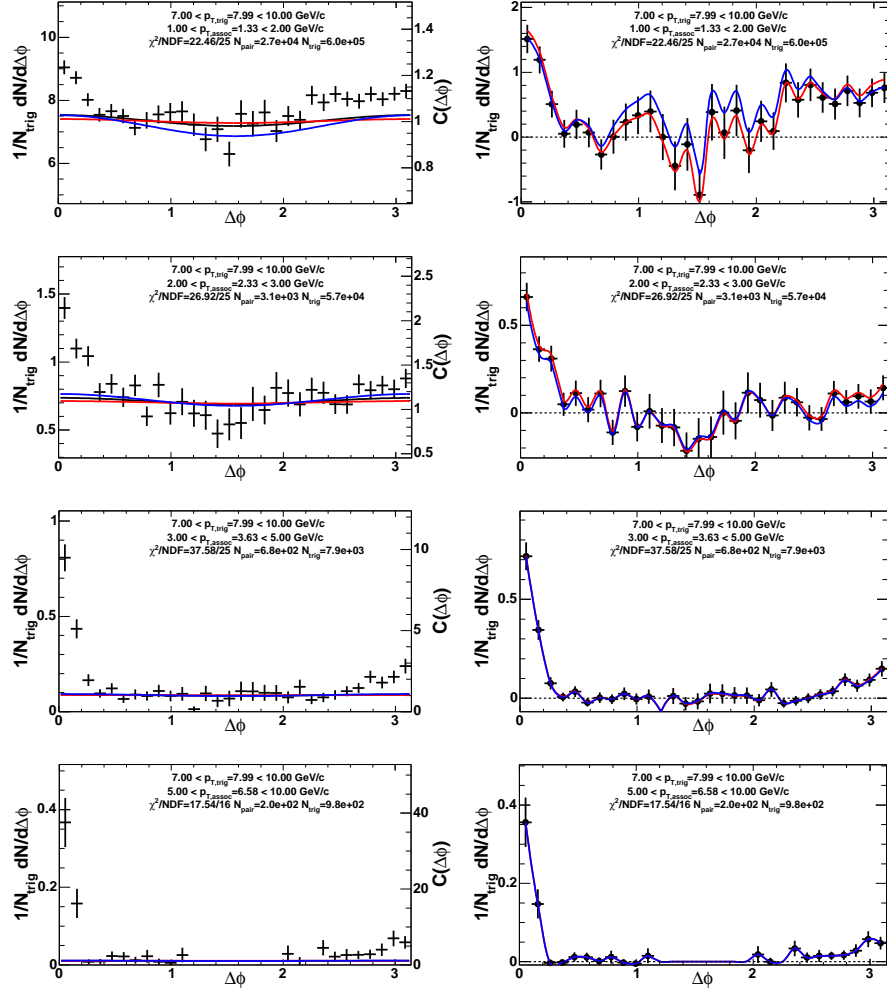traction of the elliptic flow component.
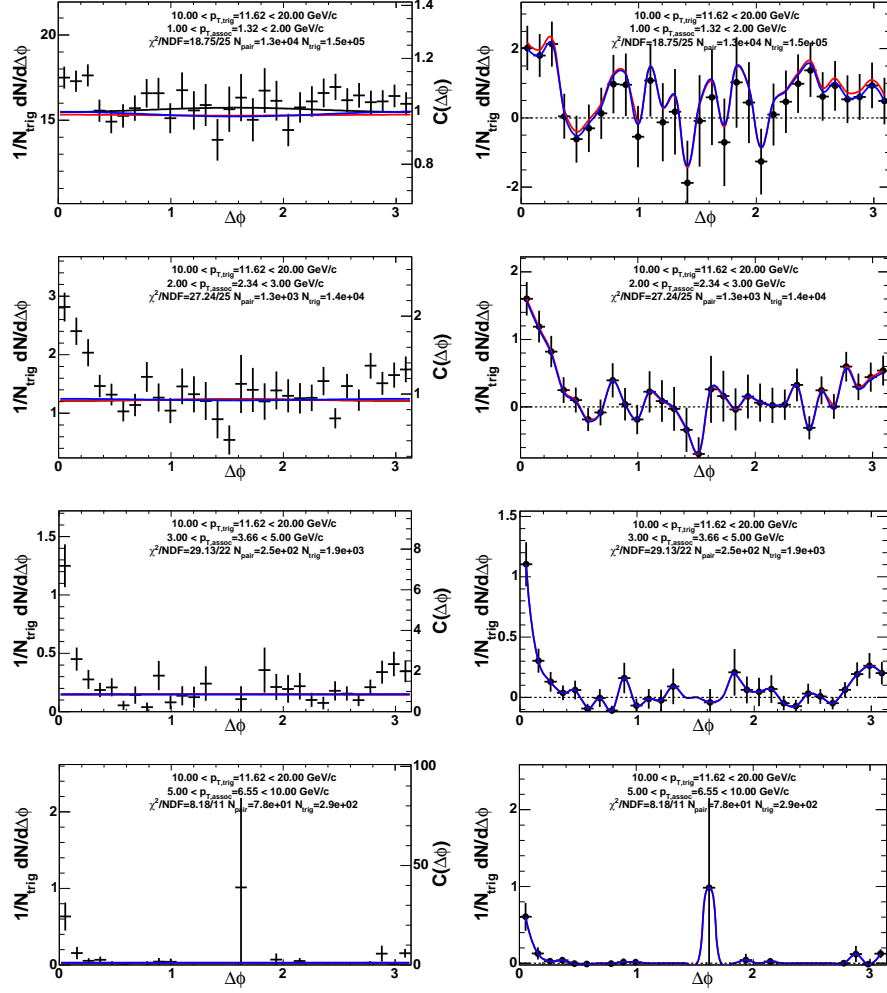
Figure D.10   The left panels are correlations in 0-20% Au+Au using π^0 triggers from 10-20 GeV/c and several different associated hadron p_T bins. The right panels are the resulting jet correlations where the background and elliptic flow have subtracted. The blue and red lines are the systematic error due to the subtraction of the elliptic flow component.
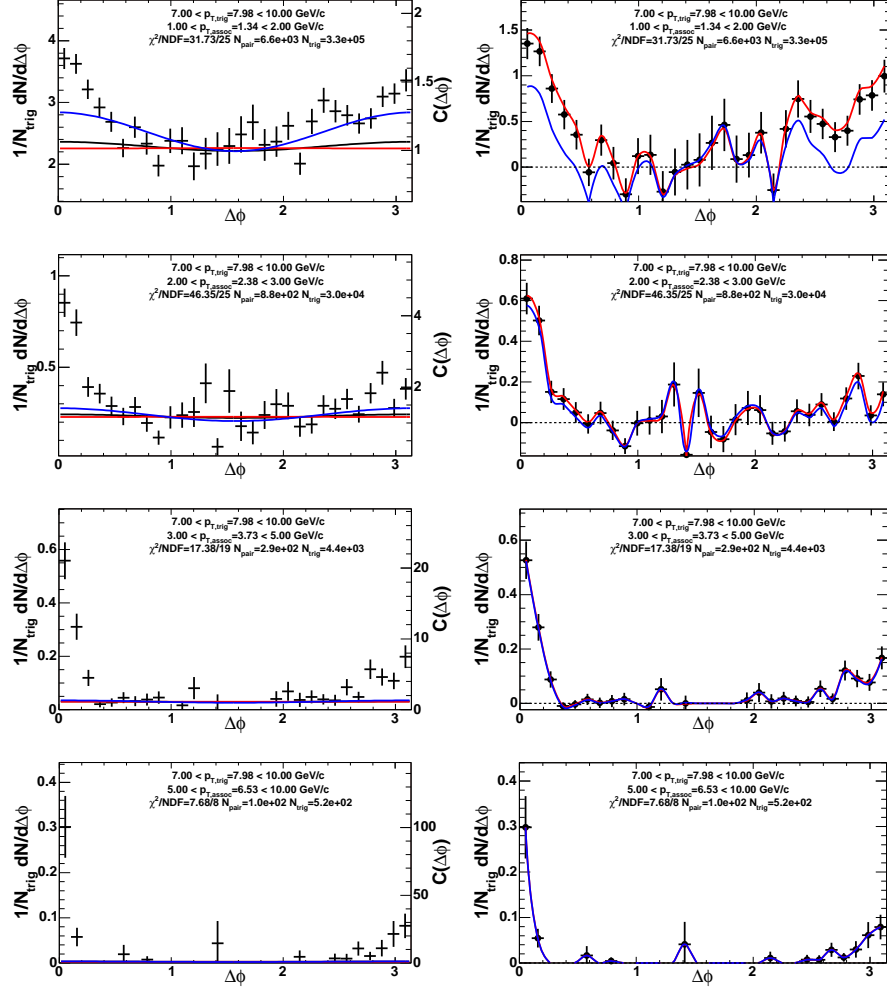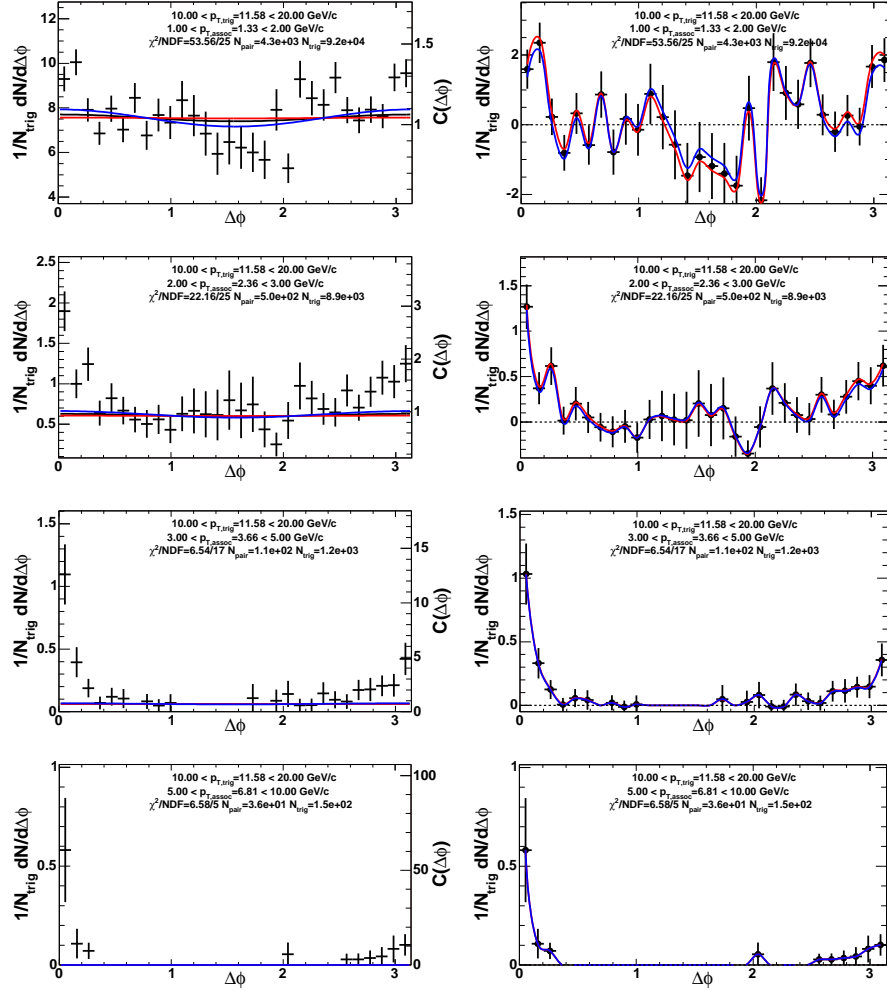
Figure D.11   The left panels are correlations in 20-40% Au+Au using π^0 triggers from 10-20 GeV/c and several different associated hadron p_T bins. The right panels are the resulting jet correlations where the background and elliptic flow have subtracted. The blue and red lines are the systematic error due to the subtraction of the elliptic flow component.
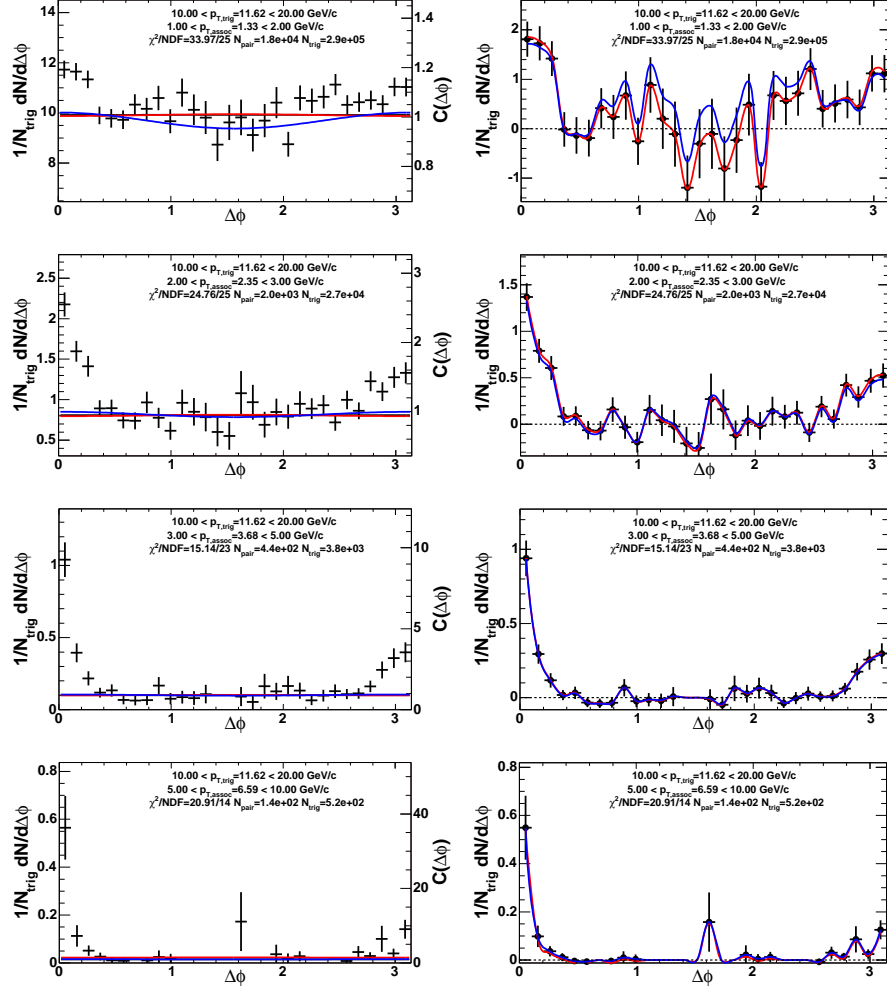
Figure D.12 The left panels are correlations in 40-92% Au+Au using π^0 triggers from 10-20 GeV/c and several different associated hadron p_T bins. The right panels are the resulting jet correlations where the background and elliptic flow have subtracted. The blue and red lines are the systematic error due to the subtraction of the elliptic flow component.
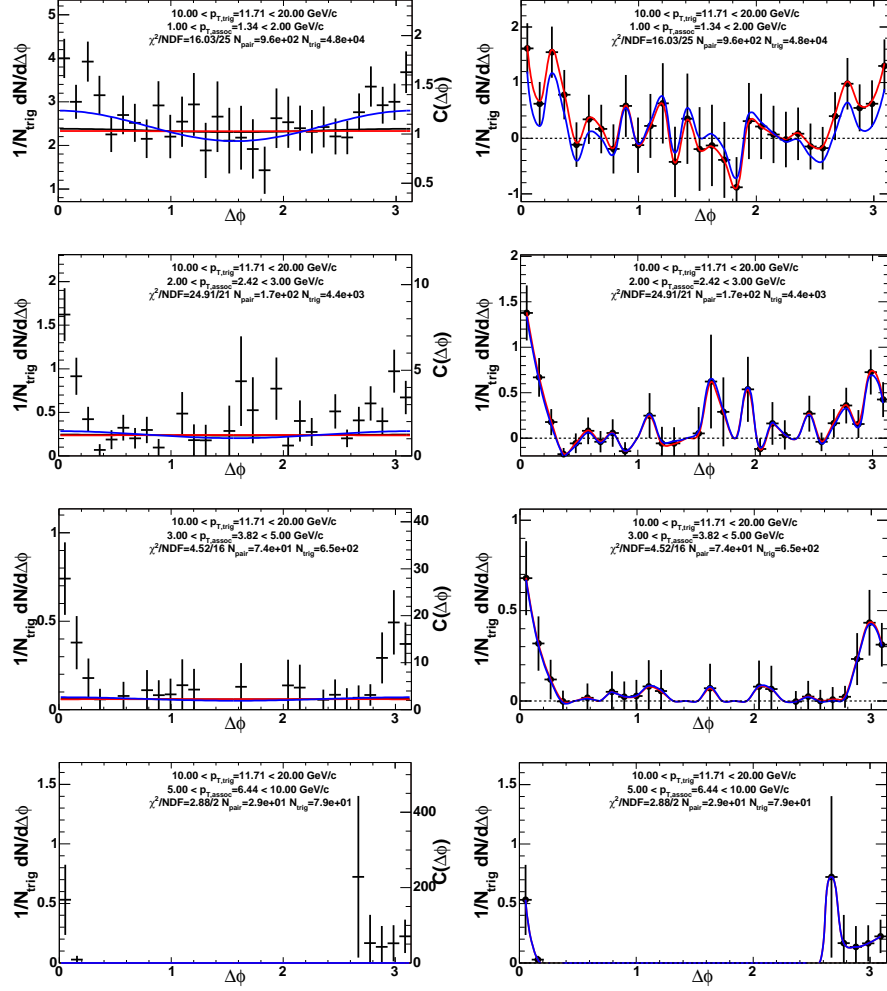
BIBLIOGRAPHY

Abbott B et al. 2001 *Phys. Rev.* **D64**, 032003.

Abe F et al. 1992 *Phys. Rev.* **D45**, 1448–1458.

Abe F et al. 1996 *Phys. Rev. Lett.* **77**, 438–443.

Accardi A 2002 *hep-ph/0212148* .

Adams J et al. 2003 *Phys. Rev. Lett.* **91**, 072304.

Adams J et al. 2004a *nucl-ex/0411003* .

Adams J et al. 2004b *Phys. Rev. Lett.* **93**, 252301.

Adams J et al. 2004c *nucl-ex/0409033* .

Adams J et al. 2005 *Nucl. Phys.* **A757**, 102–183.

Adcox K et al. 2002 *Phys. Rev. Lett.* **88**, 022301.

Adcox K et al. 2003 *Nucl. Instrum. Meth.* **A499**, 469–479.

Adcox K et al. 2005 *Nucl. Phys.* **A757**, 184–283.

Adler C et al. 2001 *Nucl. Instrum. Meth.* **A461**, 337–340.

Adler C et al. 2003a *Phys. Rev. Lett.* **90**, 082302.

Adler S S et al. 2003b *Phys. Rev. Lett.* **91**, 072301.

Adler S S et al. 2003c *Phys. Rev. Lett.* **91**, 072303.

Adler S S et al. 2003*d Phys. Rev. Lett.* **91**, 172301.

Adler S S et al. 2003*e Phys. Rev. Lett.* **91**, 241803.

Adler S S et al. 2004 *Phys. Rev.* **C69**, 034910.

Adler S S et al. 2005*a nucl-ex/0507004* .

Adler S S et al. 2005*b nucl-ex/0510021* .

Adler S S et al. 2005*c Phys. Rev.* **C71**, 034908.

Adler S S et al. 2005*d Phys. Rev.* **C71**, 051902.

Affolder T et al. 2001 *Phys. Rev.* **D64**, 032001.

Agababyan N M et al. 1994 *Phys. Lett.* **B320**, 411–416.

Aggarwal M M et al. 2002 *Eur. Phys. J.* **C23**, 225–236.

Aizawa M et al. 2003 *Nucl. Instrum. Meth.* **A499**, 508–520.

Akers R et al. 1994 *Z. Phys.* **C63**, 197–212.

Allen M et al. 2003 *Nucl. Instrum. Meth.* **A499**, 549–559.

Alner G J et al. 1986 *Z. Phys.* **C33**, 1.

Alper B et al. 1975 *Nucl. Phys.* **B87**, 19.

Angelis A L S et al. 1978 *Phys. Lett.* **B79**, 505–510.

Angelis A L S et al. 1980 *Phys. Lett.* **B97**, 163.

Angelis A L S et al. 1987 *Phys. Lett.* **B185**, 213.

Antreasyan D et al. 1979 *Phys. Rev.* **D19**, 764.

Aphecetche L et al. 2003 *Nucl. Instrum. Meth.* **A499**, 521–536.

Appel D A 1986 *Phys. Rev.* **D33**, 717.

Arnold P, Moore G D and Yaffe L G 2003 *JHEP* **05**, 051.

Aronson S H et al. 2003 *Nucl. Instrum. Meth.* **A499**, 480–488.

Arsene I et al. 2005 *Nucl. Phys.* **A757**, 1–27.

Back B B et al. 2003*a* *Phys. Rev. Lett.* **91**, 072302.

Back B B et al. 2003*b* *Phys. Rev. Lett.* **91**, 052303.

Back B B et al. 2004 *Phys. Rev. Lett.* **93**, 082301.

Back B B et al. 2005 *Nucl. Phys.* **A757**, 28–101.

Baier R, Dokshitzer Y L, Mueller A H, Peigne S and Schiff D 1997 *Nucl. Phys.* **B483**, 291–320.

Baier R, Dokshitzer Y L, Mueller A H and Schiff D 1999 *Phys. Rev.* **C60**, 064902.

Bali G S and Schilling K 1993 *Phys. Rev.* **D47**, 661–672.

Banner M et al. 1982 *Phys. Lett.* **B118**, 203–210.

Barber D P et al. 1979 *Phys. Rev. Lett.* **43**, 830.

Bauer F et al. 2003 *PHENIX Internal Analysis Note* **228**.

Baym G 2004 *J. Phys.* **G30**, xxiii–xxxii.

Berman S M, Bjorken J D and Kogut J B 1971 *Phys. Rev.* **D4**, 3388.

Bjorken J D 1969 *Phys. Rev.* **179**, 1547–1553.

Bjorken J D 1983 *Phys. Rev.* **D27**, 140–151.

Bjorken J D n.d. FERMILAB-PUB-82-059-THY.

Bjorken J D and Paschos E A 1969 *Phys. Rev.* **185**, 1975–1982.

Blaizot J P and McLerran L D 1986 *Phys. Rev.* **D34**, 2739.

Blaschke D, Kaczmarek O, Laermann E and Yudichev V 2005 *Eur. Phys. J.* **C43**, 81–84.

Bloom E D et al. 1969 *Phys. Rev. Lett.* **23**, 930–934.

Bodek A et al. 1979 *Phys. Rev.* **D20**, 1471–1552.

Brandelik R et al. 1979 *Phys. Lett.* **B86**, 243.

Breidenbach M et al. 1969 *Phys. Rev. Lett.* **23**, 935–939.

Busser F W et al. 1973 *Phys. Lett.* **B46**, 471–476.

Callan, C. G. J and Gross D J 1969 *Phys. Rev. Lett.* **22**, 156–159.

Catani S, Dokshitzer Y L, Olsson M, Turnock G and Webber B R 1991 *Phys. Lett.* **B269**, 432–
    438.

Clark A G et al. 1979 *Nucl. Phys.* **B160**, 397.

Constantin P 2004 *Ph.D. thesis, Iowa State University* .

Corcoran M D et al. 1991 *Phys. Lett.* **B259**, 209–215.

Cronin J W et al. 1975 *Phys. Rev.* **D11**, 3105.

Dainese A, Loizides C and Paic G 2005 *Eur. Phys. J.* **C38**, 461–474.

Darriulat P et al. 1976 *Nucl. Phys.* **B107**, 429.

David G et al. 2000*a IEEE Trans. Nucl. Sci.* **47**, 1982–1986.

David G et al. 2000*b PHENIX Internal Analysis Note* **009**.

Della Negra M et al. 1977 *Nucl. Phys.* **B127**, 1.

d'Enterria D 2004 *Phys. Lett.* **B596**, 32–43.

Drees A, Feng H and Jia J 2005 *Phys. Rev.* **C71**, 034909.

Eidelman S et al. 2004 *Phys. Lett. B* **592**, 1.

Feynman R P 1969 *Phys. Rev. Lett.* **23**, 1415–1417.

Feynman R P, Field R D and Fox G C 1977 *Nucl. Phys.* **B128**, 1.

Feynman R P, Field R D and Fox G C 1978 *Phys. Rev.* **D18**, 3320.

Field R D and Feynman R P 1977 *Phys. Rev.* **D15**, 2590–2616.

Friedman J I and Kendall H W 1972 *Ann. Rev. Nucl. Part. Sci.* **22**, 203–254.

Fries R J, Muller B, Nonaka C and Bass S A 2003 *Phys. Rev. Lett.* **90**, 202303.

Gordon L E and Vogelsang W 1993 *Phys. Rev.* **D48**, 3136–3159.

Gross D J and Wilczek F 1973 *Phys. Rev. Lett.* **30**, 1343–1346.

Gyulassy M, Levai P and Vitev I 2000 *Phys. Rev. Lett.* **85**, 5535–5538.

Gyulassy M, Levai P and Vitev I 2001 *Nucl. Phys.* **B594**, 371–419.

Gyulassy M and Plumer M 1990 *Phys. Lett.* **B243**, 432–438.

Gyulassy M, Vitev I and Wang X N 2001 *Phys. Rev. Lett.* **86**, 2537–2540.

Hanson G et al. 1975 *Phys. Rev. Lett.* **35**, 1609–1612.

Hwa R C and Tan Z 2005 *Phys. Rev.* **C72**, 057902.

Hwa R C and Yang C B 2004*a* *Phys. Rev. Lett.* **93**, 082302.

Hwa R C and Yang C B 2004*b* *Phys. Rev.* **C70**, 054902.

Jia J 2005 *J. Phys.* **G31**, S521–S532.

Jia J and Cole B 2004*a* *PHENIX Internal Analysis Note* **312**.

Jia J and Cole B 2004*b* *PHENIX Internal Analysis Note* **313**.

Jia J and Cole B 2004*c* *PHENIX Internal Analysis Note* **332**.

Jia J et al. 2005 *PHENIX Internal Analysis Note* **429**.

Kuhn J H 1976 *Phys. Rev.* **D13**, 2948.

Lev M and Petersson B 1983 *Z. Phys.* **C21**, 155.

Magestro D 2005 *nucl-ex/0510002* .

Majumder A and Wang X N 2004 *Phys. Rev.* **D70**, 014007.

Messer F and Jia J 2002 *PHENIX Internal Analysis Note* **127**.

Milov S et al. 2003 *PHENIX Internal Analysis Note* **210**.

Mitchell J T et al. 2002 *Nucl. Instrum. Meth.* **A482**, 491–512.

Molnar D and Voloshin S A 2003 *Phys. Rev. Lett.* **91**, 092301.

Naples D et al. 1994 *Phys. Rev. Lett.* **72**, 2341–2344.

Ogilvie C A and Rak J 2001 *PHENIX Internal Analysis Note* **083**.

Politzer H D 1973 *Phys. Rev. Lett.* **30**, 1346–1349.

Qiu J W and Vitev I 2003 *Phys. Lett.* **B570**, 161–170.

Rak J and Tannenbaum M J 2005 *PHENIX Internal Analysis Note* **455**.

Rammerstorfer M and Heinz U W 1990 *Phys. Rev.* **D41**, 306–309.

Reuter M et al. 2004 *PHENIX Internal Analysis Note* **263**.

Rossi A M et al. 1975 *Nucl. Phys.* **B84**, 269.

Sakaguchi T 2005 *nucl-ex/0504013* .

Shimomura M 2005 *nucl-ex/0510023* .

Stankus P 2005 *PHENIX Internal Technical Note* **412**.

Stewart C et al. 1990 *Phys. Rev.* **D42**, 1385–1395.

Stock R 2004 *J. Phys.* **G30**, S633–S648.

Straub P B et al. 1992 *Phys. Rev. Lett.* **68**, 452–455.

Tannenbaum M J 2001 *Phys. Lett.* **B498**, 29–34.

Tannenbaum M J 2005 *nucl-ex/0507020* .

van Apeldoorn G W et al. 1975 *Nucl. Phys.* **B91**, 1.

Vitev I 2005 *hep-ph/0501255* .

Vitev I and Gyulassy M 2002 *Phys. Rev. Lett.* **89**, 252301.

Wang X N 1992 *Phys. Rev.* **D46**, 1900–1902.

Wang X N 1993 *Phys. Rev.* **D47**, 2754–2760.

Wang X N and Gyulassy M 1991 *Phys. Rev.* **D44**, 3501–3516.

Wiedemann U A 2004 *J. Phys.* **G30**, S649–S658.

Winter D 2005 *nucl-ex/0511039* .

Winter D et al. 2005 *PHENIX Internal Analysis Note* **434**.